Artificial Intelligence and MRI as a Tool to Improve Clinical Diagnosis

Artificial Intelligence and MRI as a Tool to Improve Clinical Diagnosis

Artificial Intelligence and MRI as a Tool to Improve Clinical Diagnosis

Lead Guest Editor: Enas Abdulhay
Guest Editors: Arunkumar N and Gustavo Ramirez

Contents

WILEY | Hindawi

Research Article

Comfortable Nursing in the Intraoperative MRI Evaluation Combined with Microsurgery in the Treatment of Functional Area Glioma

Tong Shen,[1] Ran Wang,[1] Xin Zhao,[2] Lin Wang,[1] Ying Li,[1] and Ting Liu [1]

[1]*Department of Anesthesia and Surgery, Xuanwu Hospital Capital Medical University, Beijing 100053, China*
[2]*Disinfection Supply Center, Xuanwu Hospital Capital Medical University, Beijing 100053, China*

Correspondence should be addressed to Ting Liu; 14221010820@stu.cpu.edu.cn

This study was aimed to investigate the application value of magnetic resonance imaging (MRI) scanning examination in the preoperative treatment of functional glioma and to analyze the application effect of nursing intervention in the operating room in the treatment of fiber surgery. In this study, 80 patients with functional glioma were included as research objects and randomly rolled into the control group (routine nursing) and the experimental group (comfort nursing intervention in the operating room), with 40 cases in each group. All patients underwent craniocerebral MRI plain scan plus enhanced scan before surgery. The levels of the heart rate, systolic blood pressure, diastolic blood pressure, interleukin-6 (IL-6), cortisol, and anxiety before and after the intervention in the two groups were compared when patients entered the operating room (T1), when anesthesia took effect (T2), at the end of surgery (T3), when patients regained consciousness after surgery (T4), and 1 day after surgery (T5). MRI showed that the main glioma sites were located in the basal ganglia region (26.25%), followed by the central region (20.00%) and the Broca region (17.5%). The levels of IL-6 at T2, T3, and T4 in the control group were 186.45 ± 64.55 ng/L, 287.68 ± 34.59 ng/L, and 488.69 ± 81.14 ng/L, respectively, which were inferior to those at T2 (167.44 ± 15.59 ng/L), T3 (186.25 ± 52.64 ng/L), and T4 (356.57 ± 48.22 ng/L) in the test group. The SAS score of the test group after intervention (45.38 ± 2.02) was lower than that of the control group (51.03 ± 3.65) ($P < 0.05$). The levels of cortisol in the test group (T2 $8.89\ 1.23$ ng/L), T3 ($9.23\ 1.25$ ng/L), and T4 ($11.78\ 1.27$ ng/L) were lower than those in the control group (T2 (11.58 ± 2.48 ng/L), T3 (12.06 ± 2.82 ng/L), and T4 (13.04 ± 11.78)). In short, preoperative MRI scanning was beneficial to detect the location of glioma in functional area. Comfort nursing in the operating room can effectively relieve the anxiety and depression of glioma patients and improve the adverse psychological conditions of the patients.

1. Introduction

Different regions of the cerebral cortex are functionally specific and have different functions, such as sensation and movement [1]. Gliomas show invasive growth and are defined as functional gliomas when they involve cortical or subcortical structures related to sensory, motor, language, vision, and other higher cognitive functions. It mainly includes sensory motor-related functional brain regions, language-related functional brain regions, and higher

cognitive function-related brain regions [2]. As a brain tumor disease, glioma is the most common primary malignant tumor in the brain, accounting for about 40%–50% of brain tumors, with an annual incidence of 3–8/100,000 [3, 4]. It includes many pathological types, and different pathological types have different grades. The prognosis of glioma varies with different pathological types and grades [5]. Glioblastoma (GBM) accounts for about 50% of gliomas and has a very poor prognosis. After standardized treatment, the median survival time of GBM is about

14.6 months, and the 5-year survival rate is only 9.8%, which can be regarded as the "mother of cancer" [6, 7]. Because of this we often think of glioblastoma as a somewhat incurable disease. However, the prognosis of other types of gliomas is significantly better than that of GBM, and some patients can even survive for more than 10 years. If glioma patients want to achieve a better survival time, standardized treatment is the key. At present, the standardized treatment of glioma includes the following methods. Surgery: surgery is often the first step in the treatment of glioma [8]. It can not only obtain pathological diagnosis but also remove most of the tumor cells, relieve the patient's symptoms, and provide an opportunity for the next treatment. For some low-grade gliomas (generally referring to WHO grade I and II), such as pilocytic astrocytoma, complete surgical resection can make patients get a radical cure [9]. At present, glioma surgery has entered the era of minimally invasive surgery. Neuronavigation technology, subcortical electrical stimulation technology, intraoperative nuclear magnetic resonance imaging, fluorescence imaging, intraoperative B-ultrasound, and other techniques can help surgeons to distinguish the boundary more clearly between tumor and the brain tissue. In order to protect the important neurovascular structures around the tumor, glioma can be maximally resected under the premise of safety [10]. Intraoperative MRI was the best. In addition to surgery, radiotherapy, chemotherapy, and targeted therapy can also be used to improve the quality of life of the patients and prolong their survival [11].

In recent years, with the continuous promotion of nursing work in clinical depth, the corresponding preoperative, intraoperative, and postoperative nursing is also in clinical application. This comprehensive nursing greatly increases patients' nursing satisfaction, improves hospital service and treatment, and helps patients recover better and faster [12]. Comfort nursing is a comprehensive discipline, which enables people to achieve the most pleasant state in psychology, physiology, society, and spirituality through the study of nursing activities and comfort or shorten and reduce the degree of unhappiness [13]. At present, most patients with glioma are treated by surgery in clinical practice. However, surgery is a relatively large stressor, which will bring certain harm to the physical and mental health of patients with glioma. Some patients with glioma surgery often suffer from anxiety, anxiety, fear, and other adverse psychological conditions, which affect the smooth progress of clinical surgery [14, 15]. Therefore, this work selected the glioma patients in functional areas as the research objects by integrating the advantages of comfortable nursing and the psychology of the glioma patients undergoing surgery. Preoperative magnetic resonance imaging (MRI) was used to evaluate the glioma condition of the patients, and microsurgical resection was performed. Based on different nursing strategies, the anxiety of the patients under different nursing measures was observed after operation, so as to determine the intervention effect of comfortable nursing in the operating room to provide a certain reference for clinical better treatment and service of the glioma patients in functional areas.

2. Materials and Methods

2.1. Research Objects.
In this research, 80 patients with glioma in functional areas admitted to hospital from January 2018 to January 2022 were selected as the research subjects. All patients were randomly rolled into the control group (routine nursing) and the experimental group (comfort nursing intervention in the operating room), with 40 cases in each group. In the experimental group, there were 31 males and 9 females. The age distribution range was 32–73 years, and the mean age was 48.25 ± 8.27 years. The course of disease was 12.54 ± 3.68 months, and the tumor size was 4.62 ± 1.44 cm. In the control group, there were 29 males and 11 females. The age distribution range was 30–75 years, and the mean age was 48.75 ± 7.56 years. The course of disease was 12.36 ± 3.43 months, and the tumor size was 4.48 ± 1.56 cm. There were no significant differences in gender, age, disease course, and other basic information between the two groups ($P > 0.05$), which were comparable. The study was approved by the Ethics Committee of Xuanwu Hospital Capital Medical University. The patients and their family members were aware of the content and methods of the study and agreed to sign the corresponding informed consent forms.

Inclusion criteria were as follows: (1) patients with pathological diagnosis of low-grade glioma [16]; (2) patients aged ≥18 years; and (3) patients with perfect clinical data.

Exclusion criteria were as follows: (1) patients with other tumors; (2) patients with liver and kidney dysfunction; (3) patients with multifocal epilepsy; (4) patients who were unwilling to cooperate with the whole follow-up process; and (5) patients with mental illness and cognitive impairment.

2.2. Research Methods.
A total of 80 patients with glioma in the functional area were selected as the research object, and the patients were divided into a test group and a control group, with 40 patients in each group. The patients in the test group were given preoperative, intraoperative, and postoperative fine care, namely, operating room comfort care, while the patients in the control group were given routine care. The glioma was evaluated preoperatively using MRI and subsequently resected using microsurgery. Heart rate, systolic blood pressure (SBP), diastolic blood pressure (DBP), interleukin-6 (IL-6), and cortisol levels were recorded at the time of entering the operating room (T1), the time of anesthesia onset (T2), the end of surgery (T3), the time of recovery of consciousness after surgery (T4), and one day after surgery (T5), as well as the anxiety of the patients before and after intervention. After comparison, the intervention effect of comfortable nursing in the operating room was obtained.

2.3. MRI Preoperative Evaluation Combined with Microsurgery.
Before surgery, according to the examination data of diffusion tensor imaging, diffusion-weighted imaging, oxygen-dependent functional magnetic resonance imaging, hydrogen proton magnetic covibration wave

spectrum, etc., the doctors in the nuclear magnetic laboratory and the surgeons jointly assessed the high and low grade of glioma, tumor boundary, and the morphological changes of cerebral cortical fiber bundles and the relationship between them and adjacent tumors, so as to determine the degree of resection. Additionally, they also determined the scalp incision site to select the surgical incision and the surgical approach. During the operation, the functional areas were guided by referring to the results of DTI to determine the structural and spatial relationship between the tumor, fiber tracts, and important functional areas. Under the guidance of ultrasound, functional areas were avoided, and the nearest cerebral sulci and cerebral gyrus approach to the tumor with no significant large blood vessels was selected to gradually approach the resected lesions. Under ultrasonic guidance, endoscopic resection was achieved as far as possible. During the operation, repeated ultrasonic exploration was performed to evaluate the extent of resection and the degree of residual to maximize the protection of the functional cortex, and the maximum extent of resection area tumor was performed under the microscope. Then, the degree and location of residual tumor were recorded. After resection, the probe was used to probe the residual cavity and the peritumoral surface of the operative area step by step, and the preoperative ultrasonic images were compared to determine whether there was residual or not. Then, the corresponding images were retained. All patients underwent the brain MRI plain scan plus enhanced scan before surgery, and the MRI scan showed that glioma was located in the functional area.

2.4. Comfort Nursing in the Operating Room. Operating room comfort nursing included preoperative, intraoperative, and postoperative nursing contents (Table 1).

2.5. Observation Indicators. Systolic blood pressure (SBP), diastolic blood pressure (DBP), heart rate (HR), and enzyme-linked immunosorbent assay (ELISA) was adopted to measure IL-6 levels, cortisol levels were detected by radioimmunoassay, and self-rating anxiety scale (SAS) scores were measured at the time of entry into the operating room (T1), the time of onset of anesthesia (T2), the end of surgery (T3), the time of recovery of consciousness after surgery (T4), and one day after surgery (T5).

2.6. Method of Statistics. In this study, SPSS 23.0 software package was employed for statistical data analysis. The Shapiro–Wilk test was adopted to test whether the data were normally distributed. The measurement data conforming to the normal distribution were compared among multiple groups by single factor and multiple data means, and the independent sample t test was utilized between the two groups. Measurement data that did not conform to normal distribution were tested by the rank sum test. Counting data were tested using the χ^2 test. According to statistical results, $P < 0.05$ was considered statistically significant.

3. Results

3.1. MRI Examination of the Glioma Growth Site. All patients included in this study were examined for glioma growth sites in their functional regions using both plain and enhanced MRI scans of the brain, and the results are shown in Figure 1. It was visualized that the growth sites of gliomas were basically located in the basal ganglia, Broca region, simultaneous iliac-temporal lobe involvement, central region, paracentral lobular, occipital lobe, and thalamus. Of which, the proportion of basal ganglia was as high as 26.25%.

3.2. Comparison of Blood Pressure Changes at Different Time Points. The diastolic blood pressure of the control group at T2 was 77.53 ± 14.23 mmHg, which was higher than that at T1 (71.32 ± 16.53 mmHg), and the difference was statistically significant ($P < 0.05$). There was no significant difference in diastolic blood pressure between the two groups at any observation time point ($P > 0.05$). The details are shown in Figure 2. In the control group, the systolic blood pressure at T2 was 128.73 ± 16.21 mmHg, which was higher than that at T1 (109.68 ± 18.83 mmHg), and the difference was statistically significant ($P < 0.05$). At T2, the systolic blood pressure of the test group was higher than that of the control group (120.56 ± 18.12 mmHg), and the difference was statistically significant ($P < 0.05$). There was no significant difference in systolic blood pressure between the two groups at other time points ($P > 0.05$). The details are shown in Figure 3.

3.3. Comparison of Heart Rate Changes at Different Time Points. There was no significant difference in the heart rate between the test group and the control group at each time point ($P > 0.05$). The details are shown in Figure 4.

3.4. Comparison of IL-6 Changes at Different Time Points. The levels of IL-6 at T2, T3, and T4 in the control group were 186.45 ± 64.55 ng/L, 287.68 ± 34.59 ng/L, and 488.69 ± 81.14 ng/L, respectively, which were increased compared with 154.42 ± 48.63 ng/L at T1. The difference was statistically significant ($P < 0.05$). In addition, the IL-6 levels at T2 (167.44 ± 15.59 ng/L), T3 (186.25 ± 52.64 ng/L), and T4 (356.57 ± 48.22 ng/L) in the test group were lower than those in the control group at the corresponding time points, and the differences were statistically significant ($P < 0.05$). The details are shown in Figure 5.

3.5. Comparison of Cortisol Levels at Different Time Points. The cortisol levels of the control group at T2, T3, and T4 were 11.58 ± 2.48 ng/L, 12.06 ± 2.82 ng/L, and 13.04 ± 11.78 ng/L, respectively, which were increased compared with 7.22 ± 2.53 ng/L at T1, and the differences were statistically significant ($P < 0.05$). In addition, the levels of IL-6 at T2 (8.89 ± 1.23 ng/L), T3 (9.23 ± 1.25 ng/L), and T4 (11.78 ± 1.27 ng/L) in the test group were lower than those in the control group at the corresponding time points, and the differences were statistically significant ($P < 0.05$). The details are shown in Figure 6.

TABLE 1: Specific content of comfort care in the operating room.

Types	Nursing contents
Preoperative nursing	Before the operation, medical staff communicated with the patients about their physical and psychological conditions. Medical staff should pay attention to the tone and language organization of communication during communication and intuitively explain the relevant contents after operation to the patients in a simple way, such as the necessity of operation, the general process of operation, and precautions before operation, to relieve patients' preoperative tension, eliminate patients' anxiety and other adverse emotions, and increase patients' confidence in surgical treatment
Intraoperative nursing	Every operating room nurse should be energetic and focused in the work and conscientiously implement the operating procedures to ensure the safety of the patients. Itinerant nurses must know their surgical patients well and be prepared to take care of them, to fully understand the psychological changes of the patients and make necessary conversation patients as the center to eliminate their tension. During the operation, lidocaine gel was used for painless catheterization, and urine tubes were inserted after anesthesia as far as possible. When placing the patient's position, nurses should pay attention to observe and ask whether the patient was comfortable and make appropriate adjustments, scientific application of pressure ulcer protection pad, and effectively protect every patient
Postoperative nursing	After the operation, the medical staff continuously monitored the patients' ECG, paid close attention to the changes of the patients' vital signs and the movements of their limbs, wiped the residual disinfectant and blood on the patients' body surfaces, helped the patients to put on their clothes and bedding, added a bed bar and fastened their seat belts, and assisted the surgeons and anesthesiologists in transferring the patients to the ward
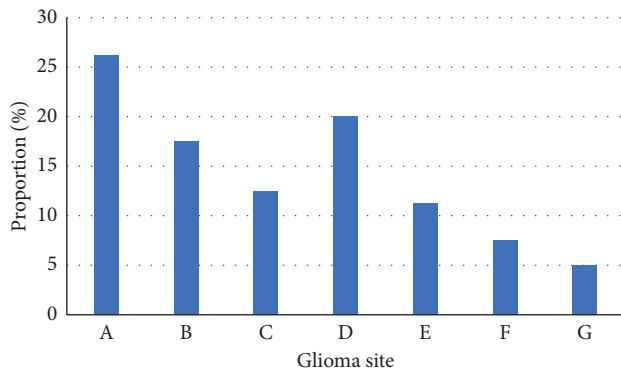
FIGURE 1: Functional area glioma growth site. A, B, C, D, E, F, and G represented the basal ganglia region, Broca region, simultaneous iliac-temporal lobe involvement, central region, paracentral lobular, occipital lobe, and thalamus, respectively.
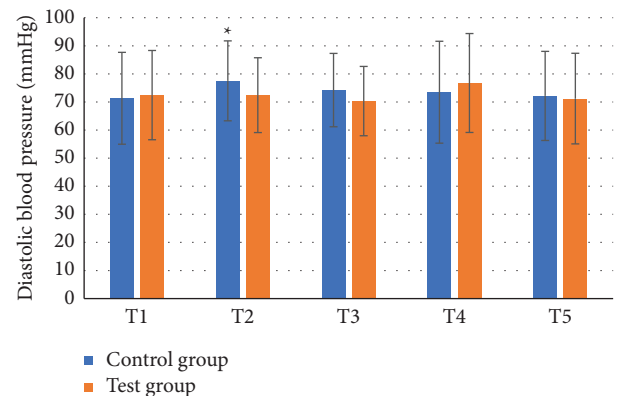
FIGURE 2: Comparison of diastolic blood pressure between the two groups at different time points. *Compared with the observation time point T1 in the same group, $P < 0.05$.

3.6. Comparison of Anxiety Scores before and after Intervention. There was no significant difference in SAS scores between the two groups before the nursing intervention ($P > 0.05$). The SAS score of the control group after intervention (51.03 ± 3.65) was lower than that before intervention (54.65 ± 5.34), and the difference was statistically significant ($P < 0.05$). The SAS score of the test group after intervention was 45.38 ± 2.02, which was lower than that before intervention (54.66 ± 5.35), and the difference was statistically significant ($P < 0.05$). The SAS score of the test group after intervention was lower than the control group, and the difference was statistically significant ($P < 0.05$). The details are shown in Figure 7.

4. Discussion

Microsurgery is an important method for the treatment of glioma. However, as a stressor, surgery will further harm patients' physical and psychological health on the basis of disease damage, causing them to have negative temperament such as anxiety and fear [17, 18]. Therefore, the development of standardized and comfortable nursing for glioma patients in microsurgery can correspondingly reduce the perioperative stress reaction of the patients and contribute to the successful completion of surgery. Comfort nursing intervention is a nursing model developed based on holistic nursing that takes patients as the center [19]. This nursing
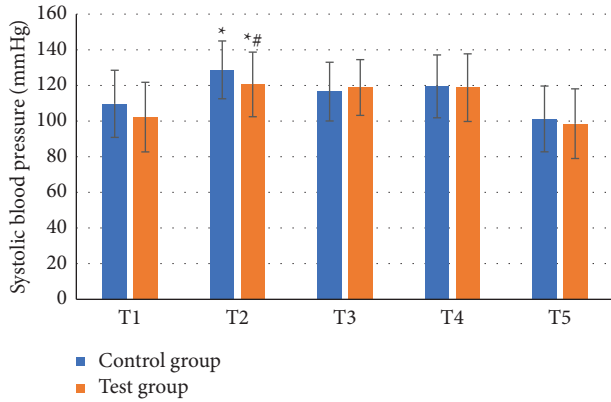
Figure 3: Comparison of systolic blood pressure between the two groups at different time points. *Compared with the observation time point T1 in the same group, $P < 0.05$; #compared with the control group at the same observation time point, $P < 0.05$.

Figure 4: Heart rate changes in the two groups at different time points.

Figure 5: Comparison of IL-6 changes between the two groups at different time points. *Compared with the observation time point T1 in the same group, $P < 0.05$; #compared with the control group at the same observation time point, $P < 0.05$.

Figure 6: Comparison of cortisol levels between the two groups at different time points. *Compared with the observation time point T1 in the same group, $P < 0.05$; #compared with the control group at the same observation time point, $P < 0.05$.

Figure 7: Comparison of SAS scores before and after nursing intervention between the two groups. *Compared with before the nursing intervention, $P < 0.05$; #compared with the control group, $P < 0.05$.

model not only gives the patients full respect, understanding, and care but also implements warm and thoughtful humanistic nursing services for patients [20]. Therefore, comfort nursing intervention for patients with glioma

surgery can meet their psychological and physiological needs as far as possible. In addition, it can obtain the full understanding and cooperation of glioma patients, thus helping to establish a good nurse-patient relationship [21]. This work showed that compared with the glioma patients in the control group, the systolic blood pressure, IL-6 level, and cortisol level of glioma patients in the experimental group were lower at T2, and the differences between groups were significant ($P < 0.05$). Compared with the glioma patients in the control group, the levels of IL-6 and cortisol at T3 and T4 in the glioma patients in the experimental group were lower, and the differences between groups were significant ($P < 0.05$). Heart rate and blood pressure are important related indicators reflecting the patient's cardiovascular system [22], while IL-6 and cortisol can reflect the severity and condition of the patient's stress response [23]. The results showed that the stress response of the experimental group was less than that of the control group. It shows that the patient's sense of security is improved and pain, fear, anxiety, and other symptoms are alleviated, in psychological and physiological satisfaction and security. In addition, in

this work, the SAS score of the glioma patients in the experimental group after nursing intervention was significantly lower than that of the glioma patients in the control group, and the difference between the groups was significant ($P < 0.05$). It shows that comfort nursing for patients with glioma can obviously relieve their anxiety and improve their bad psychology, which is worthy of popularization in clinical practice. In the study of Lank et al. [24], the experimental group adopted preoperative comfort nursing and intraoperative and postoperative comfort intervention and the results showed that the scores of anxiety and depression in the observation group were lower than those in the control group after intervention, showing $P < 0.05$. The results are similar. In addition, in the study of Meneguin et al. [25], serum cortisol of the observation group was lower than that of the control group after operation, and the difference was statistically significant; and it suggested that microsurgery can enhance the stress response of the body, and comfort nursing can reduce the stress response stimulation and maintain a good physical and mental state. This result is also consistent with the results of this work.

5. Conclusion

This study was aimed to investigate the application value of MRI scanning examination in the preoperative treatment of functional glioma and to analyze the application effect of nursing intervention in the operating room in the treatment of fiber surgery. The results showed that the preoperative MRI scan was beneficial to detect the location of glioma in the functional area. Moreover, comfort nursing in the operating room can effectively relieve the anxiety and depression of glioma patients and improve the adverse psychological conditions of the patients. However, due to the limitation of disease types, the sample size included in this study is small and the sample sources are concentrated, which may have certain influence on the final research results and lack of persuasion. Therefore, it is necessary to improve and optimize this aspect in the subsequent research.

Data Availability

The data used to support the findings of this study are available from the corresponding author upon request.

Conflicts of Interest

The authors declare that there are no conflicts of interest.

References

[1] J. Wang, Y. Yang, X. Liu, and Y. Duan, "Intraoperative contrast-enhanced ultrasound for cerebral glioma resection and the relationship between microvascular perfusion and microvessel density," *Clinical Neurology and Neurosurgery*, vol. 186, Article ID 105512, 2019.

[2] J. Bi, S. Chowdhry, S. Wu, W. Zhang, K. Masui, and P. S. Mischel, "Altered cellular metabolism in gliomas - an emerging landscape of actionable co-dependency targets," *Nature Reviews Cancer*, vol. 20, no. 1, pp. 57–70, 2020.

[3] F. Mao, B. Wang, Q. Xiao, F. Cheng, T. Lei, and D. Guo, "LRIG proteins in glioma: functional roles, molecular mechanisms, and potential clinical implications," *Journal of the Neurological Sciences*, vol. 383, no. 15, pp. 56–60, 2017.

[4] A. S. Haider, M. van den Bent, P. Y. Wen et al., "Toward a standard pathological and molecular characterization of recurrent glioma in adults: a Response Assessment in Neuro-Oncology effort," *Neuro-Oncology*, vol. 22, no. 4, pp. 450–456, 2020.

[5] W. B. Pope and G. Brandal, "Conventional and advanced magnetic resonance imaging in patients with high-grade glioma," *Q J Nucl Med Mol Imaging*, vol. 62, no. 3, pp. 239–253, 2018.

[6] K. Zhou, Z. Zhao, S. Li, Y. Liu, G. Li, and T. Jiang, "A new glioma grading model based on histopathology and Bone Morphogenetic Protein 2 mRNA expression," *Scientific Reports*, vol. 10, no. 1, Article ID 18420, 2020.

[7] M. D. Wood, A. M. Halfpenny, and S. R. Moore, "Applications of molecular neuro-oncology - a review of diffuse glioma integrated diagnosis and emerging molecular entities," *Diagnostic Pathology*, vol. 14, no. 1, p. 29, 2019.

[8] B. Zhang, Q. Li, B. Wu et al., "Long non-coding RNA TP73-AS1 is a potential immune related prognostic biomarker for glioma," *Aging (Albany NY)*, vol. 13, no. 4, pp. 5638–5649, 2021.

[9] X. Xu, Y. Ban, Z. Zhao, Q. Pan, and J. Zou, "MicroRNA-1298-3p inhibits proliferation and invasion of glioma cells by downregulating Nidogen-1," *Aging (Albany NY)*, vol. 12, no. 9, pp. 7761–7773, 2020.

[10] Y. Yang, Q. Mao, X. Wang et al., "An analysis of 170 glioma patients and systematic review to investigate the association between IDH-1 mutations and preoperative glioma-related epilepsy," *Journal of Clinical Neuroscience*, vol. 31, pp. 56–62, 2016.

[11] B. Zhang, C. Xu, J. Liu, J. Yang, Q. Gao, and F. Ye, "Nidogen-1 expression is associated with overall survival and temozolomide sensitivity in low-grade glioma patients," *Aging (Albany NY)*, vol. 13, no. 6, pp. 9085–9107, 2021.

[12] F. Tang, Z. Pan, Y. Wang et al., "Advances in the immunotherapeutic potential of isocitrate dehydrogenase mutations in glioma," *Neuroscience Bulletin*, vol. 38, no. 9, pp. 1069–1084, 2022.

[13] J. T. Fortunato, M. Van Harn, S. A. Haider, J. Phillips, and T. Walbert, "Caregiver perceptions of end-of-life care in patients with high-grade glioma," *Neuro-Oncology Practice*, vol. 8, no. 2, pp. 171–178, 2020.

[14] M. Maravat, M. Bertrand, C. Landon et al., "Complementary nuclear magnetic resonance-based metabolomics approaches for glioma biomarker identification in a *Drosophila melanogaster* model," *Journal of Proteome Research*, vol. 20, no. 8, pp. 3977–3991, 2021.

[15] S. P. Miranda, R. E. Bernacki, J. M. Paladino et al., "A descriptive analysis of end-of-life conversations with long-term glioblastoma survivors," *American Journal of Hospice and Palliative Medicine*, vol. 35, no. 5, pp. 804–811, 2018.

[16] L. Khan, H. Soliman, A. Sahgal, J. Perry, W. Xu, and M. N. Tsao, "External beam radiation dose escalation for high grade glioma," *Cochrane Database of Systematic Reviews*, vol. 1, no. 8, Article ID CD011475, 2016.

[17] V. Y. Yu, A. Landers, K. Woods et al., "A prospective 4π radiation therapy clinical study in recurrent high-grade glioma patients," *International Journal of Radiation Oncology, Biology, Physics*, vol. 101, no. 1, pp. 144–151, 2018.

[18] Z. Wan, Y. Dong, Z. Yu, H. Lv, and Z. Lv, "Semi-supervised support vector machine for digital twins based brain image fusion," *Frontiers in Neuroscience*, vol. 15, no. 9, Article ID 705323, 2021.

[19] K. Radlanski, M. Hartwig, and U. Kordes, "Coping with Diffuse Intrinsic Pontine Glioma in Children - Findings from an Interview Study on Bereaved Parents," *Klin Padiatr*, vol. 234, no. 6, pp. 374–381, 2022.

[20] M. Barbaro, C. D. Blinderman, F. M. Iwamoto et al., "Causes of death and end-of-life care in patients with intracranial high-grade gliomas: a retrospective observational study," *Neurology*, vol. 98, no. 3, pp. e260–e266, 2022.

[21] J. E. Leon-Rojas, J. O. Ekert, M. A. Kirkman, D. Sewell, S. Bisdas, and G. Samandouras, "Experience with awake throughout craniotomy in tumour surgery: technique and outcomes of a prospective, consecutive case series with patient perception data," *Acta Neurochirurgica*, vol. 162, no. 12, pp. 3055–3065, 2020.

[22] D. Kavalieratos, L. P. Gelfman, L. E. Tycon et al., "Palliative care in heart failure: rationale, evidence, and future priorities," *Journal of the American College of Cardiology*, vol. 70, no. 15, pp. 1919–1930, 2017.

[23] E. H. Stephens, J. A. Dearani, M. Y. Qureshi et al., "Toward eliminating perinatal comfort care for prenatally diagnosed severe congenital heart defects: a vision," *Mayo Clinic Proceedings*, vol. 96, no. 5, pp. 1276–1287, 2021.

[24] R. J. Lank, F. Shafie-Khorassani, X. Zhang et al., "Advance care planning and transitions to comfort measures after stroke," *Journal of Palliative Medicine*, vol. 24, no. 8, pp. 1191–1196, 2021.

[25] S. Meneguin, C. F. Pollo, C. R. Benichel, L. K. Cunha, and H. A. Miot, "Comfort and religious-spiritual coping of intensive care patients' relatives," *Intensive and Critical Care Nursing*, vol. 58, Article ID 102805, 2020.

WILEY | Hindawi

Research Article

Effect of Early Nursing Intervention under Amplitude-Integrated Electroencephalography and Magnetic Resonance Images on Brain Injury in Premature Infants

Aiyan Liu, Huangai Zhang, and Wei Guo 🄳

Department of Neonatology, Affiliated Xingtai People's Hospital of Hebei Medical University, Xingtai 054000, Hebei, China

Correspondence should be addressed to Wei Guo; 1717010111@xy.dlpu.edu.cn

To investigate the effects of early nursing intervention on brain injury among premature infants, 100 premature infants diagnosed with brain injury were included in the research and randomly divided into the control group (50 cases) and the experimental group (50 cases). The patients in the two groups were performed with the same conventional comprehensive treatment. The patients in the control group received conventional nursing while those in the experimental group underwent early nursing intervention. During follow-up, neurodevelopment, motor behavior, the incidence rate of brain injury, and nursing satisfaction of the infants in the two groups were compared. It was demonstrated that the five neurodevelopment scores of the experimental group were all higher than those of the control group. The differences showed statistical significance ($P < 0.05$). The total effective rate of motor development of the experimental group reached 94%, while that of the control group amounted to 80%. Obviously, the total effective rate of motor development of the experimental group was higher than that of the control group. The difference was statistically significant ($P < 0.05$). The nursing satisfaction of the experimental group reached 98%, which was apparently higher than that of the control group (74%). The difference suggested statistical significance ($P < 0.05$). The rates of brain injury at 1 and 2 years after the birth of the experimental group were 6% and 2%, respectively. The rates of brain injury at 1 and 2 years after the birth of the control group amounted to 18% and 14%, respectively. The rates of brain injury at 1 and 2 years after the birth of the experimental group were lower than those of the control group. The difference revealed statistical significance ($P < 0.05$). Hence, the early nursing intervention of premature infants with brain injury could promote brain development, improve neurological function, reduce the incidence of brain injury, and achieve an ideal nursing effect.

1. Introduction

Preterm infants refer to newborns whose gestational age is less than 37 weeks. In recent years, with the progress of medical technology, the birth rate and survival rate of preterm infants around the world have increased remarkably [1]. However, due to the immature development of some tissues and organs of premature infants, some complications are easily caused. Investigation showed that among all complications of premature infants, the incidence rate of brain injury in preterm infants (BIPI) can reach approximately 15% [2]. Nearly half of the premature infants born in China every year will suffer from brain injury, which usually

includes intracranial hemorrhage, white matter injury, cerebral infarction, and intracranial infection. A brain injury will lead to neurological damage in children, with varying degrees of impairment in motor function, intelligence, emotional ability, vision, and other aspects, which will remarkably reduce the quality of life of children.

Premature infants are prone to brain injury due to premature separation from the mother, insufficient gestational age, immature brain development, and low sensitivity to a hypoxic environment. Brain injury is mainly caused by infection. Premature rupture of membranes and chorioamnionitis can lead to infection in premature infants. In addition, fetal asphyxia, shock, and abnormalities

of the mother's placenta, and umbilical cord also affect the neurons of children and cause brain injury. BIPI comes in two forms, namely, hemorrhagic and nonhemorrhagic brain damage. The former can lead to neurodevelopmental disorders in severe cases, and the latter can lead to visual and hearing impairment in severe cases. Immediate intervention can reduce the risk of complications in premature infants. At present, the prevention methods of premature brain injury mainly include prenatal use of $MgSO_4$ and postpartum use of erythropoietin [3–8]. In addition to providing symptomatic treatment, it is necessary to identify as early as possible children who may encounter such conditions during late development. With the development of science and medical research, imaging examination has been widely used and accepted by the public. It has become an indispensable method to diagnose premature brain injury. Amplitude-integrated electroencephalography (aEEG) and magnetic resonance imaging (MRI) can be used for the real-time monitoring of premature infants and as predictive indicators for the diagnosis of brain injury in premature infants. AEEG can perform bedside monitoring for premature infants, display amplitude waves of EEG signals, and understand their neurophysiological activities. This method is intuitive, simple, noninvasive, and efficient [9–12]. MRI can detect small brain abnormalities and intracranial bleeding and accurately detect the scope and size of the lesion site. Its sensitivity and specificity are extremely high. MRI can predict the neurodevelopment of preschool-age infants when the gestational age is corrected to full term. The combination of the two imaging examination methods can provide a reliable basis for doctors to diagnose premature brain injury, avoid misdiagnosis and missed diagnosis, and improve the diagnosis rate [13, 14]. According to the results of aEEG and MRI, doctors can formulate appropriate treatment plans to prevent more sequelae, improve the condition of premature infants with brain injury, improve the survival rate of premature infants, and reduce the burden on families and society.

The adoption of correct and effective early nursing measures for premature infants with brain injury can promote the growth and development of children, reduce complications and the treatment time, alleviate the condition of children, and improve the cure rate, which is of great significance for the treatment of premature infants with brain injury. One hundred premature infants diagnosed with brain injury by aEEG and MRI imaging examinations were recruited. According to the random principle, they were divided into the control group and the experimental group. The two groups of patients received the same conventional comprehensive treatment. Those in the control group received conventional nursing, while those in the experimental group were given visual, motor, intelligence, and other aspects of early nursing intervention. The two groups of children were compared regarding neurological development, motor behavior, brain injury rate 1 year and 2 years later, and nursing satisfaction score to explore the clinical efficacy of the early nursing intervention on premature brain injury.

2. Methods

2.1. Basic Data. In this study, 100 premature infants delivered in a hospital with gestational age less than 37 months and confirmed by aEEG and MRI imaging examination were included. They were randomly divided into a control group and an experimental group. In the control group, there were 50 premature infants, including 28 males and 22 females, with a gestational age of 29–37 weeks. The average gestational age was 33.5 ± 3.2 weeks, body weight was 920–2,600 g, and average body weight was $1,480 \pm 350$ g. In the experimental group, there were 26 males and 24 females with gestational ages of 28–36 weeks. The mean gestational age was 31.7 ± 3.6 weeks, the body weight was 890–2,700 g, and the mean body weight was $1,390 \pm 320$ g. There was no great difference between the control group and the experimental group in sex, body weight, gestational age, or other general data, $P > 0.05$, which was comparable. All guardians signed informed consent forms, and the study was approved by the ethics committee of the hospital.

Inclusion criteria were as follows: (i) premature infants with a gestational age over 28 weeks but less than 37 weeks; (ii) no history of suffocation; (iii) the mother had no serious complications. Exclusion criteria were as follows: (i) congenital malformation; (ii) severe hypoxic-ischemic encephalopathy.

2.2. AEEG Monitoring and MRI Examination. Preterm infants with suspected brain injury were admitted for aEEG monitoring within 3 days of birth and head MRI examination at 40 weeks.

AEEG monitoring was as follows. The brain function monitor was used to perform operations according to relevant standards. Each monitoring time was over 2 h, and continuous monitoring was performed for 3 days. To avoid interference, sedatives, anesthetics, and antiepileptic drugs should not be used in the monitoring process, and the data whose impedance was higher than 10Ω in the aEEG monitoring data obtained should be discarded. The data obtained were obtained by two qualified physicians.

A head MRI examination was performed as follows: the child's head was fixed with a sponge pad using a head orthogonal coil. A 1.5 T MRI scanner was used, and the examinations included T1-weighted, T2-weighted, and diffusion-weighted imaging (T1W1, T2W1, and DW1). Normal neonatal brain MRI signals were as follows: T1W1: high cortex, low white matter, high myelination, low cerebrospinal fluid, low skull, and high fat; T2W1: low cortex, high white matter, low myelination, high cerebrospinal fluid, low skull, and high fat. MRI signals of common lesions were as follows: T1W1: high bleeding, low infarction, low edema, and low softening; T2W1: low bleeding, high infarction, high edema, and high softening.

2.3. Nursing Intervention. Both groups underwent aEEG and MRI imaging examinations and received the same conventional comprehensive treatment, including drugs and routine health care. The control group received intervention

according to routine nursing requirements for premature infants, and the children's basic state (including spirit, nutrition, sleep, and diet) was observed and recorded. The basic physical signs of the children and appropriate temperature and humidity were maintained, and relevant health guidance was provided. The experimental group of children received the early nursing intervention.

According to gestational age and degree of brain injury, early nursing programs were made for the children in the experimental group. First, the medical staff needed to create a comfortable environment for the children, and the "bird's nest" posture was established to ensure that children had the appropriate and correct posture. Second, the medical staff should gently stimulate the children to make them feel similar to the environment in the womb, maintain their breathing rate, and avoid overstimulation. Third, the medical staff touched the children and adjusted the indoor temperature and humidity to maintain the temperature at 22–24℃ and humidity between 50% and 60%. The nursing staff first washed their hands, then rubbed their hands with massage oil and heat, and then touched the children. Fifteen repeated strokes were performed on each part, including the head, chest and abdomen, back, hands, feet, and limbs. Fourth, the medical staff explained the content and purpose of early nursing intervention to the guardians, popularized training methods and nursing knowledge, and urged parents to participate in the early nursing of children. The medical staff guided parents to carry out early training and exercise children's motor ability and visual perception ability. For example, parents can play no more than 50 dB of relaxed and cheerful music every day for music intervention. Regular baby exercises were performed, such as the use of bell training motor ability. Parents can communicate with children to promote brain development. The neurobehavioral and motor abilities of the two groups were followed up. During training, children should follow the law of movement and development, avoiding excessive stimulation.

2.4. Indicators. The children were followed up, and the neurological development and motor development of the children were measured. AEEG and MRI were used to examine the brain injury rate of the children and collect the nursing satisfaction score. (I). Neonatal Behavioral Neurological Assessment (NBNA) was used to evaluate the neural development of five indexes, namely, primitive reflex ability, behavioral ability, active muscle tension, passive muscle tension, and general reaction ability. The higher the score, the better the development. (II). Sixty-one motor measurement indexes were evaluated by using the infant development test of the Child Development Center of China (CDCC) to evaluate the children's motor coordination and skill and behavioral ability. The scores were graded into five criteria, and the calculation efficiency was excellent (≥130 points), good (120–129 points), normal (110–119 points), low (90–109 points), and defective (< 80 points). (III). The children in the two groups were examined by aEEG and MRI at one year and two years after birth to analyze the rate of brain injury. (IV). A questionnaire survey was conducted, and the guardian scored nursing satisfaction in the form of anonymity. The full score was 100, and the evaluation was set as three levels as follows: very satisfied (≥ 90 points), satisfied (70–89 points), and dissatisfied (< 70 points).

$$\text{Effective rate of motor development} = \frac{(\text{excellent} + \text{good} + \text{normal})\text{cases}}{\text{total cases}} \times 100\%,$$

$$\text{Brain injury rate} = \frac{\text{number of brain injury}}{\text{total number of each group}}.$$

(1)

2.5. Statistical Methods. All data were statistically analyzed by SPSS 26.0. Count data were tested by χ^2 test, and measurement data were tested by t-test and were expressed as the mean ± standard deviation ($\overline{x} \pm s$). $P < 0.05$ indicated a considerable difference; otherwise, $P > 0.05$ indicated no statistical significance. The measurement data included the NBNA score and CDCC score.

3. Results

3.1. AEEG and MRI Imaging Results. Figures 1 and 2 below show the aEEG and MRI images of children with different brain injuries, respectively. The aEEG images showed continuous high-amplitude waves, and the patients examined by MRI had epidural hemorrhage (EDH).

3.2. Comparison of Neurodevelopmental Status. The five indicators of behavioral neuropathy in the experimental group, namely, original reflex ability, behavioral ability, active muscle tension, passive muscle tension, and general reaction ability scores, were higher than those in the control group. The total score was higher than that in the control group, and the development was stronger than that in the control group. The differences were considerable ($P < 0.05$) (Figure 3).

3.3. Comparison of Motor Behavior. 61 physical activity measurements were evaluated by CDCC in both groups. In the experimental group, 17 cases were excellent (34%), 19 cases were good (38%), 11 cases were normal (22%), 2 cases were low (4%), and 1 case was defective (<2%). In the control

FIGURE 1: AEEG imaging of premature infants with brain injury.

(a)   (b)   (c)
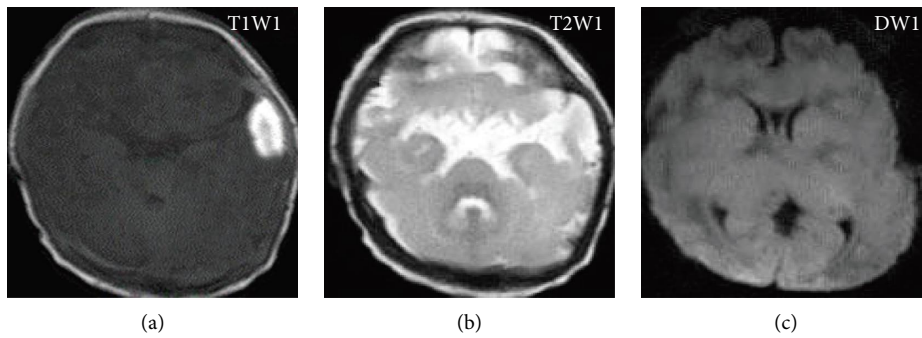
FIGURE 2: MRI imaging of premature infants with brain injury: (a) T1-weighted image; (b) T2-weighted image; (c) diffusion-weighted imaging.
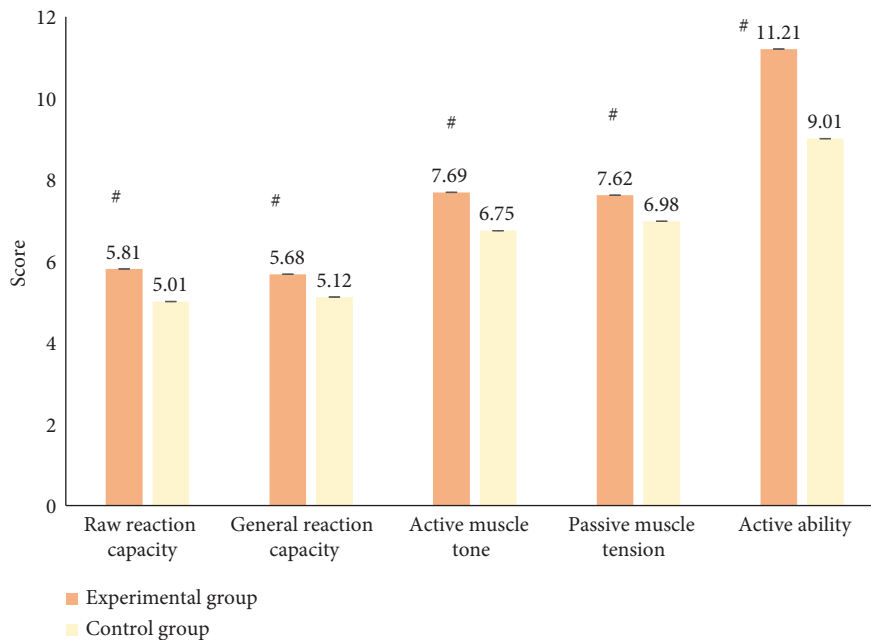
FIGURE 3: Comparison of neurodevelopmental status between the two groups ($n = 50$). #Compared with the control group, $P < 0.05$.

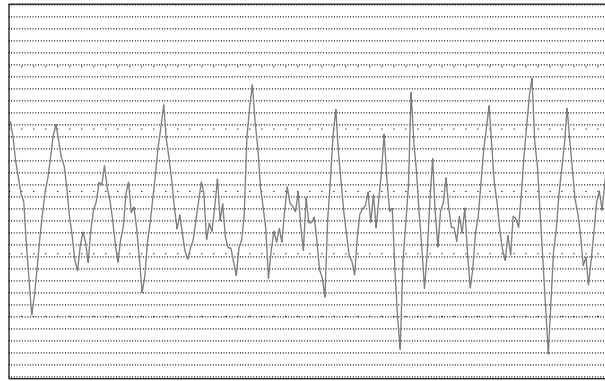group, 11 cases were excellent (22%), 15 cases were good (30%), 14 cases were normal (28%), 6 cases were low (12%), and 4 cases were defective (<8%). The motor development rate of the experimental group was higher than that of the control group, and the difference between the two groups was considerable ($P < 0.05$) (Figure 4).
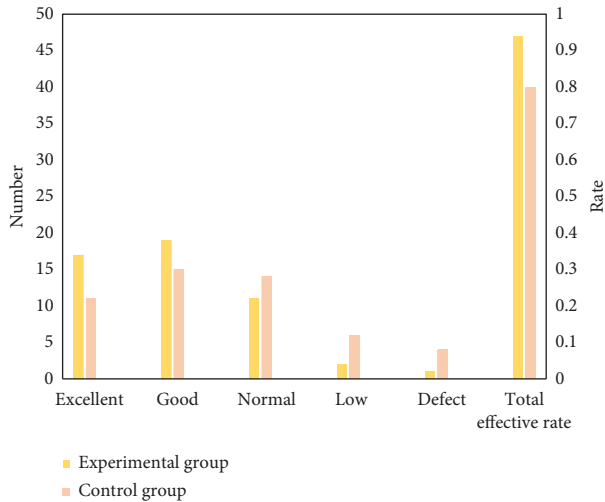
FIGURE 4: Comparison of motor development between two groups. *compared with the control group, $P < 0.05$.

3.4. Comparison of Brain Injury Rates at One Year and Two Years after Birth. In the experimental group, the rates of brain injury at 1 year and 2 years after birth were 6% (3 cases) and 2% (1 case), respectively. In the control group, the rates of brain injury at 1 year and 2 years after birth were 18% (9 cases) and 14% (7 cases), respectively. The difference in the interbrain injury rate between the two groups was considerable ($P < 0.05$) (Figure 5).

3.5. Comparison of Nursing Satisfaction. In the experimental group, 52% (26) were very satisfied, 46% (23) were satisfied, 2% (1) were dissatisfied, and 98% (49) were satisfied. In the control group, 24% (12) were very satisfied, 50% (25) were satisfied, 26% (13) were dissatisfied, and 74% (37) were satisfied. The difference in total nursing satisfaction between the two groups was considerable ($P < 0.05$) (Figure 6).

4. Discussion

Premature infants are prone to brain damage due to premature separation from the mother, insufficient gestational age, immature brain development, and low sensitivity to anoxic environments. As a result, different degrees of movement, intelligence, emotion, vision, and other disorders occur in children, which results in many sequelae and remarkably reduces their quality of life [15–17]. Research analysis found that the main causes of premature brain injury are as follows: (i) premature cells and organs are not mature and vulnerable to interference of various factors, and white matter is easily damaged, resulting in ventricular hemorrhage; (ii) premature infants suffer from insufficient blood supply to the brain and nervous system due to poor regulatory function; (iii) premature infants have underdeveloped brains and poor endocrine function and are prone to various problems caused by external factors [18]. The application of aEEG and MRI can identify children who may experience brain injury in later development as early as possible, remarkably reduce sequelae, improve the survival

rate of premature infants, and relieve the burden on families and society. Correct and effective early nursing measures for premature infants with brain injury can promote the growth and development of infants, reduce complications and treatment time, relieve the illness of infants, and improve the cure rate, which is of great significance for the treatment of premature infants with brain injury [19]. To explore the clinical efficacy of the early nursing intervention on brain injury in premature infants, 100 cases of premature infants diagnosed with brain injury by aEEG and MRI imaging examination in the hospital were included. According to the principle of randomness, they were divided into a control group with 50 cases and an experimental group with 50 cases. Both groups received the same conventional combination therapy. The control group was given routine nursing, while the experimental group was given visual, motor, intelligence, and other aspects of early nursing intervention. Neurological development, motor behavior, brain injury rate, and nursing satisfaction score were compared between the two groups after one and two years. The differences in gender, gestational age, and weight between the two groups showed no statistical significance but comparability ($P > 0.05$).

According to the research results, the scores for five indicators of behavioral neuropathy, namely, original reflex ability, behavioral ability, active muscle tension, passive muscle tension, and general reaction ability, the total effective rate of motor development assessed by CDCC, and nursing satisfaction in the experimental group were all higher than those in the control group ($P < 0.05$). The early nursing intervention involved posture, early training, and touch. A comfortable and safe environment should be created for premature infants to help them adapt to in vitro environment as soon as possible. The early nursing intervention combined with conventional nursing for premature infants with brain injury could improve infants' behavioral and communicative abilities, promote brain development, improve neurological function, and accelerate recovery. In general, it is beneficial to infants' physical and mental health as well as intelligence. The rates of brain injury in infants in the experimental group at 1 and 2 years after birth were both higher than those in the control group ($P < 0.05$), indicating that early nursing intervention could remarkably reduce brain injury. After premature infants undergoing early nursing intervention are discharged from the hospital, their parents should carry out conventional nursing to keep comfortable temperature and humidity and ensure normal basic vital signs. Breastfeeding was the preferred feeding method for premature infants because it could promote neurodevelopment [20]. The family intervention was emphasized during the early nursing intervention. Parents assisted patients to complete all activities, helped improve the compensation function of their brains, and promoted their intelligence, physical, and mental development. The research results suggested that early nursing intervention achieved ideal nursing effects. It was the preferred option for brain injury among premature infants and a purposeful and planned intervention scheme.
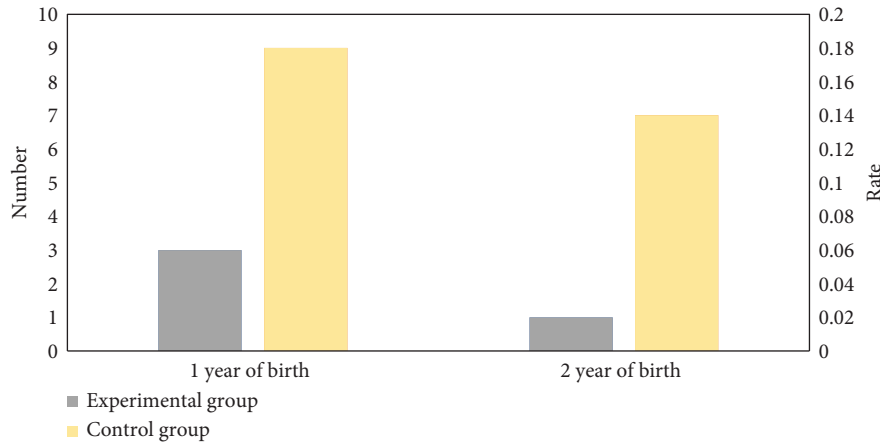
FIGURE 5: Comparison of brain injury rates between 1 year and 2 years after birth between two groups. & compared with the control group, $P < 0.05$.
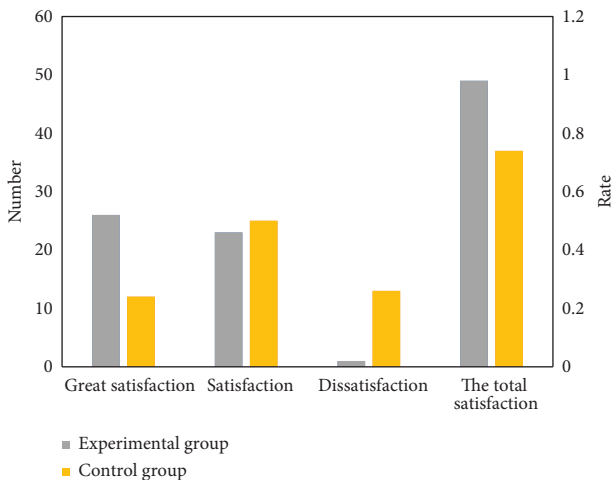
FIGURE 6: Comparison of nursing satisfaction between two groups. $ compared with the control group, $P < 0.05$.

5. Conclusion

The results indicated that the scores for five indicators of behavioral neuropathy, the total effective rate of motor development, and the total satisfaction of the experimental group were all higher than those of the control group. In contrast, the incidence rate of brain injury at 1 and 2 years after birth was lower than that of the control group. However, there were still some disadvantages to the research. Firstly, the communication with patients' parents was insufficient during early nursing intervention for the experimental group, which might make it impossible to realize the optimal nursing and training for patients. Secondly, the included cases were insufficient, which might lead to data errors. To sum up, early nursing intervention for premature infants with brain injury could improve neurological function and reduce the incidence rate of brain injury. The research provided data support for the investigation into the clinical effects of early nursing intervention on brain injury among premature infants.

Data Availability

The data used to support the findings of this study are available from the corresponding author upon request.

Conflicts of Interest

The authors declare that they have no conflicts of interest.

Acknowledgments

References

[1] M. K. Mwaniki, M. Atieno, J. E. Lawn, and C. R. Newton, "Long-term neurodevelopmental outcomes after intrauterine and neonatal insults: a systematic review," *Lancet*, vol. 379, no. 9814, pp. 445–452, 2012.

[2] B. Larroque, S. Marret, P. Y. Ancel et al., "White matter damage and intraventricular hemorrhage in very preterm infants: the EPIPAGE study," *Jornal de Pediatria*, vol. 143, no. 4, pp. 477–483, 2003.

[3] M. A. Bachnas, M. I. A. Akbar, E. G. Dachlan, and G. Dekker, "The role of magnesium sulfate ($MgSO_4$) in fetal neuro-protection," *Journal of Maternal-Fetal and Neonatal Medicine*, vol. 34, no. 6, pp. 966–978, 2021.

[4] M. Ohhashi, T. Yoshitomi, K. Sumiyoshi et al., "Magnesium sulphate and perinatal mortality and morbidity in very-low-birthweight infants born between 24 and 32 weeks of gestation in Japan," *European Journal of Obstetrics & Gynecology and Reproductive Biology*, vol. 201, pp. 140–145, 2016.

[5] S. E. Juul, B. A. Comstock, R. Wadhawan et al., "A randomized trial of erythropoietin for neuroprotection in preterm infants," *New England Journal of Medicine*, vol. 382, no. 3, pp. 233–243, 2020.

[6] J. Song, Y. Wang, F. Xu et al., "Erythropoietin improves poor outcomes in preterm infants with intraventricular hemorrhage," *CNS Drugs*, vol. 35, no. 6, pp. 681–690, 2021.

[7] G. Natalucci, B. Latal, B. Koller et al., "Neurodevelopmental outcomes at age 5 Years after prophylactic early high-dose recombinant human erythropoietin for neuroprotection in

very preterm infants," *JAMA*, vol. 324, no. 22, pp. 2324–2327, 2020.

[8] G. Natalucci, B. Latal, B. Koller et al., "Effect of early pro-phylactic high-dose recombinant human erythropoietin in very preterm infants on neurodevelopmental outcome at 2 years: a randomized clinical trial," *JAMA*, vol. 315, no. 19, pp. 2079–2085, 2016.

[9] X. Zhu, Y. Guo, Y. Liu, and K. Liu, "Amplitude-integrated electroencephalography for early diagnosis and prognostic prediction of hypoxic encephalopathy in preterm infants," *Medical Science Monitor*, vol. 24, pp. 8795–8802, 2018.

[10] A. M. Plomgaard, T. Alderliesten, T. Austin et al., "Early biomarkers of brain injury and cerebral hypo-and hyperoxia in the SafeBoosC II trial," *PLoS One*, vol. 12, no. 3, Article ID e0173440, 2017.

[11] J. De Asis-Cruz, K. Kapse, S. K. Basu et al., "Functional brain connectivity in ex utero premature infants compared to in utero fetuses," *NeuroImage*, vol. 219, Article ID 117043, 2020.

[12] S. K. Basu, S. Pradhan, K. Kapse et al., "Third trimester cerebellar metabolite concentrations are decreased in very premature infants with structural brain injury," *Scientific Reports*, vol. 9, no. 1, p. 1212, 2019.

[13] J. P. Boardman, C. J. Wusthoff, and F. M. Cowan, "Hypo-glycaemia and neonatal brain injury," *Archives of Disease in Childhood: Education and Practice Edition*, vol. 98, no. 1, pp. 2–6, 2013.

[14] F. G. Blankenberg, N. N. Loh, P. Bracci et al., "Sonography, CT, and MR imaging: a prospective comparison of neonates with suspected intracranial ischemia and hemorrhage," *AJNR American Journal of Neuroradiology*, vol. 21, no. 1, pp. 213–218, 2000.

[15] S. Epstein, S. Bauer, O. Levkovitz Stern et al., "Preterm infants with severe brain injury demonstrate unstable physiological responses during maternal singing with music therapy: a randomized controlled study," *European Journal of Pedi-atrics*, vol. 180, no. 5, pp. 1403–1412, 2021.

[16] J. Orton, A. Spittle, L. Doyle, P. Anderson, and R. Boyd, "Do early intervention programmes improve cognitive and motor outcomes for preterm infants after discharge? a systematic review," *Developmental Medicine and Child Neurology*, vol. 51, no. 11, pp. 851–859, 2009.

[17] X. L. Bao, "National cooperative research group for lowering incidence of cerebral palsy of premature infants through early intervention. (Lowering incidence of cerebral palsy of pre-mature infants through early intervention)," *Zhonghua Er Ke Za Zhi*, vol. 43, no. 4, pp. 244–247, 2005.

[18] C. W. Hu, Y. S. Wei, Y. M. Du et al., "Effect of acupoint massage dominant early comprehensive intervention on the prognosis of premature infants with brain injury," *Zhongguo Zhong Xi Yi Jie He Za Zhi*, vol. 34, no. 9, pp. 1074–1077, 2014.

[19] T. E. Inder, L. S. de Vries, D. M. Ferriero et al., "Neuroimaging of the preterm brain: review and recommendations," *The Journal of Pediatrics*, vol. 237, pp. 276–287.e4, 2021 Oct.

[20] T. Fjørtoft, T. Ustad, T. Follestad, P. I. Kaaresen, and G. K. Øberg, "Does a parent-administrated early motor in-tervention influence general movements and movement character at 3 months of age in infants born preterm?" *Early Human Development*, vol. 112, pp. 20–24, 2017.

WILEY | Hindawi

Research Article

Magnetic Resonance Imaging Characteristics of Brain Structure and Neuroendocrine Changes in Patients with First-Episode Schizophrenia

Kai Yang,[1] Xianxiang Zeng,[1] Li Hu,[1] Jinhong Chen,[1] Weiwei Zhu,[1] Yu Wang,[2] and Xiaoxiong Zhao [3]

[1]*Department of Sleeping Disorders and Neurosis, Brain Hospital of Hunan Province (The Second People's Hospital of Hunan Province), Changsha 410007, Hunan, China*
[2]*Department of Internal Neurology, Brain Hospital of Hunan Province (The Second People's Hospital of Hunan Province), Changsha 410007, Hunan, China*
[3]*Third Department of Psychiatry, Brain Hospital of Hunan Province (The Second People's Hospital of Hunan Province), Changsha 410007, Hunan, China*

Correspondence should be addressed to Xiaoxiong Zhao; 1420340345@xs.hnit.edu.cn

This research was aimed to investigate the magnetic resonance imaging (MRI) features of brain structure and neuroendocrine levels in patients with first-episode schizophrenia. 25 hospitalized patients with first-episode schizophrenia were selected as the observation group, while 25 healthy people were selected as the control group. All the objects underwent MRI examination, and the images as well as gray matter density of the original image data were analyzed under voxel-based morphometry (VBM). The cortisol and prolactin in the observation group were detected, and the levels were compared. The Pearson correlation analysis was adopted to analyze the correlation between cortisol and prolactin levels and the total score of the Positive and Negative Syndrome Scale (PANSS). The results showed that the gray matter volume of the precentral gyrus, superior frontal gyrus, middle frontal gyrus, inferior frontal gyrus, postcentral gyrus, inferior parietal lobule, superior parietal lobule, and anterior cingulate cortex of the observation group decreased, while the volume of cerebellar gray matter increased. The levels of cortisol and prolactin in the observation group ($387.54 \pm 117.69\,\mu$g/L and $804.16 \pm 267.13\,\mu$IU/mL, respectively) were significantly higher than those in the control group ($138.46 \pm 62.47\,\mu$g/L and $397.54 \pm 203.82\,\mu$IU/mL, respectively), and the differences were statistically significant ($P < 0.05$). The results of the Pearson correlation test showed that the higher the cortisol level, the more severe the schizophrenia ($r = 0.421$ and $P = 0.013$), while the prolactin level was not directly related to the severity of schizophrenia ($r = 0.019$ and $P = 0.568$). In conclusion, the MRI features based on the VBM technology can accurately assess the changes of gray matter; the levels of cortisol and prolactin in patients with first-episode schizophrenia were significantly higher than those in healthy people; and the higher the cortisol level, the more severe the schizophrenia symptoms. This study provided a certain research basis for MRI features of brain structure and neuroendocrine changes in patients with first-episode schizophrenia.

1. Introduction

Schizophrenia is a group of severe mental illnesses of unknown etiology, mostly slow or subacute in young adults. It usually presents clinically as a syndrome with various symptoms, involving sensory, perceptual, thinking, emotional, and behavioral disturbances, as well as uncoordinated

mental activities [1]. Patients with schizophrenia have clear consciousness and normal intelligence in daily life, but some patients will have cognitive impairment as the disease progresses. The course of the disease is generally protracted, repeated, aggravated, or worsened. Some patients will eventually experience mental decline and mental disability, but some patients can maintain or basically recover after

treatment [2]. Schizophrenia is a clinical syndrome consisting of a group of symptoms. It is a multifactorial disease. The possible causes of current research include family inheritance, personality disorders (introversion, withdrawal, and stubbornness), and frequent life (psychological) blows [3]. First-episode schizophrenia is defined as having been evaluated for treatment for the first episode of psychosis associated with schizophrenia spectrum disorder. Patients have a transitional process from mental health to mental illness. Patients first develop some symptoms such as depression, anxiety, obsessive-compulsive behaviors and obsessions, and insomnia and then progress to some mild psychotic symptoms, such as self-talk, transient hallucinations, and personality changes [4, 5]. If there is no intervention at this time, it will progress further, resulting in obvious psychotic symptoms, until the final official diagnosis of schizophrenia. Treatment of patients with first-episode schizophrenia must follow the principles of comprehensive therapeutic management, including pharmacotherapy, psychotherapy, and social therapy, and plans for future maintenance therapy to prevent recurrence [6].

Magnetic resonance imaging (MRI) technology is based on the principle of nuclear magnetic resonance imaging. It has the advantages of noninvasive and precise positioning. It is one of the important technologies in medical imaging. Brain function research has always been a very challenging topic, and this research direction has a significant role in promoting the field of neurology and clinical diagnosis [7]. According to a study [8], the gray matter volume of schizophrenia patients was reduced compared with normal healthy people by MRI features. At the same time, some scholars pointed out [9] that there is a certain relationship between the reduction of gray matter volume and the psychiatric symptoms and the severity of cognitive impairment in patients with schizophrenia. Several studies have found [10] that changes in gray matter volume have high diagnostic value in clinically distinguishing schizophrenia, bipolar disorder, and normal healthy populations. Voxel-based morphometry (VBM) is a technique for analyzing brain magnetic resonance images at the voxel level. It is a method to calculate the voxel size and specific structure concentration of local structures (such as brain gray and white matter) automatically and objectively by applying the voxels of spatially normalized images to evaluate the differences in brain anatomy from an overall perspective [11, 12]. At present, it is widely used in the quantitative analysis of the morphological structure of the whole brain under normal brain aging and pathological conditions.

There is also an important research direction in the etiology of schizophrenia, that is, neuroendocrine. Neuroendocrine abnormalities can cause changes in hormone levels, leading to mental and behavioral abnormalities in patients [13], among which cortisol and prolactin are strongly correlated with mental abnormalities. Cortisol is a kind of epinephrine produced by the human body in response to stress. The abnormal activity of the hypothalamic-pituitary-adrenal axis will lead to excessive secretion of cortisol, and the increase of its level is related to abnormal cognitive, emotional, and memory functions. Performance is correlated [14, 15]. Prolactin is a protein hormone produced by lactating cells in the anterior pituitary gland and is an important neuroendocrine factor. Pathological changes in the hypothalamic-pituitary-gonadal axis will change the level of prolactin. In addition, the release of prolactin is modulated and inhibited by the dopamine system, so it can be used as an observation standard for evaluating dopamine activity [16, 17], which shows that patients with schizophrenia may have abnormal dopamine function.

In this research, the voxel-based morphological analysis method was used to analyze the gray matter structure of the gray matter of first-episode schizophrenia and to detect the levels of cortisol and prolactin in plasma. The objective was to investigate the magnetic resonance imaging features of brain structure in patients with first-episode schizophrenia and to explore the pathological significance of neuroendocrine levels in schizophrenia, so as to provide a theoretical reference for the pathology of schizophrenia.

2. Materials and Methods

2.1. Research Objects. A total of 25 patients with first-episode schizophrenia admitted to the hospital from May 2019 to December 2021 were selected and set as the observation group. There were 15 males and 10 females, with an age range of 18–35 years and an average age of 23.4 ± 1.5 years. 25 healthy people who underwent physical examination in the hospital during the same period were selected as the control group, including 13 males and 12 females, with an age range of 19–34 years and an average age of 22.3 ± 1.7 years. Both the control group and the observation group received MRI examination, and the levels of cortisol and prolactin of patients in the observation group were detected. The research objects agreed to sign informed consent forms with the consent of their family members. This research had been approved by the ethics committee of hospital.

2.1.1. Inclusion Criteria. Inclusion criteria include patients whose diagnosis meeting the diagnostic criteria for schizophrenia in "Chinese Classification and Diagnostic Criteria for Mental Disorders" [18]; patients with first onset and no drug or psychological treatment; patients with no history of drug use; patients with no history of alcohol abuse within 3 months; and patients with complete clinical data.

2.1.2. Exclusion Criteria. Exclusion criteria include patients with organic mental disorders, mood disorders, and mental disorders caused by psychoactive substances; patients with serious physical diseases; those with a history of epilepsy or febrile convulsion; those who had attempted suicide; those with poor compliance and who were unable to cooperate with the experiment, or who had no guardian; pregnant or lactating women; and patients with contraindications to magnetic resonance scanning.

2.2. MRI Examination and Image Processing. 3.0T MRI system with 8-channel standard head coil was used. Before the examination, the objects were confirmed to have no

metal or magnetic substances, and the cranial MRI examination was performed in the supine position. The head was fixed to prevent artifacts, and conventional weighted T1 and T2 scans were given to monitor the morphological appearance of the brain and obtain brain anatomical images. Scanning parameters were set as follows: time of repetition (TR)/time of echo (TE) = 8.2/3.2 ms, matrix was 256×256, and layer thickness was 1 mm. After scanning, the scanned image was transmitted to the image processing system for subsequent processing.

FSL-VBM analyzed its gray matter structural changes and processes Tl 3D high-resolution images. In the first step, the average symmetrical template of the brain was established, and the initial MRI image was converted into an image with a size of about $1 \times 1 \times 1$ mm^3, and the T1 template was constructed by spatial smoothing. In the second step, the gray matter template was established, the initial MRI image was registered to the T1 template, and the gray matter was extracted and segmented. In addition, Gaussian smoothed space and averaged superposition were performed. The third step was to create a mirror image for all study objects. The fourth step was to segment the mirror images and initial MRI images of all objects to the generated template, standardize the gray matter template established by the initial gray matter image, apply the standardized parameters to the initial image, and obtain the final standardized brain image. It should segment the normalized image and smooth the gray matter image.

2.3. Detection of Neuroendocrine Levels. The patients were tested for cortisol and prolactin. At 8:00 in the morning, the venous blood was drawn when the patients were in a fasting state, left standing for half an hour, and centrifuged at 3,000 r/min to extract serum. Chemiluminescence immunoassay was used for the determination. The reagents and measuring instrument were ELISA kits and electrochemiluminescence immune-analyzer, respectively. The calibration curve and the radioactivity values of the specimens were printed with a γ-scintillation counter. The normal reference value at 8:00 in the morning ranged 140–630 nmol/L.

Prolactin was detected using the chemiluminescence method and counted using a γ-counter. The reference interval was 4.79–23.3 ng/mL. When the prolactin level was higher than the upper limit, it was determined that the prolactin was abnormally elevated. When the prolactin level was lower than the upper limit, the level was relatively low.

2.4. Psychiatric Symptom Assessment. Severity of symptoms was assessed using Positive and Negative Syndrome Scale (PANSS), which was adapted from a combination of the Brief Psychiatric Scale and the Psychopathological Rating Scale. It was mainly suitable for adults. The psychiatrist who had been trained in the use of the scale conducted psychiatric examination of the patients and evaluated the relevant information provided by the

comprehensive clinical examination and the insiders. The time frame for the assessment was specified as all the information in the week preceding the assessment, and the entire assessment took approximately 30–50 minutes.

The PANSS consisted of a 7-item positive symptom scale, a 7-item negative symptom scale, and a 16-item general psychopathology subscale. The positive symptom scale was composed of delusion, conceptual confusion, hallucinatory behavior, excitement, exaggeration, suspicion or victimization, and hostility. The negative symptom scale included affective retardation, emotional withdrawal, affective communication disturbance, passiveness or apathy, abstract thinking, lack of spontaneity and fluency in conversation, and stereotyped thinking. The general psychopathology subscale was made up of worry about physical health, anxiety, guilt ideas, nervousness, posturing, depression, slow movement, uncooperativeness, abnormal thinking, orientation disorder, attention disorder, lack of self-knowledge, volitional disorder, impulse control disorder, preoccupation, and active social avoidance. Each item was rated using a 7-point scoring method (none, very mild, mild, moderate, slightly severe, severe, and extremely severe). The scores of the positive symptom scale, negative symptom scale, and general psychopathology subscale ranged from 7 to 49, 7 to 49, and 16 to 112, respectively. The total score was the sum of scores of the three subscales, ranging 30–210. The PANSS score was closely related to the clinical features of schizophrenia. The higher the PANSS score is, the more severe the positive, negative, and general psychiatric symptoms of patients are.

2.5. Statistical Analysis. SPSS 24.0 software was used for statistical analysis of the obtained data. Measurement data were expressed as the mean +standard deviation ($\overline{x} \pm s$), and count data were inferred by χ^2 test. The measurement data conformed to the normal distribution, and the t test was used. The correlation analysis between the indicators was performed by the Pearson test. The r value represents the correlation coefficient between variables in the sample, indicating the size of the correlation; the P value was the test value, which was to test whether the two variables have the same correlation as the sample in the population from which the sample came. The larger the absolute value of the correlation coefficient r, the stronger the correlation: the closer the correlation coefficient r was to 1 or −1, the stronger the correlation, and the closer the correlation coefficient was to 0, the weaker the correlation. The correlation strength of variables was judged by the following value ranges: correlation coefficient 0.8–1.0 meant very strong correlation, 0.6–0.8 meant strong correlation, 0.4–0.6 meant moderate correlation, 0.2–0.4 meant weak correlation, and 0.0–0.2 meant very weak correlation or no correlation related. The FMRIB software library was used to analyze the gray matter density of the mirror image and the original image data based on VBM, and the international statistical parameter map was used to represent it. $P < 0.05$ was considered statistically significant.

TABLE 1: Comparison on general clinic data.

Indicators	Control group	Observation group	P value
Age (years old)	22.3 ± 1.7	23.4 ± 1.5	0.653
Gender (male/female)	13/12	15/10	0.762
Course of disease (years)	—	1.36 ± 0.15	—
PANSS score (points)			
Positive symptom score	—	20.72 ± 4.32	—
Negative symptom score	—	19.46 ± 6.84	—
General psychopathology score	—	43.26 ± 7.35	—
PANSS total score	—	83.46 ± 12.63	—

3. Results

3.1. Comparison on General Clinic Data.
Table 1 shows that there was no statistical significance in general clinical data such as age, gender ratio, and course of disease in the two groups of objects ($P > 0.05$), which were comparable.

3.2. Brain Structure Detection Results Based on VBM.
As shown in Table 2 and Figure 1, the voxel-based morphometric results found that the differences between the observation group and the control group were more obvious. The patients in the observation group had obvious gray matter volume reduction in the frontal lobe and cingulate cortex, mainly including precentral gyrus, superior frontal gyrus, middle frontal gyrus, inferior frontal gyrus, postcentral gyrus, inferior parietal lobule, superior parietal lobule, and anterior cingulate cortex ($P < 0.05$, corrected by TFCE). As shown in Table 3 and Figure 2, the voxel-based morphometric results showed that compared with the control group, patients in the observation group had increased gray matter volume in some regions ($P < 0.05$, corrected by TFCE), mainly located in the cerebellum.

3.3. Comparison of Cortisol and Prolactin Levels.
As shown in Figure 3, the plasma cortisol level of the observation group was $387.54 \pm 117.69 \, \mu g/L$, which was significantly higher than that of the control group (138.46 ± 62.47); the prolactin level of the observation group was $804.16 \pm 267.13 \, \mu IU/mL$, which was significantly higher than that of the control group (397.54 ± 203.82), and the difference was statistically significant ($P < 0.05$).

3.4. Pearson Correlation Analysis.
As shown in Table 4, the Pearson correlation analysis between the plasma cortisol level of the observation group and the PANSS total score was $r = 0.421$ and $P = 0.013$, indicating that the higher the cortisol level, the more severe the patient's schizophrenia. The Pearson correlation analysis between the prolactin level and the PANSS total score in the observation group was $r = 0.019$ and $P = 0.568$, and the significance test failed, indicating that there was no statistical correlation between the two.

4. Discussion

Schizophrenia is a rare psychiatric disorder whose etiology is still being explored, along with the potential for chronic disability. This disease is probably caused by a large number of cerebral nerve cell lesions, showing a progressive development trend, and it is also accompanied by a variety of cognitive dysfunctions. Human brain activity is realized through a complex network system. The study by Guo et al. [19] showed that functional connectivity disorder caused by abnormal gray matter structure in various brain regions was one of the important factors for the onset of schizophrenia and various clinical symptoms. The basic condition of executive function is normal gray matter structure, but some studies related to magnetic resonance imaging have shown [20] that patients with schizophrenia may have extensive gray matter structure changes. MRI can be used to study the structure of living tissue, which is an effective method to study the structure of the gray matter, and has a wide range of applications in analyzing the changes in the structure of the gray matter in patients with schizophrenia.

The article by Koelkebeck et al. [21] pointed out that the gray matter structural abnormalities appear in almost all brain regions of patients with schizophrenia, but may not change independently, but appear mutually and have a certain correlation. The VBM results of this research showed that compared with the control group, the patients in the observation group had a decrease in the gray matter volume, and the main areas included precentral gyrus, superior frontal gyrus, middle frontal gyrus, inferior frontal gyrus, postcentral gyrus, inferior parietal lobule, superior parietal lobule, and anterior cingulate cortex, while the cerebellum gray matter volume increased. Such results are basically consistent with the results of Alemán-Gómez et al. [22]. The frontal lobe accounts for about one-third of the human brain, and the prefrontal lobe is the main area for the realization of high-level cognitive tasks, and it is also closely related to human cognitive function, emotional regulation, and self-regulation. Several studies have shown that patients with schizophrenia have reduced frontal gray matter volume. Quinn et al. [23] noted that a clinically meaningful history of alcohol or marijuana use did not significantly exacerbate the gray matter deficits associated with schizophrenia. The article by Tseng et al. [24] suggested that patients with first-episode schizophrenia had abnormal frontal gray matter in the early stage of the disease. From this, it can be understood that both patients with first-episode and chronic schizophrenia may have abnormal frontal gray matter structure. Many studies suggest that inferior parietal lobule plays a role in human social cognition and working memory. The precuneus is also of great significance to the process of human neuropsychological development and has a strong correlation with human insight and self-conscious processing. Some patients with schizophrenia will

TABLE 2: Results of VBM.

Regions	Right/left	Number of voxels	Coordinate X	Coordinate Y	Coordinate Z	1-P value
Precentral gyrus	Right	735	28	−8	45	0.9996
	Left	1036	−49	8	14	0.9996
Superior frontal gyrus	Right	2168	23	47	15	0.9996
	Left	1013	−23	31	35	0.9996
Middle frontal gyrus	Right	2396	32	49	10	0.9996
	Left	2302	−30	38	24	0.9996
Inferior frontal gyrus	Right	241	34	6	32	0.9996
	Left	456	−42	8	16	0.9996
Postcentral gyrus	Right	501	35	−26	48	0.9996
	Left	622	−58	−7	28	0.9996
Inferior parietal lobule	Left	842	−47	−49	34	0.9992
Superior parietal lobule	Right	347	48	−38	61	0.9996
	Left	149	−45	−48	34	0.9996
Anterior cingulate cortex	Right	505	10	47	14	0.9996
	Left	552	−10	26	29	0.9981

(a)　　　　　　　　　　　　(b)
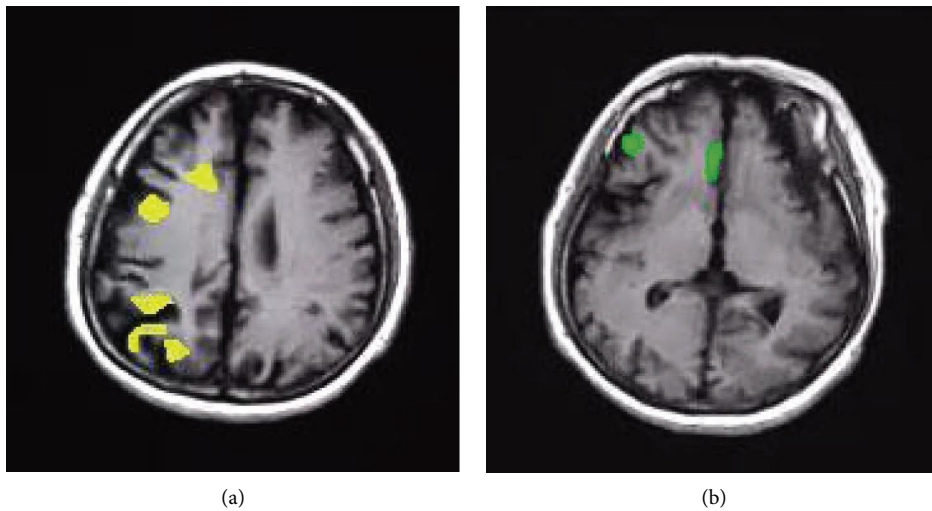
FIGURE 1: The results of VBM showed that the gray matter volume of the observation group was reduced compared to the control group. (a, b) MRI T1W1 images of the patients in the observation group. The yellow area in (a) represented precentral gyrus, superior frontal gyrus, middle frontal gyrus, postcentral gyrus, and superior parietal lobule. The green area in (b) represented inferior frontal gyrus and anterior cingulate cortex.

TABLE 3: The results of VBM show that the gray matter volume increased in the observation group compared with the control group.

Regions	Right/left	Number of voxels	Coordinate X	Coordinate Y	Coordinate Z	1-P value
Cerebellum	Right	1746	24	−73	−47	0.9996
	Left	1653	−26	−79	−39	0.9991

experience cognitive impairment and reduced insight, mainly affected by the structural changes of the parietal gray matter, which mostly occur in the superior parietal lobule and the inferior parietal lobule. Nestor et al. [25] suggested that the cortex of the superior parietal lobule in patients with schizophrenia was thinned. Schoretsanitis et al. [26] considered that first-episode schizophrenia patients had inferior parietal lobule gray matter density reduction. These all indicate that there may be abnormalities in the parietal gray matter structure in patients with schizophrenia.

The cerebellum is an important control organ that can coordinate activities in the human body and is closely related to human emotion regulation, attention management, social communication, language processing, and word memory. The findings of Cui et al. [27] showed an increase in small gray matter in patients with first-episode schizophrenia, which is consistent with the findings of this research. Patients with schizophrenia may exhibit abnormal changes in the structure of the small gray matter, manifested by increased gray matter volume. In addition, the results of this

(a)

(b)
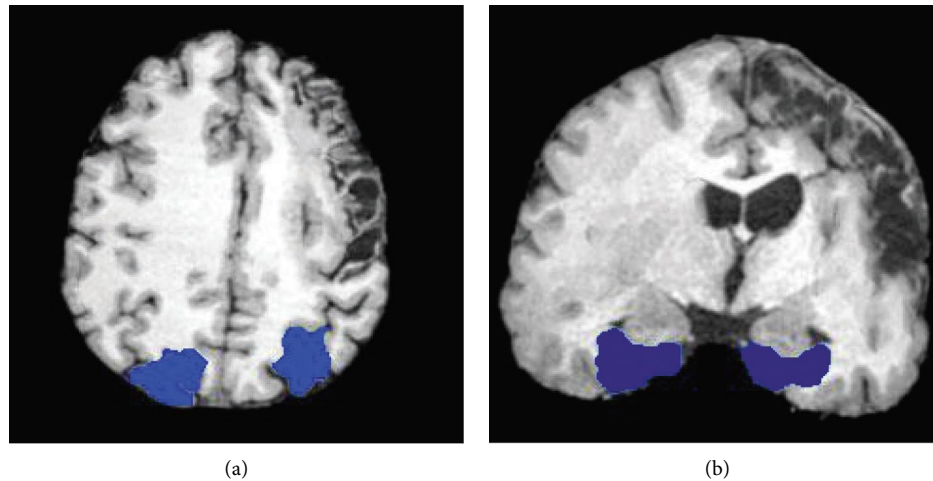
FIGURE 2: The results of VBM showed the increased gray matter volume in the observation group compared with the control group. (a) The MRI axial image, and (b) the MRI coronal image. The blue areas in the figure represented areas of the increased gray matter volume.
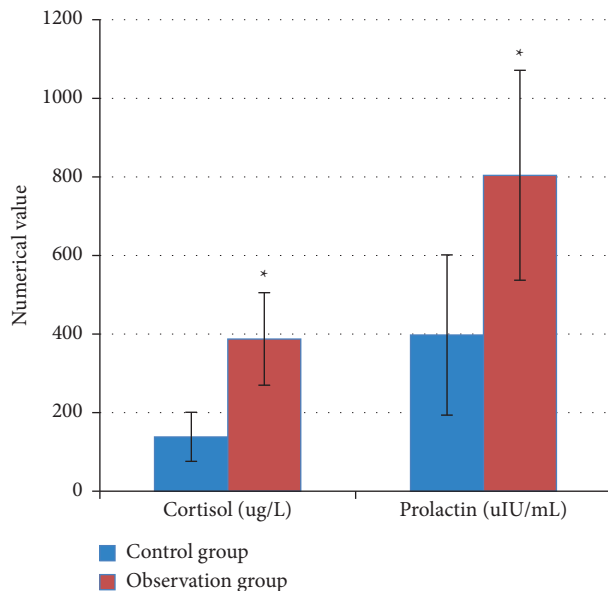
FIGURE 3: Comparison of cortisol and prolactin levels. ∗ Compared with control group, $P < 0.05$.

TABLE 4: Cortisol analysis of cortisol and prolactin levels and PANSS total score.

Indicators in observation group	R	P
Cortisol level	0.421	0.013
Prolactin level	0.019	0.568

research showed that the plasma cortisol level of the observation group was (387.54 ± 117.69) μg/L, which was significantly higher than that of the control group (138.46 ± 62.47) μg/L, and the prolactin level was (804.16 ± 267.13) μIU/mL, which was significantly higher than that of the control group (397.54 ± 203.82) μIU/mL, showing statistically significant differences $(P < 0.05)$. The results of the Pearson correlation test showed that the

cortisol level of the observation group was significantly correlated with the PANSS total score $(r = 0.421$ and $P = 0.013)$, indicating that the higher the cortisol level, the more severe the degree of schizophrenia in the patient. However, there was no significant correlation between the prolactin level and PANSS total score $(r = 0.019$ and $P = 0.568)$, indicating that the prolactin level of patients had no definite relationship with the degree of symptoms of schizophrenia. This result is consistent with the conclusion of the article by Jen et al. [28] that the level of prolactin in schizophrenia patients is not significantly different from that in healthy people. Therefore, it is still unknown whether prolactin at high levels can cause the onset of schizophrenia in patients.

5. Conclusion

This research analyzed the brain magnetic resonance images of first-episode schizophrenia patients based on VBM and compared neuroendocrine levels with healthy controls. The results showed that the gray matter volume in the precentral gyrus, superior frontal gyrus, middle frontal gyrus, inferior frontal gyrus, postcentral gyrus, inferior parietal lobule, superior parietal lobule, and anterior cingulate cortex decreased, while the gray matter volume in the cerebellum increased. The levels of cortisol and prolactin in patients with first-episode schizophrenia were significantly higher than those in healthy people, and the level of cortisol was directly proportional to the severity of the patients' psychiatric symptoms, while the level of prolactin was not directly related to the severity of symptoms. The disadvantage of this research was that only the default setting parameters in the software were used in the voxel-based morphometric processing, and it was necessary to change the parameters to analyze the brain magnetic resonance images in more detail and comprehensively in the future. In conclusion, MRI-based voxel morphometry can accurately and reliably assess brain structure, and the levels of cortisol and prolactin in patients with first-episode schizophrenia

were significantly higher than those in healthy people. The higher the cortisol level, the more severe the schizophrenia symptoms. This research provided a reference for the pathological study of first-episode schizophrenia.

Data Availability

The data used to support the findings of this study are available from the corresponding author upon request.

Conflicts of Interest

The authors declare that they have no conflicts of interest.

References

[1] F. C. Nucifora, E. Woznica, B. J. Lee, N. Cascella, and A. Sawa, "Treatment resistant schizophrenia: clinical, biological, and therapeutic perspectives," *Neurobiology of Disease*, vol. 131, Article ID 104257, 2019.

[2] N. Müller, "Inflammation in schizophrenia: pathogenetic aspects and therapeutic considerations," *Schizophrenia Bulletin*, vol. 44, no. 5, pp. 973–982, 2018.

[3] B. Batinic, "Cognitive models of positive and negative symptoms of schizophrenia and implications for treatment," *Psychiatria Danubina*, vol. 31, no. 2, pp. 181–184, 2019.

[4] M. Mak, J. Samochowiec, D. Frydecka et al., "First-episode schizophrenia is associated with a reduction of HERV-K methylation in peripheral blood," *Psychiatry Research*, vol. 271, pp. 459–463, 2019.

[5] M. Xu, Y. Guo, J. Cheng et al., "Brain iron assessment in patients with First-episode schizophrenia using quantitative susceptibility mapping," *Neuroimage Clin*, vol. 31, Article ID 102736, 2021.

[6] A. Puranen, M. Koponen, A. Tanskanen, J. Tiihonen, and H. Taipale, "Use of antidepressants and mood stabilizers in persons with first-episode schizophrenia," *European Journal of Clinical Pharmacology*, vol. 76, no. 5, pp. 711–718, 2020.

[7] M. D. Grier, J. Zimmermann, and S. R. Heilbronner, "Estimating brain connectivity with diffusion-weighted magnetic resonance imaging: promise and peril," *Biol Psychiatry Cogn Neurosci Neuroimaging*, vol. 5, no. 9, pp. 846–854, 2020.

[8] Y. Ji, X. Zhang, Z. Wang et al., "Genes associated with gray matter volume alterations in schizophrenia," *NeuroImage*, vol. 225, Article ID 117526, 2021.

[9] M. Jáni, Z. Kikinis, J. Lošák et al., "Emotional awareness in schizophrenia is associated with gray matter volume of right precuneus," *Frontiers in Psychiatry*, vol. 12, Article ID 601742, 2021.

[10] K. Rootes-Murdy, E. Zendehrouh, V. D. Calhoun, and J. A. Turner, "Spatially covarying patterns of gray matter volume and concentration highlight distinct regions in schizophrenia," *Frontiers in Neuroscience*, vol. 15, Article ID 708387, 2021.

[11] S. Ponticorvo, R. Manara, M. C. Russillo et al., "Magnetic resonance T1w/T2w ratio and voxel-based morphometry in multiple system atrophy," *Scientific Reports*, vol. 11, no. 1, Article ID 21683, 2021.

[12] H. Takao, S. Amemiya, O. Abe, and Alzheimer's Disease Neuroimaging Initiative, "Reproducibility of brain volume changes in longitudinal voxel-based morphometry between non-accelerated and accelerated magnetic resonance imaging," *Journal of Alzheimer's Disease*, vol. 83, no. 1, pp. 281–290, 2021.

[13] E. G. Severance, F. Dickerson, and R. H. Yolken, "Complex gastrointestinal and endocrine sources of inflammation in schizophrenia," *Frontiers in Psychiatry*, vol. 11, p. 549, 2020.

[14] K. Bolhuis, H. Tiemeier, P. R. Jansen et al., "Interaction of schizophrenia polygenic risk and cortisol level on pre-adolescent brain structure," *Psychoneuroendocrinology*, vol. 101, pp. 295–303, 2019.

[15] F. Yang, X. Cao, X. Sun, H. Wen, J. Qiu, and H. Xiao, "Hair cortisol is associated with social support and symptoms in schizophrenia," *Frontiers in Psychiatry*, vol. 11, Article ID 572656, 2020.

[16] M. Tost, J. A. Monreal, A. Armario et al., "Targeting hormones for improving cognition in major mood disorders and schizophrenia: thyroid hormones and prolactin," *Clinical Drug Investigation*, vol. 40, no. 1, pp. 1–14, 2020.

[17] J. Lally, A. B. Sahl, K. C. Murphy, F. Gaughran, and B. Stubbs, "Serum prolactin and bone mineral density in schizophrenia: a systematic review," *Clin Psychopharmacol Neurosci*, vol. 17, no. 3, pp. 333–342, 2019 Aug 31.

[18] Y. F. Chen, "Chinese classification of mental disorders (CCMD-3): towards integration in international classification," *Psychopathology*, vol. 35, no. 3, pp. 171–175, 2002.

[19] F. Guo, Y. Q. Zhu, C. Li et al., "Gray matter volume changes following antipsychotic therapy in first-episode schizophrenia patients: a longitudinal voxel-based morphometric study," *Journal of Psychiatric Research*, vol. 116, pp. 126–132, 2019.

[20] Z. T. Gao, Y. L. Li, S. Q. Guo, and Y. H. Xia, "Brain gray matter volume alterations and cognitive function in first-episode childhood-and adolescence-onset schizophrenia," *Zhonghua Yixue Zazhi*, vol. 99, no. 45, pp. 3581–3586, 2019.

[21] K. Koelkebeck, U. Dannlowski, P. Ohrmann et al., "Gray matter volume reductions in patients with schizophrenia: a replication study across two cultural backgrounds," *Psychiatry Research: Neuroimaging*, vol. 292, pp. 32–40, 2019.

[22] Y. Alemán-Gómez, E. Najdenovska, T. Roine et al., "Partial-volume modeling reveals reduced gray matter in specific thalamic nuclei early in the time course of psychosis and chronic schizophrenia," *Human Brain Mapping*, vol. 41, no. 14, pp. 4041–4061, 2020.

[23] M. Quinn, M. McHugo, K. Armstrong, N. Woodward, J. Blackford, and S. Heckers, "Impact of substance use disorder on gray matter volume in schizophrenia," *Psychiatry Research Neuroimaging*, vol. 280, pp. 9–14, 2018.

[24] H. H. Tseng, C. D. Chiu, K. C. Chen, I. H. Lee, P. S. Chen, and Y. K. Yang, "Absence of negative associations of insular and medial frontal gray matter volume with dissociative symptoms in schizophrenia," *Journal of Psychiatric Research*, vol. 138, pp. 485–491, 2021.

[25] P. G. Nestor, M. Forte, T. Ohtani et al., "Faulty executive attention and memory interactions in schizophrenia: prefrontal gray matter volume and neuropsychological impairment," *Clinical EEG and Neuroscience*, vol. 51, no. 4, pp. 267–274, 2020.

[26] G. Schoretsanitis, K. Stegmayer, N. Razavi et al., "Inferior frontal gyrus gray matter volume is associated with aggressive

behavior in schizophrenia spectrum disorders," *Psychiatry Research: Neuroimaging*, vol. 290, pp. 14–21, 2019.

[27] X. Cui, Q. Deng, B. Lang et al., "Less reduced gray matter volume in the subregions of superior temporal gyrus predicts better treatment efficacy in drug-naive, first-episode schizo- phrenia," *Brain Imaging and Behavior*, vol. 15, no. 4, pp. 1997–2004, 2021.

[28] Y. W. Jen, T. J. Hwang, H. Y. Chan et al., "Abnormally low prolactin levels in schizophrenia patients after switching to aripiprazole in a randomized trial: a biomarker for rebound in psychotic symptoms?" *BMC Psychiatry*, vol. 20, no. 1, p. 552, 2020.

WILEY | Hindawi

Research Article

Analysis of Changes in Brain Region and Connectomics in the Acute Stage of Sudden Sensorineural Hearing Loss in the Resting State via Functional Magnetic Resonance Imaging

Zhonghua Li ⓘ

Department of E.N.T.(Ear-Nose-Throat), Affiliated Hospital of Beihua University, Jilin City 132000, Jilin, China

Correspondence should be addressed to Zhonghua Li; 2020212235@mail.chzu.edu.cn

To explore the functional changes in the whole brain network in patients with sudden sensorineural hearing loss (SHL) at the acute stage from functional magnetic resonance imaging (fMRI) imaging evaluation results, 80 patients with sudden right SHL were selected as subjects (patient group). In addition, 40 healthy volunteers who underwent physical examination in the hospital during the same period were recruited as a control group. fMRI imaging was performed to analyze functional parameters and core nodes of the whole brain network. It was found that at all thresholds, the fMRI parameters C_p and L_p of the patient group were dramatically superior to those of the control group. The fMRI parameter E_{global} of the patient group was substantially lower than that of the control group ($P < 0.05$). At most of the thresholds, the fMRI parameter λ in patients was dramatically superior to that in the control group ($P < 0.05$). There were ten specific network core nodes in patients, including the right parahippocampal gyrus, right supra-occipital gyrus, left suboccipital gyrus, right fusiform gyrus, right parietal lobule, right subparietal lobule, right superior temporal gyrus, left superior marginal gyrus, and right superior temporal gyrus. In summary, the whole brains of patients with sudden SHL still had small-world attributes, but some characteristics of the brain network had changed, and there was a trend of transformation to a regular network. The connection between the auditory brain area and the functional areas related to language and vision was weakened, and the distribution of core nodes changed. This study provides a reference basis for exploring the changes in local brain and connectome levels in patients with sudden sensorineural hearing loss in the acute phase based on resting-state fMRI.

1. Introduction

When the lesions are in the hair cells, auditory nerves, or hearing centers at all levels of the helical organ and the sensation of sound and conduction of nerve impulses are impaired, resulting in hearing loss, it is called sensorineural hearing loss (SHL) [1–3]. Hearing loss caused by hair cell disease is called SHL (cochlear or terminal hearing loss). Hearing loss caused by lesions located in the auditory nerve and its conduction pathway is called neural hearing loss (retrocochlear or postcochlear) and is characterized by a marked decline in speech discrimination. Lesions occurring in the auditory center of the cerebral cortex are called central deafness and are often accompanied by neurological symptoms [4, 5]. SHL patients mainly have symptoms such as high-frequency hearing loss, reinvigorating phenomenon, tinnitus, and vertigo. This kind of deafness cannot change sound waves into nerve signals, or nerves, and their central way of producing obstacles cannot transmit nerve signals to the brain, which is the most difficult to treat and the most troublesome form of deafness. It is usually caused by congenital or acquired causes of cochlear auditory nerve or auditory center lesions, resulting in deafness [6–8]. According to current clinical and experimental studies, hearing loss often caused by SHL is irreversible and cannot be cured by drugs or surgery, which has been fully confirmed by massive basic and clinical studies and experiments over the years [9, 10]. Although the data showed that a small

number of people's sudden deafness can be cured automatically, for the occurrence of sudden deafness, it is still recommended for timely hospital diagnosis.

Common clinical diagnosis methods for deafness include vestibular function tests, hearing examinations, X-rays, computed tomography (CT), and MRI [11–14]. Patients with vertigo can undergo a cold temperature test and an electronystagmus examination to determine vestibular damage and exclude central dysfunction after the condition becomes stable [15]. Pure tone audiometry can show typical SHL, and the hearing curve of moderate, severe, or more severe hearing loss patients is usually flat or descending. The pure tone supramural function test, the Bekesy test, speech audiometry, and acoustic immittance test can determine cochlear deafness. X-ray or CT scans of the inner ear canal can rule out sudden deafness caused by external neuroma or other intracranial occupying lesions [16]. However, the above methods can only make a preliminary judgment on the lesion degree of patients but cannot evaluate the changes in cerebral cortical functional activities after deafness [17]. Functional magnetic resonance imaging (fMRI) is a new neuroimaging method that uses magnetic resonance imaging to measure the hemodynamic changes caused by neuronal activity. It has been widely used to map brain activation in humans and animals. The change of local deoxyhemoglobin concentration in the brain will lead to the change of magnetic resonance signal intensity, which indirectly reflects neuronal activity and then reflects the change of brain function in real time [18]. In recent years, fMRI has become the tool of choice for visualizing neural activity in the human brain due to its noninvasive nature, reproducibility, and lack of radiation exposure. In resting-state fMRI, subjects are scanned while lying flat, eyes closed, awake, and not thinking about a problem without a specific task. Resting-state fMRI is very suitable for the study of clinical diseases, especially neurological diseases because of its simple experimental design, simple operation, and ability to observe the spontaneous brain activity of subjects without subjects completing specific tasks [19]. The brain is one of the major parts of the central nervous system. It can transmit, store, and process information, make people do various psychological activities, and dominate and control people's behavior. Although they are composed of various brain regions that are independent of each other in space, these brain regions are functionally interconnected and constantly flow information with each other [20]. Therefore, it is significant to explore sudden deafness from the perspective of brain functional network changes.

In summary, this study aimed to analyze the functional parameters and core nodes of the whole brain network based on resting-state fMRI by conducting fMRI scanning and constructing the brain functional networks of 80 patients with severe right sensorineural hearing loss and 40 healthy volunteers. It was hoped to provide a reference for the study of the changes in the functional connectivity level of the whole brain network in patients with sudden sensorineural hearing loss in the acute stage.

2. Materials and Methods

2.1. Research Objects. Eighty patients with severe right SHL who visited the hospital from October 2019 to October 2021 were selected as study subjects (patient group), including 34 males and 46 females. The average age was 35.36 ± 10.34 years (range, 25–67 years). After pure tone audiometry, the hearing threshold of the affected ear of the patient group was more than 70 dB, and the hearing threshold of the healthy ear was in the normal range. In addition, 40 healthy volunteers who underwent physical examination in the hospital during the same period were selected as a control group, including 15 males and 25 females. The age ranged from 24 to 65 years, with an average age of 37.11 ± 8.95 years. After pure-tone audiometry, the hearing threshold of both ears was less than 25 dB. This study was approved by the ethics committee of the hospital. The subjects and their families were informed of the study and signed informed consent forms.

Inclusion criteria are as follows: (i) all subjects were right-handed; (ii) subjects had complete basic information; (iii) subjects had no previous history of mental illness; and (iv) subjects were older than 18 years.

Exclusion criteria are as follows: (i) subjects with contraindications to MRI examination; (ii) subjects with history of cardiovascular disease; and (iii) subjects complicated with serious damage to the heart, liver, and kidney organs.

2.2. Resting fMRI Examination. A 3.0 T superconducting magnetic resonance imaging system with 12 channel coils was used. First, the subjects were placed in a supine position and put on an eye mask and soundproof earplugs to avoid interference from the outside environment. The subjects were guided to remain in a resting state. After the scan, if the patient was found not to remain in a resting state during the scan, the sample would be removed. A total of 300 time points were collected by resting whole brain volume scanning for each subject. The scanning parameters were as follows: repeat time (TR) = 1.800 ms, echo time (TE) = 20 ms, layer thickness = 3.5 ms, layer spacing = 0, layer number = 65, field of vision = 256 × 256, matrix = 256 × 256, and flip angle = 90 degrees.

2.3. Image Preprocessing. The data processing assistant for resting-state fMRI (DPARSF) based on MATLAB R2014b-2020b was used to preprocess the obtained images. The volume data of the first 10 points of each subject were removed. Time correction and head correction were carried out for the remaining 290 time points. Sample data of head movement exceeding 2 mm and rotation exceeding 2 degrees were removed. Linear regression was adopted to remove white matter and cerebrospinal fluid signals from the image data, and then it was standardized to the spatial coordinates of the Montreal Neurological Institute for resampling. Spatial smoothing was performed on standardized data, and time-domain bandpass filtering with a bandwidth of approximately 0.05 Hz was used to reduce the

influence of low-frequency drift and high-frequency physiological noise.

2.4. Construction of the Brain Functional Network.
GRETNA, developed by Professor Yong He's team from Beijing Normal University, was used to construct the brain functional networks of subjects. The subjects' brains were registered on an automatic anatomical marker map, which divided the cerebral cortex into 90 regions. Each region represented a node, and the time correlation of the blood oxygen level-dependent signal in each brain region was called an edge. The average time series of all voxels in each brain region was extracted, and the Pearson correlation coefficient between them was calculated to obtain the correlation matrix R. Then, the Fisher Z transformation was performed on the matrix R to obtain the correlation matrix Z, which was converted to the correlation matrix C for parameter calculation.

2.5. Brain Functional Network Parameters.
Given that the network node set is U and the network edge set is I, the complex network can be represented by the image $F(U$ and $I)$. Then, the node clustering coefficient C_x is expressed as follows:

$$C_x = \frac{2E_x}{L_x(L_x - 1)} C_y = \frac{2E_y}{L_y(L_y - 1)}. \quad (1)$$

L_x represents the number of nodes constituting subgraph F_x, L_y represents the number of nodes constituting subgraph F_y, and E represents local efficiency. The average value of C_x of all nodes is the network clustering coefficient C_p, which can be used to evaluate the degree of network collectivization. The average value of E_x of all nodes is the network local efficiency E_{local}, which can be used to evaluate the network defense capability. The average maximum short-circuit length L_p is the average time l_{xy} of all nodes to ensure effective integration and fast transmission of information in distant brain regions. Global efficiency E_{global} evaluates the global transport capacity of a network.

The standardized coefficient γ reflects the transformation from the real brain network to the regular network, and the standardized average shortest path length λ reflects the transformation from the real brain network to the random network, which can be expressed as follows:

$$\gamma = \frac{C_p}{C_{rand}},$$

$$\lambda = \frac{L_p}{L_{rand}}, \quad (2)$$

$$\sigma = \frac{\gamma}{\lambda}.$$

C_{rand} represents the clustering coefficient of the random network, L_{rand} represents the shortest path length of the random network, and $\sigma > 1$ indicates that the network has a high clustering coefficient and a short characteristic path length.

The intermediate centricity method was used to find the core nodes of the whole brain network. In this experiment, the threshold range was 0.1–0.2 with an interval of 0.02.

2.6. Statistical Methods.
SPSS 19.0 statistical software was used for data processing in this study. The mean ± standard deviation ($\overline{x} \pm s$) was used for measurement data, and the percentage (%) was used for counting data. Pairwise comparison was performed by one-way ANOVA. $P < 0.05$ suggests that the difference was statistically significant.

3. Results

3.1. General Information.
In Table 1, the ratio of male to female, age, course of disease, height, weight, years of education, THI score, and left ear PTA score in the patient group were not significantly different from those in the normal group ($P > 0.05$). The PTA score of the patient group (85.71 ± 9.01) was significantly higher than that of the normal group (20.77 ± 3.81), and the difference was statistically significant ($P < 0.05$).

3.2. Comparison of fMRI Global Parameters.
Figure 1 shows the comparison of the fMRI parameters E_{global}, E_{local}, C_p, and L_p between the two groups. The fMRI parameters E_{global}, E_{local}, and C_p of the two groups showed an increasing trend with an increasing threshold, while L_p showed a decreasing trend with an increasing threshold. At all thresholds, the fMRI parameters, C_p and L_p, in patients were dramatically superior to those in the control group, and the differences were considerable ($P < 0.05$). At most of the thresholds, the fMRI parameter E_{global} of the patient group was substantially lower than that of the control group, and the differences were considerable ($P < 0.05$). At all thresholds, there was no considerable difference in the fMRI parameter E_{local} between the patient group and the control group ($P > 0.05$).

Figure 2 shows the comparison of fMRI parameters γ, λ, and σ between the two groups. The fMRI parameters γ, λ and σ of the two groups showed a decreasing trend with an increasing threshold value. At most of the thresholds, the fMRI parameter λ of the patient group was dramatically superior to that of the control group, and the differences were considerable ($P < 0.05$). At all thresholds, fMRI parameters γ and σ in the patient group were not substantially different from those in the control group ($P > 0.05$).

3.3. FMRI Image Data.
Figure 3 shows MRI images of one patient in the patient group. Physical examination suggested a clear mind, vague language, decreased vision, no nystagmus, deafness in both ears, muscle strength level V, bilateral calcaneus shin test (+), and acceptable finger and nose rotation. Obviously, the surface of the midbrain, pons, vermis of the cerebellum and sulci, bilateral lateral fissure, underside of the frontal lobe, and spinal cord were surrounded by short T2 signals with bands.

TABLE 1: Comparison of basic data of medical staff between the two groups.

Basic information	Patient group ($n = 80$)	Control group ($n = 40$)	P
Sex ratio (male/female)	42.5/57.5	37.5/62.5	1.457
Age (years old)	35.36 ± 10.34	37.11 ± 8.95	2.568
Duration of disease (days)	9.16 ± 1.76	—	—
Height (cm)	160.44 ± 11.42	158.33 ± 10.68	1.496
Body weight (kg)	57.03 ± 5.82	55.81 ± 7.03	1.733
Years of education (years)	12.35 ± 3.25	11.09 ± 2.88	2.024
THI score (points)	49.68 ± 13.06	51.66 ± 16.77	2.145
Auris sinistra/Auris dextra	$21.74 \pm 4.11/85.71 \pm 9.01$	$21.33 \pm 3.57/20.77 \pm 3.81^{*}$	0.0378

*indicated a statistically significant difference compared with the patient group ($P < 0.05$).

Figure 4 shows the MRI data of a healthy volunteer in the control group. The T1 weighted image presented a high signal, and the T2 weighted image presented an equal signal. The position of the brain stem and cerebellum was normal without displacement or deformation, and the surface of the midbrain, pons, vermis, and sulci was normal.

3.4. Analysis Results of Functional Core Nodes of the Whole Brain Network.

In Figure 5, this analysis showed that there were 10 specific network core nodes in the patient group, including the right parahippocampal gyrus, right suproccipital gyrus, left suproccipital gyrus, right fusiform gyrus, right parietal lobule, right subparietal lobule, right superior temporal gyrus, left superior marginal gyrus, and right superior temporal gyrus temporal pole. There were eight specific network core nodes in the control group, including the left inferior frontal gyrus orbital, right insula, left insula, left parietal lobule,, right pea shell, left superior temporal gyrus temporal pole, and right middle temporal gyrus temporal pole. Subjects in both groups had a total of five network core nodes, including the right inferior frontal gyrus orbital region, left posterior central gyrus, right superior marginal gyrus, left middle cingulate gyrus, and right superior frontal gyrus medial orbital region.

4. Discussion

Sudden sensorineural deafness refers to the sudden occurrence of SHL of unknown cause, which can develop from mild hearing loss to severe hearing loss within minutes, hours, or 1–2 days [21]. There is no specific diagnosis and treatment method for approximately 90% of cases of sudden sensorineural deafness because the cause is unclear. In addition, the lack of high-quality clinical research and evidence-based medical proof makes the diagnosis and treatment of sudden inductive neural deafness controversial. Therefore, seeking an efficient diagnostic method is a reliable way to achieve clinical treatment optimization [22]. In this study, 80 patients with severe right SHL who visited the hospital were selected as the study subjects (patient group), and 40 healthy volunteers who underwent physical examination in the hospital during the same period were selected as the control group. FMRI imaging was performed on all patients. GRETNA was used to construct the subjects' brain functional networks, and the functional parameters and core

nodes of the whole brain network were analyzed. First, the basic data of the two groups of subjects were compared. The results showed that the ratio of males to females, age, course of disease, height, weight, years of education, THI score, and left ear PTA score in the patient group were not significantly different from those in the control group ($P > 0.05$), which provided a baseline for subsequent studies. In addition, the PTA score of the patient group (85.71 ± 9.01) was dramatically superior to that of the control group (20.77 ± 3.81), and the difference was significant ($P < 0.05$), which was consistent with the control study between the patient group and control group.

The functional network of the human brain is a complex and real network between a random network and a regular network, and its small-world attributes can ensure that the brain can efficiently integrate and separate information under relatively low energy consumption [23]. This study found that at all thresholds, the fMRI parameters C_p and L_p of the patient group were dramatically superior to those of the control group. At most of the thresholds, the fMRI parameter E_{global} of the patient group was substantially lower than that of the control group, and the differences were considerable ($P < 0.05$). This is generally consistent with the research results of Minosse et al. [24]. Although the whole brain of patients with sudden sensorineural hearing loss still had the small-world property, some characteristics of the brain network had changed. The increase of parameters meant that the information processing ability of some brain regions of patients was enhanced, indicating that the contralateral superiority of hearing conduction was weakened, and intrachannel reorganization occurred in the auditory cortex. The increase in parameters L_p and E_{local} suggested that the information processing ability of the patient's remote brain region was weakened, which was consistent with the general deletion hypothesis [25]. At most of the thresholds, the fMRI parameter λ of the patient group was dramatically superior to that of the control group, and the differences were considerable ($P < 0.05$). At all thresholds, fMRI parameters γ and σ in the patient group were not substantially different from those in the control group ($P > 0.05$). Wang et al. [26] also pointed out that this indicates that the brain functional network of patients with sudden sensorineural hearing loss has a trend of changing to a regular network, with enhanced information integration ability and weakened separation transmission ability. The results indicate that the brain functional network of patients
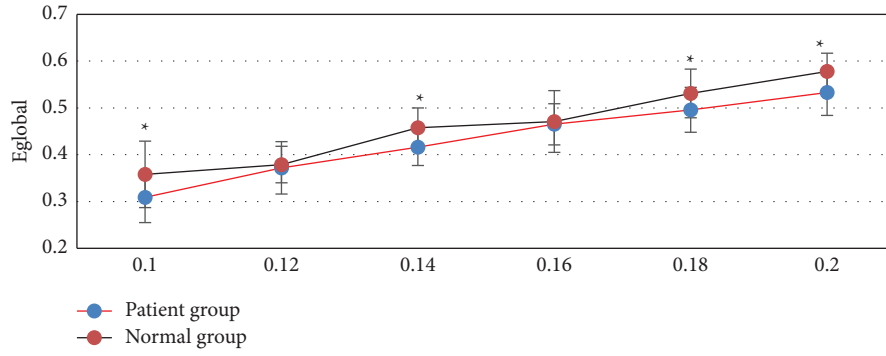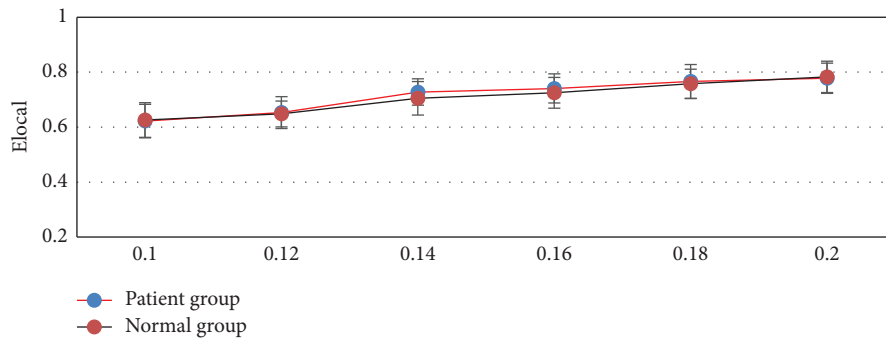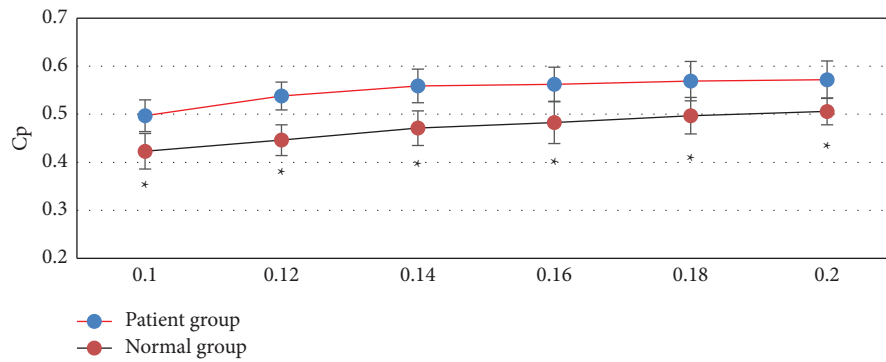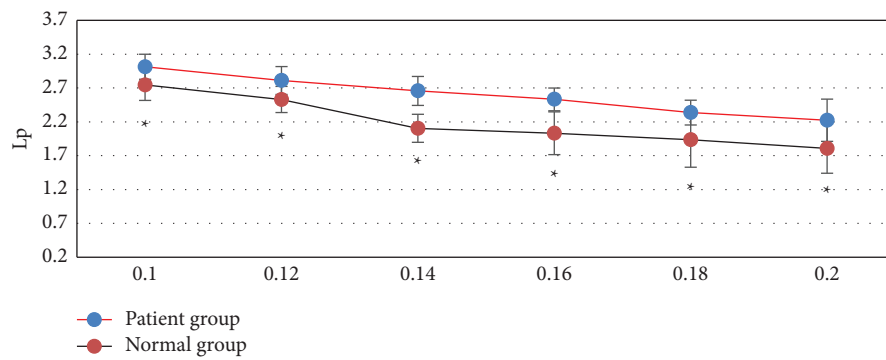
FIGURE 1: Comparison of the fMRI parameters E_{global}, E_{local}, C_p, and L_p between the two groups. (a–d) represented E_{global}, E_{local}, C_p, and L_p, respectively. *represents that the fMRI parameters of the patient group, including E_{global}, C_p, and L_p, were significantly different from those in the normal group ($P < 0.05$).

(a)

(b)

(c)
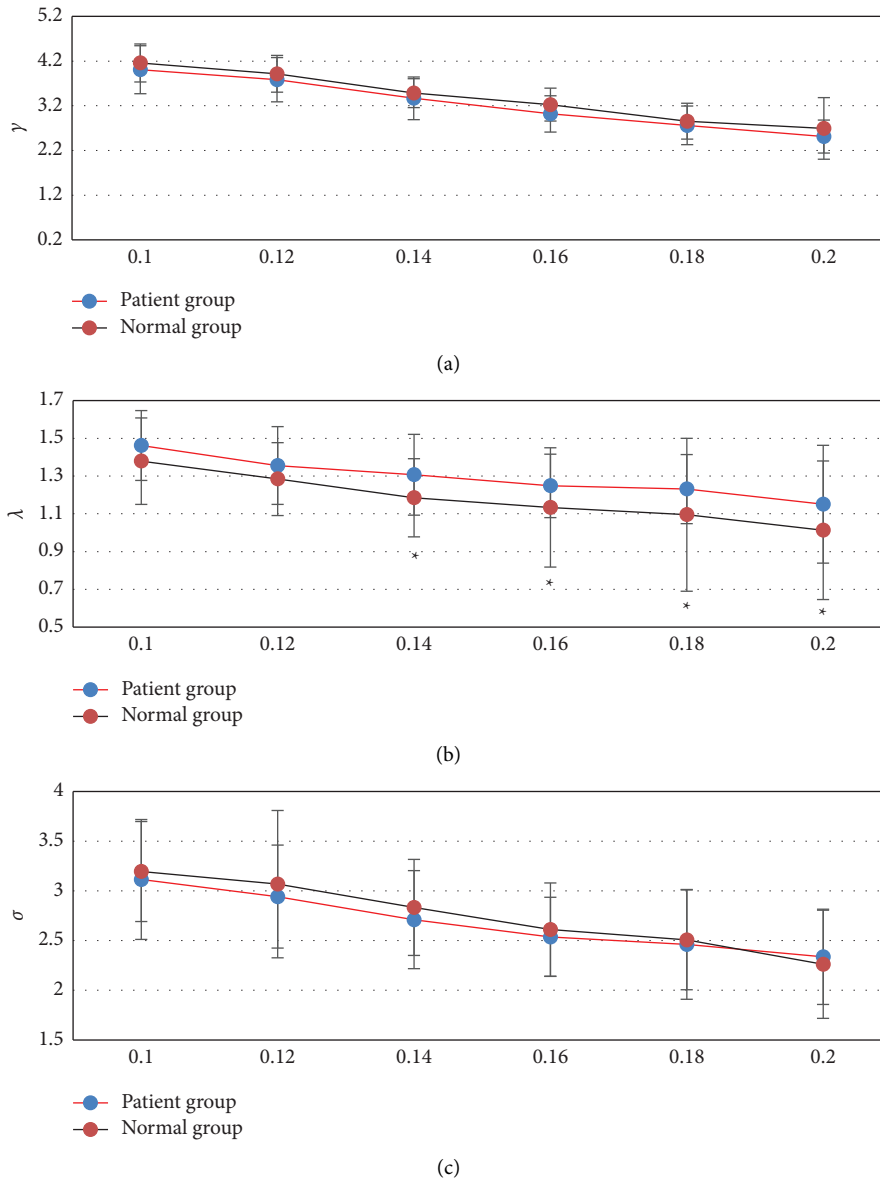
FIGURE 2: Comparison of fMRI parameters γ, λ, and σ between the two groups. (a–c) represented γ, λ, and σ, respectively. *Compared with the normal group, $P < 0.05$.

| (a) | (b) | (c) | (d) |
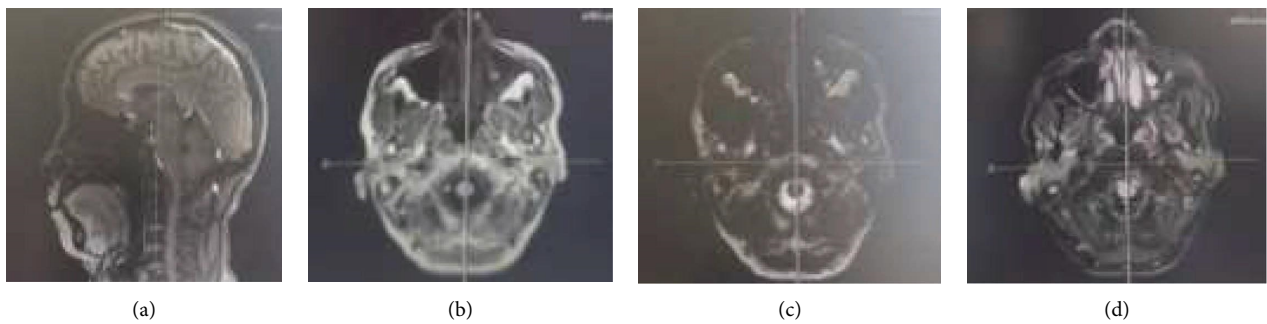
FIGURE 3: MRI image data of a patient. Female, 58 years old, high tinnitus in both ears without obvious inducement, followed by hearing loss, and gradually aggravated, with basic hearing loss in the recent six months, unstable walking, and tremor on both upper limbs. (a) MRI sagittal image; (b-c) T1 weighted image; and (d) T2 weighted image.
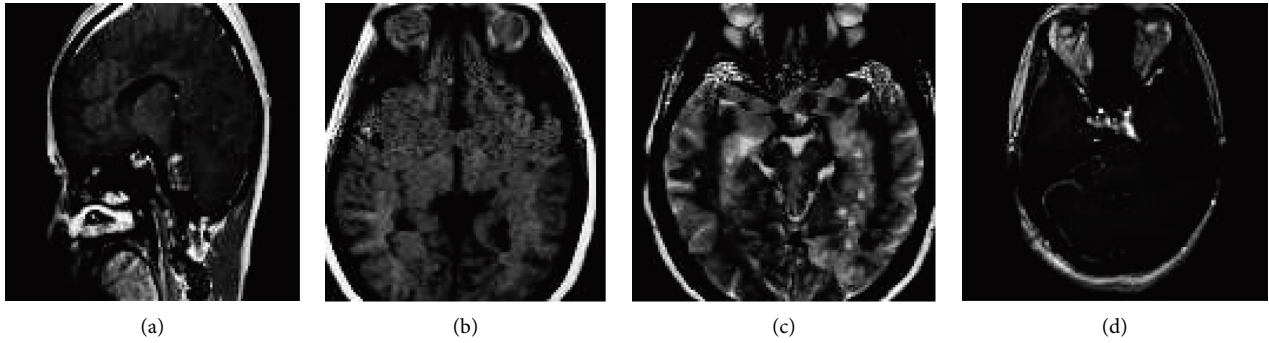
FIGURE 4: MRI image data of a healthy volunteer in the control group. Female, 50 years old, physical examination showed normal body function but no liver or kidney damage. (a) MRI sagittal image; (b-c) T1 weighted image; (d) T2 weighted image.
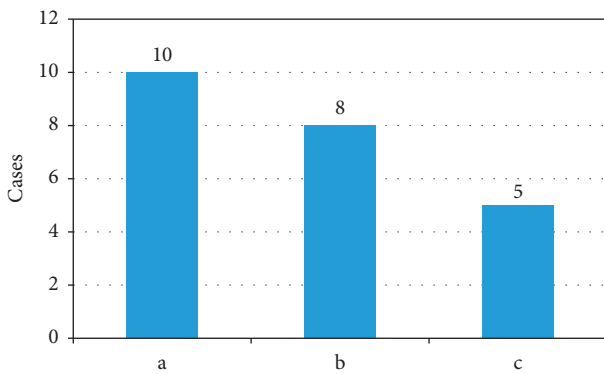
FIGURE 5: Analysis results of functional core nodes of the whole brain network in two groups. (a) The specific network core node of patient group; (b) the network core node unique to control group; and (c) the network core nodes shared by both groups.

with sudden SHL tended to change to a regular network, and the ability of information integration was enhanced, while the ability of separation and transmission was weakened. All the above results confirm to some extent that the connection between auditory brain areas and language and vision-related functional areas was weakened in patients with burst SHL, and their language perception and understanding ability were decreased [27].

There were ten specific network core nodes in patients, including the right parahippocampal gyrus, right supraoccipital gyrus, left suboccipital gyrus, right fusiform gyrus, right parietal lobule, right subparietal lobule, right superior temporal gyrus, and left superior marginal gyrus. Among them, the superior occipital gyrus, fusiform gyrus, superior marginal gyrus, temporal pole, inferior parietal lobule, and parietal lobule are related to visual and auditory information processing. The increase in the importance of these core nodes indicates that other sensory channels are compensatory and that the advantage of coping is weakened after hearing loss. There were eight specific network core nodes in the control group, including the left inferior frontal gyrus orbital, right insula, left insula, left parietal lobule, left parietal lobule, right pea shell, left superior temporal gyrus temporal pole, and right middle temporal gyrus temporal pole. Most of these nodes belong to the limbic or parlimbic system, but they were absent in the patient group, possibly because of the recombination of these nodes after deafness [28].

5. Conclusion

In this study, the functional parameters and core nodes of the whole brain network were analyzed by fMRI scanning and GRETNA software to construct the brain functional network of subjects. The results showed that the brains of patients with sudden sensorineural deafness still had a small-world nature. However, some characteristics of the brain network had changed, and there was a trend to transform to a regular network. The connection between the auditory brain region and language and visual related functional regions was weakened, and the distribution of core nodes was changed, which enhanced the information integration ability of local brain regions and weakened the separation transmission ability. However, the limitation of this study is that the included sample size was small and all of them were from the same hospital, and the evaluation of patient samples was insufficient. The visual and language function evaluation data of the patients were not obtained from the side, and the correlation between right deafness and different functions could not be verified. Therefore, the sample size will be expanded in the later stage, and the patient case data will be increased to explore the difference in brain network function between left and right deafness patients. In conclusion, this study provides data reference for the study of brain network function in patients with sudden right sensorineural hearing loss.

Data Availability

The data used to support the findings of this study are available from the corresponding author upon request.

Conflicts of Interest

The author declares that there are no conflicts of interest.

References

[1] M. Herrera, J. R. García Berrocal, A. García Arumí, M. J. Lavilla, G. Plaza, and Grupo de Trabajo de la Comisión de Audiología de la SEORL, "Update on consensus on diagnosis and treatment of idiopathic sudden sensorineural hearing loss," *Acta Otorrinolaringológica Española*, vol. 70, no. 5, pp. 290–300, 2019.

[2] J. Jeong and H. S. Choi, "Sudden sensorineural hearing loss after COVID-19 vaccination," *International Journal of Infectious Diseases*, vol. 113, pp. 341–343, 2021.

[3] Y. H. Young, "Contemporary review of the causes and differential diagnosis of sudden sensorineural hearing loss," *International Journal of Audiology*, vol. 59, no. 4, pp. 243–253, 2020.

[4] J. G. Doo, D. Kim, Y. Kim et al., "Biomarkers suggesting favorable prognostic outcomes in sudden sensorineural hearing loss," *International Journal of Molecular Sciences*, vol. 21, no. 19, p. 7248, 2020.

[5] M. Marx, E. Younes, S. S. Chandrasekhar et al., "International consensus (ICON) on treatment of sudden sensorineural hearing loss," *European Annals of Otorhinolaryngology, Head and Neck Diseases*, vol. 135, no. 1, pp. S23–S28, 2018.

[6] J. W. Wood, A. D. Shaffer, D. Kitsko, and D. H. Chi, "Sudden sensorineural hearing loss in children-management and outcomes: a meta-analysis," *The Laryngoscope*, vol. 131, no. 2, pp. 425–434, 2021.

[7] Y. C. Chen, S. J. Tsai, J. C. Chen, and J. H. Hwang, "Risks of tinnitus, sensorineural hearing impairment, and sudden deafness in patients with non-migraine headache," *PLoS One*, vol. 14, no. 9, Article ID e0222041, 2019.

[8] C. Mirian and T. Ovesen, "Intratympanic vs. systemic corticosteroids in first-line treatment of idiopathic sudden sensorineural hearing loss: a systematic review and meta-analysis," *JAMA Otolaryngol Head Neck Surg*, vol. 146, no. 5, pp. 421–428, 2020.

[9] T. M. Rhee, D. Hwang, J. S. Lee, J. Park, and J. M. Lee, "Addition of hyperbaric oxygen therapy vs. medical therapy alone for idiopathic sudden sensorineural hearing loss: a systematic review and meta-analysis," *JAMA Otolaryngol Head Neck Surg*, vol. 144, no. 12, pp. 1153–1161, 2018.

[10] A. Ponzetto, G. Cavallo, and N. Figura, "Sudden sensorineural hearing loss," *JAMA Otolaryngol Head Neck Surg*, vol. 146, no. 2, p. 211, 2020.

[11] A. D. P. Prince and E. Z. Stucken, "Sudden sensorineural hearing loss: a diagnostic and therapeutic emergency," *The Journal of the American Board of Family Medicine*, vol. 34, no. 1, pp. 216–223, 2021.

[12] J. W. Ma and J. C. C. Wei, "Correspondence on: "Antidepressants and risk of sudden sensorineural hearing loss"," *International Journal of Epidemiology*, vol. 50, no. 5, pp. 1748-1749, 2021.

[13] H. Zhang, W. Lv, H. Diao, and L. Shang, "Reconstruction algorithm-based CT imaging for the diagnosis of hepatic ascites," *Computational and Mathematical Methods in Medicine*, vol. 2022, Article ID 1809186, 11 pages, 2022.

[14] M. M. Wang, Y. J. Wang, N. Hu et al., "3D-FLAIR MRI findings in idiopathic sudden sensorineural hearing loss and the correlations with clinical features and prognosis," *Zhonghua er bi Yan Hou Tou Jing Wai ke za Zhi*, vol. 56, no. 5, pp. 424–430, 2021.

[15] J. Wang, T. Ren, W. Sun, Q. Liang, and W. Wang, "Post-contrast 3D-FLAIR in idiopathic sudden sensorineural hearing loss," *European Archives of Oto-Rhino-Laryngology*, vol. 276, no. 5, pp. 1291–1299, 2019.

[16] Y. Islamoglu, G. G. Kesici, K. Ercan, and M. A. Babademez, "Single-sided deafness after sudden hearıng loss: late effect on cochlear nerve size," *European Archives of Oto-Rhino-Laryngology*, vol. 277, no. 9, pp. 2423–2426, 2020.

[17] X. Min, H. Gu, Y. Zhang, K. Li, Z. Pan, and T. Jiang, "Clinical value of abnormal MRI findings in patients with unilateral sudden sensorineural hearing loss," *Diagn Interv Radiol*, vol. 26, no. 5, pp. 429–436, 2020.

[18] C. J. Yang, T. Yoshida, S. Sugimoto et al., "Lesion-specific prognosis by magnetic resonance imaging in sudden sensorineural hearing loss," *Acta Oto-Laryngologica*, vol. 141, no. 1, pp. 5–9, 2021.

[19] X. Chen, Q. Zhang, C. Yang, Y. Liu, and L. Li, "GRβ regulates glucocorticoid resistance in sudden sensorineural hearing loss," *Current Pharmaceutical Biotechnology*, vol. 22, no. 9, pp. 1206–1215, 2021.

[20] N. Mehta and S. Mehta, "Comparative evaluation of injection dexamethasone and oral glycerol versus injection dexamethasone alone in the treatment of sudden onset sensorineural deafness," *Ear, Nose, & Throat Journal*, vol. 100, pp. 317S–324S, 2021.

[21] T. G. Joshua, A. Ayub, P. Wijesinghe, and D. A. Nunez, "Hyperbaric oxygen therapy for patients with sudden sensorineural hearing loss: a systematic review and meta-analysis," *JAMA Otolaryngol Head Neck Surg*, vol. 148, no. 1, pp. 5–11, 2022.

[22] W. W. Jung and C. Hoegerl, "Sudden sensorineural hearing loss and why it's an emergency," *Cureus*, vol. 14, no. 1, Article ID e21418, 2022.

[23] H. Wong, Y. Amoako-Tuffour, K. Faiz, and J. J. S. Shankar, "Diagnostic yield of MRI for sensorineural hearing loss - an audit," *The Canadian Journal of Neurological Sciences*, vol. 47, no. 5, pp. 656–660, 2020.

[24] S. Minosse, F. Garaci, F. Martino et al., "Global and local brain connectivity changes associated with sudden unilateral sensorineural hearing loss," *NMR in Biomedicine*, vol. 34, no. 8, Article ID e4544, 2021.

[25] R. G. Yoon, Y. Choi, and H. J. Park, "Clinical usefulness of labyrinthine three-dimensional fluid-attenuated inversion recovery magnetic resonance images in idiopathic sudden sensorineural hearing loss," *Current Opinion in Otolaryngology & Head and Neck Surgery*, vol. 29, no. 5, pp. 349–356, 2021.

[26] S. Wang, B. Chen, Y. Yu et al., "Altered resting-state functional network connectivity in profound sensorineural hearing loss infants within an early sensitive period: a group ICA study," *Human Brain Mapping*, vol. 42, no. 13, pp. 4314–4326, 2021.

[27] M. Wang, N. Hu, Y. Wang, X. Sun, Z. Fan, and H. Wang, "Clinical value of 3D-FLAIR MRI in idiopathic sudden sensorineural hearing loss," *ACS Chemical Neuroscience*, vol. 13, no. 1, pp. 151–157, 2022.

[28] L. D. Dumberger, T. P. Hwa, K. Panara, S. Husain, C. Yver, and D. C. Bigelow, "Profound sudden sensorineural hearing loss in hematologic malignancy: a case for urgent cochlear implantation with discussion and systematic review of the literature," *Otology & Neurotology*, vol. 42, no. 7, pp. e815–e824, 2021.

WILEY | Hindawi

Research Article

Magnetic Resonance Diffusion-Weighted Imaging to Evaluate the Clinical Efficacy of CalliSpheres Drug-Loaded Microspheres in the Treatment of Advanced Bladder Cancer

Xi Yang and Wei Chen [ID]

Department of Radiology, Xingtai People's Hospital, Xingtai 054000, Hebei, China

Correspondence should be addressed to Wei Chen; 201308416@stu.lzjtu.edu.cn

The MR diffusion-weighted imaging technique was used to evaluate the efficacy and safety of CalliSpheres drug-loaded microspheres for transarterial chemoembolization in the treatment of advanced bladder cancer. 35 patients with advanced bladder cancer were treated with CalliSpheres DLMS for transarterial chemoembolization. Imaging techniques such as magnetic resonance (MR) diffusion-weighted imaging were used to evaluate the therapeutic effect. The changes in serum tumor markers, immune function indexes, and oxidative stress indexes in patients before and after treatment were compared, and the quality of life of patients and the incidence of adverse reactions during follow-up were also evaluated. The results showed that the overall response rate (ORR) was 74.29% and that the disease control rate (DCR) was 97.14%. Compared with that before treatment, the ADC value of the tumor in patients with advanced bladder cancer detected by MR diffusion-weighted imaging technology was significantly increased after treatment and the maximum tumor diameter was significantly decreased ($P < 0.05$). Compared with those before treatment, the levels of serum tumor markers (CA199, CA724, and CA125) in advanced bladder cancer patients after treatment decreased ($P < 0.05$). The levels of T-lymphocyte subsets (CD3+ and CD4+) decreased, and CD8+ levels increased ($P < 0.05$). The levels of superoxide dismutase decreased ($P > 0.05$). At the same time, the subscale evaluation of function, symptoms, quality of life, adverse reactions, and economics of patients with advanced bladder cancer on the QLQ-C30 scale improved after treatment, and the incidence rate and recurrence rate during the follow-up period were 8.57% and 11.43%, respectively. It showed that CalliSpheres DLMS had a good clinical effect and high safety in the treatment of advanced bladder cancer and was a safe and feasible treatment method. The use of MR diffusion-weighted imaging technology could achieve quantitative evaluation of clinical efficacy of advanced bladder cancer.

1. Introduction

Bladder cancer is a very common urological malignant tumor in clinical practice, and most patients are accompanied by symptoms such as painless or intermittent urinary frequency, urgency, and hematuria. In recent years, there has been a trend of increasing incidence rates [1]. According to the degree of tumor invasion, bladder cancer can be divided into muscle-invasive bladder cancer and non-muscle-invasive bladder cancer. Among them, muscle-invasive bladder cancer has a high degree of malignancy and a high risk of metastasis and recurrence after treatment [2].

Radical cystectomy is a common method for clinical surgical treatment of muscle-invasive bladder cancer. However, surgical treatment brings great trauma to patients, and the postoperative complication rate and the recurrence rate are high, which can easily affect the bladder function of patients and then easily lead to a poor prognosis of patients [3]. Therefore, transcatheter internal iliac artery infusion chemotherapy has become one of the important methods for the treatment of bladder cancer. When bladder cancer patients cannot undergo radical cystectomy, transcatheter internal iliac artery infusion chemotherapy can significantly improve the patients' quality of life and prolong survival [4].

The traditional embolic agent (Lipiodol) is not easy to enter the blood-supplying artery of the tumor, which affects the therapeutic effect of transarterial chemoembolization. Drug-loaded microsphere (DLMS)-transarterial chemoembolization is a new type of drug-loaded embolization system. It can prolong the action time of the drug by injecting high doses of chemotherapy drugs into the tumor and reduce adverse reactions caused by chemotherapy drugs entering systemic blood circulation [5]. Compared with traditional transarterial chemoembolization, DLMS-transarterial chemoembolization has been demonstrated to have lower treatment toxicity and a lower incidence of postoperative adverse events [6, 7]. CalliSpheres DLMS is a novel drug-loaded embolization system made in China. At present, studies have confirmed that CalliSpheres DLMS can significantly improve the clinical symptoms of patients with lung cancer and help in its treatment, and it has good safety [8]. However, there are relatively few studies on the application of CalliSpheres DLMS for transarterial chemoembolization in bladder cancer.

Conventional MRI technology can evaluate the treatment effect through the morphological changes in the tumor, but it cannot distinguish the internal state of the tumor tissue during the treatment process, which is not conducive to the optimization of the treatment method. MR diffusion-weighted imaging technology is a kind of noninvasive functional examination method, which can assist in the diagnosis of diseases and the detection of curative effects through the changes in the diffusion movement of water molecules in tumor tissue. Therefore, this work selected patients with advanced bladder cancer who could not be treated with radical bladder cancer as research objects. First, the clinical effect of CalliSpheres drug-loaded microsphere-transarterial chemoembolization on patients was analyzed by MR diffusion-weighted imaging technology. Then, the effects of the immune function, oxidative stress level, quality of life, and incidence of adverse reactions were also detected. It aimed to provide reference for the popularization and application of CalliSpheres drug-loaded microsphere-transarterial chemoembolization.

2. Materials and Methods

2.1. Research Objects. 35 patients diagnosed with advanced bladder cancer in hospital from May 2019 to December 2021 were selected as the research subjects, including 21 males and 14 females. The age ranged from 48 to 75 years, with an average of 59.5 ± 4.9 years, the disease duration was 3–5 years, with an average of 3.6 ± 0.7 years, and 18 cases were in T3 stage and 17 cases were in T4 stage. This study was approved by the ethics committee of hospital, and all patients gave informed consent.

Inclusion criteria were as follows: those who were unable or unwilling to undergo surgical treatment; those who were staged as T3 or T4 according to the TNM staging standard developed by the International Union Against Cancer [9]; those with obvious clinical symptoms, such as repeated hematuria, dysuria, and bladder irritation; and those who received transarterial chemoembolization for the first time.

Exclusion criteria were as follows: those with a history of surgical treatment such as radical cystectomy; those with liver or kidney insufficiency and coagulation dysfunction; patients with secondary active infection and hypersensitivity to contrast agents; and those with the Karnofsky score less than 70 and expected survival less than 3 months.

2.2. Treatment Methods. The right or left femoral artery was selected as the puncture vessel, and after laying a sterile drape, 2% lidocaine was used for local anesthesia; the modified Seldinger technique was used to puncture the femoral artery. A 5 F catheter sheath was placed, and the guide wire was introduced into the Cobra catheter. After internal iliac arteriography, the blood supply artery to the bladder tumor was searched and the location, number, size, and staining of the tumor were confirmed. 50–100 mg of oxaliplatin was injected into the blood vessel of the bladder tumor. Then, 20–40 mg of pirarubicin was mixed with CalliSpheres drug-loaded microspheres and mixed with the contrast agent 10 min later. The prepared CalliSpheres drug-loaded microspheres were embolized slowly at the blood supply artery of the bladder tumor, and the chemical embolism treatment was performed. The contralateral target vessel was selected using the looping technique, and chemoembolization was performed using the same method. For patients with difficulty in the arterial supply of bladder tumors, internal iliac transarterial chemoembolization should be performed, and the superior gluteal artery should be avoided during embolization. After treatment, hydration and diuresis should be given, and anti-infective treatment should be carried out according to the actual situation of the patient. The evaluation of the embolization effect of CalliSpheres DLMS using contrast imaging technology should be carried out. If the drug-loaded microspheres cannot reach the end point of embolization, drug-loaded microspheres can be mixed with the appropriate blank microspheres of equal specification before embolization treatment.

2.3. MR Diffusion-Weighted Imaging. 50 minutes before the MR diffusion-weighted imaging scan was performed, the patient was instructed to drink 500–1,000 ml of water without urinating, so that the patient's bladder could be filled. Cross-sectional MR diffusion-weighted imaging scans were performed with PHILIPS Achieva 3.0T MR, 4-channel torso coils were selected, and respiratory gating was not used. MR diffusion-weighted imaging scans used a spin-echo-echo planar imaging sequence. The parameters were set as follows: repetition time = 1,000 ms, echo time = minimum, number of excitations = 8, matrix = 125×125, field of view = 40×40 cm^2, slice thickness = 5 mm, and slice spacing = 1 mm. The diffusion sensitive gradient factor in the scanning process, that is, the b value, was taken as 1,500 s/mm^2. At the same time, the array spatial sensitivity encoding technique (APSET) was collected, the acceleration factor R value was set to 2, and MRI examinations before and after interventional treatment were performed. The MRI images obtained by scanning were transmitted to the workstation, the images were read by 2 professional radiologists, and the

region of interest at the lesion was manually delineated. Irregular margins of the lesions were delineated into hyperintense lesions, and the mean tumor ADC values were calculated.

2.4. Efficacy Evaluation and Observation Indicators. The treatment effect of solid tumors was evaluated as follows: The evaluation of the treatment effect of patients with solid tumors was carried out 4 weeks after embolization. Imaging techniques were used to measure the maximum tumor diameter, and treatment effects were classified into complete remission (CR), partial remission (PR), stable disease (SD), and progressive disease (PD). It was considered that the imaging technology examination showed that the tumor completely disappeared as CR, that the tumor diameter was reduced by 30% or more after treatment as PR, that the tumor diameter decreased by −20%–30% after treatment as SD, and that the tumor diameter increased by 20% or more after treatment was considered as PD. The overall response rate (ORR) = (CR + PR)/total number ∗ 100%. The disease control rate (DCR) = (CR + PR + SD)/total number ∗ 100%.

Fasting venous blood was collected from patients before treatment and 15 days after treatment, serum was extracted, and the levels of tumor markers were detected. An automatic electrochemiluminescence immunoassay was used to detect the content of tumor markers of carcinoembryonic antigen (CEA), carbohydrate antigen 199 (CA199), carbohydrate antigen 724 (CA724), and carbohydrate antigen 125 (CA125) in serum.

Before treatment and 15 days after treatment, the patient's venous blood was collected and the serum was extracted. An automatic cell analyzer was used to detect the levels of T-lymphocyte subsets (CD3+, CD4+, and CD8+) in the serum, and CD4+/CD8+ was calculated at the same time.

Before and 15 days after treatment, venous blood was collected and serum was extracted from patients. The xanthine oxidase method was used to detect the oxidative stress index superoxide dismutase (SOD) level in serum.

The quality of life of patients was assessed using the Quality of Life Core Questionnaire containing 30 items (QLQ-C30) [10] prepared by the European Organization for Cancer Research and Treatment. The five functional subscales on the QLQ-C30 scale were the physical function, role function, cognitive function, emotional function, and social function. The 3 symptom subscales were fatigue, pain, and nausea; there was 1 overall quality of life subscale; 5 adverse reactions were dyspnea, insomnia, loss of appetite, constipation, and diarrhea; and 1 economic item was an economic impact. The higher the score of the functional scale and the overall quality of the life scale on the QLQ-C30 scale and the lower the score of the symptom and adverse reactions scale, the better the patient's quality of life.

A follow-up period of 36 months was selected after treatment, with the patient's death or the study period as the termination date. The incidence of adverse reactions such as hematuria, urinary incontinence, and bladder perforation during the follow-up period of the patients was counted.

2.5. Statistical Processing. Statistical analysis of the data was performed using SPSS 19.0 software. Enumeration data were expressed as frequencies (percentages), and differences between groups were compared using the chi-square test. Enumeration data were expressed as a mean ± standard deviation, and differences between groups were compared using the independent samples t-test. $P < 0.05$ meant that the difference was statistically significant.

3. Results

3.1. Clinical Outcomes of CalliSpheres DLMS in Patients with Advanced Bladder Cancer. The clinical effect of CalliSpheres DLMS in the treatment of advanced bladder cancer was analyzed, and the results are shown in Figure 1. After CalliSpheres DLMS treatment of 35 advanced bladder cancer patients, the clinical treatment effect was evaluated as CR in 4 patients (11.43%), PR in 22 patients (62.86%), SD in 8 patients (22.86%), and PD in 1 patient (2.86%). After calculation of ORR and DCR, 26 cases (74.29%) had ORR and 34 cases (97.14%) had DCR.

3.2. Imaging Evaluation of CalliSpheres DLMS in Patients with Advanced Bladder Cancer. Quantitative evaluation of the effect of advanced bladder cancer before and after CalliSpheres DLMS treatment using conventional MRI, MR diffusion-weighted imaging, and CT imaging was performed. Evaluation indicators included ADC and the maximum tumor diameter, and the results are shown in Figure 2. The ADC value and the maximum diameter of the bladder tumor before treatment were $1.19 \pm 0.10 \times 10^{-3}$ mm^2/s and 5.82 ± 1.33 cm, respectively, and the quantitative indexes after treatment were $1.42 \pm 0.11 \times 10^{-3}$ mm^2/s and 1.71 ± 0.46 cm, respectively. After treatment, the ADC value of the tumor in advanced bladder cancer patients was significantly higher than that before treatment, while the maximum tumor diameter was significantly smaller than that before treatment, and the difference was statistically significant ($P < 0.05$).

3.3. Changes in Serum Tumor Markers in Advanced Bladder Cancer Patients Treated with CalliSpheres DLMS. The differences in the levels of serum tumor markers (CEA, CA199, CA724, and CA125) in advanced bladder cancer patients before and after CalliSpheres DLMS treatment were detected, and the results are shown in Figure 3. Before treatment, the serum levels of CEA, CA199, CA724, and CA125 were 41.25 ± 5.36 ng/mL, 122.58 ± 7.54 U/mL, 89.37 ± 8.97 U/mL, and 71.22 ± 8.05 U/mL, respectively. The levels of each index after treatment were 15.61 ± 4.75 ng/mL, 38.93 ± 6.12 U/mL, 21.60 ± 5.63 U/mL, and 30.95 ± 6.61 U/
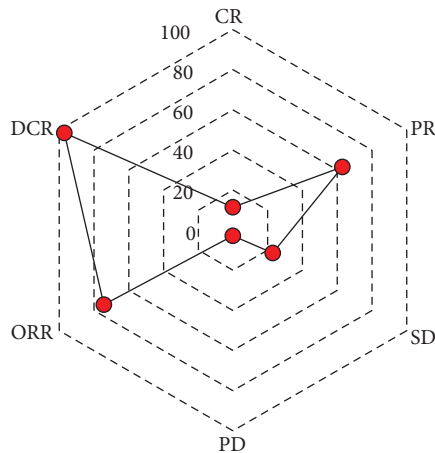
Figure 1: Evaluation of the clinical treatment effect of advanced bladder cancer patients. CR, complete remission; PR, partial remission; SD, stable disease; PD, disease progression; ORR, overall response rate; DCR, disease control rate.

mL, respectively. The serum levels of various tumor markers in advanced bladder cancer patients after treatment were significantly lower than those before treatment, and the difference was statistically significant ($P < 0.05$).

3.4. Changes in the Immune Function in Advanced Bladder Cancer Patients Treated with CalliSpheres DLMS.

The differences between the levels of serum T-lymphocyte subsets (CD3+, CD4+, and CD8+) and the CD4+/CD8+ ratio in advanced bladder cancer patients before and after CalliSpheres DLMS treatment were detected, and the results are shown in Figure 4. Before treatment, serum CD3+, CD4+, and CD8+ levels and the CD4+/CD8+ ratio indexes were $64.58 \pm 5.91\%$, $44.75 \pm 4.42\%$, and $23.94 \pm 2.16\%$ and 1.82 ± 0.41, respectively, while those after treatment were $58.11 \pm 4.32\%$, $34.66 \pm 5.10\%$, and $25.72 \pm 2.05\%$ and 1.53 ± 0.39, respectively. After treatment, the levels of CD3+, CD4+, and CD4+/CD8+ in serum of advanced bladder cancer patients were significantly lower than those before treatment, while the level of CD8+ was significantly higher than that before treatment, and the difference was statistically significant ($P < 0.05$).

3.5. Changes in Oxidative Stress Levels in Advanced Bladder Cancer Patients Treated with CalliSpheres DLMS.

The differences in serum levels of oxidative stress index SOD in advanced bladder cancer patients before and after CalliSpheres DLMS treatment were detected, and the results are shown in Figure 5. Before treatment, the serum SOD level was 136.53 ± 15.51 U/mL, while that after treatment was 109.22 ± 11.74 U/mL. After treatment, the levels of SOD in serum of advanced bladder cancer patients were slightly lower than those before treatment, but the difference was not statistically significant ($P > 0.05$).

3.6. Evaluation of Quality of Life in Advanced Bladder Cancer Patients Treated with CalliSpheres DLMS.

The QLQ-C30 was used to evaluate the quality of life of advanced bladder cancer patients before and after CalliSpheres DLMS treatment. The results are shown in Figure 6. It was found that the five item scores and QOL scores on the functional subscale of advanced bladder cancer patients after treatment were significantly higher than those before treatment, and the difference was statistically significant ($P < 0.05$). After treatment, the scores of 3 items on the symptom subscale, the score of 5 items in on adverse reaction subscale, and the Econ score of patients with advanced bladder cancer after treatment were significantly lower than those before treatment, and the differences were statistically significant ($P < 0.05$).

3.7. Safety Evaluation of CalliSpheres DLMS in Advanced Bladder Cancer Patients.

The safety of CalliSpheres DLMS in the treatment of advanced bladder cancer was analyzed, and the results are shown in Figure 7. After CalliSpheres DLMS treatment of 35 advanced bladder cancer patients, 2 patients (5.71%) developed hematuria, 2 patients (5.71%) developed urethral stricture, 1 patient (2.86%) developed urinary incontinence, no patients developed bladder perforation (0.00%), and 4 cases (11.43%) with recurrence.

4. Discussion

Bladder cancer is a type of urological malignancy that occurs on the bladder mucosa with a high incidence rate and mortality. Transarterial chemoembolization has been used in the treatment of advanced bladder cancer patients with excellent therapeutic effects [11]. However, problems such as gene mutation and drug resistance prevent patients from benefiting from targeted therapy in the long term. Therefore, finding a more effective treatment method is of great significance for improving the prognosis of patients and their quality of life and prolonging the survival period. The inner diameter of drug-loaded microspheres is the key to affecting the efficacy of transarterial chemoembolization. Currently, the diameter of drug-loaded microspheres used in clinical treatment of liver metastases is 100–$300\,\mu m$ [12]. CalliSpheres DLMS is a new type of drug-loaded microsphere system, and its volume will be significantly reduced after drug loading. After 20 days of interventional therapy, with the gradual release of chemotherapy drugs, the volume of CalliSpheres DLMS will gradually recover, so it can effectively block the blood vessels supplying tumors and prolong the recanalization time of the blood vessels supplying tumors [13, 14].

In this work, CalliSpheres DLMS-transarterial chemoembolization was used for the treatment of advanced bladder cancer patients and imaging techniques such as MR were used to evaluate the therapeutic effect. It was found that the ADC value of the tumor increased significantly after treatment, while the maximum diameter of the tumor decreased significantly. MR diffusion-weighted imaging is a noninvasive functional examination method that can reflect the diffusion of water molecules in tissues. Since the diffusion of water molecules is affected by the microstructure of cells, it can be used in disease diagnosis and therapeutic
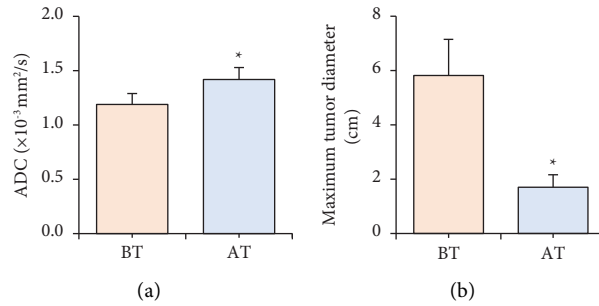
FIGURE 2: Comparison of MR quantitative parameters in advanced bladder cancer patients before and after treatment. (a) The ADC value of the tumor and (b) the maximum diameter of the tumor. BT: before treatment and AT: after treatment. *Compared with that before treatment, $P < 0.05$.
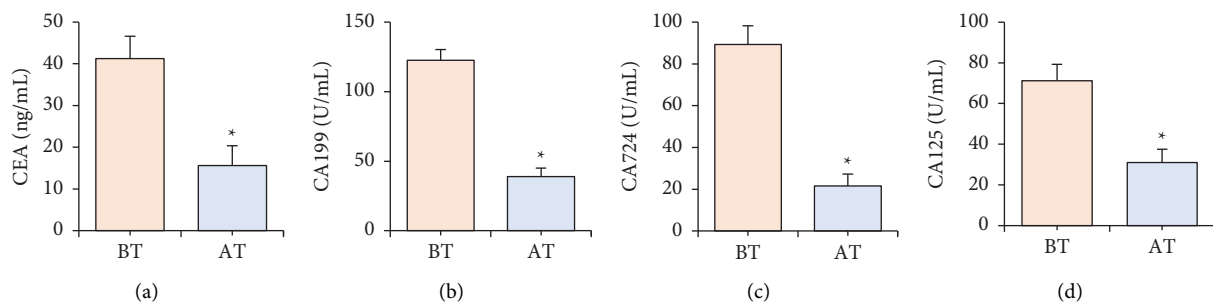
FIGURE 3: Comparison of serum tumor markers in advanced bladder cancer patients before and after treatment. (a–d) The comparison of CEA, CA199, CA724, and CA125, respectively. BT: before treatment and AT: after treatment. *Compared with that before treatment, $P < 0.05$.
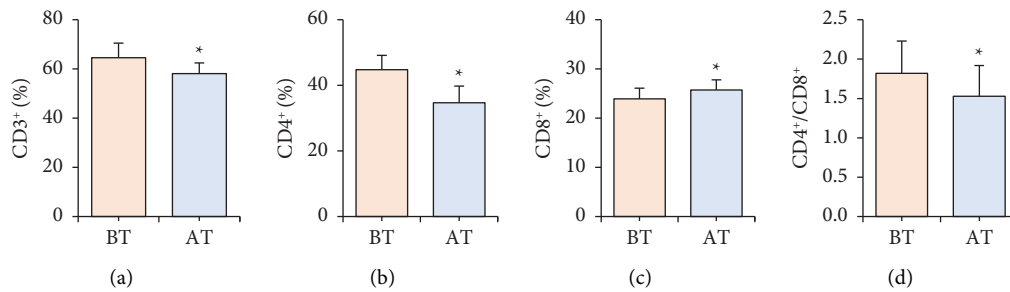
FIGURE 4: Comparison of serum T-lymphocyte subset levels in advanced bladder cancer patients before and after treatment. (a–d) The comparison of CD3+, CD4+, CD8+, and CD4+/CD8+, respectively; BT: before treatment and AT: after treatment. *Compared with that before treatment, $P < 0.05$.
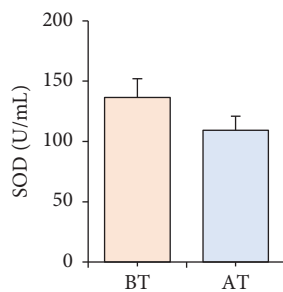
FIGURE 5: Comparison of serum levels of oxidative stress indexes in advanced bladder cancer patients before and after treatment. BT: before treatment and AT: after treatment.

efficacy monitoring [15]. MR diffusion-weighted imaging and changes in the ADC value can be used to evaluate the dynamic evaluation of the treatment effect of malignant tumors. The decrease in the ADC value in malignant tumors is related to the high density and volume of cells [16]. This work found that the ADC value of tumors in advanced bladder cancer patients was significantly increased after CalliSpheres DLMS-transarterial chemoembolization. It indicated that the bladder cancer cell membrane was destroyed after interventional therapy, that the tumor volume and tumor cell density decreased after cell necrosis, and that the increase in the intercellular space provided space for the diffusion of water molecules. An increase in the ADC
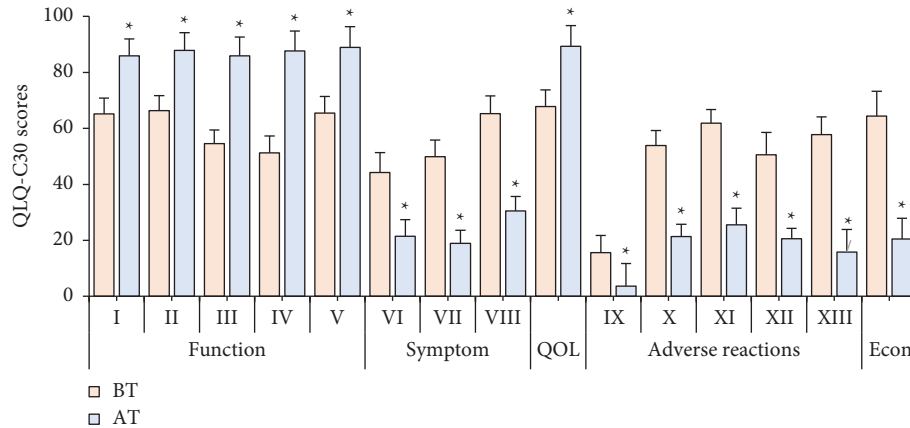
FIGURE 6: Comparison of QLQ-C30 scores in advanced bladder cancer patients before and after treatment. I–XIII refer to physical function, role function, cognitive function, emotional function, social function, fatigue, pain, malignant vomiting, dyspnea, insomnia, anorexia, constipation, and diarrhea, respectively; QOL, quality of life; Econ, economy; BT, before treatment; AT, after treatment. *Compared with that before treatment, $P < 0.05$.
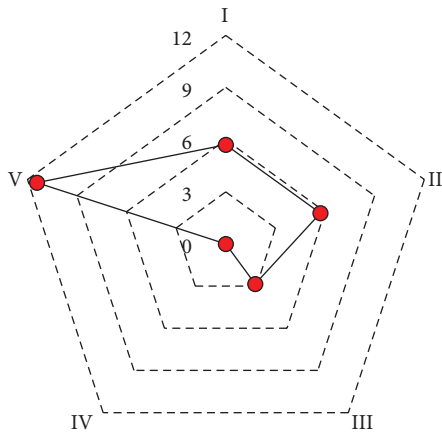
FIGURE 7: Evaluation of the incidence of adverse reactions in advanced bladder cancer patients. I: hematuria; II: urethral stricture; III: urinary incontinence; IV: bladder perforation; V: recurrence.

value was associated with a reduction in tumor volume [17], which is consistent with the findings of this work. In addition, it was found in this work that the serum levels of tumor markers [18, 19] (CEA, CA199, CA724, and CA12) in advanced bladder cancer patients after CalliSpheres DLMS-transarterial chemoembolization were significantly decreased, that the ORR was 74.29%, and that the DCR was 97.14%. CEA, CA199, CA724, and CA125 are common tumor markers, which are often used in disease diagnosis and treatment evaluation. It indicated that CalliSpheres DLMS-transarterial chemoembolization has a good clinical effect in the treatment of advanced bladder cancer.

Abnormal immune function can induce the occurrence and development of tumors. Immune dysfunction is not conducive to the recovery of the patient's body function and also increases the risk of postoperative recurrence and metastasis in tumor patients [20]. T lymphocytes mediate cellular immunity, and studies have confirmed that the levels of T-lymphocyte subsets in patients with bladder cancer are significantly disrupted [21]. This work found that the levels of serum T-lymphocyte subsets in advanced bladder cancer patients were altered after CalliSpheres DLMS-transarterial chemoembolization. This suggests that CalliSpheres DLMS-transarterial chemoembolization directly infuses chemotherapeutic drugs into target organs and prolongs the drug release time, which helps rapidly kill tumor cells, thereby reducing the impact of tumor infiltration on the immune function of patients. In addition to immune function, oxidative stress is also involved in tumor progression and can also reflect the traumatic stress of patients receiving treatment [22]. SOD can capture and scavenge free radicals in the body [23, 24]. This work found that serum SOD was significantly decreased in advanced bladder cancer patients after CalliSpheres DLMS-transarterial chemoembolization. This suggests that a certain degree of oxidative stress appears in advanced bladder cancer patients after CalliSpheres DLMS-transarterial chemoembolization, but the level of oxidative stress is relatively stable. Yang et al. [25] confirmed that the oxidative stress state can aggravate the expression of inflammatory factors, which in turn promotes the infiltration of tumor cells. This work found that the incidence of adverse reactions such as hematuria, urethral stricture, and urinary incontinence in patients with advanced bladder cancer after CalliSpheres DLMS-transarterial chemoembolization was relatively low, and the incidence and recurrence rates were also relatively low.

5. Conclusion

CalliSpheres DLMS-transarterial chemoembolization is effective for advanced bladder cancer with higher ORR. It can reduce the level of tumor markers in patients, reduce the oxidative stress response caused by surgery, and have a low impact on the immune function of patients, which can help improve the prognosis of patients. Using MR diffusion-weighted imaging technology, it was found that the ADC value of patients with advanced bladder cancer was

significantly reduced after CalliSpheres drug-loadedmicrosphere-transinternal iliac artery chemoembolization. However, this work only compared and analyzed the index changes in advanced bladder cancer before and after CalliSpheres DLMS-transarterial chemoembolization. No randomized controlled trials have been designed to evaluate the efficacy and safety of CalliSpheres DLMS-transarterial chemoembolization. In future studies, more samples need to be included to compare the efficacy and safety of CalliSpheres DLMS-transarterial chemoembolization and traditional transarterial chemoembolization in the treatment of advanced bladder cancer. In conclusion, the results of this work can provide reference for the clinical application of CalliSpheres DLMS-transarterial chemoembolization and improve the prognosis of patients.

Data Availability

The data used to support the findings of this study are available from the corresponding author upon request.

Conflicts of Interest

The authors declare that they have no conflicts of interest.

References

[1] K. C. DeGeorge, H. R. Holt, and S. C. Hodges, "Bladder cancer: diagnosis and treatment," *American Family Physician*, vol. 96, no. 8, pp. 507–514, 2017.

[2] A. Pham and L. K. Ballas, "Trimodality therapy for bladder cancer: modern management and future directions," *Current Opinion in Urology*, vol. 29, no. 3, pp. 210–215, 2019.

[3] M. W. Vetterlein, S. A. M. Wankowicz, T. Seisen et al., "Neoadjuvant chemotherapy prior to radical cystectomy for muscle-invasive bladder cancer with variant histology," *Cancer*, vol. 123, no. 22, pp. 4346–4355, 2017.

[4] X. Mu, K. Wu, Y. Zhu et al., "Intra-arterial infusion chemotherapy utilizing cisplatin inhibits bladder cancer by decreasing the fibrocytic myeloid-derived suppressor cells in an m6A-dependent mannerfibrocytic myeloid-derived suppressor cells in an m6A-dependent manner," *Molecular Immunology*, vol. 137, pp. 28–40, 2021.

[5] I. Gibson, A. Momeni, and M. Filiaggi, "Minocycline-loaded calcium polyphosphate glass microspheres as a potential drug-delivery agent for the treatment of periodontitis," *Journal of Applied Biomaterials & Functional Materials*, vol. 17, no. 3, 2019.

[6] J. Kettenbach, A. Stadler, I. V. Katzler et al., "Drug-loaded microspheres for the treatment of liver cancer: review of current results," *CardioVascular and Interventional Radiology*, vol. 31, no. 3, pp. 468–476, 2008.

[7] D. H. Kim, W. Li, J. Chen et al., "Multimodal imaging of nanocomposite microspheres for transcatheter intra-arterial drug delivery to liver tumors," *Scientific Reports*, vol. 6, Article ID 29653, 2016.

[8] B. Shang, J. Li, X. Wang et al., "Clinical effect of bronchial arterial infusion chemotherapy and CalliSpheres drug-eluting beads in patients with stage II-IV lung cancer: a prospective cohort study," *Thorac Cancer*, vol. 11, no. 8, pp. 2155–2162, 2020.

[9] P. S. Karia, A. Jambusaria-Pahlajani, D. P. Harrington, G. F. Murphy, A. A. Qureshi, and C. D. Schmults, "Evaluation of American joint committee on cancer, international union against cancer, and brigham and women's hospital tumor staging for cutaneous squamous cell carcinoma," *Journal of Clinical Oncology*, vol. 32, no. 4, pp. 327–334, 2014.

[10] S. Nolte, G. Liegl, M. A. Petersen et al., "General population normative data for the EORTC QLQ-C30 health-related quality of life questionnaire based on 15,386 persons across 13 European countries, Canada and the Unites States," *European Journal of Cancer*, vol. 107, pp. 153–163, 2019.

[11] N. Kakuta, T. Yasumoto, Y. Yoshida et al., "Spontaneous regression of lung metastases after transarterial chemoembolization for hepatocellular carcinoma," *Radiol Case Rep*, vol. 16, no. 6, pp. 1530–1534, 2021.

[12] W. Chen, J. Clauser, A. L. Thiebes et al., "Gefitinib/gefitinib microspheres loaded polyurethane constructs as drug-eluting stent coating," *European Journal of Pharmaceutical Sciences*, vol. 103, pp. 94–103, 2017.

[13] E. Lu, G. Shao, J. Ma et al., "Optimized loading of idarubicin in CalliSpheres® drug-eluting beads and characterization of release profiles and morphological properties," *Pharmaceutics*, vol. 13, no. 6, p. 799, 2021.

[14] X. Chang, P. Sun, J. Zhang et al., "CalliSpheres drug-eluting beads transarterial-chemoembolization in the treatment of liver metastases from breast cancer: initial experience in 14 patients," *Medicine (Baltimore)*, vol. 100, no. 52, Article ID e28407, 2021.

[15] J. Zhang, Y. Huang, J. Chen, X. Wang, and H. Ma, "Potential of combination of DCE-MRI and DWI with serum CA125 and CA199 in evaluating effectiveness of neoadjuvant chemotherapy in breast cancer," *World Journal of Surgical Oncology*, vol. 19, no. 1, p. 284, 2021.

[16] B. B. Choi, "Effectiveness of ADC difference value on pre-neoadjuvant chemotherapy MRI for response evaluation of breast cancer," *Technology in Cancer Research and Treatment*, vol. 20, Article ID 15330338211039129, 2021.

[17] Y. Zhang, Q. Zhang, X. X. Wang, X. F. Deng, and Y. Z. Zhu, "Value of pretherapeutic DWI in evaluating prognosis and therapeutic effect in immunocompetent patients with primary central nervous system lymphoma given high-dosemethotrexate-based chemotherapy: ADC-based assessment," *Clinical Radiology*, vol. 71, no. 10, pp. 1018–1029, 2016.

[18] Y. Chen, S. G. Gao, J. M. Chen et al., "Serum CA242, CA199, CA125, CEA, and TSGF are biomarkers for the efficacy and prognosis of cryoablation in pancreatic cancer patients," *Cell Biochemistry and Biophysics*, vol. 71, no. 3, pp. 1287–1291, 2015.

[19] E. Benaiges, V. Ceperuelo-Mallafré, A. Madeira et al., "Survivin drives tumor-associated macrophage reprogramming: a novel mechanism with potential impact for obesity," *Cellular Oncology*, vol. 44, no. 4, pp. 777–792, 2021.

[20] D. Ribatti, "The concept of immune surveillance against tumors. The first theories," *Oncotarget*, vol. 8, no. 4, pp. 7175–7180, 2017.

[21] D. Y. Oh, S. S. Kwek, S. S. Raju et al., "Intratumoral CD4+ T cells mediate anti-tumor cytotoxicity in human bladder cancer," *Cell*, vol. 181, no. 7, pp. 1612–1625.e13, 2020.

[22] F. Mendes, E. Pereira, D. Martins et al., "Oxidative stress in bladder cancer: an ally or an enemy?" *Molecular Biology Reports*, vol. 48, no. 3, pp. 2791–2802, 2021.

[23] E. Cecerska-Heryć, O. Surowska, R. Heryć, N. Serwin, S. Napiontek-Balińska, and B. Dołęgowska, "Are antioxidant enzymes essential markers in the diagnosis and monitoring of

cancer patients - a review," *Clinical Biochemistry*, vol. 93, pp. 1–8, 2021.

[24] Z. Lepara, O. Lepara, A. Fajkić, D. Rebić, J. Alić, and H. Spahović, "Serum malondialdehyde (MDA) level as a potential biomarker of cancer progression for patients with bladder cancer," *Romanian Journal of Internal Medicine*, vol. 58, no. 3, pp. 146–152, 2020.

[25] Y. Yang, S. Y. Neo, Z. Chen et al., "Thioredoxin activity confers resistance against oxidative stress in tumor-infiltrating NK cells," *Journal of Clinical Investigation*, vol. 130, no. 10, pp. 5508–5522, 2020.

WILEY | Hindawi

Research Article

Super-Resolution Reconstruction Algorithm-Based MRI Diagnosis of Prostate Cancer and Evaluation of Treatment Effect of Prostate Specific Antigen

Biao Liu,[1] Rongping Tan,[1] Baogao Tan,[1] Chenhui Huang,[1] and Keqin Yang [2]

[1]*Department of Radiology, Guigang People's Hospital, Guigang 537100, Guangxi, China*
[2]*Department of Orthopaedics, Guigang People's Hospital, Guigang 537100, Guangxi, China*

Correspondence should be addressed to Keqin Yang; 2011151110@hbut.edu.cn

MRI of prostate cancer (PCa) was performed using a projection onto convex sets (POCS) super-resolution reconstruction algorithm to evaluate and analyze the treatment of prostate-specific antigen (PSA) and provide a theoretical reference for clinical practice. A total of 110 patients with PCa were selected as the study subjects. First, the modified POCS algorithm was used to reconstruct the MRI images, and the gradient interpolation algorithm was used instead of the traditional bilinear algorithm to preserve the edge information. The diagnostic and therapeutic effects of MRI examination, PSA examination, and MRI combined with PSA based on a super-resolution reconstruction algorithm were then compared. The simulation results showed that the POCS algorithm was superior to the bilinear interpolation results and was superior to the common POCS algorithm. After adding noise artificially, the restoration algorithm was effective and could preserve the details in the image. The performance indexes of PSA in the diagnosis of PCa were 75.4%, 60.1%, 70.08%, 72.2%, and 60.3%, respectively; the performance indexes of MRI in the diagnosis of PCa were 84.6%, 61.4%, 71.11%, 73.08%, and 61.9%, respectively; and the performance indexes of MRI combined with PSA based on the super-resolution reconstruction algorithm in the diagnosis of PCa were 96.05%, 88.3%, 95.1%, 93.6%, and 92.7%, respectively. The indicators of MRI combined with PSA based on the super-resolution reconstruction algorithm were significantly higher than those of the other two methods ($P < 0.05$). The signal-to-noise ratio of MRI of PCa based on the super-resolution reconstruction algorithm has been greatly improved, with good clarity, which can improve the diagnostic accuracy of PCa patients and has certain advantages in the examination. MRI based on the super-resolution reconstruction algorithm has a high value in the diagnosis and treatment of PCa.

1. Introduction

Prostate cancer (PCa) is one of the most common malignant tumors threatening the life safety of men, and worldwide, the incidence of PCa ranks second among male malignant tumors [1]. Although the incidence of PCa is currently low in China, the incidence of the disease in China has shown a significant increase in recent years [2]. With the increasing aging of the population in China, as well as the gradual hyper-lipidation of dietary patterns and the popularization of examinations in elderly men, the incidence of the disease remains an increasing possibility [3]. For the determination of PCa diagnosis and treatment options as well as its

prognosis, the early diagnosis of tumors and the clinical staging of tumors play a decisive role. For lesions localized in the capsule, radical PCa resection is one of the effective treatments for the disease [4]. At present, prostate biopsy remains the gold standard for preoperative examination of PCa in China, but this examination method is not applicable to patients with smaller lesions because the lesions are limited by the number of puncture needles when they are small, and the diseased tissue cannot be removed, resulting in low sensitivity. The results of relevant clinical studies showed that the missed diagnosis rate of needle biopsy was about 30% [5]. In addition, most elderly patients are not well tolerated and accepted for the examination, resulting in a

low proportion of patients receiving puncture techniques and their clinical popularity. At present, MRI and prostate specific antigen (PSA) are the main noninvasive methods used for PCa, but there are differences in the sensitivity and specificity of various examination techniques. PSA is a serine protease secreted by prostate epithelial cells that is significantly present in both normal and abnormal prostate tissues, so PSA can be used as a sensitive indicator for PCa examination [6]. The normal range of this index is 0~4 ng/mL. BPH is predominant in patients with PSA < 4.0 ng/mL, and PCa is predominant in patients with PSA > 10 ng/mL. Overall, PSA values are positively correlated with the incidence of PCa, and this index has now become a commonly used indicator for the diagnosis of PCa [7]. However, PSA is used as a prostate specific indicator rather than a specific indicator of PCa. It is therefore nonspecific in diagnosing PCa. Prostatic hyperplasia, prostatitis, acute urinary retention, and cystoscopy can cause PSA increase. Moreover, a significant disadvantage of the PSA test is the inability to stage PCa.

In recent years, with the gradual application of high-field MRI, rectal coil, body coil, and other techniques in clinical practice, the prostate results can be clearly visualized on MRI T2W1 sequence and hypointense nodules located in the peripheral zone can be sensitively detected, so its sensitivity and specificity in the diagnosis of PCa have been significantly improved. The sensitivity can reach 70%~90%, and the accuracy of diagnosis is also significantly higher than that of ultrasound and CT. However, the results of current clinical studies have shown that some benign diseases such as prostatitis and PIN will also show the central zone in the T2WI sequence of MRI, and hypointense areas will appear in the hyperintense peripheral zone [8]. It has led to decreased sensitivity and specificity of MRI for the diagnosis of PCa. In recent years, MRI technology has been continuously developed, and new technologies such as DCE-MRI have been gradually developed. However, some scholars believe that the sensitivity and specificity of DCE-MRI in the diagnosis of PCa should be further studied and confirmed. There are many reports on MRI and MRD in the diagnosis of prostate cancer, and studies have found that MRI-guided prostate biopsy technique has a significant role in increasing the positive rate of repeated puncture [9]. Overall, the sensitivity and specificity of MRI or PSA alone in the diagnosis of PCa are not too high.

Although MRI has been widely used in clinical practice, however, its disadvantages are also obvious, for example, compared with other imaging methods, the imaging speed of MRI is significantly slower, which leads to an examination time of 15 minutes to an hour or even longer. Maintaining a maneuver for a long time in a closed environment is difficult for some patients, especially elderly and pediatric patients. In addition, high-resolution images can hardly be obtained in the case of movement, so their scanning speed must be fast to avoid artifacts in the case of movement, and if the patient and the examiner cooperate improperly, they need to be reexamined [10, 11]. How to improve the image quality and resolution after acquisition has become the focus of researchers' attention. Super-resolution technology has been widely used and popularized in astronomy, medical imaging, monitoring, and detection. Traditional super-resolution reconstruction techniques for single images are defined as observing and recovering high-resolution images (HR) from low-resolution images (LR). The results of subsequent related studies showed that the algorithm was greatly affected by noise, and the reconstructed images were less effective [12]. Therefore, this algorithm has not been widely popularized, but it is helpful to the research of super-resolution algorithms. After continuous development and progress, ultrasonic resolution technology has also been greatly developed and advanced. The projection onto convex sets (POCS) algorithm has been widely used and has achieved good results. Some scholars use the POCS algorithm to input the super-resolution algorithm of cardiac images. In this experiment, three-dimensional super-resolution images were reconstructed by using multiple low-resolution two-dimensional cardiac MRI images. This algorithm can not only be used for cardiac MRI image reconstruction but can also be applicable to other anatomical structures [13]. There are many similar related studies, but there are few studies and analyses for PCa.

This study was aimed at investigating the value of MRI and PSA techniques in PCa based on super-resolution reconstruction algorithms in prostate diagnosis. PCa patients were selected as the study subjects to compare MRI examination, PSA examination, and MRI combined with PSA diagnosis and treatment based on super-resolution reconstruction algorithms. It was to provide a reference and basis for the treatment of related diseases in clinical practice.

2. Materials and Methods

2.1. Subjects. A total of 110 PCa patients who visited the hospital from March 2020 to March 2021 were selected as the study subjects. There were 56 male patients and 54 female patients, with a mean age of 66.3 ± 12.8 years. Informed consent was obtained from patients and this study was approved by the ethics committee of the hospital.

2.1.1. Inclusion Criteria. Patients with suspected prostate lesions or abnormal serum PSA were identified by digital rectal examination and B-ultrasonography; patients' age ranged from 35 to 80 years; patients' education level was primary school or above; patients had no communication barriers and were able to communicate normally with researchers.

2.1.2. Exclusion Criteria. Patients with visual acuity or reading and writing disorders; Patients with clinical diagnosis of mental illness; Patients with other serious physical or organ function diseases; Patients with a history of prostate-related surgery.

2.2. Test Methods

2.2.1. PSA Examination. All patients underwent fasting venous blood sampling. Digital rectal examination, catheterization, cystoscopy, prostate biopsy, and other examinations should be avoided before blood collection.

2.2.2. MRI Examination. A 3.0 T MRI scanner was used and placed in the body phased array coil, and axial and coronal fat-compression fast spin echo T2WI scans were performed locally in the prostate, and pelvic midsagittal T1WI scans were performed. Magnetic resonance perfusion imaging was performed: scan parameters were: TR 4.0 ms, TE 1.4 ms, using the fat suppression technique; flip angle 90°; matrix 203×320; FOV 317×350; slice thickness 2 mm; slice distance 0 mm. A high-pressure syringe was used to inject contrast medium Gd-DTPA at a flow rate of 1.5 mL/s through the cubital vein at a dose of 0.2 mol/kg, and the injection time was 1 to 2 stages from the beginning of the scan, with a scanning time of 13 to 16 s in each stage, for a total of 30 stages of the scan. The obtained images were processed using the software system.

2.3. Image Processing and Analysis. The POCS algorithm is used to reconstruct the MRI image. The image reconstruction mainly includes four parts: the feature extraction and enhancement module; the information refinement module; the fusion reconstruction; and the loss function. The specific details are as follows:

2.3.1. Feature Extraction and Enhancement Module. It is supposed C_1 and C_3 represent the convolution function with size of 1×1 and 3×3, R represents the ReLU function, O_C^i represents the convolution output of the layer i, O_i represents the output of the layer i, and $O_C^1 = C_3(I_{SR}), O_1 = R(O_C^1)$. The subsequent convolution output representation is shown in the following equation.

$$O_C^i = \begin{cases} C_3(O_{i=1}), i \text{ is odd number} \\ C_1(O_{i=1}), i \text{ is even number} \end{cases}. \qquad (1)$$

$i \in (2, 17)$ represents the layer index. The output representation of each layer is shown in the following equation.

$$O_j = \begin{cases} R\left(O_C^j + \sum_{j=1}^{j=2} O_C^j\right), j \text{ is odd number} \\ R\left(O_C^j\right), j \text{ is even number} \end{cases}. \qquad (2)$$

$j \in (2, 17)$, the expression method of feature extraction and enhancement module output is shown in the following equation.

$$O_{17} = R\left(O_C^{17} + \sum_{j=1}^{15} O_C^i\right). \qquad (3)$$

"+" means residual learning, and O_{17} will eventually be input into the informatization module.

2.3.2. Information Refinement Module. In the initial stage, in order to optimize the input feature F_{in}^t with the feedback information F_{in}^{t-1}, F_{in}^t and F_{out}^{t-1} are spliced and compressed to generate the refined initial feature L_0^t by Conv$(1, m)$, as shown in the following equation.

$$L_0^t = C_0\left(F_{out}^{t-1}, F_{in}^t\right). \qquad (4)$$

C_0 is the initial compression operation, $(F_{out}^{t-1}, F_{in}^t)$ indicates the splicing of F_{out}^{t-1} and F_{in}^t. It is assumed that LR and HR characteristic maps are given by the g characteristic mapping structure of the t iteration, and the H_g^t representation method of the HR characteristic map is shown in the following equation.

$$H_g^t = G_g^{\uparrow}\left(L_0^t, L_1^t, \ldots, L_{g-1}^t\right). \qquad (5)$$

$G_g^{\uparrow}$ indicates that the down-sampling operation is performed using Deconv (k,m) in the g feature mapping structure. The representation method of the characteristic diagram L_g^t corresponding to LR is shown in the following equation.

$$L_g^t = G_g^{\downarrow}\left(H_1^t, H_2^t, \ldots, H_g^t\right). \qquad (6)$$

$G_g^{\downarrow}$ indicates that the down-sampling operation is performed using Conv (k,m) in the g feature mapping structure.

In order to make full use of the structural information of each feature map, it fuses the feature LR generated by the feature map structure, and the output of the generated information refinement module is as follows:

$$F_{out}^t = C_{FF}^t\left(L_1^t, L_2^t, \ldots, L_G^t\right). \qquad (7)$$

C_{FF}^t means the function of Conv (1, m).

2.3.3. Fusion and Reconstruction Module. The expression method of feature fusion process is as follows:

$$O_{RB} = R\left(O_1 + F_{out}^t\right), \qquad (8)$$

O_1 and F_{out}^t represent the low-level feature and the high-level feature, respectively, and O_{RB} indicates the output of fast information fusion.

The function description of the reconstruction module is as follows:

$$O_{SR} = C_3\left(R\left(C_3\left(R\left(C_3\left(R\left(C_3\left(O_{RB}\right)\right)\right)\right)\right)\right)\right). \qquad (9)$$

Loss function: the L1 loss function is selected to optimize the network model. The specific network loss function is as follows:

$$L(\theta) = \frac{1}{T}\sum_{i=0}^{T}\left\|I_{HR}^t - I_{SR}^t\right\|. \qquad (10)$$

T represents the total number of iterations, I_{HR}^t represents the label of the LR image input in the t iteration, and I_{SR}^t represents the reconstructed image generated in the t iteration.

2.4. Evaluation of Image Reconstruction Effect. Peak signal-to-noise ratio (PSNR) and structural similarity (SSIM) were used to evaluate the performance of the algorithm. PSNR evaluates the image reconstruction quality by calculating the pixel difference between images. The specific principle is as follows:

$$\text{MSE} = \frac{1}{mn} \sum_{i=0}^{m-1} \sum_{j=0}^{n-1} (X(i,j), Y(i,j))^2,$$

$$\text{PSNR} = 10 \log_{10} \left(\frac{\left(2^k - 1\right)^2}{\text{MSE}} \right).$$

$$(11)$$

The calculation method of SSIM is as follows:

$$l(X,Y) = \frac{2\mu X \mu Y + C_1}{\mu_X^2 + \mu_Y^2 + C_1}, \tag{12}$$

$$c(X,Y) = \frac{2\sigma X \sigma Y + C_2}{\sigma_X^2 + \sigma_Y^2 + C_2}, \tag{13}$$

$$s(X,Y) = \frac{\sigma XY + C_3}{\sigma X \sigma Y + C_3}, \tag{14}$$

$$\text{SSIM}(X,Y) = l(X,Y) \cdot c(X,Y) \cdot s(X,Y). \tag{15}$$

2.5. Statistical Methods. SPSS 22.0 statistical software was used for data analysis. Measurement data were expressed as mean $\pm$ standard deviation ($\overline{x} \pm s$). The t-test was used for comparison between groups. Analysis of variance was used for comparison within groups. The χ^2 test was used for enumeration data. $P < 0.05$ was considered statistically significant.

3. Results

3.1. Patient's MRI Image. MRI images of patients before and after processing are shown in Figure 1. Compared with the original image, the image quality of MRI images processed by high-resolution reconstruction algorithm was significantly improved; the image sharpness was also increased; and the edge; characteristics; and details of the lesion were clearer and more prominent.

3.2. Evaluation Results of Algorithm Reconstruction Performance. The evaluation results of the image reconstruction quality of traditional image processing techniques and the proposed algorithm are shown in Figures 2 and 3. The PSNR and SSIM values of the traditional algorithm were 22.3 and 0.735, respectively, and the PSNR and SSIM values of the proposed algorithm were 28.6 and 0.89, respectively. It can be found that the proposed algorithm performed significantly better than the traditional algorithm.

3.3. Judgment of PCa Results by Different Diagnostic Methods. The results of different diagnostic methods for PCa are judged as shown in Figures 4–6. Analysis of Figures 4–6 showed that the performance indicators of PSA in the diagnosis of PCa were 75.4%, 60.1%, 70.08%, 72.2%, and 60.3%, respectively; the performance indicators of MRI in the diagnosis of PCa were 84.6%, 61.4%, 71.11%, 73.08%, and 61.9%, respectively; and the performance indicators of MRI combined with PSA based on super-resolution reconstruction algorithm in the diagnosis of PCa were 96.05%, 88.3%, 95.1%, 93.6%, and 92.7%, respectively. The indicators of MRI combined with PSA based on the super-resolution reconstruction algorithm were significantly higher than those of the other two methods (Figure 7).

4. Discussion

PCa, is a highly prevalent and common malignant tumor disease in men in Europe and the United States. Globally, PCa has the second highest incidence among all male malignancies [14]. In the US, PCa has surpassed lung cancer as the biggest threat to men's health in cancer rankings that threaten men's health. Although its incidence in China is lower than that in Europe and the United States, it has shown a significant increase in recent years and has become the third most important malignant tumor threatening male health after male urinary and reproductive system tumors [15]. In half of the cases, PCa progresses more slowly and the clinical symptoms are very insignificant. In addition, the disease is often easily misdiagnosed as benign prostatic hyperplasia, which leads to delayed diagnosis and treatment. It leads to missed timing of radical prostatectomy. In summary, it has a very important role and significance for the early diagnosis of PCa treatment. In recent years, PSA and MRI technology have developed rapidly and have been widely used in multiple disease areas. The above two techniques are also of great help and advancement for the diagnosis of PCa [16].

PSA is a serine protease secreted by prostate tissue. Currently, its criteria for PCa diagnosis are RPSA > 10 ng/mL for PCa and RPSA < 10 ng/mL for prostate cancer hyperplasia [17, 18]. In general, PSA is characterized by high sensitivity and low specificity for the diagnosis of PCa. The gray zone of PSA detection is 4 ng/mL < PSA < 10 ng/mL, and the overlap zone between benign prostatic hyperplasia and PCa is large. In general, PSA is specific for prostate tissue but not for PCa. It has some impact on the accuracy and sensitivity of PSA for the diagnosis of PCa [19]. PSA was applied to diagnose PCa. The results showed that the negative predictive value, positive predictive value, accuracy, specificity, and sensitivity of PCa were 75.4%, 60.1%, 70.08%, 72.2%, and 60.3%, respectively. It can be found that its performance is general in PCa diagnosis.

MRI can provide physiological, pathological, biochemical, and anatomical information about the prostate. It has high sensitivity for both diagnosis and staging of PCa. This method is considered to be the most effective and ideal noninvasive test for PCa. MRI can quantitatively measure and display the characteristics of water molecules in the microscopic water environment in tissues, thus further providing information on tissue spatial results, so it has the advantages of multi-directional imaging and good tissue resolution [20]. Therefore, it has high application value and potential in the detection of tiny lesions, differentiation of benign and malignant tumors, tumor staging, and helping doctors develop scientific and effective treatment plans. However, MRI also has deficiencies, such as significant changes in metabolic information in patients who have undergone digital examination of tissues and organs, and therefore MRI is clearly not applicable to such patients [21].
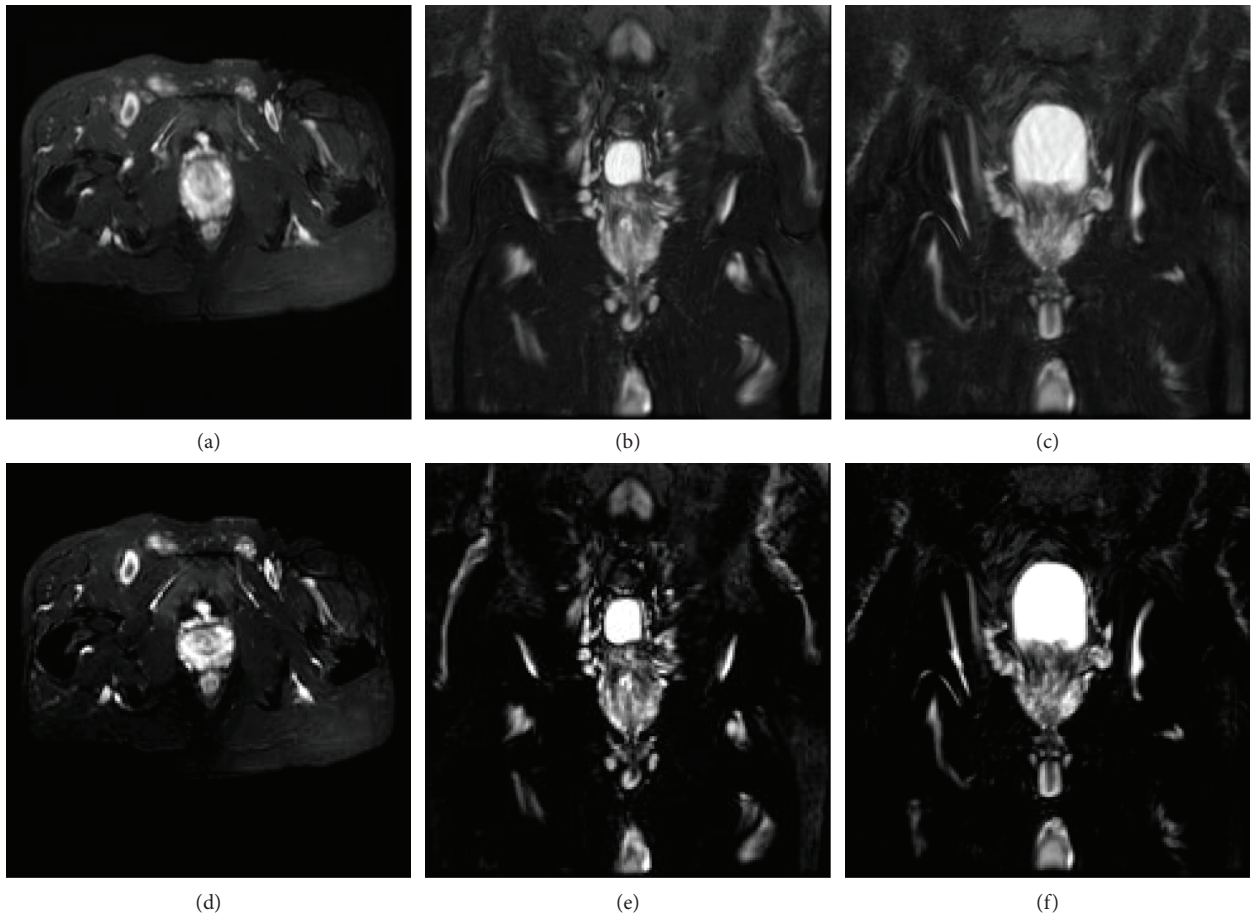
FIGURE 1: MRI images presentation of the typical case. (a)–(c): pre-processing image; (d)–(f): processed image.
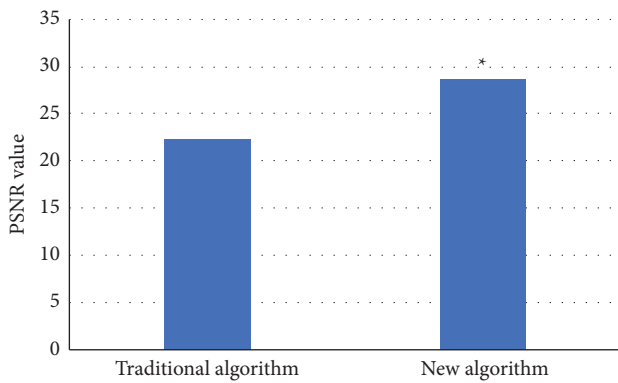
FIGURE 2: Comparison of PSNR index results. *Compared with traditional algorithm, $P < 0.05$.
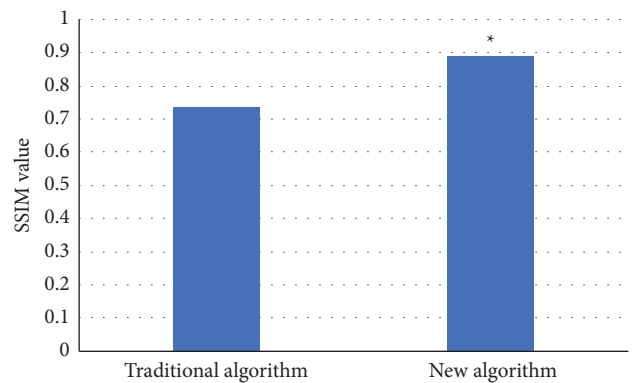
FIGURE 3: Comparison of SSIM index results. *Compared with traditional algorithm, $P < 0.05$.

MRI was used to diagnose PCa. The results showed that the negative predictive value, positive predictive value, accuracy, specificity, and sensitivity of PCa were 84.6%, 61.4%, 71.11%, 73.08%, and 61.9%, respectively. It can be found that its performance in PCa diagnosis is slightly better than in PSA diagnosis.

In recent years, computer and network technology have developed rapidly and advanced, gradually penetrating into various fields. It has also been applied and developed in the medical field, and one of the more interesting technologies is super-resolution technology [22]. In the 1960s, high-resolution images can be obtained by mining the prior knowledge of low-resolution images and reconstructing image information for images with lower resolution. However, the results of further research show that the reconstructed image quality is interfered with greatly by noise and its quality is not high, so this algorithm has not been widely popularized and applied. After continuous

FIGURE 4: PSA diagnosis results.

FIGURE 5: MRI diagnostic results.

FIGURE 6: Diagnostic results of MRI combined with PSA based on super-resolution reconstruction algorithm.

FIGURE 7: Comparison of performance indicators of each method in the diagnosis of PCa. *Compared with MRI-PSA-POCS, $P < 0.05$.

resolution reconstruction algorithm were combined to diagnose PCa. The results showed that the negative predictive value, positive predictive value, accuracy, specificity, and sensitivity of PCa were 96.05%, 88.3%, 95.1%, 93.6%, and 92.7%, respectively. Its performance in PCa diagnosis is significantly better than PSA or MRI alone. This indicates that MRI technology based on the super-resolution reconstruction algorithm has high application value in PCa diagnosis. It provides a reference and a basis for clinical treatment of related diseases.

5. Conclusions

Prostate cancer patients were selected as the study subjects. All patients underwent PSA and MRI examinations. The obtained MRI images were processed by the super-resolution reconstruction algorithm. The PSNR and SSIM indexes were used to evaluate the image reconstruction performance of the algorithm. The accuracy, sensitivity, specificity, positive predictive value, and negative predictive value of PSA, MRI, and MRI combined with PSA based on the super-resolution reconstruction algorithm in the diagnosis of PCa were compared. The results show that the quality of the image processed by the super-resolution reconstruction algorithm was significantly improved, and the scores of PSNR and SSIM indexes of the proposed algorithm were significantly higher than those of the traditional image processing method. MRI combined with PSA based on the super-resolution reconstruction algorithm had significantly higher scores than PSA and MRI alone in the diagnosis of PCa. It provides a new idea and reference for the diagnosis of PCa in clinical practice. However, there are still some defects and deficienci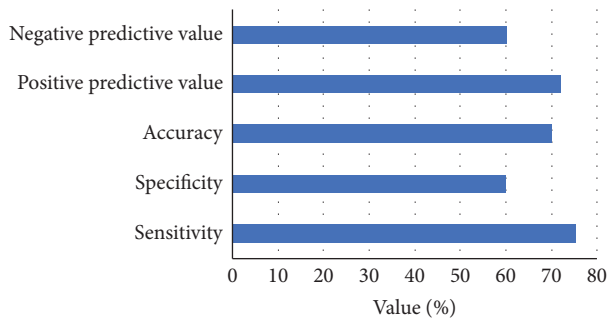es. The POCS algorithm was only introduced into MRI image processing of PCa patients. Moreover, more excellent algorithms are introduced, which makes it impossible to guarantee that the image processing algorithm is optimal. In the future, more algorithms will be introduced into MRI image processing of PCa patients in order to find the optimal image processing algorithm.

development and progress, super-resolution technology has been continuously improved and innovated, of which the technology that has received more attention and higher performance is POCS [23]. The convergence speed of the algorithm is fast, and the image reconstruction time is greatly shortened. In recent years, there have also been many studies on the application of related technical medical fields. For example, some scholars use the POCS algorithm to input the super-resolution algorithm of cardiac images, and in the experiment, multiple low-resolution two-dimensional cardiac magnetic resonance images were reconstructed into three-dimensional super-resolution images, which can not only complete the reconstruction of cardiac magnetic resonance images but also be suitable for other human anatomical structures. There are many similar related studies, but there are few studies and analyses for PCa [24, 25]. MRI technology and the super-

Data Availability

The data used to support the findings of this study are available from the corresponding author upon request.

Conflicts of Interest

The authors declare that they have no conflicts of interest.

References

[1] J. K. Sehn, "Prostate cancer pathology: recent updates and controversies," *Missouri Medicine*, vol. 115, no. 2, pp. 151–155, 2018.

[2] M. C. Haffner, W. Zwart, M. P. Roudier et al., "Genomic and phenotypic heterogeneity in prostate cancer," *Nature Reviews Urology*, vol. 18, no. 2, pp. 79–92, 2021.

[3] H. Schatten, "Brief overview of prostate cancer statistics, grading, diagnosis and treatment strategies," *Advances in Experimental Medicine and Biology*, vol. 1095, pp. 1–14, 2018.

[4] K. Komura, C. J. Sweeney, T. Inamoto, N. Ibuki, H. Azuma, and P. W. Kantoff, "Current treatment strategies for advanced prostate cancer," *International Journal of Urology*, vol. 25, no. 3, pp. 220–231, 2018.

[5] M. Y. Teo, D. E. Rathkopf, and P. Kantoff, "Treatment of advanced prostate cancer," *Annual Review of Medicine*, vol. 70, pp. 479–499, 2019.

[6] C. Ritch and M. Cookson, "Recent trends in the management of advanced prostate cancer," *F1000Research*, vol. 7, 2018.

[7] T. Tsujino, K. Komura, T. Inamoto, and H. Azuma, "CRISPR screen contributes to novel target discovery in prostate cancer," *International Journal of Molecular Sciences*, vol. 22, no. 23, 2021.

[8] M. Matsushita, K. Fujita, and N. Nonomura, "Influence of diet and nutrition on prostate cancer," *International Journal of Molecular Sciences*, vol. 21, no. 4, p. 1447, 2020.

[9] D. Termini, D. J. Den Hartogh, A. Jaglanian, and E. Tsiani, "Curcumin against prostate cancer: current evidence," *Biomolecules*, vol. 10, no. 11, p. 1536, 2020.

[10] M. T. Vietri, G. D'Elia, G. Caliendo et al., "Hereditary prostate cancer: genes related, target therapy and prevention," *International Journal of Molecular Sciences*, vol. 22, no. 7, p. 3753, 2021.

[11] C. DE Nunzio, F. Presicce, S. Giacinti, M. Bassanelli, and A. Tubaro, "Castration-resistance prostate cancer: what is in the pipeline?" *Minerva Urology and Nephrology*, vol. 70, no. 1, pp. 22–41, 2018.

[12] X. Zhang, "Interactions between cancer cells and bone microenvironment promote bone metastasis in prostate cancer," *Cancer Communications*, vol. 39, no. 1, p. 76, 2019.

[13] J. Mayor de Castro, J. Caño Velasco, J. Aragón Chamizo, G. Andrés Boville, F. Herranz Amo, and C. Hernández Fernández, "Cáncer de próstata localmente avanzado. Definición, diagnóstico y tratamiento (Locally advanced prostate cancer. Definition, diagnosis and treatment)," *Archivos Españoles de Urología*, vol. 71, no. 3, pp. 231–238, 2018.

[14] C. C. Foster, R. R. Weichselbaum, and S. P. Pitroda, "Oligometastatic prostate cancer: reality or figment of imagination?" *Cancer*, vol. 125, no. 3, pp. 340–352, 2019.

[15] T. Gourdin, "Recent progress in treating advanced prostate cancer," *Current Opinion in Oncology*, vol. 32, no. 3, pp. 210–215, 2020.

[16] D. A. Siegel, M. E. O'Neil, T. B. Richards, N. F. Dowling, and H. K. Weir, "Prostate cancer incidence and survival, by stage and race/ethnicity-United States, 2001–2017," *MMWR Morb Mortal Wkly Rep*, vol. 69, no. 41, pp. 1473–1480, 2020.

[17] M. Rosellini, M. Santoni, V. Mollica et al., "Treating prostate cancer by antibody-drug conjugates," *International Journal of Molecular Sciences*, vol. 22, no. 4, p. 1551, 2021.

[18] T. Kimura and S. Egawa, "Epidemiology of prostate cancer in Asian countries," *International Journal of Urology*, vol. 25, no. 6, pp. 524–531, 2018.

[19] K. M. Wheeler and M. A. Liss, "The microbiome and prostate cancer risk," *Current Urology Reports*, vol. 20, no. 10, p. 66, 2019.

[20] A. Sokolova and H. Cheng, "Germline testing in prostate cancer: when and who to test," *Oncology*, vol. 35, no. 10, pp. 645–653, 2021.

[21] F. Preisser, M. R. Cooperberg, J. Crook et al., "Intermediate-risk prostate cancer: stratification and management," *European Urology Oncology*, vol. 3, no. 3, pp. 270–280, 2020.

[22] Z. Wan, Y. Dong, Z. Yu, H. Lv, and Z. Lv, "Semi-supervised support vector machine for digital twins based brain image fusion," *Frontiers in Neuroscience*, vol. 15, Article ID 705323, 2021.

[23] P. C. Albertsen, "Prostate cancer screening and treatment: where have we come from and where are we going?" *BJU International*, vol. 126, no. 2, pp. 218–224, 2020.

[24] S. Xie, Z. Yu, and Z. Lv, "Multi-disease prediction based on deep learning: a survey," *Computer Modeling in Engineering and Sciences*, vol. 128, no. 2, pp. 489–522, 2021.

[25] J. L. Mohler and E. S. Antonarakis, "NCCN guidelines updates: management of prostate cancer," *Journal of the National Comprehensive Cancer Network*, vol. 17, no. 5.5, pp. 583–586, 2019.

WILEY | Hindawi

Research Article

Clinical Observation of Modified Implantation of ASD Closure Device to Treat BPFs

Yangfei Lu,[1,2,3] Jisong Zhang,[1,2] Enguo Chen,[1,2] and Kejing Ying [1,2]

[1]*Department of Pulmonary and Critical Care Medicine, Regional Medical Center for National Institute of Respiratory Disease, Sir Run Run Shaw Hospital, School of Medicine, Zhejiang University, Hangzhou 310016, China*
[2]*Cancer Center, Zhejiang University, Hangzhou 310058, China*
[3]*Hangzhou Fuyang District First People's Hospital, Hangzhou 31000, China*

Correspondence should be addressed to Kejing Ying; lyfsyfyy1223@163.com

Objectives. The aim of the paper is to explore the clinical efficacy and prognosis of the modified implantation of atrial septal defect (ASD) closure device to treat bronchopleural fistulas (BPFs). *Methods*. This paper has reviewed the results of 13 BPF patients implanted with a modified ASD closure device in Shaw Hospital Affiliated with the Medical College of Zhejiang University from October 2018 to November 2021. Anesthesia was selected based on the patient's condition. Different sizes of ASD closures were selected based on the characteristics of fistulas. The modified implantation of the ASD closure device was applied to treat BPFs. The closure effects, closure time, and Borg score were observed at 4 weeks, 8 weeks, and 12 weeks after the surgery. *Results*. All 13 BPF patients were successfully implanted with the ASD closure device, and the immediate clinical remission rate was 100%. Follow-up at 4 weeks after the surgery showed that 2 cases were automatically discharged within a few days and 4 cases had closed fistula at 1 day after the surgery; follow-up at 8 weeks after the surgery showed that 1 case with fistula closure was observed at 55 days after the surgery; follow-up at 12 weeks after the surgery showed that 1 case with fistula closure was observed at 82 days after the surgery. T/P values ($T = 7.90, 5.99, 7.44, P < 0.05$) of paired *t*-tests before surgery and 4 weeks, 8 weeks, and 12 weeks after the surgery were rated by the Borg scale. The data were statistically different, and the clinical symptoms improved significantly. As of publication, the follow-up at 12 weeks after the surgery showed that the clinical remission rate was 9/11, namely, 81.8%, 3 of 11 cases had relieved clinical symptoms but still needed continuous drainage, and 2 cases had fistula closure. The median time of thoracic extubation was 63 (3,120) days. No patients died from surgical complications or BPF recurrence during the prognosis and the follow-up period. *Conclusions*. The modified implantation method has a high success rate and clinical remission rate, quick and early fistula closure, and simple and noninvasive operation, without the need for a dedicated delivery sheath and rigid endoscopy. Moreover, it has accurate positioning, reliable closure efficiency, and prognosis, and can be completed under local anesthesia. This reduces the operation time, difficulty, and risks of anesthesia.

1. Introduction

BPF is an abnormal sinus tract among the trunk, pulmonary lobe, or segmental bronchial tract and the pleural cavity. Although it is relatively rare, BPF has a life-threatening postoperative complication. Its postoperative morbidity after total pneumonectomy is 2~20%; postoperative morbidity after lobectomia pulmonalis is 0.5~3%, and its mortality is 16~71% [1]. BPF recurrence rate after surgical repair is as high as 23.6% [2]. In clinical work, we found that

patients generally have contraindications. Interventional treatment such as a stent, plugging agent, or closure can effectively control BPF-related symptoms [3].

ASD closure was reported to treat BPFs in 2008 [4–6], which requires fluoroscopic positioning, rigid endoscopy, and intravenous general anesthesia. Fluorescein angiography can draw the outline of fistula anatomic structure, diameter, length, and deep structure, as well as the relative position of ASD closure to stump and fistula after operation [7]; rigid endoscopy provides a temporary channel for

(a)   (b)   (c)
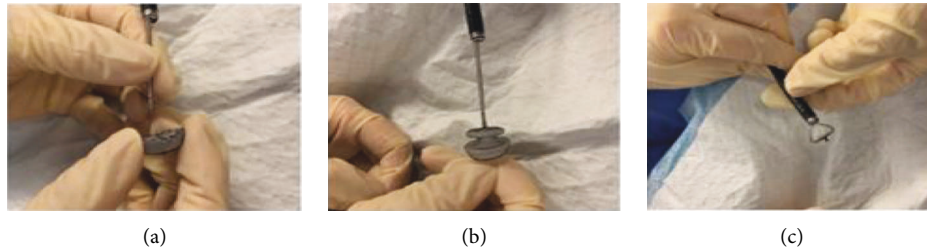
Figure 1: Installation of ASD closure at the top of the bronchoscope.

bronchoscopy and dedicated delivery sheath to pass through rima glottidis simultaneously [8]; intravenous general anesthesia can provide better operation conditions and reduce surgical accidents caused by the patient's failure to cooperate. However, when recovering from intravenous general anesthesia, the patient may have temporary increases in BP and HR. Such side effects are generally controllable. But serious side effects may lead to terrible cardiovascular and cerebrovascular accidents, such as cerebral hemorrhage and myocardial ischemia [9]. The efficacy and prognosis of closure surgery are reliable, but the risk of rigid endoscopy and intravenous general anesthesia limits the feasibility of interventional treatment [5, 6]. To reduce the difficulty of closure surgery and anesthesia risks, improve the feasibility of the surgery, simplify cumbersome steps, and overcome the high requirements of rigid endoscopy in traditional closure surgery, our hospital modified the implantation of ASD closure by hiding the dedicated delivery sheath in the bronchoscope working channel in 2018. This method reduces the diameter of operating equipment passing through the rima glottidis and does not require rigid endoscopy, intravenous general anesthesia, or dedicated delivery sheath. Moreover, it uses bronchoscope direct vision instead of fluorescein angiography for fistula evaluation. To explore the application of this modified implantation, this paper analyzed the clinical data of 13 BPF patients treated with modified implantation of ASD closure from October 2018 to November 2021.

2. Data and Methods

2.1. General Data. 13 BPF patients treated with modified implantation of ASD closure from October 2018 to November 2021 were reviewed, including 12 males and 1 female aged 40–73 years old. They were all patients with a previous history of pulmonectomy and had signed informed consent prior to the surgery.

2.2. Clinical Instruments and Materials. BF-1T260 with an external diameter of 6.0 mm and a 2.8 mm working channel (OLYMPUS, Japan) was selected as the bronchoscope, and different types of ASD closures (Shandong Weixin Medical Device Co., Ltd.) were selected based on the characteristics of the fistulas. ASD closure is woven by a shape-memory alloy-nickel-titanium alloy wire. It has a double-disc structure (12–56 mm), which was connected through the waist (4–38 mm) with PE-coated film.

2.3. Preoperative Preparation. (1) Fasting for 8 hours before surgery; (2) preoperative tests are carried out before planned surgery, including routine blood tests, blood biochemistry, preoperative immunization, urine routine, ECG, cardiac ultrasound, and chest CT; (3) preoperative supportive treatment includes anti-infection, nutritional support, and closed thoracic drainage.

2.4. Anesthesia. Choose the following anesthesia method based on the patient's condition:

(1) Local anesthesia combined with compound sedation and analgesia: atomization inhalation of 2% lidocaine 10 ml (about 15 min), intravenous infusion of midazolam 2.5 mg, intravenous infusion of sufentanil 0.025 mg.

(2) Intravenous general anesthesia: venous channels were established and ECG, heart rate, blood pressure, SPO2, and ETCO2 were monitored. Patients intravenously received 0.02–0.04 mg/kg midazolam, 0.3–0.5 μg/kg sufentanil, 1.0–2.0 mg/kg propofol, and 0.12–0.15 mg/kg cis-atracurium in turn. The anesthesia machine was connected by a three-way tube. During surgery, propofol 4–6 mg/(kg·h) was infused continuously by a pump, with an intermittent intravenous injection to deliver anesthetic as needed. Spontaneous breathing was maintained after the recovery of muscle relaxation, and intermittent assisted respiration was maintained till the end of the surgery.

2.5. Operation Process. In the supine position, the patient was administered general anesthesia or local anesthesia. A tracheoscope was inserted to determine the location, diameter, and structure of BPFs. Different sizes of ASD closures were selected based on the characteristics of the fistulas. A guide wire passed through the working channel via the biopsy hole and connected with the ASD closure which has a special nut structure at the bottom of the inner disc. The ASD closure device was tested for release and folding. After the device is confirmed to meet the requirements, a bronchoscope with the ASD closure device at its top was inserted into the fistula. The guide wire was pushed to release the far-sided disk. After the bronchoscope and guide wire were kept relatively fixed, the far-sided disk was pushed and pulled to make it cling to the internal wall of the fistula

TABLE 1: General conditions of patients.

No.	Gender/age	Pulmonary surgery site	Fistula location	Histopathology	Time of fistula occurrence (day)	Fistula diameter (mm)
1	F/73	Right lower lung	Right lower lung	Adenocarcinoma	240	10
2	M/64	Right lower lung	Right lower lung	Squamous cell carcinoma	20	8
3	M/66	Left lung	Left main lung	Squamous cell carcinoma	9	8
4	M/71	Left upper lung	Left upper lung	Non-small-cell carcinoma	40	8
5	M/70	Right lung	Right main lung	Non-small-cell carcinoma	60	10
6	M/56	Right middle bottom lung	Right middle lung	Squamous cell carcinoma	30	6
7	M/44	Left upper lung	Left upper lung	Granulomatous	50	5
8	M/40	Left upper lung	Left upper lung	Tuberculosis	60	5, 3, 2, 2
9	M/66	Right middle, upper lung posterior segment	Right middle lung	Adenocarcinoma	11	5
10	M/71	Left upper lung	Left upper lung	Adenocarcinoma	21	7
11	M/67	Right lower lung	Right lower lung	Squamous cell carcinoma	30	5, 5
12	M/73	Right middle bottom lung	Right middle lung	Squamous cell carcinoma	120	7
13	M/40	Right upper lung	Right upper rear lung	Tuberculosis	1	5, 3
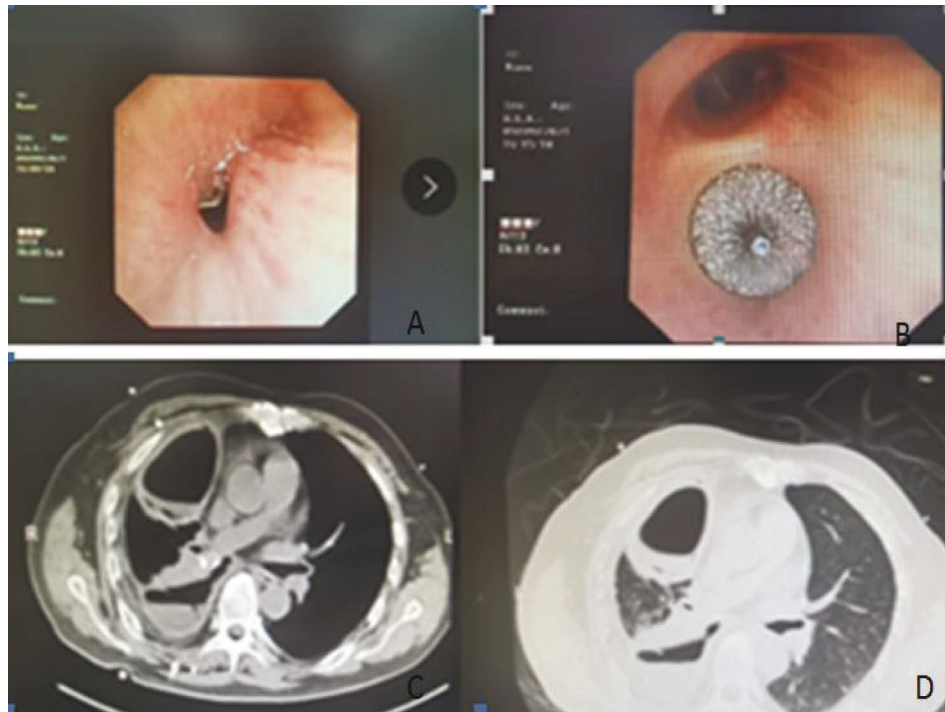
FIGURE 2: After implantation of the ASD closure device in the right middle lung lobe (Table 1 No.6).

after being fully unfolded. The near-sided disk was not released until the far-sided disk was confirmed to cling to the internal wall of the fistula. After the release, the guide wire was pulled to observe whether it was firm enough. Then, the guide wire was released by rotating the nut structure. And the patient was pushed to the postanesthesia care unit (PACU) after the surgery. Figure 1 shows the steps of installing the occluder and storing it at the head end of the working channel of the tracheoscope. Figure 1(a) shows the guide wire is extended and connected with the inner disc port of the occluder by a rotating nut structure. Figure 1(b) shows the successful connection between the guide wire and

(a)
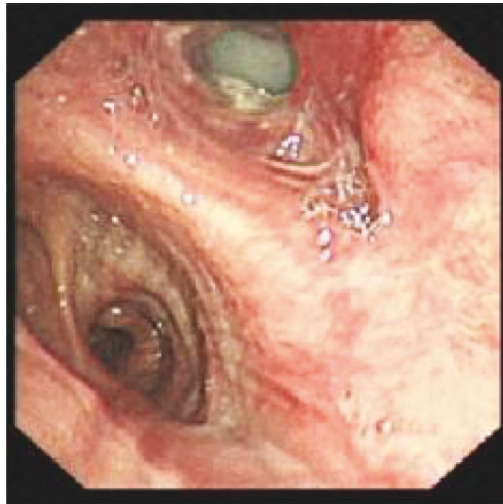
(b)

(c)

(d)

(e)

(f)

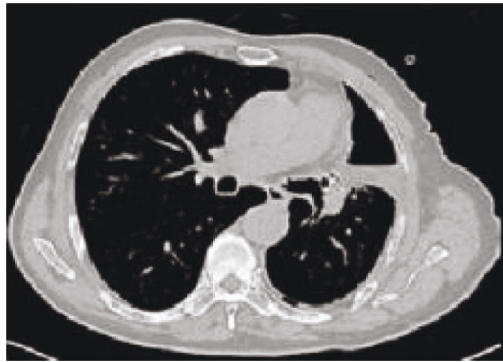FIGURE 3: After implantation of the ASD closure device in the left upper lung lobe (Table 1 No.4).

TABLE 2: Efficacy of postoperative follow-up.

	4 weeks	8 weeks	12 weeks
CR	4	5	6
CCR	2	3	2
PR	4	2	1
NR	1	1	2
Number of cases	11*	11	11
Clinical remission rate**	90.9%	90.9%	81.8%

Note. * 2 cases were discharged a few days after the surgery; ** Clinical remission rate = (CR + CCR + PR)/number of cases.

the inner disc of the occluder. Figure 1(c) shows the occluder is stored at the head end of the working channel of the tracheoscope.

2.6. Indications and Contraindications

Indications: (1) fistula diameter >5 mm; (2) the anatomy of the fistula is similar to ASD [10];

Contraindications: (1) fistula periphery has or is near the large vessel [11]; (2) the fistula is located at the bronchus below the pulmonary segment; (3) incomplete lung fissure or cribriform fistulas (many small fistulas) appears in the lung section after pulmonary wedge resection.

2.7. Observation Indicators.
The fistula closure, length of fistula closure, thoracic extubation time, and Borg score of the patient were observed at 4 weeks, 8 weeks, and 12 weeks after the surgery [12].

2.8. Criteria of Fistula Closure Efficacy.
Based on experience, Professor Wang Hongwu and his team formulated a criterion for evaluating the efficacy of fistula closure [13]. Cure (CR) denotes that the fistula is healed and clinical symptoms are completely relieved for 1 month; clinical remission (CCR) indicates that the fistula is not healed, but completely occluded by the stent, and symptoms such as coughing while drinking liquids or fever are completely relieved for more than 1 month; partial relief (PR) means that fistula is not closed, but partially occluded by the stent, and clinical symptoms are partially relieved; invalid (NR) represents that fistula is neither closed nor occluded by the stent, and clinical symptoms are not relieved.

2.9. Statistical Methods.
SPSS26 is used for statistical analysis of patients' general conditions, operation minutes, Borg scores, etc. Categorical data results are expressed as constitutive ratios and the measurement results are expressed as $x \pm s$. A paired t-test is conducted before and after the surgery and $P < 0.05$ is considered statistically significant.

3. Results

3.1. Clinical Data.
Basic information through Table 1, we know that there were 13 patients with BPFs, including 12 males (92.3%) and 1 female (7.7%), aged 61.62 ± 12.43. Different pulmonary surgery sites occurred in 13 cases (including 2 cases of pneumonectomy and 11 cases of lobectomy or segmentectomy). In the 13 cases, fistulas were located at different parts of the lungs, including 1 at the left mainstem bronchus, 1 at the right mainstem bronchus, 4 at the left upper lung lobe, 1 at the right upper lung lobe, 3 at the right middle lobe, and 3 at the right lower lobe. Among 13 patients with BPFs, there were 5 squamous cell carcinoma, 3 adenocarcinomas, 2 non-small-cell carcinomas, 2 tuberculosis, and 1 granulomatous. The median time for patients to develop postoperative fistulas was 30 days (15.5, 60) days, the total number of fistulas was 18, and the diameter of the fistula was 5.57 ± 2.44 mm. Figure 2 treatment picture information comes from NO.6 patient in Table 1. The patient had right mesobronchial lung cancer, and the fistula appeared 30 days after the operation. The diameter of the fistula was 6 mm. Figure 2(a) shows the fistula after tracheoscopy, and Figure 2(b) shows the fistula after successful closure. Figures 2(c) and 2(d) are preoperative chest CT images. Figure 3 treatment data are from NO.4 patient in Table 1. This patient had left upper lung cancer, and the fistula appeared 40 days after the operation. The diameter of the fistula was 8 mm. Figure 3(a) is the preoperative chest CT of the patient, Figure 3(b) is the fistula under the intraoperative tracheoscope, Figure 3(c) is the fistula after the successful placement of the occluder, Figures 3(d) and 3(f) are the postoperative chest CT Reexamination results, and Figure 3(e) is the postoperative drainage bag drainage of the patient.

3.2. Postoperative Follow-Up Efficacy.
According to the statistical data in Table 2, the follow-up after 4 weeks of the surgery showed that 2 patients died (nonsurgery caused) and 11 patients survived, including 4 CR, 2 CCR, 4 PR, and 1 NR, with the fistula closure rate of 36.4%, and the clinical remission rate of 90.9%. The follow-up after 8 weeks of the surgery showed that there were 5 CR, 3 CCR, 2 PR, and 1 NR, with a fistula closure rate of 45.5%, and a clinical remission rate of 90.9%. The follow-up after 12 weeks of the surgery showed that there were 6 CR, 2 CCR, 1 PR, and 2 NR, with a fistula closure rate of 54.5%, and a clinical remission rate of 81.8%, as well as 1 BPF recurrence.

According to relevant data in Table 3, we know that 12 received chest drains prior to the surgery and 13 received chest drains after the surgery. After the surgery, 8 patients stopped leaking air bubbles immediately (66.7%), and 4 patients leaked fewer bubbles than before (33.3%). 4 patients received thoracic extubation within 4 weeks, 5 of them within 8 weeks, and 6 patients were removed from the tube within 12 weeks. After 12 weeks, other 3 patients had the chest drain removed and 4 did not meet the criteria (Among the 4 patients, 2 had persistent fistulas and 2 were discharged a few days after the surgery). 8 cases had a closed fistula

TABLE 3: Surgery and follow-up.

No.	Preoperative thoracic drainage	Postoperative thoracic drainage	Bubbles stop overflowing after thoracic drainage	Length of fistula closure (day)	Thoracic extubation (day)	Extubation success	Follow-up period as of publication (month)	Survival	Anesthesia method	Operation time (min)	ASD closure waist diameter (mm)
1	Yes	Yes	Immediately	1	3	Yes	37.4	Yes	Local anesthesia	7	10
2	Yes	Yes	Immediately	1	82	Yes	35.1	Yes	Intravenous general anesthesia	23	8
3	Yes	Yes	Immediately	1	No extubation	No	0.1	No	Intravenous general anesthesia	25	12
4	Yes	Yes	Fewer	55	55	Yes	32.3	Yes	Intravenous general anesthesia	22	8
5	No	Yes	Free of bubbles	1	No extubation	No	16.8	Yes	Local anesthesia	20	10
6	Yes	Yes	Fewer	120	120	Yes	29.6	Yes	Intravenous general anesthesia	15	12
7	Yes	Yes	Fewer	195	195	Yes	21.8	Yes	Local anesthesia	17	8
8	Yes	Yes	Fewer	No closure	No extubation	No	12.8	Yes	Local anesthesia	14	8
9	Yes	Yes	Immediately	1	No extubation	No	0.2	No	Intravenous general anesthesia	16	6
10	Yes	Yes	Immediately *	No closure	540*	Yes	20.6	Yes	Intravenous general anesthesia	19	8
11	Yes	Yes	Immediately	1	1	Yes	28.4	Yes	Local anesthesia	10	8
12	Yes	Yes	Immediately	1	2	Yes	12.2	Yes	Local anesthesia	7	8
13	Yes	Yes	Immediately	1	14	Yes	15.8	Yes	Local anesthesia	23	6

Note. * Bubbles overflowed during thoracic drainage again 70 days after the surgery.

TABLE 4: Comparison of Borg scores before and after the surgery.

	Before surgery	4 weeks after the surgery	8 weeks after the surgery	12 weeks after the surgery
Borg score	5.15 + 2.23	0.73 + 0.90	0.82 + 1.78	0.3 + 0.48
Number of cases	13	11	11	11
t		7.9	5.99	7.44
P		<0.001	0.0001	<0.001

immediately after the surgical treatment. The longest time for the fistula to heal was 195 days. The success rate of extubation was 9/11, namely, 81.8%. The median time of extubation was 63 (3,120) days. As of publication, the follow-up period was 20.2 ± 12.2 months, with the longest of 37.4 months and the shortest of 0.1 months. During the follow-up period, 11 patients survived and 2 died of aggravated pulmonary abscess or empyema. As for anesthesia, 7 patients received local anesthesia and 6 had intravenous general anesthesia. The operation time was 16.8 ± 6.0 min, with the shortest of 7 min and the longest of 25 min. The waist diameter of the ASD closure device was 8.6 ± 1.9 mm, with the maximum and minimum diameters of 12 mm and 6 mm, respectively.

According to the treatment information in Table 4, there were statistically significant differences between the Borg scores 4, 8, and 12 weeks after the surgery and before surgery ($P < 0.05$), indicating clinically meaningful improvement in symptoms and quality of life.

3.3. Postoperative Complications. After the surgery, the patient's cough, purulent sputum, chest tightness, and shortness of breath were significantly reduced, and the Borg score became much lower. Three patients had mild pharyngalgia and globus sensation within 1 week after the ASD closure device was implanted. It may be related to bronchoscopy. Therefore, the patients were given budesonide suspension (2 mg/time, twice/d) for oral inhalation (Pmiklingshu 1 mg/2 ml, AstraZeneca Pharmaceutical Co., LTD.) and their symptoms were thus relieved. After the surgery, pulmonary abscesses were reported by four patients, two of whom were discharged a few days after the surgery and one had fistula closure after debridement. Another one had fistula closure but required continuous chest drain. This may be caused by lung abscess combined with pulmonary Aspergillus.

4. Discussion

ASD closure for the treatment of BPFs requires fluoroscopic positioning, rigid endoscopy, and intravenous general anesthesia. Fluorescein angiography can draw the outline of fistula anatomic structure, diameter, length, and deep structure, as well as the relative position of the ASD closure to stump and fistula after operation; rigid endoscopy provides a temporary channel to ensure that bronchoscopy and dedicated delivery sheath pass through rima glottidis simultaneously [8]; intravenous general anesthesia can provide better operation conditions, reduce surgical accidents caused by the patient's failure to cooperate. However, rigid endoscopy requires a high level of operation, and there is a risk of respiratory tract contusion; intravenous general

anesthesia increases surgical compliance and reduces fear, and large doses of anesthetics will lead to respiratory depression, delayed recovery, or symptoms of hypoxemia; Fluorescein angiography increases radiation exposure to the body and harms health and safety [7]. The average diameter of the widest cauda commissure of adult rima glottidis is 8 mm, and the diameters of a dedicated delivery sheath (diameter 2 mm) and tracheoscope (outer diameter 5.0 mm) are too large to pass through an adult's rima glottides [14]. If the diameter of operating equipment can be reduced, then passing through the rima glottidis will become easier, without the need for rigid endoscopy or intravenous general anesthesia. This can simplify the operation and reduce the risk of anesthesia.

Our hospital modified the implantation of ASD closure by discarding the dedicated delivery sheath and replacing it with the bronchoscope working channel, which reduces the diameter of operating equipment that passes through the rima glottidis. This operation requires no rigid endoscopy, and it can be completed under local anesthesia. In this way, the anesthesia intensity and risks as well as the operation time and difficulty can both be reduced. 7 cases were successfully implanted with the ASD closure device under local anesthesia, with a reduced operation time (16.8 ± 6.0 min) of only 7 min (Table 2 No.1) at a minimum.

The modified implantation of ASD closure has its limitations. The top of the bronchoscopy working channel (inner diameter 2.8 mm) can release and fold ASD closure, but it is not applicable to ASD closure devices with a diameter of more than 2.8 mm after folding. In addition, different brands of ASD closure devices may have different sizes of discs after folding, the surgeons should mind this during operation.

Our modified implantation of ASD closure device has a high success rate and clinical remission rate, quick and early fistula closure, and simple and noninvasive operation, without the need for dedicated delivery sheath or rigid endoscopy. It has accurate positioning, reliable closure efficiency, and prognosis and can be carried out under local anesthesia. With shorter operation time and lower risks of anesthesia, it is worth promoting as a minimally invasive, efficient, and safe method.

Data Availability

The datasets used and/or analyzed during the current study are available from the corresponding author upon reasonable request.

Conflicts of Interest

The authors declare that there are no conflicts of interest regarding the publication of this paper.

References

[1] F. Petrella and L. Spaggiari, "Bronchopleural fistula treatment: from the archetype of surgery to the future of stem cell therapy," *Lung India*, vol. 32, no. 2, pp. 100-101, 2015.

[2] A. Bribriesco and G. A. Patterson, "Management of post-pneumonectomy bronchopleural fistula: from thoracoplasty to transsternal closure," *Thoracic Surgery Clinics*, vol. 28, no. 3, pp. 323–335, 2018.

[3] M. Lois and M. Noppen, "Bronchopleural fistulas: an overview of the problem with special focus on endoscopic management," *Chest*, vol. 128, no. 6, pp. 3955–3965, 2005.

[4] M. R. Kramer, N. Peled, D. Shitrit et al., "Use of amplatzer device for endobronchial closure of bronchopleural fistulas," *Chest*, vol. 133, no. 6, pp. 1481–1484, 2008.

[5] O. Fruchter, B. A. El Raouf, N. Abdel-Rahman, M. Saute, E. Bruckheimer, and M. R. Kramer, "Efficacy of bronchoscopic closure of a bronchopleural fistula with amplatzer devices: long-term follow-up," *Respiration*, vol. 87, no. 3, pp. 227–233, 2014.

[6] O. Fruchter, M. R. Kramer, T. Dagan et al., "Endobronchial closure of bronchopleural fistulae using amplatzer devices: our experience and literature review," *Chest*, vol. 139, no. 3, pp. 682–687, 2011.

[7] O. Fruchter, E. Bruckheimer, Y. Raviv, D. Rosengarten, M. Saute, and M. R. Kramer, "Endobronchial closure of bronchopleural fistulas with Amplatzer vascular plug," *European Journal of Cardio-Thoracic Surgery*, vol. 41, no. 1, pp. 46–49, 2012.

[8] H. W. Wang, Y. Z. Zhou, D. M. Li, J. Li, H. Zou, and N. Zhang, "Treatment of central malignant tumors under TV rigid tracheoscopy," *Chinese Journal of Tuberculosis and Respiration*, vol. 34, no. 3, pp. 230–232, 2011.

[9] M. H. Hung, H. H. Hsu, Y. J. Cheng, and J. S. Chen, "Nonintubated thoracoscopic surgery: state of the art and future directions," *Journal of Thoracic Disease*, vol. 6, no. 1, pp. 2–9, 2014.

[10] V. Marwah, R. Ravikumar, A. K. Rajput, and A. Singh, "Transcutaneous closure of chronic broncho pleuro cutaneous fistula by duct occluder device," *Lung India*, vol. 33, no. 2, pp. 216–218, 2016.

[11] W. H. Cao, D. P. Xia, and Y. Hu, "Research progress in endoscopic interventional diagnosis and treatment of bronchopleural fistula," *Journal of Clinical Lung*, vol. 24, no. 11, pp. 2079–2083, 2019.

[12] Asthma Group, Respiratory Branch, and Chinese Medical Association, "Guidelines for the diagnosis and treatment of cough (2015)," *Chinese Journal of Tuberculosis and Respiration*, vol. 39, no. 5, pp. 323–354, 2016.

[13] H. W. Wang, D. M. Li, N. Zhang et al., "Endotracheal covered metal stent implantation for the treatment of esophageal and tracheal fistula," *Chinese Journal of Tuberculosis and Respiration*, vol. 36, no. 5, pp. 390–392, 2013.

[14] Y. H. Jiang and Y. Tan, "Cause analysis of laryngeal complications after intubation general anesthesia," *Journal of Clinical and Experimental Medicine*, vol. 8, no. 1, pp. 51–53, 2019.

WILEY | Hindawi

Research Article

MRI Features and Significance of Serum miRNAs and Inflammatory Cytokines in Patients with Temporal Lobe Epilepsy

Nengyun Yao,[1] Yanmei She,[2] Songlin Tang,[1] Huafei Liu,[1] and Fang Liu [3]

[1]*Department of Neurology, The First Affiliated Hospital of Shaoyang College, Shaoyang 422000, Hunan, China*
[2]*Department of Endocrinology, The First Affiliated Hospital of Shaoyang College, Shaoyang 422000, Hunan, China*
[3]*Department of Psychiatry, Affiliated Hospital of Weizhou Medical University, Wenzhou 325035, Zhejiang, China*

Correspondence should be addressed to Fang Liu; 1440340306@xs.hnit.edu.cn

This study was aimed to investigate the changes of brain MRI features and serum biological parameters in patients with TLE. 30 patients with unilateral TLE confirmed by surgical pathology were selected as study subjects, and 30 subjects without a history of epilepsy who underwent health examinations during the same period were selected as controls. The brain MRI features of the patients were explored and the T2 relaxation time (HCT2) indexes of the bilateral hippocampus were extracted. The differences in levels of peripheral blood T lymphocyte subsets, inflammatory cytokines, and miRNAs were measured. The results showed that the hippocampal volume of TLE patients was significantly reduced, and the HCT2 value of the hippocampus was greater than that of the control group ($P < 0.05$). CD^{3+} (77.9 ± 4.4)%, CD^{4+} (45.6 ± 2.2)%, CD^{8+} (22.1 ± 1.9)%, and CD^{3+}/CD^{8+} (2.24 ± 0.22) in peripheral blood T lymphocyte subsets of epileptic patients, compared with control group, CD^{3+}, CD^{4+}, and CD^{4+}/CD^{8+} levels were significantly increased and CD^8+ concentration was significantly decreased in epileptic patients ($P < 0.05$); inflammatory cytokines TNF-α was (2.63 ± 0.26) pg/mL, IL-1β was (4.61 ± 0.57) pg/mL, IL-2 was (1.59 ± 0.21) pg/mL, IL-6 was (2.28 ± 0.19) pg/mL, and ICAM-1 was (1.89 ± 0.30) pg/mL in peripheral blood of epileptic patients, which was significantly increased compared with control group, while IL-10 was significantly decreased in epileptic patients ($P < 0.05$); miR-146a was (2.14 ± 0.28) and miR-210 was (1.89 ± 0.31), miR-221 (2.44 ± 0.35), miR-34a (0.59 ± 0.14), miR-135b (10.17 ± 0.16), miR-33 (0.26 ± 0.09) in peripheral blood miRNA levels of epileptic patients, and miR-146a, miR-210, miR-221, and miR-34a levels of epileptic patients were significantly increased compared with control group, while MiR-135b and miR-33 levels of epileptic patients were significantly reduced ($P < 0.05$). In summary, patients with TLE have hippocampal lesions, which may be related to peripheral blood T lymphocyte subsets imbalance, chronic inflammatory response, and abnormal expression of miRNAs.

1. Introduction

There are many factors that induce epilepsy, which are mainly characterized by transient central nervous cell dysfunction due to recurrent episodes of abnormal neuronal discharges, so it belongs to chronic neurological diseases [1]. The medial temporal lobe structures of the brain are mainly composed of hippocampal regions, amygdala regions, and internal olfactory cortex. When these structures are abnormal, it will lead to the occurrence of TLE [2]. Studies have confirmed that hippocampal sclerosis is one of the main factors leading to TLE [3]. Epilepsy patients will be accompanied by different degrees of psychological and

behavioral disorders, which has seriously affected the quality of life of patients. Therefore, how to effectively control seizures has become the focus of current research. The pathogenesis of epilepsy is complex and not fully elucidated. However, the evidence shows that immune factors play an important role in seizures [4, 5]. CD^{4+} and CD^{8+} i*n T* lymphocyte subsets have been confirmed to be related to the degree of neuronal injury in the hippocampus, which in turn is involved in the process of TLE [6]. In addition, neuronal apoptosis and abnormal inflammatory response are also important pathological links causing seizures. The overexpression of promoting apoptotic factors, the excessive accumulation of inflammatory factors, and abnormal

neuronal function are all related to the occurrence and development of epilepsy [7]. MiRNAs, as a class of noncoding RNA molecules about 20~24 bp in length, are involved in the regulation of a variety of gene expression and signaling pathways in the body. At present, it has also been confirmed that miRNAs are involved in the regulation of the function of the nervous system, including the development of nerve cells, neuronal apoptosis, and the differentiation of neural stem cells [8].

Drugs are the treatment of choice for epilepsy, appropriate and standardized antiepileptic drugs are used for the treatment of patients with primary epilepsy, but about 30% of patients are still difficult to control the condition. Medical refractory epilepsy can be treated with surgical resection of the lesion, and 70% of patients with refractory epilepsy are effectively controlled for seizures after surgical treatment [9]. For this reason, preoperative identification of the lesion is important for the success rate of surgery. The clinical methods used for the diagnosis of epilepsy include clinical features, EEG detection, and imaging examination. EEG is effective for the qualitative diagnosis of TLE, but it is not able to localize epileptic foci [10]. Medical imaging enables the assessment of pathological changes through quantitative changes in texture characteristics. MRI is one of the main modalities used for the evaluation of hippocampal lesions in preoperative TLE. The main MRI features of TLE patients are atrophy of hippocampal volume and enhancement of T2WI signal, so it can be used for quantitative evaluation of hippocampal lesions [11].

There are relatively few studies on the measurement of hippocampal T2 relaxation time (HCT2), an MRI characteristic indicator of TLE, as well as the analysis of serum biological parameters. Therefore, patients with unilateral TLE were selected as the study subjects, and the characteristics of brain lesions were evaluated using MRI techniques, followed by the changes in the expression levels of peripheral blood T lymphocyte subsets, inflammatory cytokines, and miRNAs, providing a reference for early diagnosis and treatment of TLE.

2. Materials and Methods

2.1. Subjects. Thirty patients with unilateral TLE confirmed by surgical pathology from June 2020 to March 2022 were selected as study subjects. 30 subjects without a history of seizures who underwent health examinations during the same period were selected as controls. This study had been approved by the ethics committee of the hospital and the patient signed the informed consent form.

Inclusion criteria: (1) according to the guidelines for epilepsy prevention and treatment issued by the International League Against Epilepsy in 2017 [12], combined with clinical features, EEG, and auxiliary examination methods, patients were diagnosed with unilateral TLE; (2) preoperative conventional MRI examination, scanning sequence including T2-FLAIR, and image texture without artifacts; (3) no family history of seizures; (4) no recent immunosuppressive agents, hormones, and other drug treatment. Exclusion criteria: (1) combined with brain diseases, such as

intraluminal tumors, traumatic brain injury, stroke, hysteria, and other diseases; (2) secondary TLE caused by central nervous system infection; (3) combined with systemic lupus erythematosus and other autoimmune diseases; (4) incomplete clinical data.

2.2. Imaging Examination. 3.0T MRI instrument was selected for conventional MRI scanning. The scanning sequences included: (1) axial T1-FLAIR, T2WI, T2-FLAIR; (2) sagittal T2WI; (3) dual-echo oblique coronal plane of SE sequence with the vertical long axis of the hippocampus. The region of interest was selected as far as possible to avoid the influence of cerebrospinal fluid and skull base structures. FLAIR scan parameters were set: (1) repetition time 8,800 ms; (2) recovery time 95 ms; (3) slice thickness 3 mm; (4) interslice distance 0 mm; (5) matrix 512×512. SE scan parameters were set: (1) repetition time 3,000 ms; (2) recovery time 20 ms; (3) slice thickness 4 mm; (4) interslice distance 0 mm; (5) matrix 512×512. T2 relaxation diagram was calculated for each slice using T2 relaxation diagram, and hippocampal HCT2 were measured. The measured area did not encase the border of the hippocampal region, cystic areas, and cerebrospinal fluid in a hippocampal fissure.

2.3. Detection of Peripheral Blood T Lymphocyte Subsets. In 5 mL of fasting venous blood was collected and anticoagulated with ethylenediaminetetraacetic acid, and TLE patients were seizure free for 72 hours before blood collection. Patients with TLE had no seizures within 72 hours before blood sampling. Fluorescence staining agent was added to label CD^3, CD^4, and CD^8 molecules on the lymphocyte surface; 100 μL anticoagulation was added and mixed well; it was incubated in the dark at room temperature for 15 min. 2 mL FACSLysing solution was added; it was incubated in the dark at room temperature for 10 min; it was centrifuged at 300 rpm for 5 min. After discarding the supernatant, the cells were washed with phosphate buffer, and CD^3+, CD^4+, CD^8+, and CD^4+/CD^8+ of peripheral blood T lymphocyte subsets were detected using a flow cytometer.

2.4. Detection of Inflammatory Cytokines in Peripheral Blood. 5 mL of fasting venous blood was collected from both groups of study subjects, and serum was separated and stored in a $-80°C$ freezer. The serum levels of TNF-α, IL-1β, IL-2, IL-6, IL-10, and ICAM-1 were measured by an ELISA detection kit (Shanghai mlbio). The antibody coating of the microtiter plate was performed, the standards were diluted in turn and mixed with serum, and the reaction was performed at 37°C for 1.5 h after sealing; 100 μL of TNF-α, IL-1β, IL-2, IL-6, IL-10, and ICAM-1 antibody working solutions were added, respectively, and the reaction was performed at 37°C for 1 h after sealing; after washing the microtiter plate with buffer, 100 μL of diluted ABC working solution was added, and the reaction was performed at 37°C for 30 min after sealing; after washing the microtiter plate with buffer, 90 μL of TMB chromogenic solution was added, and the reaction was

performed in the dark at 37°C for 20 min after sealing; 100 μL of stop solution was added, and the O.D. value of each well was measured using a microplate reader.

2.5. Detection of miRNAs in Peripheral Blood.

An additional 5 mL of fasting venous blood was collected and serum was separated and stored in a −80°C freezer. Serum/plasma miRNA extraction and isolation kit was used for the extraction and reverse transcription of miRNAs in serum, and the cDNA obtained by reverse transcription was used as a template for subsequent PCR detection. Quantitative detection of miR-146a, miR-210, miR-221, miR-34a, miR-135b, and miR-33 were performed using the miRcute enhanced miRNA SYBR Green fluorescence quantitative detection kit.

2.6. Statistical Analysis.

Statistical analysis of the experimental data was performed using SPSS 19.0 software. Enumeration data were expressed as frequency (percentage), and differences were compared using the chi-square test. Measurement data were expressed as mean ± SD, and differences were compared using an independent sample t-test. Differences were considered statistically significant at $P < 0.05$.

3. Results

3.1. Comparison of General Data.

The differences in the basic data of patients in the epilepsy and control groups were compared. There was no significant difference in sex ratio, age, BMI, history of diabetes, and history of hypertension between the epilepsy and control groups ($P > 0.05$) (Table 1).

3.2. Analysis of Brain MRI Characteristics.

Brain MRI images of a 43-year-old male patient with TLE were analyzed. The patient's right hippocampus was significantly reduced in size and increased in signal (Figure 1).

The difference between HCT2 values in the patient's hippocampus was subsequently measured by SE sequence dual-echo oblique coronal plane (Figure 2). The right HCT2 values were (85.6 ± 2.4) ms and (92.3 ± 1.8) ms, the left HCT2 values were (86.1 ± 1.2) ms and (92.7 ± 2.0) ms, and the right/left HCT2 ratios were (0.97 ± 0.12) and (1.02 ± 0.20) in the control and epileptic groups, respectively. Compared with the control group, HCT2 values in the right and left hippocampus were significantly increased in the epileptic group ($P < 0.05$); however, there was no difference in the right/left HCT2 ratio ($P > 0.05$).

3.3. Changes of Peripheral Blood T Lymphocyte Subsets Levels.

The differences in the levels of CD^{3+}, CD^{4+}, CD^{8+}, and CD^{4+}/CD^{8+} of peripheral blood T lymphocyte subsets between the two groups were compared (Figure 3). Peripheral blood CD^{3+} was (73.4 ± 3.1)% and (77.9 ± 4.4)%, CD^{4+} was (41.5 ± 2.7)% and (45.6 ± 2.2)%, CD^{8+} was (25.7 ± 1.5)% and (22.1 ± 1.9)%, and CD^{4+}/CD^{8+} was (1.61 ± 0.10) and (2.24 ± 0.22) in the control and epileptic groups, respectively.

Compared with the control group, the levels of CD^{3+}, CD^{4+}, and CD^{4+}/CD^{8+} in the peripheral blood of patients in the epilepsy group were significantly increased, while the level of CD^{8+} in the epilepsy group was significantly decreased ($P > 0.05$).

3.4. Changes of Inflammatory Cytokine Levels in Peripheral Blood.

The differences in the levels of inflammatory cytokines TNF-α, IL-1β, IL-2, IL-6, IL-10, and ICAM-1 in peripheral blood between the two groups were compared. It can be observed that the peripheral blood TNF-α levels were (0.97 ± 0.11) pg/mL and (2.63 ± 0.26) pg/mL, IL-1β levels were (1.70 ± 0.33) pg/mL and (4.61 ± 0.57) pg/mL, IL-2 levels were (0.83 ± 0.15) pg/mL and (1.59 ± 0.21) pg/mL, IL-6 levels were (1.01 ± 0.14) pg/mL and (2.28 ± 0.19) pg/mL, IL-10 levels were (1.31 ± 0.14) pg/mL and (0.25 ± 0.09) pg/mL, and ICAM-1 levels were (1.03 ± 0.22) pg/mL and (1.89 ± 0.30) pg/mL in the control and epileptic groups, respectively. Compared with the control group, the levels of inflammatory cytokines TNF-α, IL-1β, IL-2, IL-6, and ICAM-1 in peripheral blood of patients in the epilepsy group were significantly increased, while IL-10 in the epilepsy group was significantly decreased ($P < 0.05$) (Figure 4).

3.5. Changes in Peripheral Blood miRNAs Levels.

The differences in peripheral blood miR-146a, miR-210, miR-221, miR-34a, miR-135b, and miR-33 levels between the two groups were compared. The peripheral blood miR-146a levels were (1.00 ± 0.13) and (2.14 ± 0.28), miR-210 levels were (1.00 ± 0.15) and (1.89 ± 0.31), miR-221 levels were (1.00 ± 0.20) and (2.44 ± 0.35), miR-34a levels were (1.00 ± 0.18) and (1.59 ± 0.13), miR-135b levels were (1.00 ± 0.31) and (0.17 ± 0.16), and miR-33 levels were (1.00 ± 0.22) and (0.26 ± 0.09) in the control and epileptic groups, respectively. Compared with the control group, the levels of miR-146a, miR-210, miR-221, and miR-34a in the peripheral blood of patients in the epilepsy group were significantly increased, while the levels of miR-135b and miR-33 in the epilepsy group were significantly decreased ($P < 0.05$) (Figure 5).

4. Discussion

Epilepsy is one of the very common diseases in neurology, which has paroxysmal, repetitive, and transient characteristics, but the pathogenesis of this disease is not clear at present [13]. The characteristics of the brain in patients with TLE were analyzed using MRI techniques, and it was found that the patients developed significant hippocampal atrophic lesions, and HCT2 in the bilateral hippocampus was significantly increased. Studies have confirmed that there is a close relationship between hippocampal atrophy and neuronal loss and gliosis [14]. Increased HCT2 values may be due to pathological basis such as neuronal loss and proliferation of glial cells in the hippocampus of TLE patients [15]. In addition, evidence shows that peripheral blood T lymphocytes are involved in the process of epilepsy, especially TLE with hippocampal sclerosis [16]. The results

TABLE 1: Comparison of general data of patients.

Item	Epilepsy group ($n = 30$)	Control group ($n = 30$)	Statistical value	P
Gender [n (%)]			$\chi^2 = 0.192$	0.513
Male	19 (63.3)	18 (60.0)		
Female	11 (36.7)	12 (40.0)		
Age (years)	55.9 ± 4.6	56.1 ± 3.8	$t = 0.319$	0.440
BMI (kg/m^2)	23.4 ± 3.1	23.7 ± 2.2	$t = 0.233$	0.561
History of diabetes [n (%)]			$\chi^2 = 0.207$	0.352
Yes	21 (70.0)	22 (73.3)		
No	9 (30.0)	8 (26.7)		
History of hypertension [n (%)]			$\chi^2 = 0.188$	0.303
Yes	12 (40.0)	13 (43.3)		
No	18 (60.0)	17 (56.7)		

(a)   (b)   (c)
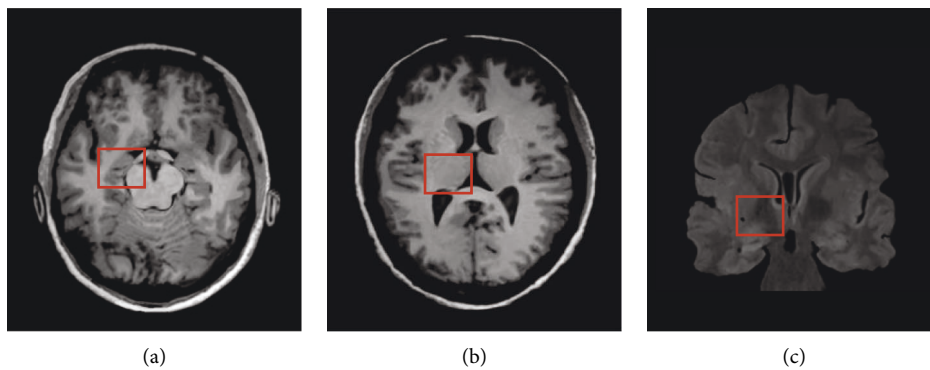
FIGURE 1: MRI image of patient. (a) axial T1WI; (b) axial T2WI; (c) coronal T2-FLAIR; red box: lesion.

(a)   (b)   (c)
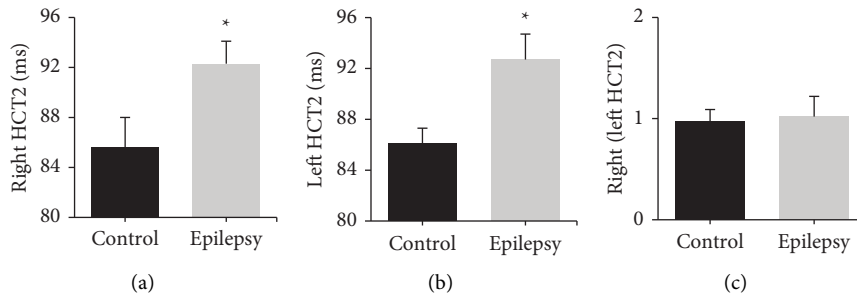
FIGURE 2: Comparison of hippocampal HCT2 values in patients. (a) right HCT2 value; (b) left HCT2 value; (c) right/left HCT2 ratio. *Compared with control group, $P < 0.05$.

(a)   (b)   (c)   (d)
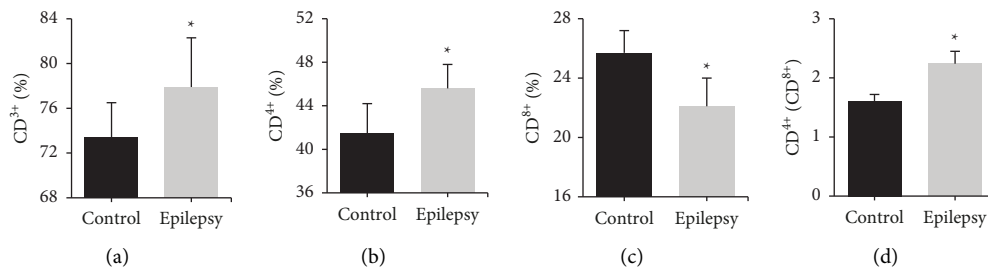
FIGURE 3: Comparison of peripheral blood T lymphocyte subsets levels in patients. (a) CD^{3+} level; (b) CD^{4+} level; (c) CD^{8+} level; (D) CD^{4+}/CD^{8+} ratio; *Compared with the control group, $P < 0.05$.
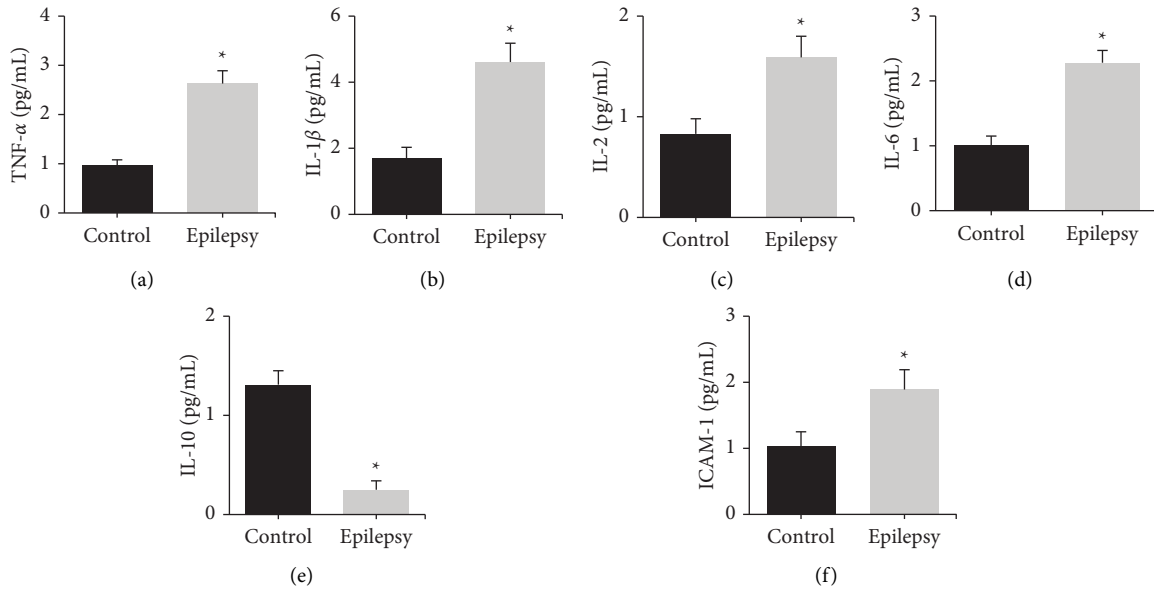
FIGURE 4: Comparison of peripheral blood inflammatory cytokine levels in patients. (a) TNF-α level; (b) IL-1β level; (c) IL-2 level; (d) IL-6 level; (e) IL-10 level; (f) ICAM-1 level. *Compared with the control group, $P < 0.05$.
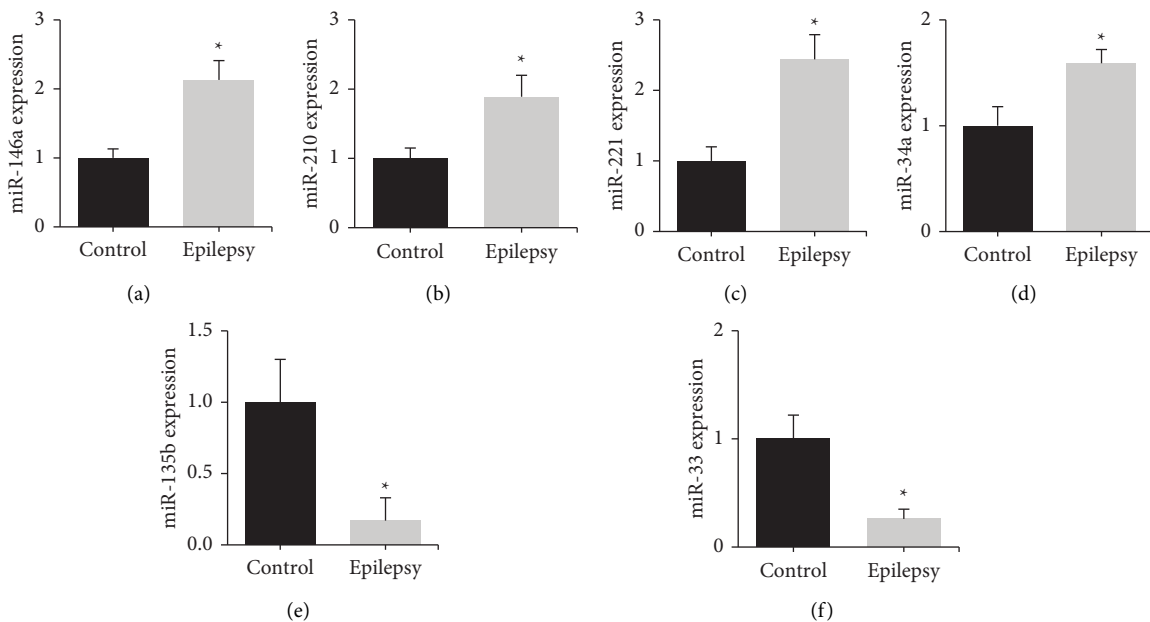
FIGURE 5: Comparison of peripheral blood miRNAs levels in patients. (a) miR-146a level; (b) miR-210 level; (c) miR-221 level; (d) miR-34a level; (e) miR-135b level; (f) miR-33 level. *Compared with control group, $P < 0.05$.

showed that the proportion of CD^{3+} and CD^{4+} cells in peripheral blood T lymphocyte subsets was significantly increased, while the proportion of CD^{8+} cells was significantly decreased in TLE patients compared with normal subjects. Pitsch et al. [17] concluded that CD^{8+} T lymphocytes can specifically target the expression of OVA and cause apoptotic neurodegeneration, astrogliosis, and microglial activation, and maybe the cause of hippocampal sclerosis with TLE after marginal encephalitis. This suggests that the level of T lymphocyte subsets in the peripheral blood

of TLE patients is found to be disturbed, which may be related to abnormal structural changes such as hippocampal atrophy.

TNF-α belongs to a class of inflammatory cytokines with multiple biological effects, which can induce epileptic discharges by stimulating glutamate and then affecting hippocampal CA3 pyramidal cells in the central nervous system, inhibiting the postsynaptic potential activity of nerve, and leading to epileptic discharge [18]. The results showed that the levels of TNF-α, IL-1β, IL-2, IL-6, and ICAM-1 in the

peripheral blood of TLE patients were significantly increased, while the level of IL-10 was significantly decreased. Yang et al. [19] detected the changes of TNF-α and IL-6 levels in peripheral blood of children with epilepsy and found that the levels of TNF-α and IL-6 in T lymphocytes were significantly increased in the child. Liu et al. [20] detected the changes of serum inflammatory markers IL-2, IL-6, and hs-CRP levels in children with epilepsy and found that the serum levels of IL-2, IL-6, and hs-CRP in children were significantly increased, while sodium valproate combined with levetiracetam treatment could reduce the levels of these markers. Leo et al. [21] demonstrated that anti-IL-6R antibodies were effective in reducing the number of absence seizures and depression-like behavior in a rat model of convulsive epilepsy, and they concluded that IL-6 plays an important role in seizure induction and seizure process. Basnyat et al. [22] demonstrated that serum levels of IL-10 were significantly lower in patients with refractory TLE and that IL-10 levels showed a negative relationship with the course of epilepsy. The above-given results suggest that inflammatory mediators are involved in the process of TLE disease, which may be involved in the regulation of epileptogenesis through processes such as activation of glial cells, changes in gene expression levels, and neuronal loss.

Studies have confirmed that miRNAs have a close relationship with the function of the nervous system. MiR-146a and miR-221 are miRNAs that regulate the generation of inflammatory factors [23]. In response to IL-1β stimulation, miR-146a and miR-221 are upregulated and can promote the expression of downstream multiple classes of inflammatory factors as well as adhesion factors. MiR-34a belongs to miRNA that regulate the expression of apoptotic factors [24]. The results showed that miR-126a, miR-221, and miR-34a were up-regulated in the peripheral blood of TLE patients. These results suggest that miRNAs can participate in the process of TLE by regulating the release of inflammatory factors and the expression of apoptotic factors. In addition, the expression levels of miR-210, miR-135b, and miR-33 in peripheral blood of TLE patients were further detected. Chen et al. [25] confirmed that miR-210 showed a high expression level in the hippocampus of epileptic animal models, while inhibition of miR-210 expression was able to inhibit seizure-induced apoptosis. Li et al. [26] showed that miR-135b-5p expression levels were significantly lower in children with TLE, and overexpression of miR-135b-5p was able to target SIRT1 to reduce apoptosis after epilepsy. Hu et al. [27] explored the expression profile of miRNAs in TLE rats, and miRNA microarray revealed 9 up-regulated miRNAs such as miR-146a and mR-210 and 15 down-regulated miRNAs such as miR-135b and miR-33. This is consistent with the results that miR-210 expression was up-regulated and miR-135b and miR-33 expression was down-regulated in peripheral blood of TLE patients.

5. Conclusion

TLE patients are usually accompanied by pathological changes in the hippocampal formation, and peripheral blood T lymphocyte subsets disorders, the release of inflammatory cytokines, and regulation of miRNAs expression are involved in seizures and neuronal damage. The changes of MRI image characteristics and serum biological indicators in patients with TLE were detected, and the correlation between MRI image characteristics and serum biological indicators was not deeply explored. Peripheral blood samples were collected from patients to detect the expression levels of various indicators. In subsequent studies, tissue or cerebrospinal fluid samples will be collected for analysis of changes in lymphocytes, cytokines, and miRNAs, and their mechanism of action on the degree of neurons will be analyzed. In conclusion, patients with TLE have hippocampal lesions, which may be associated with imbalances in peripheral blood T lymphocyte subsets, chronic inflammatory responses, and abnormal miRNA expression. The results can provide experimental materials for understanding the pathogenesis of TLE, as well as the search for therapeutic targets.

Data Availability

The data used to support the findings of this study are available from the corresponding author upon request.

Conflicts of Interest

The authors declare that there are no conflicts of interest.

References

[1] E. Beghi, G. Giussani, and J. W. Sander, "The natural history and prognosis of epilepsy," *Epileptic Disorders*, vol. 17, no. 3, pp. 243–253, 2015.

[2] J. Falco-Walter, "Epilepsy-definition, classification, pathophysiology, and epidemiology," *Seminars in Neurology*, vol. 40, no. 6, pp. 617–623, 2020.

[3] K. L. Gawelek, J. M. Gales, and R. A. Prayson, "Hamartia in hippocampal sclerosis-associated mesial temporal lobe epilepsy," *Annals of Diagnostic Pathology*, vol. 32, pp. 63–66, 2018.

[4] F. M. Noé and N. Marchi, "Central nervous system lymphatic unit, immunity, and epilepsy: is there a link?" *Epilepsia Open*, vol. 4, no. 1, pp. 30–39, 2019.

[5] S. Koh, N. Dupuis, and S. Auvin, "Ketogenic diet and neuroinflammation," *Epilepsy Research*, vol. 167, Article ID 106454, 2020.

[6] D. Pan, X. Li, J. Jiang, and L. Luo, "Effect of levetiracetam in combination with topiramate on immune function, cognitive function, and neuronal nutritional status of children with intractable epilepsy," *American Journal of Translational Research*, vol. 13, no. 9, pp. 10459–10468, 2021.

[7] M. K. M. Alvim, M. E. Morita-Sherman, C. L. Yasuda et al., "Inflammatory and neurotrophic factor plasma levels are related to epilepsy independently of etiology," *Epilepsia*, vol. 62, no. 10, pp. 2385–2394, 2021.

[8] J. Baloun, P. Bencurova, T. Totkova et al., "Epilepsy miRNA profile depends on the age of onset in humans and rats," *Frontiers in Neuroscience*, vol. 14, p. 924, 2020.

[9] J. Engel Jr., "Evolution of concepts in epilepsy surgery," *Epileptic Disorders*, vol. 21, no. 5, pp. 391–409, 2019.

[10] G. Fernandez-Baca Vaca and J. T. Park, "Focal EEG abnormalities and focal ictal semiology in generalized epilepsy," *Seizure*, vol. 77, pp. 7–14, 2020.

[11] J. Shawarba, B. Kaspar, S. Rampp et al., "Advantages of magnetoencephalography, neuronavigation and intraoperative MRI in epilepsy surgery re-operations," *Neurological Research*, vol. 43, no. 6, pp. 434–439, 2021.

[12] J. Zelano, J. Klecki, J. Christensen, T. Tomson, K. Malmgren, and ESBACE consortium Collaborators, "The provision of epilepsy care across Europe 2017: a 17-year follow-up survey," *Epilepsia Open*, vol. 4, no. 1, pp. 144–152, 2019.

[13] W. Löscher, H. Potschka, S. M. Sisodiya, and A. Vezzani, "Drug resistance in epilepsy: clinical impact, potential mechanisms, and new innovative treatment options," *Pharmacological Reviews*, vol. 72, no. 3, pp. 606–638, 2020.

[14] P. M. Gonçalves Pereira, E. Oliveira, and P. Rosado, "Apparent diffusion coefficient mapping of the hippocampus and the amygdala in pharmaco-resistant temporal lobe epilepsy," *AJNR American Journal of Neuroradiology*, vol. 27, no. 3, pp. 671–683, 2006.

[15] W. Van Paesschen, T. Revesz, J. S. Duncan, M. D. King, and A. Connelly, "Quantitative neuropathology and quantitative magnetic resonance imaging of the hippocampus in temporal lobe epilepsy," *Annals of Neurology*, vol. 42, no. 5, pp. 756–766, 1997.

[16] H. Nakahara, Y. Konishi, T. G Beach, N. Yamada, S. Makino, and I. Tooyama, "Infiltration of T lymphocytes and expression of icam-1 in the hippocampus of patients with hippocampal sclerosis," *Acta Histochemica et Cytochemica*, vol. 43, no. 6, pp. 157–162, 2010.

[17] J. Pitsch, K. M. J. Loo, M. Gallus et al., "CD8+ T-lymphocyte-driven limbic encephalitis results in temporal lobe epilepsy," *Annals of Neurology*, vol. 89, no. 4, pp. 666–685, 2021.

[18] T. Kamaşak, B. Dilber, S. Ö. Yaman et al., "HMGB-1, TLR4, IL-1R1, TNF-α, and IL-1β: novel epilepsy markers?" *Epileptic Disorders*, vol. 22, no. 2, pp. 183–193, 2020.

[19] J. Yang, C. Hu, and X. Jiang, "Activation of peripheral T lymphocytes in children with epilepsy and production of cytokines," *Xi Bao Yu Fen Zi Mian Yi Xue Za Zhi*, vol. 32, no. 9, pp. 1234–1237, 2016.

[20] Z. Liu, J. Li, F. Yang et al., "Sodium valproate combined with levetiracetam in pediatric epilepsy and its influence on NSE, IL-6, hs-CRP and electroencephalogram improvement," *Experimental and Therapeutic Medicine*, vol. 20, no. 3, pp. 2043–2048, 2020.

[21] A. Leo, V. Nesci, M. Tallarico et al., "IL-6 receptor blockade by tocilizumab has anti-absence and anti-epileptogenic effects in the WAG/rij rat model of absence epilepsy," *Neurotherapeutics*, vol. 17, no. 4, pp. 2004–2014, 2020.

[22] P. Basnyat, M. Pesu, M. Söderqvist et al., "Chronically reduced IL-10 plasma levels are associated with hippocampal sclerosis in temporal lobe epilepsy patients," *BMC Neurology*, vol. 20, no. 1, p. 241, 2020.

[23] Y. L. Su, X. Wang, M. Mann et al., "Myeloid cell-targeted miR-146a mimic inhibits NF-κB-driven inflammation and leukemia progression in vivo," *Blood*, vol. 135, no. 3, pp. 167–180, 2020.

[24] J. H. Li, J. Dai, B. Han, G. H. Wu, and C. H. Wang, "MiR-34a regulates cell apoptosis after myocardial infarction in rats through the Wnt/β-catenin signaling pathway," *European Review for Medical and Pharmacological Sciences*, vol. 23, no. 6, pp. 2555–2562, 2019.

[25] L. Chen, H. Zheng, and S. Zhang, "Involvement of upregulation of miR-210 in a rat epilepsy model," *Neuropsychiatric Disease and Treatment*, vol. 12, pp. 1731–1737, 2016.

[26] R. Li, J. Hu, and S. Cao, "The clinical significance of miR-135b-5p and its role in the proliferation and apoptosis of hippocampus neurons in children with temporal lobe epilepsy," *Developmental Neuroscience*, vol. 42, no. 5-6, pp. 187–194, 2020.

[27] K. Hu, Y. Y. Xie, C. Zhang et al., "MicroRNA expression profile of the hippocampus in a rat model of temporal lobe epilepsy and miR-34a-targeted neuroprotection against hippocampal neurone cell apoptosis post-status epilepticus," *BMC Neuroscience*, vol. 13, p. 115, 2012.

WILEY | Hindawi

Research Article

Efficacy Evaluation of Modified Siwu Decoction to Treat Osteoporosis in Patients with Poststroke Hemiplegia by Using the Magnetic Resonance Imaging Features

Jing Wang,[1] Xiuyun Liu,[1] Yanni Chen,[2] Bingjie Zhang,[1] Yi Peng,[3] Zhipeng Sun,[4] and Tao Yang [ID][5]

[1]*Department of Rehabilitation, The First Hospital of Zhangjiakou, Zhangjiakou 075000, Hebei, China*
[2]*Department of Research, The First Hospital of Zhangjiakou, Zhangjiakou 075000, Hebei, China*
[3]*Department of Endocrinology, The First Hospital of Zhangjiakou, Zhangjiakou 075000, Hebei, China*
[4]*Department of Medical Imaging, The First Hospital of Zhangjiakou, Zhangjiakou 075000, Hebei, China*
[5]*Department of Traditional Chinese Medicine, The First Hospital of Zhangjiakou, Zhangjiakou 075000, Hebei, China*

Correspondence should be addressed to Tao Yang; 14221010817@stu.cpu.edu.cn

This study was focused on the clinical efficacy and safety of magnetic resonance imaging (MRI)-based Siwu decoction for poststroke hemiplegia complicated with osteoporosis. 120 patients with poststroke hemiplegia and osteoporosis were divided into an observation group (modified Siwu decoction based on the treatment scheme of control group, 60 cases) and a control group (conventional drugs in neurology + neurology-based rehabilitation training treatment of muscle enhancement surgery, 60 cases). They all underwent MRI scans. The results showed that the bone mineral density (BMD) of lumbar spine, ipsilateral femoral neck, and ipsilateral patella in the observation group was higher than that in the control group 180 days after treatment ($P < 0.05$). MRI showed restricted diffusion and edema in the left frontoparietal cortex and subcortical white matter. The levels of 25-hydroxy-vitamin D (25-OH-VD) and bone gla-containing protein (BGP) in the observation group 180 days after treatment were higher, and the type I collagen n-terminal propeptide (PINP) and type I collagen cross-linked C-terminal telopeptide (β-CTX) were lower ($P < 0.05$). The visual analogue scale (VAS) score of the observation group at 180 days after treatment was lower, while the quality of life score was higher ($P < 0.05$). The median cell count in the observation group at 180 days after treatment was less, while the lymphocytes showed a higher level ($P < 0.05$). In conclusion, the Siwu decoction could effectively improve the bone metabolism of patients with poststroke hemiplegia and osteoporosis, promote the proliferation and differentiation of osteocytes, and improve the BMD and quality of life of patients.

1. Introduction

Stroke, also known as cerebrovascular accident, is a local brain dysfunction caused by acute cerebrovascular disease. Its clinical symptoms persist for more than 24 hours and are characterized by high morbidity, mortality, disability, and recurrence [1, 2]. Stroke is common in people aged 50 and older, and clinically manifests as symptoms and signs of transient or permanent brain dysfunction. It usually manifests as sudden weakness, clumsiness, heaviness, or numbness on one side of the limbs, numbness on one side of the face or skewed corners of the mouth, slurred speech accompanied by disturbance of consciousness or convulsions, etc. [3, 4]. It ranks first in the cause of death of urban residents [5]. The most serious consequence of cerebral stroke is hemiplegia, which will lead to long-term bed rest, greatly reduce the amount of exercise, and disrupt the balance of bone resorption and bone formation in the human body, which is prone to disuse osteoporosis [6, 7]. Disuse osteoporosis caused by poststroke hemiplegia is a type of secondary

osteoporosis. If not treated in time, it will cause more pain to patients and cause a series of complications such as kidney stones, pathological fractures, and heterotopic ossification [8].

The clinical treatment principles for patients with disuse osteoporosis are to increase calcium intake, reduce calcium excretion, guide the deposition of calcium salts at the target site, and improve bone strength. Common treatment options include surgery, physical therapy, and drug therapy [9, 10]. The use of internal fixation can better help patients to get out of bed as soon as possible and avoid the aggravation of osteoporosis caused by long-term bed rest, but the effectiveness is not high [11]. Guiding patients to perform appropriate physiological exercise can stimulate the increase of bone mass, reduce the fracture rate, and improve the body's agility. Physical therapy includes ultraviolet therapy, high-frequency electrotherapy, and specific frequency vibration stimulation to promote bone growth in patients [12]. In terms of drug treatment, bone resorption and bone metabolism balance can be improved by supplementing calcium and other drugs, such as calcium gluconate, calcigard, alfacalcidol, sodium alendronate, calcitonin, and compound estrogen [13]. Siwu Decoction is a classic traditional Chinese medicine (TCM) for nourishing and nourishing blood. It is composed of four herbs: angelica sinensis, ligusticum wallichii, rehmannia glutinosa, and radix paeoniae alba. It is mainly used for the treatment of Chong-Ren deficiency, irregular menstrual flow, umbilical-abdominal pain, metrorrhagia, and fetal uneasiness during pregnancy [14].

With the development of imaging technology, clinical imaging examinations are often used to evaluate disuse osteoporosis caused by post-stroke hemiplegia, including X-ray films, quantitative ultrasound, quantitative computed tomography (CT), and magnetic resonance imaging (MRI) [15–17]. X-ray films can clearly show the osteoporosis in patients with advanced disuse osteoporosis (at least 30% of bone mass has been lost), which is simple, easy to operate, and low in cost, but has little significance for the diagnosis of early osteoporosis. Quantitative ultrasound can clearly display the mechanical strength, bone mineral density (BMD), and elastic structure of patients' bones. It is an economical, simple, and non-radioactive detection method, but there is a certain rate of missed diagnosis and misdiagnosis. Quantitative CT can detect changes in bone mineral content in patients early by measuring cortical bone and cancellous bone, so as to predict the degree of the patient's disease. As a new non-invasive imaging technology, MRI is widely used in clinical medical disease assessment, and has the advantages of high resolution, multi-parameter, and high accuracy. The manifestations of osteoporosis on MRI images are usually marked xanthosis of the vertebral body, and high signal intensity on T1-weighted and T2-weighted images. When a fracture occurs, the edema in the vertebral body shows long T1 and long T2 signals, and the edema signal is not good in the background of high signal intensity on T2 weighted imaging (T2WI) of osteoporosis [18].

To sum up, post-stroke hemiplegia and osteoporosis will have a very serious impact on patients, and even life-threatening if not treated early. 120 patients with post-stroke hemiplegia complicated with osteoporosis random were divided into observation group and control group, and all underwent MRI imaging scans. It compared the X-ray measurement indicators, bone metabolism indicators, visual analog pain score, and clinical efficacy of the two groups of patients to deeply understand the clinical efficacy and safety of the modified Siwu Decoction treatment on post-stroke hemiplegia patients with osteoporosis.

2. Materials and Methods

2.1. Research Objects. A total of 120 patients with post-stroke hemiplegia and osteoporosis who were treated in our hospital from October 2020 to May 2022 were selected as the research objects. The informed consents are obtained from all patients and their families and this study was approved by ethics committee of hospital.

2.1.1. Inclusion Criteria. (i) Patients with symptoms of hemiplegia on one limb; (ii) Patients with Fug1-Meyer motor function score of the hemiplegic limb less than 50; (iii) patients with stable vital signs within two days; (iv) patients with good nutritional status; and (v) patients who were conscious and able to cooperate with treatment.

2.1.2. Exclusion Criteria. (i) Patients with Glasgow coma scale (GCS) less than 8 points; (ii) patients who had received thrombolytic therapy; (iii) patients with limb hemiplegia caused by other factors; (iv) patients with severe heart, lung, kidney, and other major organ insufficiency; (v) patients with hemiplegia in all four limbs; and (vi) patients who had used glucocorticoids and immunosuppressants.

2.2. Treatment Schemes. The patients were randomly divided into 60 cases in the observation group and 60 cases in the control group. The patients in control group received conventional drug therapy in neurology and rehabilitation training based on neuromuscular stimulation. It mainly included rhythmic initiation, compound isotonic exercise, repetitive contraction technique, hold-relax technique, and hold-relax-active movement. Each treatment time was generally 1 hour, 2 times a day, and 5 days a week. The patients in observation group were given modified Siwu Decoction on the basis of treatment scheme of the control group. Recipe was as follows: angelica sinensis 10 g, ligusticum wallichii 10 g, peach kernel 10 g, rhizoma zingiberis preparata 10 g, astragalus membranaceus 30 g, leonurus japonicus 15 g, radix rehmanniae recens 15 g, rehmannia glutinosa 15 g, radix paeoniae rubra 15 g, radix paeoniae alba 15 g, radix angelicae 10 g, teasel 30 g, rubia cordifolia 15 g, honeysuckle rattan 20 g, and white flower patrinia 15 g. It should be taken with decoction in water, 1 dose per day, orally in 3 doses for 3 to 6 days.

2.3. MRI Scan. The MRI system was used. The patient was required to keep a supine position with the feet inside the coil. Scanning parameters were set as follows: the time of
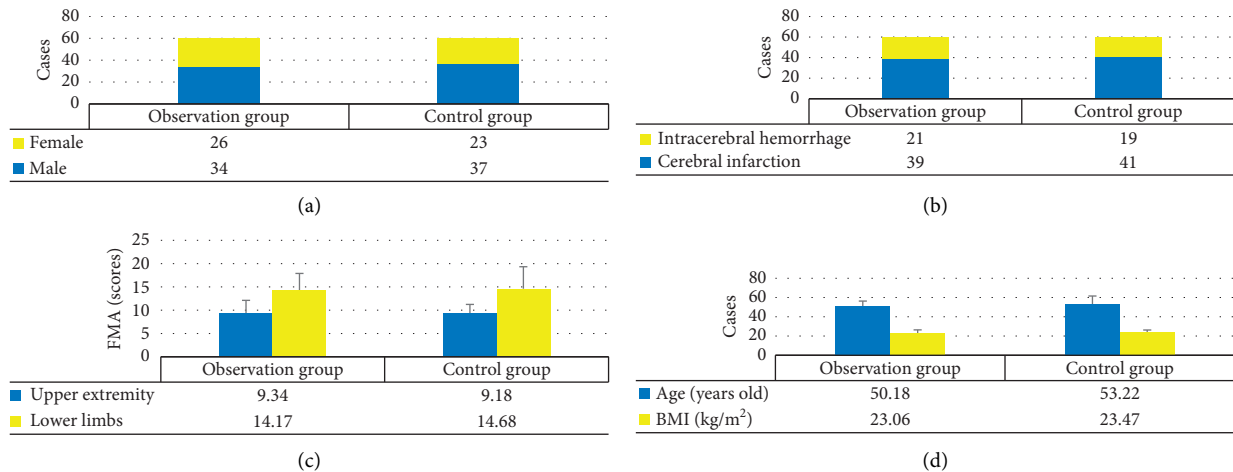
FIGURE 1: Comparison of general data between the two groups before treatment. (a)~(d) show the comparisons of gender, numbers of patients with cerebral infarction and cerebral hemorrhage, FMA score, and age and BMI, respectively.

echo (TE) = 4.65 ms, the time of repetition (TR) = 12.5 ms, layer thickness = 0.8 mm, layer spacing = 0.15 mm, matrix = 325×256, and flip angle = $30°$. On average, three images were collected per scan. The acquired images were sent to the workstation for processing.

2.4. Observation Indicators. The bone mineral density (BMD) of the lumbar spine, ipsilateral femoral neck, ipsilateral patella, and ipsilateral forearm was measured on the first day of admission, 60 days after treatment, and 180 days after treatment.

6 mL of fasting venous blood was collected in the morning on the 1st day after admission and 60th and 180th day after treatment and we coagulated it naturally at 25°C for 15 minutes. The blood samples were centrifuged at 3500 rpm for 20 minutes, and the supernatant was transferred to a 1 mL centrifuge tube and stored at low temperature.

Safety was observed by comparing the changes of blood routine, liver function (including alanine aminotransferase (ALT) and aspartate aminotransferase (AST)) and renal function (including serum creatinine (Scr) and urea) before and after treatment in the two groups.

The changes of bone metabolism indicators in the two groups of patients were measured, including 25-hydroxy-vitamin D (25-OH-VD), bone gla-containing protein (BGP), type I collagen n-terminal propeptide (PINP), and type I collagen cross-linked C-terminal telopeptide (β-CTX) levels.

The pain level of the patients was assessed using a visual analog scale (VAS). The World Health Organization Quality of Life Scale (WHOQOL-100) was adopted to evaluate patients' life treatment before and after treatment. According to the clinical symptoms, the clinical efficacy was evaluated and divided into markedly effective (clinical symptoms and signs completely disappeared), effective (clinical symptoms and signs were alleviated), and ineffective (clinical symptoms and signs did not improve or worsened). In addition, the effective rate of treatment was calculated.

2.5. Statistical Methods. The data processing in this work was analyzed by SPSS 19.0 statistical software, the measurement data was expressed as mean ± standard deviation ($\overline{x} \pm s$), and the count data was expressed as percentage (%). Pairwise comparisons were made using one-way ANOVA. The difference was statistically significant at $P < 0.05$.

3. Results

3.1. Comparison of General Data of Two Groups. As shown in Figure 1, there was no significant difference in gender, number of patients with cerebral infarction, number of patients with cerebral hemorrhage, FMA score, age, and body mass index (BMI) between the observation group and the control group ($P > 0.05$).

3.2. Case Data. Figure 2 shows the brain MRI images of a 63-year-old female patient. Physical examination showed that the heart rate was 67 times/min, and the blood pressure was 208/156 mmHg. She was comatose with eyes open, unresponsive, cataracts on the right side of both pupils, 1.5 mm, 1 mm on the left, with presence of light reflexes. The low breath sounded in both lungs, no rales, low heart sounds, no murmurs, and soft abdomen. The right limb can move voluntarily, and the mobility was worse than that of the left. The right Pap's sign was positive and the left was negative.

3.3. Comparison of BMD. As shown in Figure 3, there was no significant difference in BMD of the lumbar spine, ipsilateral femoral neck, and ipsilateral patella between the two groups on the first day of admission and 60 days after treatment ($P > 0.05$). The BMD of the lumbar spine, ipsilateral femoral neck, and ipsilateral patella at 180 days after treatment in the two groups were significantly higher than those on the first day of admission, and the differences were statistically significant ($P < 0.05$). The BMD of
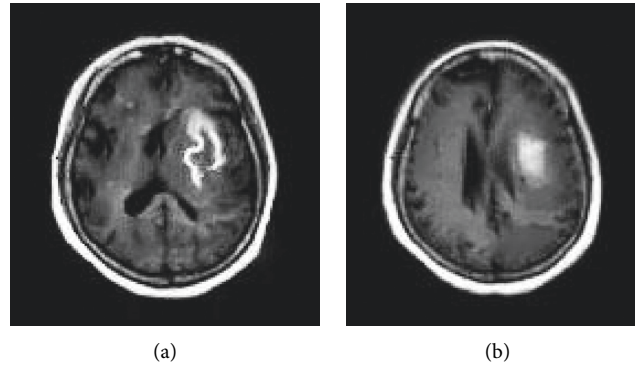
(a)   (b)

FIGURE 2: MRI image data of patient. (a) There were irregularly shaped near-oval high-density shadows in the left corona radiata-basal ganglia region; (b) there were long T1 isometric T2 signals inside the lesion in the left corona radiata-basal ganglia region.

lumbar spine, ipsilateral femoral neck, and ipsilateral patella in the observation group at 180 days after treatment were significantly higher in contrast to the BMD values in the control group, and the differences were statistically significant ($P < 0.05$). There was no significant difference in the BMD of the affected side forearm 180 days after treatment between the two groups ($P > 0.05$).

3.4. Comparison of Bone Metabolism Indicators. As illustrated in Figure 4, the levels of 25-OH-VD and BGP 180 days after treatment in the two groups were significantly higher than those on the first day of admission, while PINP and β-CTX were significantly lower than those on the first day of admission, and the differences were statistically significant ($P < 0.05$). The levels of 25-OH-VD and BGP in the observation group at 180 days after treatment were significantly higher than those in the control group, while PINP and β-CTX were significantly lower than those in the control group, and the differences were statistically significant ($P < 0.05$).

3.5. Comparison of Pain Scores. As shown in Figure 5, the VAS scores 180 days after treatment in the two groups were significantly lower than those on the first day of admission, and the difference was statistically significant ($P < 0.05$). The VAS score 180 days after treatment in the observation group (0.55 ± 0.14) was significantly lower than that in the control group (2.27 ± 0.49), and the difference was statistically significant ($P < 0.05$).

3.6. Comparison of Quality of Life Scores. As demonstrated in Figure 6, the quality of life scores of the two groups of patients 180 days after treatment were significantly higher than those on the first day of admission, and the difference was statistically significant ($P < 0.05$). The quality of life score 180 days after treatment in the observation group was significantly higher than that in the control group, and the difference was statistically significant ($P < 0.05$).

3.7. Comparison of Blood Routine Indexes. The median cell count of the two groups of patients 180 days after treatment was significantly lower than that on the first day of admission, while the level of lymphocytes was significantly higher than that on the first day of admission, and the difference was statistically significant ($P < 0.05$). The median cell count of the observation group at 180 days after treatment was significantly lower than that of the control group, while the level of lymphocytes was significantly higher than that of the control group, and the difference was statistically significant ($P < 0.05$). However, there was no significant difference in the erythrocyte volume and platelet count between the two groups on the first day of admission, 60 days after treatment, and 180 days after treatment ($P > 0.05$). The specific results are demonstrated in Figure 7.

3.8. Comparison of Clinical Efficacy. In Figure 8, we compared the clinical efficacy between two groups of patients. After treatment, 42 cases were markedly effective, 11 cases were effective, and 7 cases were ineffective in the observation group; in the control group, 27 cases were markedly effective, 20 cases were effective, and 13 cases were ineffective. It suggested that the total effective rate (88.33%) of the observation group was significantly higher than that of the control group (78.33%), and the difference was statistically significant ($P < 0.05$).

4. Discussion

Poststroke hemiplegia osteoporosis is a type of disuse osteoporosis. The main pathological mechanism is that, in the process of bone metabolism, there are problems in bone resorption and new bone formation, resulting in abnormal calcium and phosphorus metabolism in the human body, decreased BMD, and many clinical symptoms [19, 20]. Therefore, how to improve the bone metabolism pathway of the patient's body and improve the patient's BMD is the focus of current clinical treatment. This work used the random number table method to divide 120 patients with poststroke hemiplegia complicated with osteoporosis into 60 patients in the observation group (on the basis of the control group, they were given Siwu decoction) and 60 patients in

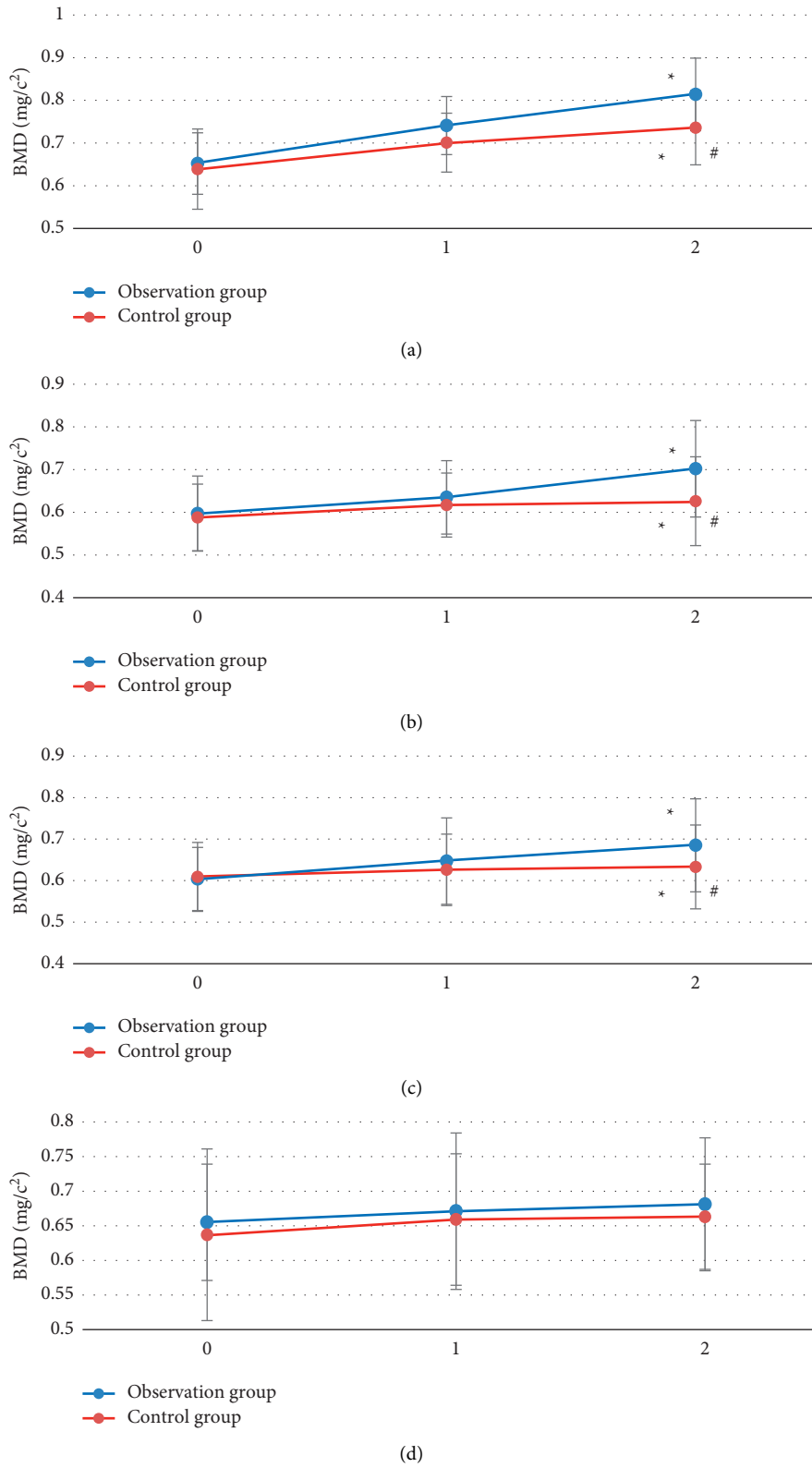FIGURE 3: Comparison of BMD before and after treatment in the two groups. (a) The BMD in the lumbar spine; (b) the BMD in ipsilateral femoral neck; (c) the BMD in ipsilateral patella; and (d) the BMD in affected forearm. 1–3 refer to the first day of admission, the 60th day after treatment, and the 180th day after treatment, respectively. *Compared with the first day of admission, $P < 0.05$; #compared with control group, $P < 0.05$.
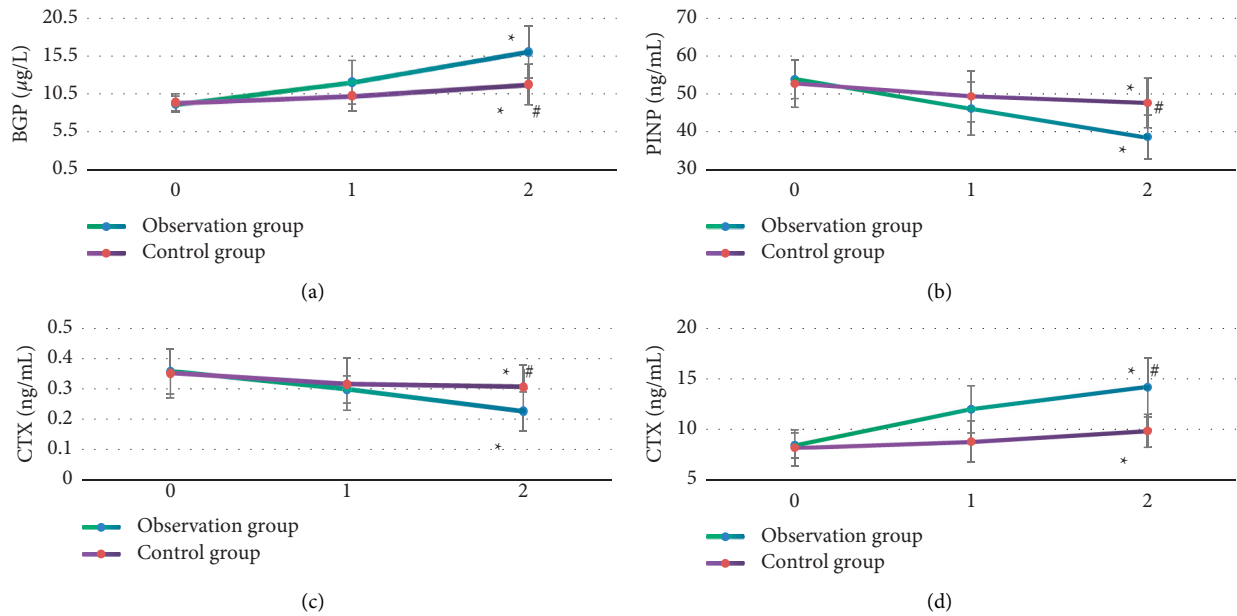
Figure 4: Comparison of bone metabolism indicators between the two groups before and after treatment. (a)~(d) show the comparisons of BGP, PINP, β-CTX, and 25-OH-VD, respectively. 1–3 refer to the first day of admission, the 60th day after treatment, and the 180th day after treatment, respectively. *Compared with the first day of admission, $P < 0.05$; #compared with control group, $P < 0.05$.
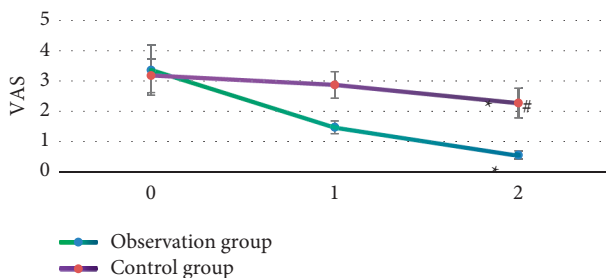
Figure 5: Comparison of pain scores in the two groups before and after treatment. 1–3 refer to the first day of admission, the 60th day after treatment, and the 180th day after treatment, respectively. *Compared with the first day of admission, $P < 0.05$; #compared with control group, $P < 0.05$.

Figure 6: Comparison of quality of life scores between the two groups before and after treatment. 1–3 refer to the first day of admission, the 60th day after treatment, and the 180th day after treatment, respectively. *Compared with the first day of admission, $P < 0.05$; #compared with control group, $P < 0.05$.
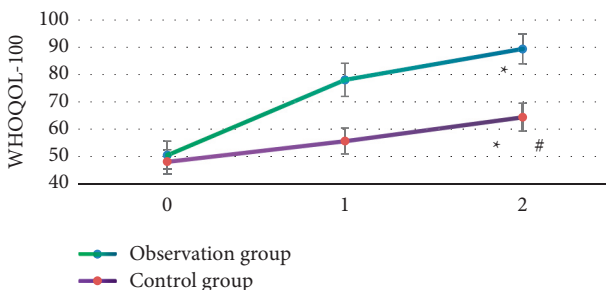
the control group (neural Internal medicine routine drug treatment and neuromuscular promotion-based rehabilitation training treatment), and all underwent MRI imaging scans. First, the basic data of the two groups of patients were compared, and it was found that there were no statistically significant differences in gender, number of patients with cerebral infarction, number of patients with cerebral hemorrhage, FMA score, age, and BMI between the observation group and the control group ($P > 0.05$). Such results ensure the feasibility of follow-up studies. From brain MRI images, patients with poststroke hemiplegia osteoporosis have limited diffusion and edema in the left frontoparietal cortex and subcortical white matter.

Then, the BMD changes of the two groups of patients before and after treatment were compared. It was found that the BMD values of the lumbar spine, ipsilateral femoral neck, and ipsilateral patella of the observation group at 180 days after treatment were significantly higher than those of the control group, showing statistically significant differences ($P < 0.05$). BMD can reflect the bone strength of patients and help physicians to detect the signs of osteoporosis more accurately. The results indicated that the Siwu Decoction formula can effectively improve the BMD of patients with poststroke hemiplegia osteoporosis, improve bone strength, and help patients recover more [21]. 25-OH-VD is the main form of vitamin D in the human body, which is mainly synthesized by human skin after ultraviolet radiation. A small portion of it comes from food or supplements and has an important role in the human skeleton. BGP is an active polypeptide synthesized and secreted by osteoblasts and plays an important role in regulating bone metabolism, and its level reflects osteoblast activity [22, 23]. In this work, the analysis of bone metabolism indicators showed that the 25-
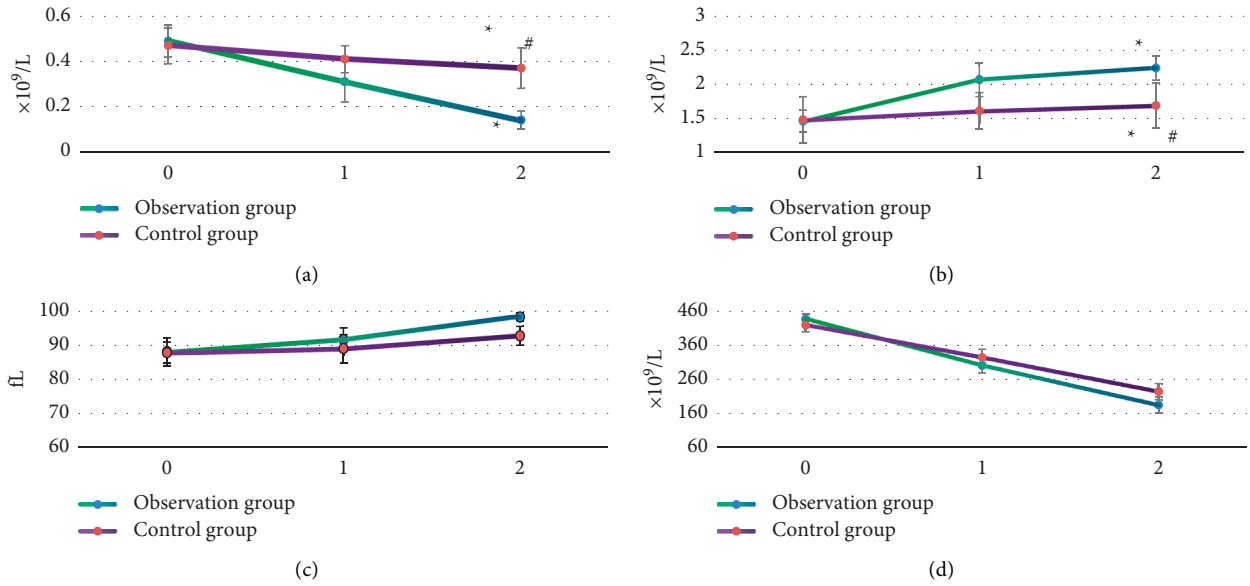
FIGURE 7: Comparison of blood routine indicators before and after treatment in two groups. (a)~(d) show the comparisons of median cell count, lymphocyte level, erythrocyte volume, and platelet count, respectively. 1–3 refer to the first day of admission, the 60th day after treatment, and the 180th day after treatment, respectively. *Compared with the first day of admission, $P > 0.05$; #compared with control group, $P < 0.05$.
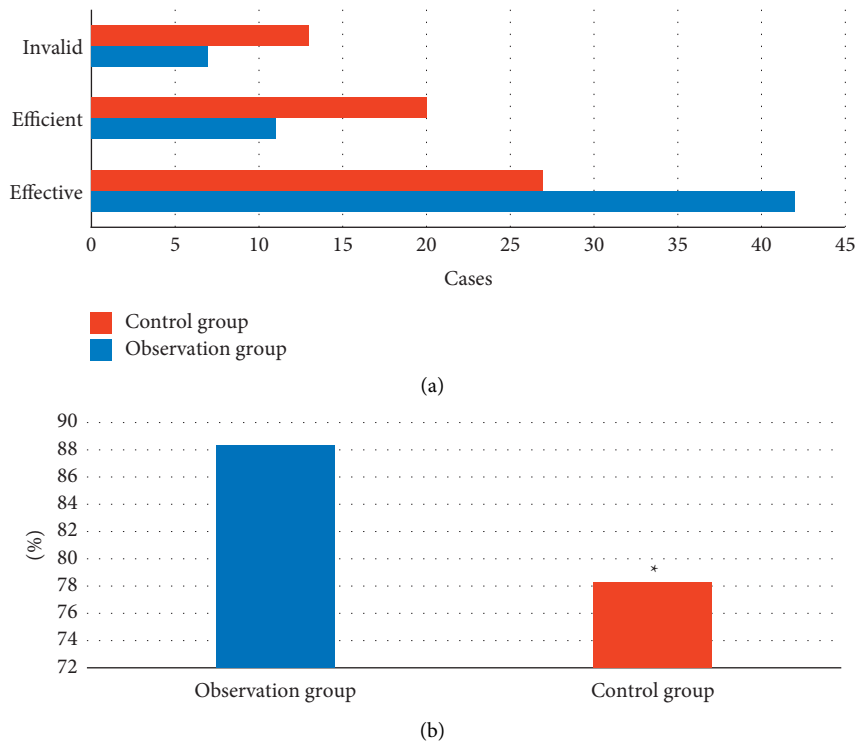
FIGURE 8: Comparison of clinical efficacy between the two groups. (a) The numbers of markedly effective, effective, and ineffective cases. (b) The total effective rate of treatment. *Compared with control group, $P < 0.05$.

OH-VD and BGP of the observation group were significantly higher than those of the control group at 180 days after treatment, with statistically significant differences ($P < 0.05$). This indicates that the Siwu decoction can treat poststroke hemiplegia osteoporosis patients by increasing

the levels of 25-OH-VD and BGP and improving bone metabolism. In addition, the PINP and β-CTX of the observation group 180 days after treatment were significantly lower than those of the control group, and the differences were statistically significant ($P < 0.05$). Such results are

similar to the results of He et al. [24]. The content of PINP in serum reflects the ability of osteoblasts to synthesize collagen and has high specificity and sensitivity in predicting the occurrence of osteoporosis, evaluating bone mass, and monitoring the efficacy of antiosteoporosis. The level of β-CTX reflects the bone resorption activity of osteoclasts and is an important biochemical marker of bone resorption, indicating that the Siwu decoction has a regulatory effect on bone metabolism and promotes the proliferation and differentiation of osteocytes and the efficiency of bone formation [25].

In addition, it was found that the VAS score of the observation group 180 days after treatment was significantly lower than that of the control group, and the difference was statistically significant ($P < 0.05$). This shows that the Siwu decoction not only has a significant clinical effect, but also can relieve the pain of patients with poststroke hemiplegia osteoporosis, so it is safe. The quality of life score 180 days after treatment in the observation group was significantly higher than that in the control group, showing statistically significant difference ($P < 0.05$). Such results are similar to the findings of Shapiro et al. [18]. This indicates that the Siwu decoction can effectively improve the quality of life and prognosis of patients with poststroke hemiplegia and osteoporosis. From the blood routine indicators, the median cell count of the observation group 180 days after treatment was significantly lower than that of the control group, while the level of lymphocytes was significantly higher than that of the control group ($P < 0.05$). It shows that the Siwu decoction can reduce the number of intermediate cells in patients, increase the volume of red blood cells, and elevate the level of lymphocytes. From the perspective of clinical efficacy, the total effective rate (88.33%) of the observation group was significantly higher than that of the control group (78.33%), and the difference was statistically significant ($P < 0.05$). This indicates that the Siwu decoction has significant curative effect in the treatment of patients with poststroke hemiplegia and osteoporosis, showing high clinical application value.

5. Conclusion

In this study, the modified Siwu decoction was applied in the treatment of poststroke hemiplegia patients with osteoporosis. It was finally found that Siwu decoction can effectively improve bone metabolism in patients with poststroke hemiplegia and osteoporosis, promote the proliferation and differentiation of bone cells, and improve the BMD and quality of life of patients. However, the patients selected in this work all came from the same hospital, and the long-term follow-up time was short, so no longer-term patient prognosis data were obtained. Therefore, in the following research, it would include stroke patients with osteoporosis in different hospitals as the research object and further analyze the clinical application value of traditional Chinese medicine Siwu decoction. All in all, the results of this work could provide a reference for the nursing treatment of poststroke hemiplegia complicated with osteoporosis.

Data Availability

The data used to support the findings of this study are available from the corresponding author upon request.

Conflicts of Interest

The authors declare that there are no conflicts of interest.

Authors' Contributions

Jing Wang and Xiuyun Liu contributed equally to this work.

Acknowledgments

References

[1] F. Z. Caprio and F. A. Sorond, "Cerebrovascular disease: primary and secondary stroke prevention," *Medical Clinics of North America*, vol. 103, no. 2, pp. 295–308, 2019.

[2] G. Ntaios, "Embolic stroke of undetermined source: JACC review topic of the week," *Journal of the American College of Cardiology*, vol. 75, no. 3, pp. 333–340, 2020.

[3] J. W. Doria and P. B. Forgacs, "Incidence, implications, and management of seizures following ischemic and hemorrhagic stroke," *Current Neurology and Neuroscience Reports*, vol. 19, no. 7, p. 37, 2019.

[4] A. Knight-Greenfield, J. J. Q. Nario, and A. Gupta, "Causes of acute stroke: a patterned approach," *Radiologic Clinics of North America*, vol. 57, no. 6, pp. 1093–1108, 2019.

[5] P. Tater and S. Pandey, "Post-stroke movement disorders: clinical spectrum, pathogenesis, and management," *Neurology India*, vol. 69, no. 2, pp. 272–283, 2021.

[6] R. Srivastava and A. Kirton, "Perinatal stroke: a practical approach to diagnosis and management," *Neoreviews*, vol. 22, no. 3, pp. e163–e176, 2021.

[7] K. Tomida, S. Sonoda, S. Hirano et al., "Randomized controlled trial of gait training using gait exercise assist robot (GEAR) in stroke patients with hemiplegia," *Journal of Stroke and Cerebrovascular Diseases*, vol. 28, no. 9, pp. 2421–2428, 2019.

[8] S. Jan, A. Arsh, H. Darain, and S. Gul, "A randomized control trial comparing the effects of motor relearning programme and mirror therapy for improving upper limb motor functions in stroke patients," *Journal of Pakistan Medical Association*, vol. 69, no. 9, pp. 1242–1245, 2019.

[9] E. B. Küçük, E. Küçük, E. Kaydok, K. R. Zor, and G. Y. Biçer, "Dry eye in chronic stroke patients with hemiplegia: a cross-sectional study," *Topics in Stroke Rehabilitation*, vol. 27, no. 8, pp. 630–635, 2020.

[10] T. E. Johnston, S. Keller, C. Denzer-Weiler, and L. Brown, "A clinical practice guideline for the use of ankle-foot orthoses and functional electrical stimulation post-stroke," *Journal of Neurologic Physical Therapy*, vol. 45, no. 2, pp. 112–196, 2021.

[11] A. G. Austin, W. Y. Raynor, C. C. Reilly et al., "Evolving role of MR imaging and PET in assessing osteoporosis," *PET Clinics*, vol. 14, no. 1, pp. 31–41, 2019.

[12] L. Wang, W. Yu, X. Yin et al., "Prevalence of osteoporosis and fracture in China: the China osteoporosis prevalence study," *JAMA Network Open*, vol. 4, no. 8, Article ID e2121106, 2021.

[13] E. Tsourdi, B. Langdahl, M. Cohen-Solal et al., "Discontinuation of Denosumab therapy for osteoporosis: a systematic review and position statement by ECTS," *Bone*, vol. 105, pp. 11–17, 2017.

[14] J. A. Kanis, N. C. Harvey, E. McCloskey et al., "Algorithm for the management of patients at low, high and very high risk of osteoporotic fractures," *Osteoporosis International*, vol. 31, no. 1, pp. 1–12, 2020.

[15] J. Xia, S. Y. Xie, K. Q. Liu et al., "Systemic evaluation of the relationship between psoriasis, psoriatic arthritis and osteoporosis: observational and Mendelian randomisation study," *Annals of the Rheumatic Diseases*, vol. 79, no. 11, pp. 1460–1467, 2020.

[16] F. Wu, Y. Huang, J. Hu, and Z. Shao, "Mendelian randomization study of inflammatory bowel disease and bone mineral density," *BMC Medicine*, vol. 18, no. 1, p. 312, 2020.

[17] C. Beaudart, Y. Rolland, A. J. Cruz-Jentoft et al., "Assessment of muscle function and physical performance in daily clinical practice," *Calcified Tissue International*, vol. 105, no. 1, pp. 1–14, 2019.

[18] C. L. Shapiro, C. Van Poznak, C. Lacchetti et al., "Management of osteoporosis in survivors of adult cancers with nonmetastatic disease: ASCO clinical practice guideline," *Journal of Clinical Oncology*, vol. 37, no. 31, pp. 2916–2946, 2019.

[19] T. N. Filipović, M. P. Lazović, A. N. Backović et al., "A 12-week exercise program improves functional status in post-menopausal osteoporotic women: randomized controlled study," *European Journal of Physical and Rehabilitation Medicine*, vol. 57, no. 1, pp. 120–130, 2021.

[20] X. H. Yu, Y. Q. Yang, R. R. Cao et al., "Rheumatoid arthritis and osteoporosis: shared genetic effect, pleiotropy and causality," *Human Molecular Genetics*, vol. 30, no. 21, pp. 1932–1940, 2021.

[21] Y. Q. Liu, Y. Liu, Z. Y. Chen, H. Li, and T. Xiao, "Rheumatoid arthritis and osteoporosis: a bi-directional Mendelian randomization study," *Aging*, vol. 13, no. 10, pp. 14109–14130, 2021.

[22] M. Rauner, H. Taipaleenmäki, E. Tsourdi, and E. M. Winter, "Osteoporosis treatment with anti-sclerostin antibodies—mechanisms of action and clinical application," *Journal of Clinical Medicine*, vol. 10, no. 4, p. 787, 2021.

[23] Y. Zhao, M. Huang, J. Ding et al., "Prediction of abnormal bone density and osteoporosis from lumbar spine MR using modified dixon quant in 257 subjects with quantitative computed tomography as reference," *Journal of Magnetic Resonance Imaging*, vol. 49, no. 2, pp. 390–399, 2019.

[24] B. He, L. Xia, J. Zhao et al., "Causal effect of serum magnesium on osteoporosis and cardiometabolic diseases," *Frontiers in Nutrition*, vol. 8, Article ID 738000, 2021.

[25] Q. Zhang, J. Greenbaum, H. Shen et al., "Detecting causal relationship between metabolic traits and osteoporosis using multivariable Mendelian randomization," *Osteoporosis International*, vol. 32, no. 4, pp. 715–725, 2021.

WILEY | Hindawi

Research Article

Effect of Nursing Intervention on Self-Management and Quality of Life in Patients with Chronic Kidney Disease Evaluated by Renal Diffusion Tensor Imaging Features Using Image Registration Algorithm

Zongqiong Zhou (ID)

Department of Nephrology, Chongqing Fuling Central Hospital, Chongqing 408000, China

Correspondence should be addressed to Zongqiong Zhou; 2018211303@mail.chzu.edu.cn

The aim of this research was to explore the effect of nursing intervention on self-management and quality of life in patients with chronic kidney disease (CKD) by using the renal diffusion tensor imaging (DTI) feature of image registration algorithm. A total of 100 patients with CKD were randomly divided into experimental group (nursing maintenance guidance intervention) and control group (routine nursing), with 50 cases in each group. The image effect before and after registration, self-management behavior after 6 months, quality of life, DTI-related parameters, and renal function indicators were collected and analyzed. The results showed that the images were clearer than those before registration, the self-management ability in the control group (92.81 ± 19.32) was smaller than that in the experimental group (107.12 ± 18.78), the quality of life in the experimental group (121.47 ± 11.21) was greater than that in the control group (104.89 ± 12.11), and the corresponding magnetic resonance apparent diffusion coefficient (ADC) (2.54 ± 0.28) and fractional anisotropy (FA) (0.28 ± 0.07) in the cortex were greater than those in the control group $(2.35 \pm 0.21, 0.23 \pm 0.04)$. The differences were statistically significant $(P < 0.05)$. The corresponding ADC value (2.32 ± 0.22) and FA value (0.59 ± 0.02) of medulla were greater than those of the control group $(2.12 \pm 0.24$ and $0.41 \pm 0.17)$. The levels of serum creatinine (Scr) $(\mu mol/L)$ (421.38 ± 42.78) and 24 h urinary protein (24 h-Upro) (mg/d) $(1,836.7 \pm 545.98)$ were lower than those of the control group, and the differences had statistical significance $(P < 0.05)$. In summary, the registration algorithm can enhance the effect of image presentation and nursing intervention has positive significance for the self-management and quality of life of patients with CKD.

1. Introduction

Chronic kidney disease (CKD) is defined as a disease with a duration of more than 3 months, which causes changes in renal structure as well as disturbances in renal function. In the treatment, some existing therapeutic measures mainly include taking drugs for treatment, giving nutritional support to the body, and alternative treatment for severe patients [1]. Therefore, for some end-stage patients, their kidneys have been severely damaged and some corresponding physiological functions have been lost, and replacement therapy will be considered in clinical practice. Replacement therapy is also divided into three categories, including hemodialysis, peritoneal dialysis, and renal transplantation. Some drugs such as angiotensin-converting enzyme inhibitors (ACEI), angiotensin II receptor blockers (ARB), and erythropoiesis-stimulating agents (ESA) are mainly used in the use of drugs [2]. However, the treatment of the disease only using drugs and surgery is not necessarily the best for the rehabilitation effect of patients. The long treatment course of patients with CKD will lead to physical and mental suffering of patients if their daily diet and life are not controlled, and it is also detrimental to the recovery of patients. Therefore, in addition to basic treatment, the addition of nursing intervention will be more helpful for the remission of the patient's condition.

Nursing intervention is proposed based on certain physiological and pathological scientific theories, is through some corresponding scientific experiments, and can indeed help doctors give more comprehensive treatment to patients in clinical practice to a certain extent. Nursing intervention requires comprehensive consideration of many aspects such as disease, family, and psychology according to the specific circumstances of patients in clinical practice and then making the corresponding diagnosis, and the corresponding nursing staff needs sequential, targeted, and scientific nursing according to nursing guidance [3, 4]. In this process, reasonable reference to the existing research results, analysis of various functional indicators of patients and expected degree of recovery, and professional clinical knowledge can achieve a good intervention effect, so as to achieve the expected results of helping the patient's physical and mental recovery, preventing complications and promoting, maintaining, or restoring the patient's physical and psychological function [5]. Interventions can be divided into different processes due to different nursing operators and nursing environments: first, it is necessary to create a rehabilitation environment with comfortable environment and complete equipment; furthermore, it is necessary for nurses with professional literacy and skills to carry out corresponding rehabilitation nursing operations; in this process, it is also necessary to obtain the assistance of family members and provide corresponding health education for family members; in addition to physical care, it is necessary to care for the psychological problems of patients, regularly carry out psychological guidance, timely respond to the consultation from family members and patients, and continue the follow-up of patients after discharge [6, 7]. It brings great help to the physical and psychological rehabilitation of patients to a certain extent.

Diffusion tensor imaging (DTI) is one of the magnetic resonance imaging techniques [8]. DTI is based on the diffusion-weighted imaging (DWI) technology because the water molecules contained in human organs have different presentation characteristics and different diffusion coefficients in all directions, which cannot well reflect the pathological characteristics of the corresponding organs if measured with a scalar. To explore a DTI technique, it is necessary to refer to fractional anisotropy (FA value) and magnetic resonance apparent diffusion coefficient (ADC value), which reflect the direction and rule of diffusion movement [9]. It can control the magnetization state of H_2O molecules and can well ensure the diffusion process of H_2O molecules, so as to obtain the specific diffusion situation, which makes DTI technology gradually rise to occupy an important position. It has also led to the rapid development of this technology in recent years. It is also widely used in cerebral ischemia and leukoaraiosis in clinical practice. Although DTI technology has been mature research and, on this basis, high-angular resolution diffusion magnetic resonance imaging technology has also been derived, there are still some shortcomings in the tensor model, so it is of positive significance to carry out image registration and explore tensor-based registration algorithms to improve the resolution of images and make the registration accuracy

higher [10]. In DTI acquisition, although the quality of echo-planar imaging can be improved by improving the hardware, thereby improving the quality of diffusion tensor images, this requires a relatively expensive cost; DWI images can also be used for registration, followed by tensor calculation again, but this also has some limitations. In addition, in some processes, the original data formed cannot be obtained, so it cannot be improved in scalar or imaging. It is very meaningful to improve the image resolution or registration accuracy by using different interpolation methods from the software algorithm. Therefore, the results were analyzed by DTI with effect registration through an image registration algorithm to explore the effect of nursing intervention on the self-management and quality of life of patients with CKD, in order to provide a certain reference for clinical management of patients.

2. Materials and Methods

2.1. General Information.
One hundred patients with CKD (50 males and 50 females, aged 30–65 years) treated in hospital from January 2021 to January 2022 were randomly selected as the subjects. The patients were randomly divided into the experimental group and the control group, with 25 males and 25 females in the experimental group: 19 cases of hypertensive renal arteriosclerosis, 12 cases of diabetic nephropathy, 8 cases of chronic uric acid nephropathy, and 11 cases of glomerulonephritis; there were 25 males and 25 females in the control group: 20 cases of hypertensive renal arteriosclerosis, 11 cases of diabetic nephropathy, 9 cases of chronic uric acid nephropathy, and 10 cases of glomerulonephritis. This research had been approved by the ethics committee of hospital, and patients and their families signed the informed consent form.

The inclusion criteria are as follows: patients meet the diagnostic criteria of CKD, patients aged 30–65 years old, and patients with complete medical records.

The exclusion criteria are as follows: patients younger than 30 years or older than 65 years, patients suffering from other serious diseases and serious complications such as thyroid dysfunction, immune system disease, and acute renal failure, breastfeeding or pregnant women, and patients with mental disorders.

2.2. Treatment Methods.
In the control group, in addition to the routine nephrology nursing operation, the patients were regularly transmitted with health knowledge and some specific operations for the prevention and treatment of CKD, guiding the patients to self-manage according to the corresponding measures. In addition to these basic operations in the control group, the experimental group also underwent nursing maintenance guidance intervention, which included preparation before nursing nutrition guidance intervention, development of guidance intervention plan, nursing nutrition guidance, and intervention measures [11] (Figure 1).

2.3. Technical Inspection and Image Processing.
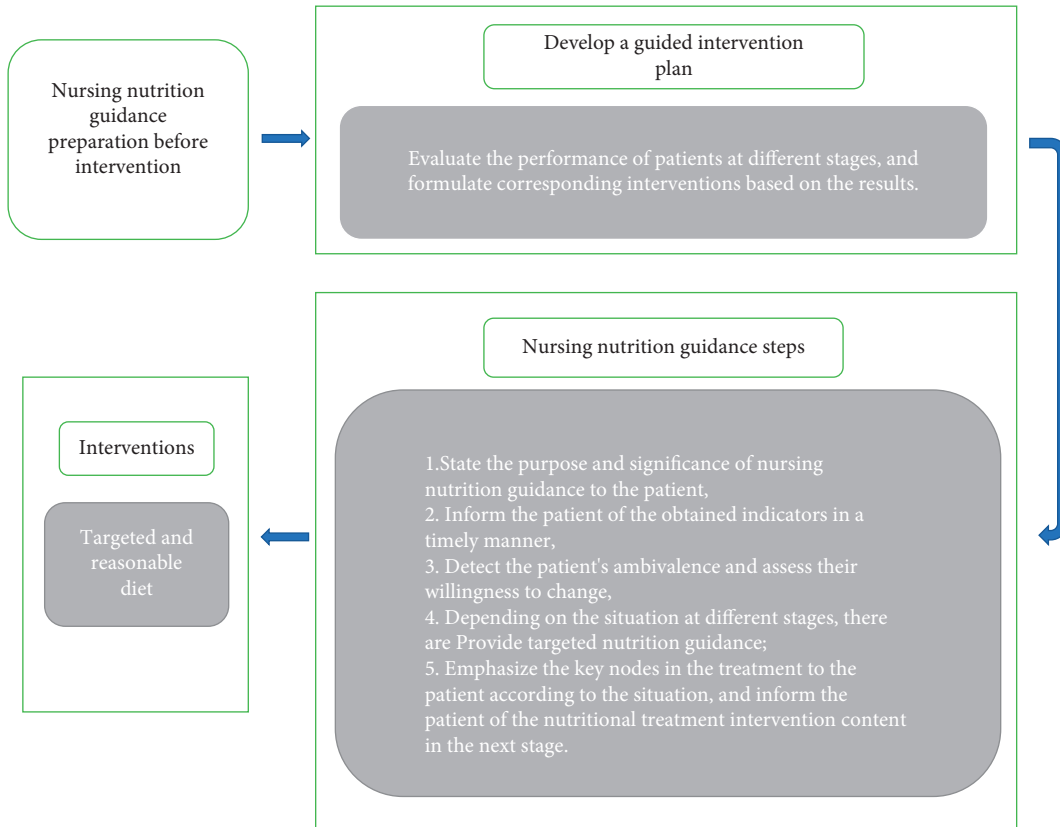A 3.0T magnetic resonance scanner was used for routine MRI

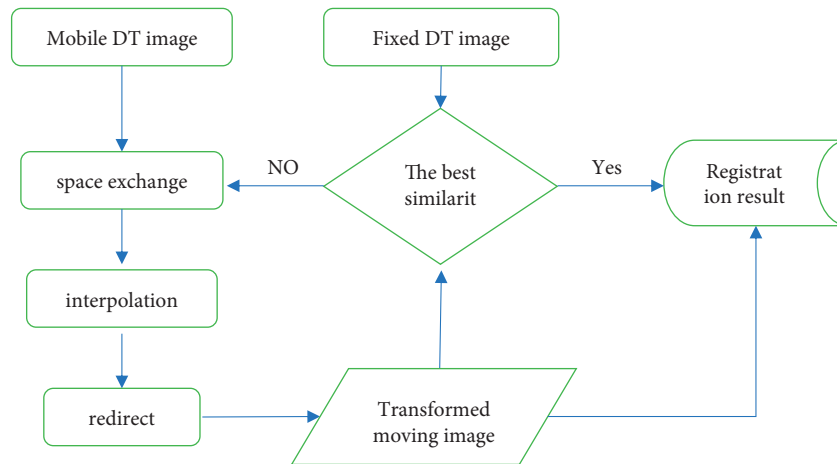FIGURE 1: Specific procedure of nursing intervention.

FIGURE 2: Schematic of diffusion tensor image registration algorithm.

scanning. The patients were examined by the DTI technique. The patients were not allowed to eat for more than 8 hours before the examination. The scanning was performed in the supine position. The scanning position was axial and coronal. Information was collected parallel to the oblique coronal view of both kidneys, and scans were performed continuously to ensure the comprehensiveness of the scans. DTI used single-shot spin echo-planar imaging (SSEPI); the scanning time was about 20 s, the scanning thickness and spacing were 6 mm and 1 mm, the matrix range was 256×256, and the field of view was $25\,cm \times 25\,cm$. The obtained images were smoothed and denoised, so as to calculate and generate FA and ADC maps using Extended MR WorkSpace workstation image processing software.

2.4. Diffusion Tensor Image Registration.

The diffusion tensor image registration algorithm [12, 13] mainly includes the following flow, which is shown in Figure 2.

First, spatial transformation and reorientation are carried out: reorientation is divided into rigid transformation, affine transformation, and high-order transformation
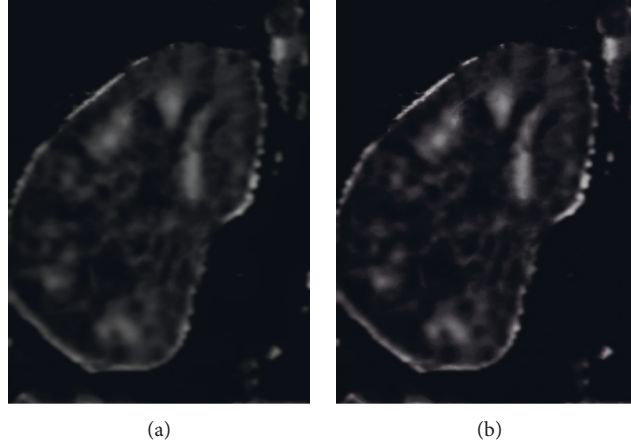
(a)   (b)

FIGURE 3: Comparison of effect before and after registration. (a) Original image; (b) the image after registration transformation.

according to different spatial transformations. The reorientation under rigid transformation can be expressed as follows:

$$B' = RBR^T. \tag{1}$$

The tensor B of the image after rigid body transformation E is replaced by tensor B' using the microstrain method [14]. R (rotation component of rigid body transformation) represents the rotation transformation matrix of transformation E decomposed by the polar coordinate decomposition method; redirection under affine transformation is as follows:

$$F = UR, \tag{2}$$

$$R = \left(TT^T\right)^{-(1/2)}F. \tag{3}$$

Using the finite strain method [15], according to the polar coordinate decomposition theory, the deformation matrix is decomposed into the rotation component R of the rigid body transformation and another deformation component U, and equation (2) is obtained. The rotation component R is extracted and converted by equation (1) to obtain equation (3).

Then, the similarity is measured: the sum of squared differences (SSD) [16, 17], which is the difference of some scalar properties used in the early image registration. SSD is defined as the sum of squares of the difference of the corresponding elements of two tensor matrices, which is expressed as follows:

$$SSD = \sum_{a=1}^{3} \sum_{b=1}^{3} \left(B_{ab}^1 - B_{ab}^2\right)^2. \tag{4}$$

The DTI standard is judged, and the average overlap of eigenvalues-eigenvector (AOE) is used for comparison to determine the impact of reorientation on the registration results.

$$AOE = \frac{1}{n} \sum_{a=1}^{n} \left(\sum_{b=1}^{3} \lambda_b^a \lambda_b^{*a} \left(\vec{e}_b^{\,a} \cdot \vec{e}_b^{\,*a}\right)^2 \cdot \frac{1}{\sum_{b=1}^{3} \lambda_b^a \lambda_b^{*a}} \right), \tag{5}$$

where λ_b^a, $\vec{e}_b^{\,a}$, λ_b^{*a}, and $\vec{e}_b^{\,*a}$ mean feature vector of the bth eigenvalue of the ath position of the target image and the original image.

2.5. Outcome Measures. Outcome measures mainly included four aspects of observation indicators: self-management behavior, quality of life, DTI-related parameters (ADC and FA values of cortex and medulla), and renal function indicators (serum creatinine (Scr), urinary protein (24 h-Upro), and estimated glomerular filtration rate (eGFR)).

2.6. Statistical Processing. Statistical software SPSS 20.0 was used to process and analyze the data of the experimental data. The measurement data were expressed as mean ± standard deviation ($\bar{x} \pm s$). The independent sample t-test was used for comparison. $P < 0.05$ was considered statistically significant.

3. Results

3.1. Comparison before and after Image Registration Algorithm Processing. The results of diffusion tensor object after image registration are shown in Figure 3. Figure 3(a) is the original image, Figure 3(b) is the image after registration transformation, and the image contour and internal texture are clearer than those before registration.

3.2. Self-Management Behavior Scores before and after Intervention. The nursing intervention was maintained for 6 months, and various observation indicators were recovered and statistically analyzed after 6 months. The statistical results showed that the self-management ability was improved to a certain extent compared with that before intervention and the level of self-management ability in the control group (92.81 ± 19.32) was slightly lower than that in the experimental group (107.12 ± 18.78), and the difference had statistical significance ($P < 0.05$) (Figure 4).

3.3. Scores of Quality-of-Life Indicators before and after Intervention. The scores of all indicators of quality of life in
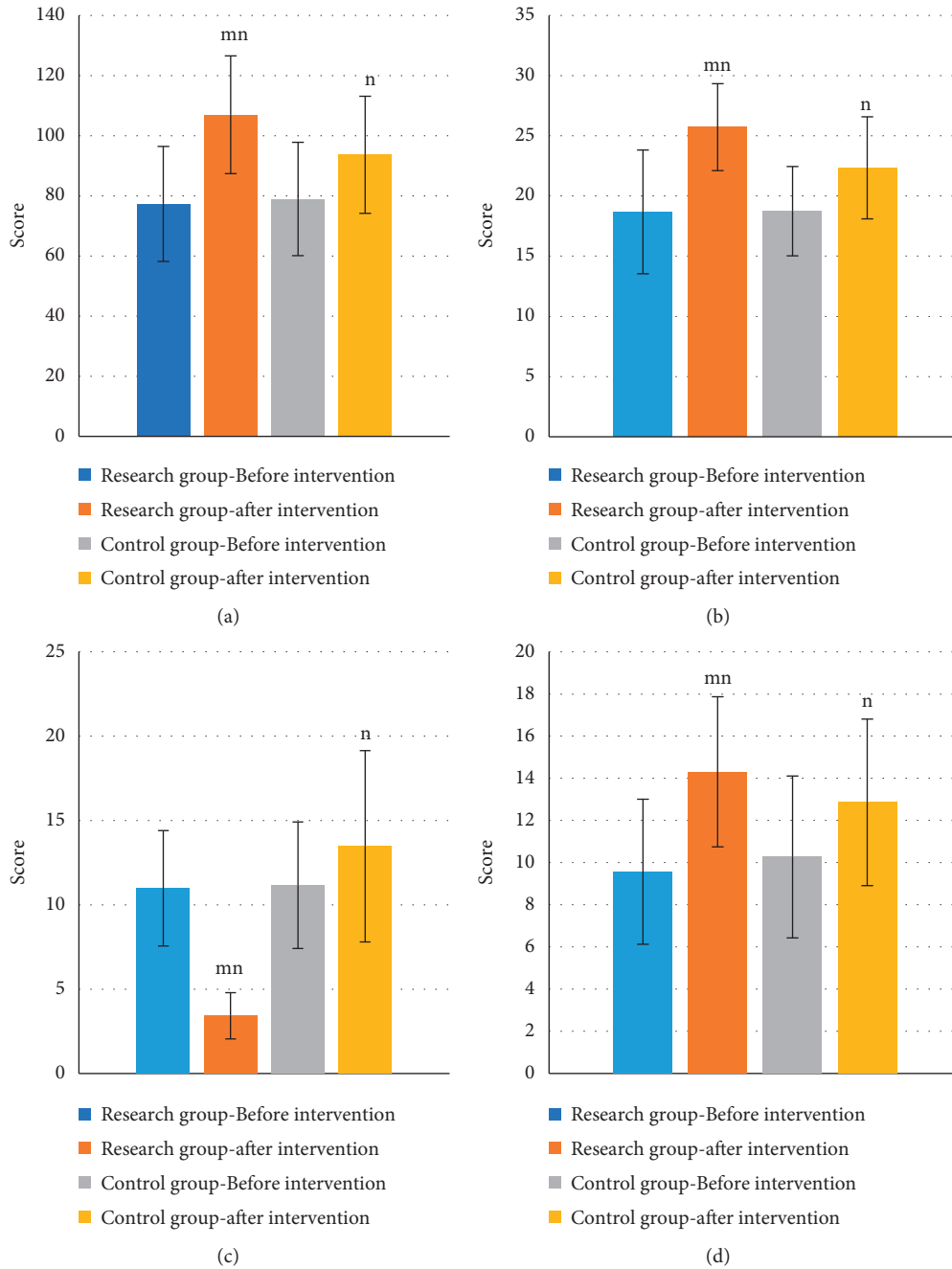
Figure 4: Comparison of self-management behavior scores before and after intervention between the two groups. (a–d) The self-management skills, diet control, regular exercise, and the ability to follow doctor's orders before and after the intervention in the experimental group and the control group, respectively. ^{m}Compared with that before intervention, $P < 0.05$; ^{n}compared with the control group after 6 months of intervention, $P < 0.05$.

the experimental group and the control group showed a certain degree of improvement after 6 months of intervention, and the comparison revealed that the experimental group (121.47 ± 11.21) had certain advantages over the control group (104.89 ± 12.11), with a slightly higher score, and the difference had statistical significance ($P < 0.05$) (Figure 5).

3.4. Comparison of ADC and FA Values of Cortex and Medulla before and after Intervention. According to statistical

data, compared with the control group, the corresponding ADC value (2.54 ± 0.28) and FA value (0.28 ± 0.07) of the cortex in the experimental group were significantly greater than those in the control group (2.35 ± 0.21 and 0.23 ± 0.04), and the differences had statistical significance ($P < 0.05$). The corresponding ADC value (2.32 ± 0.22) and FA value (0.59 ± 0.02) of the medulla in the experimental group were also greater than those in the control group (2.12 ± 0.24 and 0.41 ± 0.17), and the differences had statistical significance ($P < 0.05$) (Table 1 and Figure 6).
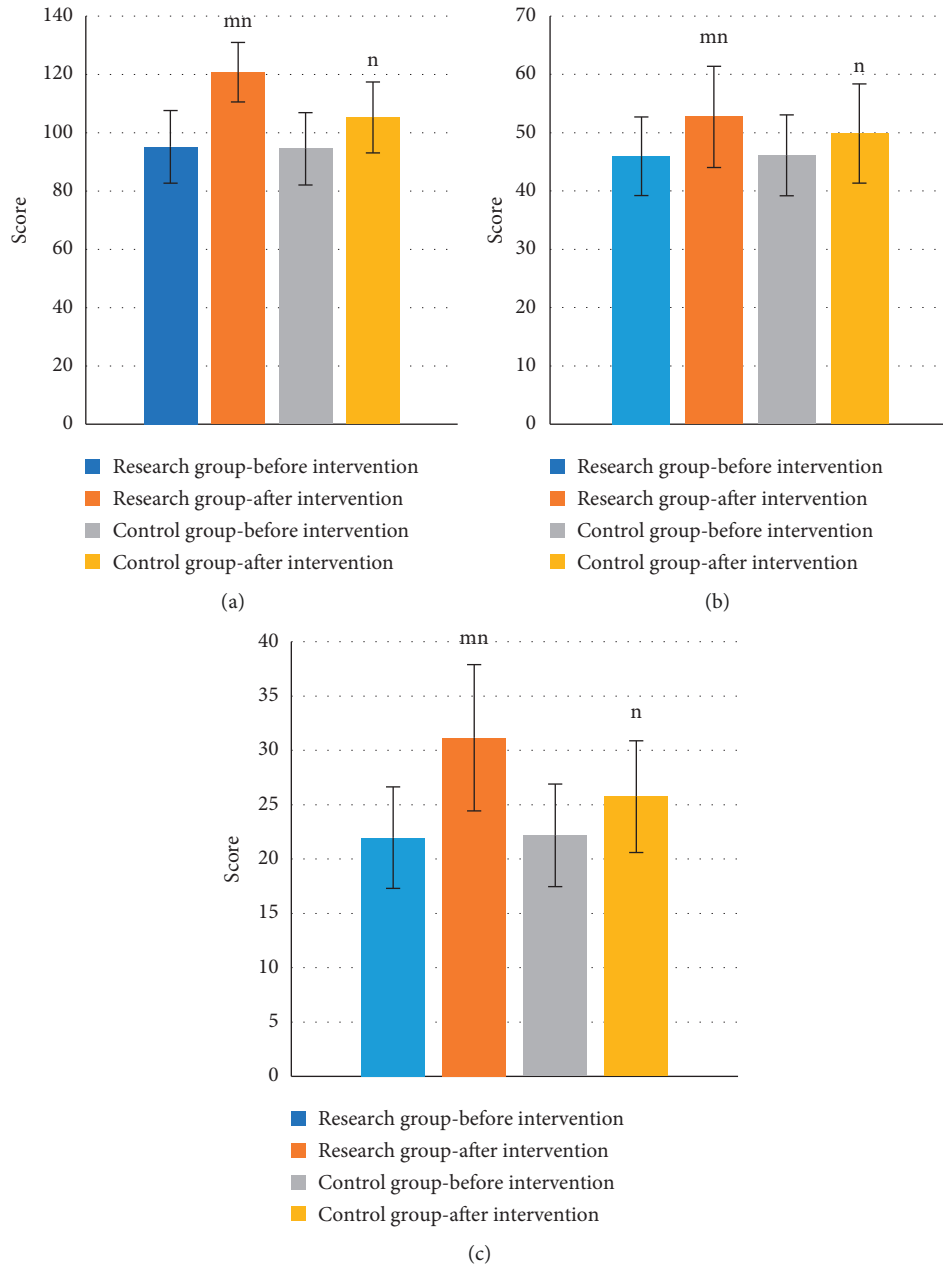
(a)

(b)

(c)

FIGURE 5: Comparison of scores of quality-of-life indicators before and after intervention between the two groups. (a–c) The level of quality-of-life mental function and physiological function before and after intervention in the experimental group and control group, respectively. [m]Compared with that before intervention, $P < 0.05$; [n]compared with the control group after 6 months of intervention, $P < 0.05$.

3.5. *Comparison of Renal Function Parameters.* One-way ANOVA showed that compared with the experimental group, the levels of Scr (μmol/L) (421.38 ± 42.78) and 24 h-Upro (mg/d) ($1,836.7 \pm 545.98$) were higher in the control group, and the eGFR (mL/min) (22.56 ± 2.35) was lower in the control group than in the experimental group. The difference had statistical significance ($P < 0.05$) (Figure 7).

4. Discussion

In recent years, with the changes in living environment and dietary structure, CKD has become a major disease endangering human health and has become a public health problem that is concerned and strongly solved worldwide [18, 19]. CKD refers to the gradual damage of renal function under the influence of various adverse factors, forming developmental damage to the structure of the kidney. Popularly speaking, CKD is not a sudden attack, but a consequence of long-term neglect of the accumulation of kidney disease by patients. There are three types of CKD that mainly endanger the health of the population in China: hypertension, glomerulonephritis, and diabetic nephropathy [20, 21]. According to Liu Wenhu, director of the Nephrology Department of Beijing Friendship Hospital, "only

TABLE 1: Comparison of ADC and FA values of cortex and medulla.

Group	Cortex		Medulla	
	ADC value	FA value	ADC value	FA value
Experimental group	2.54 ± 0.28*	0.28 ± 0.07*	2.32 ± 0.22*	0.59 ± 0.02*
Control group	2.35 ± 0.21	0.23 ± 0.04	2.12 ± 0.24	0.41 ± 0.17
F	20.987	6.768	20.141	32,523
P	<0.001	<0.001	<0.001	<0.001

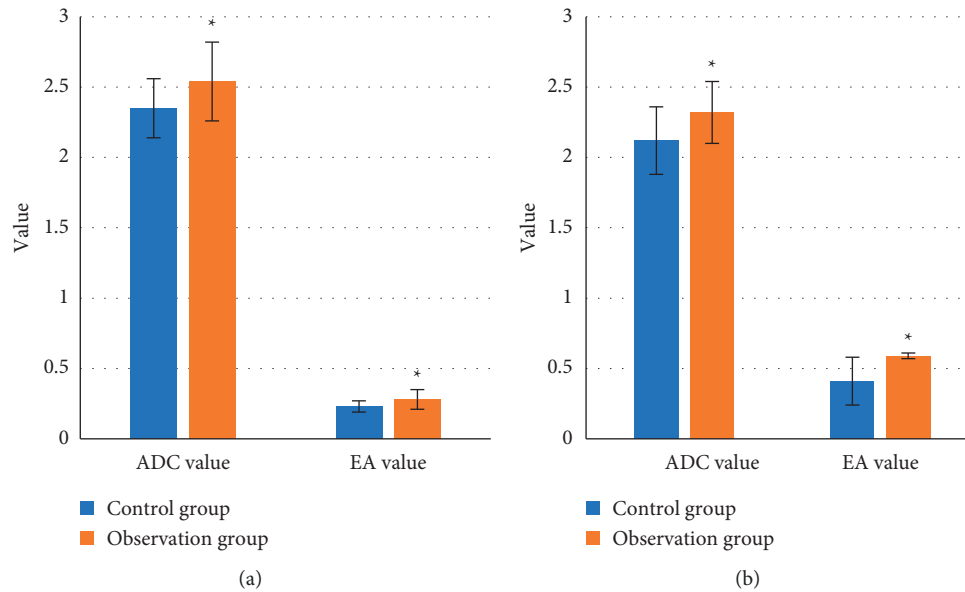*Compared with the control group, $P < 0.05$.

FIGURE 6: ADC and FA values of cortex and medulla before and after intervention. (a) Comparison between the ADC value of the cortex and the FA value; (b) comparison of the ADC value of the medulla and the FA value. *Compared with the control group, $P < 0.05$.

about 12.5% of Chinese patients with CKD have been diagnosed." This also maps to the phenomenon from the side that only one in eight of these patients is aware of their disease and thus obtains the corresponding treatment [22, 23]. DTI, as a special form of magnetic resonance imaging, plays a crucial role in the diagnosis of kidney disease. Image registration technology can help phase to a certain extent and play a quite important and indelible role in medical image processing. Moreover, it helps doctors to accurately find lesions with the help of images. With the continuous progress of the technology, the corresponding functions of medical image extraction equipment have been improved to a great extent, not only the images containing detailed image information such as CT and MRI can be collected, but also a large number of images about functional information such as SPECT can be collected [24]. Since image registration technology can capture and collect dynamic images at different time points and use the equation for registration, the resulting image of registration is more accurate and facilitates the doctor to carefully analyze the size of the lesion site and the lesion condition, so that medical diagnosis, surgical planning, and radiotherapy planning become more accurate and reliable [25, 26]. Nursing intervention can help patients to recover to a certain extent, so the characteristics of renal DTI with an image

registration algorithm are used to explore the effect of nursing intervention on self-management and quality of life in patients with CKD.

The image registration algorithm was used to optimize the phase of DTI. By observing various indicators, it was found that the subjects were randomly divided into the experimental group and the control group. The control group was mainly given routine nephrology nursing and health education, while the experimental group carried out nursing guidance intervention based on the control group. The data of self-management behavior, quality of life, DTI-related parameters, and renal function indicators after 6 months were collected and analyzed. The results showed that the image outline and internal texture of the diffusion tensor image were clearer after image registration. After 6 months of nursing intervention, the self-management ability score of the control group was 92.81 ± 19.32, while that of the experimental group was 107.12 ± 18.78, which was lower in the control group than in the experimental group, and the difference had statistical significance ($P < 0.05$). The scores of all indicators of quality of life in the experimental group and the control group showed a certain degree of improvement after 6 months of intervention. The experimental group (121.47 ± 11.21) was greater than the control group (104.89 ± 12.11), and the difference had statistical
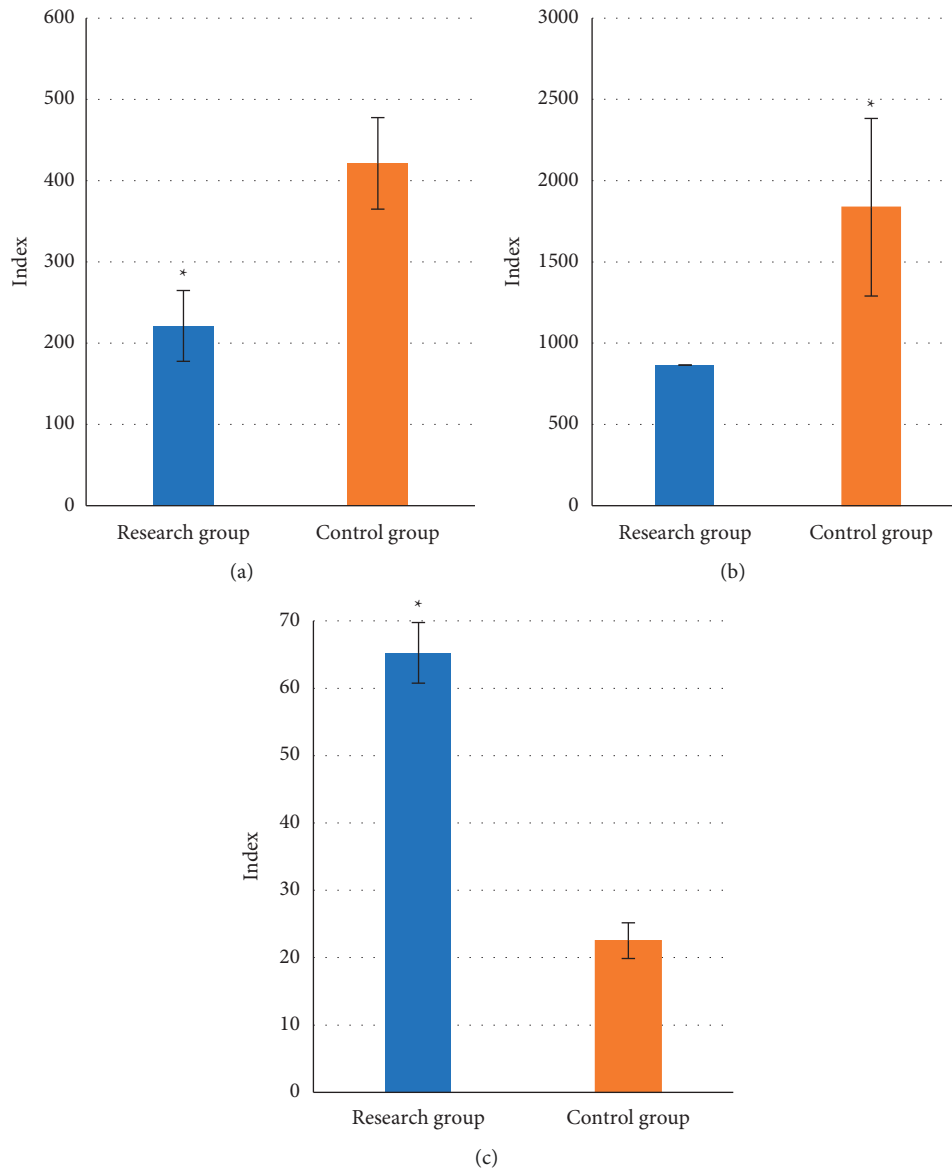
FIGURE 7: Comparison of renal function parameters in CKD patients. (a–c) The serum creatinine, 24 h urine protein, and estimated glomerular filtration rate of the experimental group and control group, respectively. *Compared with the control group, $P < 0.05$.

significance ($P < 0.05$). The self-management ability and quality of life of the experimental group showed a certain degree of improvement, which indicated that under the nursing intervention, the lifestyle of the patients had a certain change and the cognition about the disease and the coping strategies were more scientific. The physical performance status through exercise had also changed, and these comprehensive changes made the patients' recovery superior to the common treatment. Compared with the control group, the corresponding ADC value (2.54 ± 0.28) and FA value (0.28 ± 0.07) of the cortex in the experimental group were significantly greater than those in the control group (2.35 ± 0.21 and 0.23 ± 0.04), and the differences had statistical significance ($P < 0.05$). The corresponding ADC value (2.32 ± 0.22) and FA value (0.59 ± 0.02) of the medulla were also numerically greater than those of the control group

(2.12 ± 0.24 and 0.41 ± 0.17), and the differences had statistical significance ($P < 0.05$). The ADC value and FA value show the performance of the direction of water molecule transport in organs. In patients with kidney disease, due to the change in renal function and structure, the corresponding water molecule movement direction will be changed and the ADC value and FA value will also be reduced. In this experiment, the corresponding ADC value and FA value in the cortex and medulla in the experimental group were greater than those in the control group. This result was caused by the reduction of renal necrosis, the gradual recovery of renal structure, and the reduction of the change degree of internal water molecule movement direction under the intervention treatment compared with the common treatment method. One-way ANOVA showed that compared with the experimental group, the levels of Scr

(μmol/L) (421.38 $\pm$ 42.78) and 24 h-Upro (mg/d) (1,836.7 $\pm$ 545.98) were higher in the control group and the eGFR (mL/min) (22.56 $\pm$ 2.35) was lower in the control group than in the experimental group. The difference had statistical significance ($P < 0.05$). It is reported in the relevant literature that Scr, 24 h-Upro, and eGFR can reflect the change in renal function. The greater the Scr and 24 h-Upro values, the more severe the renal injury, and the smaller the eGFR, the more severe the renal injury [27]. The experimental results showed that the Scr and 24 h-Upro values in the experimental group of nursing intervention were less than those in the control group and the eGFR value was greater than that in the control group, that is, the better the recovery of renal function under nursing intervention.

5. Conclusion

DTI through image registration, image outline, and internal texture is clearer. Nursing intervention has certain positive significance for self-management and quality of life of patients with CKD. However, the sample size of this experiment is limited and adjustment is needed in the extensiveness of the study subjects. In conclusion, this experiment can provide some reference value for the clinical treatment of CKD.

Data Availability

The data used to support the findings of this study are available from the corresponding author upon request.

Conflicts of Interest

The author declares no conflicts of interest.

References

[1] Kidney Disease: Improving Global Outcomes (KDIGO) Diabetes Work Group, "KDIGO 2020 clinical practice guideline for diabetes management in chronic kidney disease," *Kidney International*, vol. 98, 2020.

[2] S. Erraez, M. López-Mesa, and P. Gómez-Fernández, "Mineralcorticoid receptor blockers in chronic kidney disease," *Nefrología (English Edition)*, vol. 41, no. 3, pp. 258–275, 2021.

[3] Y. Wang, Y. Sun, N. Lu et al., "Diagnosis and treatment rules of chronic kidney disease and nursing intervention models of related mental diseases using electronic medical records and data mining," *Journal of Healthcare Engineering*, vol. 2021, Article ID 5187837, 13 pages, 2021.

[4] Z. M. Jenkins, E. J. Tan, E. O'Flaherty et al., "A psychosocial intervention for individuals with advanced chronic kidney disease: a feasibility randomized controlled trial," *Nephrology (Carlton)*, vol. 26, no. 5, pp. 442–453, 2021.

[5] Y. Zhou and X. Li, "Effect assessment of the application value of evidence-based nursing intervention in operating room nursing," *Medicine*, vol. 100, no. 32, Article ID e26867, 2021.

[6] E. S. Mousavinasab, S. R. N. Kalhori, N. Zarifsanaiey, M. Rakhshan, and M. Ghazisaeedi, "Nursing process education: a review of methods and characteristics," *Nurse Education in Practice*, vol. 48, Article ID 102886, 2020.

[7] J. M. Mancuso, "Perceptions of distance education among nursing faculty members in North America," *Nursing and Health Sciences*, vol. 11, no. 2, pp. 194–205, 2009.

[8] S. J. Cheng, P. H. Tsai, Y. T. Lee, Y. T. Li, H. W. Chung, and C. Y. Chen, "Diffusion tensor imaging of the spinal cord," *Magnetic Resonance Imaging Clinics of North America*, vol. 29, no. 2, pp. 195–204, 2021.

[9] A. T. Mazal, O. Ashikyan, J. Cheng, L. Q. Le, and A. Chhabra, "Diffusion-weighted imaging and diffusion tensor imaging as adjuncts to conventional MRI for the diagnosis and management of peripheral nerve sheath tumors: current perspectives and future directions," *European Radiology*, vol. 29, no. 8, pp. 4123–4132, 2019.

[10] M. Perri, M. D'Elia, G. Castorani et al., "Assessment of lumbar disc herniaton using fractional anisotropy in diffusion tensor imaging along with conventional T2-weighted imaging," *Neuroradiology Journal*, vol. 33, no. 1, pp. 24–31, 2020.

[11] D. A. Richards, A. Hilli, C. Pentecost, V. A. Goodwin, and J. Frost, "Fundamental nursing care: a systematic review of the evidence on the effect of nursing care interventions for nutrition, elimination, mobility and hygiene," *Journal of Clinical Nursing*, vol. 27, no. 11-12, pp. 2179–2188, 2018.

[12] J. Gerhardt, N. Sollmann, P. Hiepe et al., "Retrospective distortion correction of diffusion tensor imaging data by semi-elastic image fusion - evaluation by means of anatomical landmarks," *Clinical Neurology and Neurosurgery*, vol. 183, Article ID 105387, 2019.

[13] F. Machado-Rivas, O. Afacan, S. Khan et al., "Spatiotemporal changes in diffusivity and anisotropy in fetal brain tractography," *Human Brain Mapping*, vol. 42, no. 17, pp. 5771–5784, 2021.

[14] F. G. Zöllner, A. Šerifović-Trbalić, G. Kabelitz, M. Kociński, A. Materka, and P. Rogelj, "Image registration in dynamic renal MRI-current status and prospects," *MAGMA*, vol. 33, no. 1, pp. 33–48, 2020.

[15] J. S. Giudice, A. Alshareef, T. Wu et al., "An image registration-based morphing technique for generating subject-specific brain finite element models," *Annals of Biomedical Engineering*, vol. 48, no. 10, pp. 2412–2424, 2020.

[16] A. Ghaffari and E. Fatemizadeh, "Image registration based on low rank matrix: rank-regularized SSD," *IEEE Transactions on Medical Imaging*, vol. 37, no. 1, pp. 138–150, 2018.

[17] X. Liu, D. Jiang, M. Wang, and Z. Song, "Image synthesis-based multi-modal image registration framework by using deep fully convolutional networks," *Medical & Biological Engineering & Computing*, vol. 57, no. 5, pp. 1037–1048, 2019.

[18] B. S. Reynolds and H. P. Lefebvre, "Feline CKD," *Journal of Feline Medicine & Surgery*, vol. 15, pp. 3–14, 2013.

[19] A. Gafter-Gvili, A. Schechter, and B. Rozen-Zvi, "Iron deficiency anemia in chronic kidney disease," *Acta Haematologica*, vol. 142, no. 1, pp. 44–50, 2019.

[20] D. C. Wheeler, B. V. Stefánsson, N. Jongs et al., "Effects of dapagliflozin on major adverse kidney and cardiovascular events in patients with diabetic and non-diabetic chronic kidney disease: a prespecified analysis from the DAPA-CKD trial," *Lancet Diabetes & Endocrinology*, vol. 9, no. 1, pp. 22–31, 2021.

[21] H. W. Kim, J. T. Park, Y. S. Park et al., "Systolic blood pressure and chronic kidney disease progression in patients with primary glomerular disease," *Journal of Nephrology*, vol. 34, no. 4, pp. 1057–1067, 2021.

[22] X. N. Ng, C. C. Tang, C. H. Wang, J. P. Tsai, and B. G. Hsu, "Positive correlation of serum resistin level with peripheral artery disease in patients with chronic kidney disease stage 3

to 5," *International Journal of Environmental Research and Public Health*, vol. 18, no. 23, Article ID 12746, 2021.

[23] GBD 2017 DALYs and HALE Collaborators, "Global, regional, and national disability-adjusted life-years (DALYs) for 359 diseases and injuries and healthy life expectancy (HALE) for 195 countries and territories, 1990-2017: a systematic analysis for the Global Burden of Disease Study 2017," *Lancet*, vol. 392, no. 10159, pp. 1859–1922, 2018.

[24] H. Dai, C. Jiang, G. Wu et al., "A combined DTI and resting state functional MRI study in patients with postherpetic neuralgia," *Japanese Journal of Radiology*, vol. 38, no. 5, pp. 440–450, 2020.

[25] C. Lock, J. Kwok, S. Kumar et al., "DTI profiles for rapid description of cohorts at the clinical-research interface," *Frontiers of Medicine*, vol. 5, p. 357, 2019.

[26] M. Liu, Y. Wu, X. Wu et al., "White matter microstructure changes and cognitive impairment in the progression of chronic kidney disease," *Frontiers in Neuroscience*, vol. 14, Article ID 559117, 2020.

[27] R. L. Chevalier, "Evolution, kidney development, and chronic kidney disease," *Seminars in Cell & Developmental Biology*, vol. 91, pp. 119–131, 2019.

WILEY | Hindawi

Research Article

Deep Learning-Based Magnetic Resonance-Ultrashort Time of Echo Imaging for Analyzing Degeneration of Intervertebral Disc Cartilage Endplate and Rehabilitation Nursing

Sainan Jiang [ID],[1] **Xiaoyun Song** [ID],[1] **and Chengming Jiang** [ID][2]

[1]*Department of Science and Education, The First Hospital of Changsha, Changsha 410005, Hunan, China*
[2]*Department of Spine Surgery, The First Hospital of Changsha, Changsha 410005, Hunan, China*

Correspondence should be addressed to Chengming Jiang; 202111120911186@zcmu.edu.cn

This study was focused on the magnetic resonance-ultrashort time of echo (MR-UTE) imaging technology based on the convolution residual network (CRN) algorithm to evaluate the degeneration of intervertebral disc endplate (DIDCE) and the efficacy of rehabilitation nursing intervention. In this study, 90 patients with intervertebral disc degeneration in the hospital were randomly divided into an intervention group (45 cases) and a control group (45 cases). All patients were scanned by a magnetic resonance imaging system, and the original UTE images were postprocessed. The control group received routine nursing. The intervention group used massage and rehabilitation nursing intervention measures. The CRN algorithm is used to reconstruct the undersampled MR image and compared with ESPIRiT algorithm and the Regridding algorithm. The result found that CRN has more advantages than ESPIRiT and Regridding reconstruction algorithms. The proportion of partial disappearance and complete disappearance of fibrous ring structure in the low back pain group was higher than that in the non-low back pain group, with a statistical difference ($P < 0.05$). 90 patients with intervertebral disc cartilage endplate degeneration were divided into lumbago group (62 cases) and nonlumbago group (28 cases) according to whether they had lumbago. The nursing satisfaction of patients in the intervention group (97%) is significantly higher than that of patients in the control group (69%) ($P < 0.05$). In conclusion, the CRN algorithm successfully removes artifacts and noise in the undersampled image. Cartilage endplate, annulus fibrosus, and bony endplate partially disappeared by the MR-UTE imaging technique. Rehabilitation intervention proved to have a positive effect on the treatment of patients with intervertebral disc degeneration and can improve patients' satisfaction.

1. Introduction

The intervertebral disc is a fibrous cartilaginous structure that connects the adjacent vertebrae of the spine and consists of a central nucleus pulposus and the surrounding annulus fibrosus. It is located within the boundary of the intervertebral space. The upper and lower boundaries of the intervertebral space are the endplate of the vertebral body, and the surrounding boundaries of the intervertebral space are the plane of the bony edge of the spine [1, 2]. The main function of the disc is to bear the pressure, load the flexibility and elasticity of the spine, and cushion the shock. Degeneration of intervertebral disc endplate (DIDCE) arises from the natural aging of the body and the joint action of various

factors. It manifests as a series of cascade reactions in various parts of the cartilage endplate of the intervertebral disc under various mechanisms of action such as pathophysiology, biochemistry, and biomechanics [3–5]. DIDCE is a prerequisite and pathological basis for spinal degenerative osteoarthropathy and is one of the main causes of low back pain.

With the development of imaging technology, the main methods for clinical examination of the lumbar spine include *X*-ray, CT examination, and magnetic resonance (MR) [6]. *X*-ray examination is the most commonly used imaging examination in clinical practice, which is simple and of low cost, but cannot directly show the internal structure of the intervertebral disc [7]. CT examination has obvious

advantages in the bone examination due to its short scanning time and high-density resolution, but its soft tissue contrast is poor and it cannot display the structure of cartilage endplate and annulus fibrosus [8]. MR has the advantages of no radiation, high soft tissue resolution, and no overlapping image, showing great potential in the morphology and functional display of intervertebral disc and becoming the main imaging examination method of the lumbar spine [9–12]. With the continuous progress of imaging technology, magnetic resonance-ultrashort time of echo (MR-UTE) technology can significantly shorten the echo time and collect and display short T2 tissue signals, pointing out a new research path for DIDCE [13]. The MR-UTE double-echo sequence can directly display the cartilage endplate, improve the intertissue contrast of the vertebral disc junction area, and visually distinguish the annulus fibrosus, cartilage endplate, and bone endplate, facilitating the comparison of DIDCE imaging with conventional MR sequences [14].

As a data-oriented processing method, deep learning can classify and segment common features among complex training data sets. In addition, deep learning is widely used in image deblurring, denoising, and image enhancement. In this study, the convolution residual network (CRN) algorithm was constructed to learn the mapping relationship between undersampled and fully-sampled MRI images. Then, it was required to predict the signals lacking in undersampled images to obtain approximately fully-sampled MRI images [15, 16].

In this study, 90 patients with intervertebral disc cartilage endplate degeneration were selected, and all of them underwent MR-UTE examination. The MR-UTE images of patients were processed by constructing a convolution residual network algorithm, aiming at analyzing whether low back pain will cause the difference in the degenerative intervertebral disc and whether it will affect the morphological structure and distribution of annulus fibrosus, cartilage endplate, and bony endplate, so as to provide an earlier and more accurate diagnosis basis for the clinic.

2. Materials and Methods

2.1. Subjects. In this study, 90 DIDCE patients enrolled in the hospital from November 20, 2019, to December 20, 2020, were divided into an intervention group (45 cases) and a control group (45 cases) according to the presence or absence of low back pain, with a total of 450 discs. There were 35 males and 55 females, aged 25–75 years, with an average weight of 51.26 ± 12.64 kg. There was no significant difference in general data between the two groups ($P > 0.05$), indicating comparability. This study had been approved by the ethics committee of the hospital, and patients and their families signed the informed consent form.

Inclusion criteria are as follows: (1) conventional MRI showed different degrees of lumbar disc degeneration; (2) patients with previous lumbosacral stiffness or pain are included; (3) MRI imaging data were complete.

Exclusion criteria are as follows: (1) patients with previous infections, diseases of the blood system, and metabolic diseases; (2) history of spinal surgery, spinal malformation surgery, spinal trauma, etc.; (3) with claustrophobia, IUDS, spinal metal implantation, early pregnancy, and other MRI scan contraindications.

2.2. MR-UTE Examination. All patients were examined by a 3.0 T magnetic resonance imaging system, using the whole spine coil. The patient was in a supine position, with the head advanced, at the level of the third lumbar spine. The entire lumbar spine was scanned, ranging from the T12/L1 to the L5/S1 discs. Each patient underwent a conventional sagittal scan with T1WI, T2WI, and UTE double-echo sequences. Table 1 showed the scan sequence parameters.

2.3. Construction of CRN Algorithm. As an important technique to interpolate nonuniformly sampled data points into a straight line grid, the gridding algorithm has been widely researched and innovated. The improved gridding algorithm is defined as the gridding algorithm, which is used for MR image reconstruction in experiments.

The Kaiser-Bessel function used by the Jackson gridding algorithm is

$$
\left\{
\begin{array}{ll}
\omega(\lambda) = \dfrac{I_0\left(\alpha\sqrt{1 - (2\lambda/W)^2}\right)}{I_0(\beta)}, & |\lambda| \le \dfrac{W}{2} \\[2ex]
\omega(\lambda) = 0, & |\lambda| > \dfrac{W}{2}
\end{array}
\right\},
\tag{1}
$$

where (λ) is the Kaiser-Bessel window function, I_0 is the zero-order modified Bessel function, and W is the window length.

The calculation formula of the MRI image finally reconstructed by the gridding algorithm is

$$
M_i(x, y) = M_r(x, y) \cdot \frac{f(x, y)}{r(x, y)},
\tag{2}
$$

where M_i is the reconstructed MRI image, M_r is the inverse Fourier transform of, f is the inverse Fourier transform of, and r is a rectangular function.

To improve the accuracy under undersampling technical conditions, this study proposes a deep learning-based artifact removal method, the CRN algorithm. Firstly, the undersampled MR image is reconstructed and processed using the following equation.

$$
\mathrm{MR_{high\,quality}} = F\left(\mathrm{MR_{low\,quality}}\right),
\tag{3}
$$

where $\mathrm{MR_{low\,quality}}$ represents the MR image reconstructed from undersampled data, which contains a large number of noise points and artifacts. $\mathrm{MR_{high\,quality}}$ represents the MR image reconstructed from fully sampled data, used as the gold standard for image reference. F function, learned by CNN, is used to process undersampled MR images with artifacts and noise.

There are mainly three steps. First, MR data of full sampling and undersampling are obtained by 3D-UTE

TABLE 1: The scan parameters of T1WI, T2WI, and UTE.

	T1WI	T2WI	UTE
Repetition time (ms)	450	4200	87.3
Time of echo 1 (ms)	20	120	0.029
Time of echo 2 (ms)	—	—	7.2
Flip angle	90°	90°	15°
Layer thickness (mm)	2.5	2.5	2.5
Layer spacing (mm)	1	1	1
Matrix	385×258	385×258	512×512
Number of layers	16	16	32
Echo train length	9	25	—
Scanning time	136 s	110 s	506 s
Number of excitation	1.5	1	1

sequence acquisition, and a reconstruction algorithm is used to reconstruct the image, with the full sampling MR image taken as the gold standard. Then, a three-layer neural network is constructed and trained with undersampled and fully sampled image data at different echo times, so that it can effectively remove the noise and artifacts from undersampled images [17, 18]. Finally, the CRN algorithm is used to predict MR images of high quality. The structure diagram of the CRN algorithm is shown in Figure 1.

The CRN algorithm is calculated as follows.

FIGURE 1: Schematic diagram of the structure of the CRN algorithm.

$$M_0 = M_i + W_1 \times \mathrm{RO}\left(\mathrm{ReLU}\left(W_2 \times \mathrm{RO}\left(\mathrm{ReLU}\left(W_2 \times M_i + a_1\right)\right) + a_2\right)\right) + a_3, \tag{4}$$

where M_i represents the undersampled MR image whose undersampled multiple is 2; W_1, W_2, and W_1 all represent the weight, which contains the convolution kernel of 5×5; a_1, a_2, and a_3 represent the bias quantity, ReLU represents the activation function, and RO represents the normalization operation. The loss function is expressed as follows.

$$L(A, B) = \frac{1}{N} \times \sum_{j=1}^{N} |A_i - B_i|, \tag{5}$$

where A_i represents pixels in the undersampled MR image, B_i represents B_i pixels in the fully sampled MR image, and A_i and B_i correspond to each other. $L(A, B)$ represents the loss function, and N represents the number of pixels in the MR image.

2.4. MR-UTE Image Postprocessing and Data Measurement. After the scanning, the UTE original image was postprocessed. First, the original UTE images of each patient were uploaded to the workstation under the same repetition time and different echo times. The image positions were consistent at each echo time, and the two groups of images with the same number of layers at each echo time were silhouetted by postprocessing software. The original image of the second layer echo time was subtracted from the original image of the first layer echo time, the image after silhouette was retained, and the original image of the first echo time was saved.
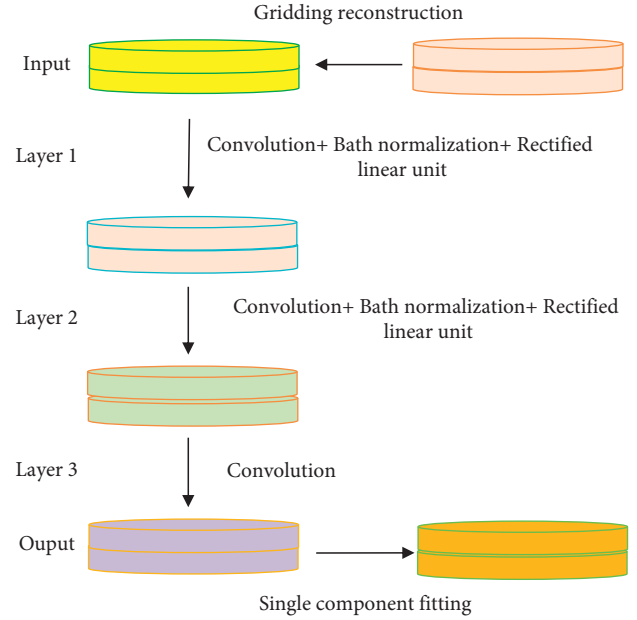
The sharpness of anatomical structures in T1WI, T2WI, and UTE images was compared semiquantitatively with conventional MR sequences, and the articulation of intervertebral disc and surrounding structures, annulus fibrosus (AF), cartilage end plate (CEP), and vertebral end plate (VEP) was assessed.

2.5. Imaging Indicators of DIDCE. At present, the Pfirrmann grading method is commonly used clinically (Table 2) [19], which often requires sagittal images of the T2WI sequence for diagnosis. Two physicians independently evaluated the degeneration signs of each intervertebral disc segment, and any inconsistency was solved through consultation and discussion.

2.6. Sagittal Double-Echo MR-UTE Image. The MR-UTE was used to analyze the cartilaginous endplates, annulus fibroids, and vertebral endplates in DIDCE patients: complete, partially absent, and completely absent according to their structural integrity. Integrity refers to the continuity of structural morphology observed at all sagittal levels; partial disappearance refers to the continuous interruption of structural signals at two consecutive levels observed at the sagittal level, and the interruption length is less than half of the transverse diameter of the structure; complete disappearance refers to the continuous interruption of the structural signal from the sagittal plane, and the interruption length reaches more than half of the transverse diameter of

TABLE 2: DIDCE Pfirrmann grading.

Characteristics	Grade I	Grade II	Grade III	Grade IV	Grade V
Structure of nucleus pulposus	Even, bright white	Uneven, horizontal band can be observed	Uneven, gray	Uneven, gray to black	Uneven, black
Nucleus pulposus-annulus fibrosus boundary	Clear	Clear	Unclear	Lost	Lost
Nucleus pulposus signal intensity	High (comparable to cerebrospinal fluid)	High (comparable to cerebrospinal fluid)	Medium	Medium to low	Low
Disc height	Normal	Normal	Slightly reduced	Moderately reduced	Severely reduced

the structure. Two physicians read the films independently. Any disagreement was solved through consultation and discussion. The imaging findings should be observed, recorded, and counted.

2.7. Rehabilitation Nursing Intervention Methods. The control group received routine nursing. In the intervention group, on the basis of routine nursing, massage and rehabilitation nursing intervention measures were used, and the patients' waist acupoints were professionally massaged. At the same time, health education, rehabilitation nursing, rehabilitation training, and retraining were given to the patients. Rehabilitation nursing intervention is as follows.

Monitoring of respiration, blood pressure, blood oxygen saturation, and electrocardiogram: all patients in this group had different degrees of anemia after the operation, and extubation was delayed for 16 hours after anesthesia. After the patient returned to the ward, he was given 3 L/min of oxygen, monitored by bedside ECG, and closely monitored pulse, respiration, blood pressure, oxygen saturation, and ECG. Observe and record every 30 min minutes within 6 hours after the operation, and change to 1 hour after stabilization until 48 hours or 72 hours. After treatment and nursing, he was discharged from the hospital.

And the monitoring of spinal cord and nerve function: make the patient move both lower limbs, and evaluate whether the muscle strength is back to normal. Observe and record every 30 minutes in the first 12 hours after operation to prevent the occurrence of spinal cord ischemia-reperfusion injury.

Comprehensive functional exercise: on the day of operation, encourage and assist patients to stretch and bend their ankles and knees, improve the muscle fatigue of supine limbs, and relax muscles after operation and operation. On the first day after the operation, respiratory function training was added, and the frequency and intensity of training were determined according to the patient's personal tolerance and the patient's basic exercise. On the third day after the operation, the exercise of both upper limbs was increased, including fist-clenching, chest-expanding, shoulder-shrugging, shoulder-lifting, abduction, and rotation, so as to promote the recovery of vital capacity and prevent scapulohumeral periarthritis and joint stiffness. One week after the operation, after the patient's body temperature dropped, pain improved, and physique recovered, four-point support training was conducted to train the back extension function.

2.8. Statistical Methods. SPSS 21.0 statistical software was used for the statistical analysis of the data. The calculated data conforming to normal distribution were represented by the mean standard deviation ($\overline{X} \pm S$) and the T-test was adopted. The in-conforming data were expressed as the percentage (%) and the χ^2 test was used. The structural integrity and distribution of cartilage end plate, annulus fibrosus, and osseous end plate at different DIDCE levels were examined by $R \times C$ chi-square. Kendall's rank correlation was used to analyze the correlation of dichotomous variables. $P < 0.05$ indicated significant differences.

3. Results

3.1. Experimental Results of Different Algorithms. Select the region of interest (ROI) in the experiment; an MR image reconstructed from full sampling data is the gold standard of the image reference. The Regridding algorithm, ESPIRiT algorithm, and CRN algorithm were used to reconstruct MR images, respectively. Then, the 10 echo signals of single exponential fitting were compared with the gold standard for F-test, to judge whether the fitting results obtained by the three algorithms were significantly different from the gold standard.

As shown in Figure 2, the 10 echo signals of ESPIRiT algorithm and CRN algorithm had higher numerical similarity with gold standard echo signals, and the attenuation trend of echo signals was more similar to the gold standard. According to Figure 3, the reconstruction results of the Regridding algorithm were statistically different from the gold standard, while the results of ESPIRiT algorithm and CRN algorithm were not significantly different from the gold standard. Compared with ESPIRiT reconstruction algorithm, the CRN reconstruction algorithm had more advantages.

3.2. UTE Imaging Analysis of Bone Integrity of Cartilage Endplate, Annulus Fibrosus, and Vertebral Endplate. In the UTE image in the first echo signal, the nucleus pulposus showed a uniform low signal; the cartilaginous endplate between the nucleus pulposus and the upper and lower vertebral bodies showed continuous high signal; the vertebral endplate showed continuous and complete isosignal; the annulus fibrosus of the nucleus pulposus had a spindle shape and slightly higher signal. After the UTE image was silhouetted, the nucleus pulposus still showed uniform low
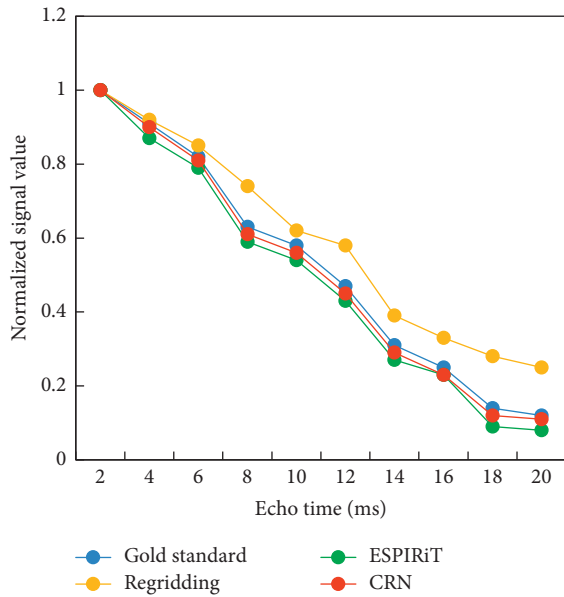
FIGURE 2: Line chart of 10 echo signals of Regridding, ESPIRiT, and CRN algorithms.
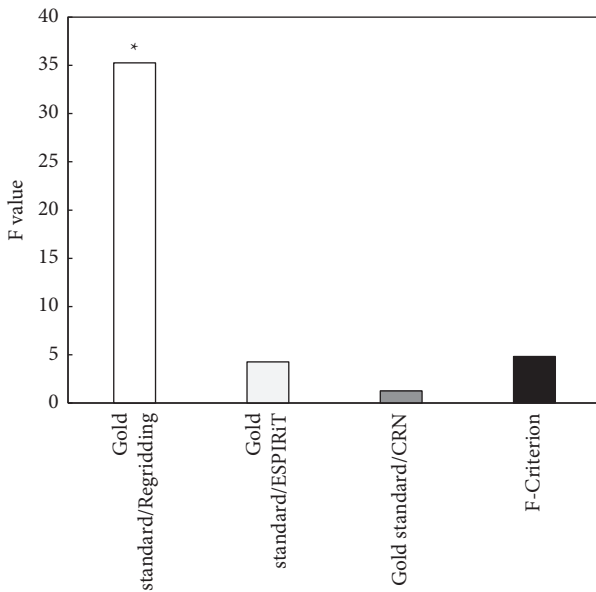

FIGURE 3: F-test results of Regridding, ESPIRiT, and CRN algorithms. *Compared with F-standard, $P < 0.05$.

signal; the cartilaginous endplate showed linear continuous high signal; the upper and lower layers of the vertebral endplate were intact and continuous, presenting slightly low signal; the annulus fibrosus was complete in shape, and the signal was continuously slightly higher (Figure 4).

The UTE images of moderate DIDCE in the first echo signal and after silhouette showed that the morphological structure of the cartilage endplate, annulus fibrosus, and vertebral endplate was partially disappeared and that the structure of one side was incomplete (Figure 5).

The UTE images of severe DIDCE in the first echo signal and after silhouette showed that the morphological structure

of the cartilage endplate, annulus fibrosus, and vertebral endplate was absent and that the structures of the upper and lower sides were absent (Figure 6).

3.3. Bone Integrity Distribution and Composition Ratio of Cartilage Endplate, Annulus Fibrosus, and Vertebral Endplate. 90 patients with intervertebral disc cartilage endplate degeneration were divided into the lumbago group (62 cases) and nonlumbago group (28 cases) according to whether they had lumbago. The bone integrity of the cartilaginous endplate and bony endplate structure showed no statistical difference between the two groups ($P > 0.05$). They had the highest proportion of partial disappearance and the lowest proportion of complete disappearance in both groups. As for the structural integrity distribution of annulus fibrosus, the proportions of partial disappearance and complete disappearance were higher in the lumbago group than in the nonlumbago group, with statistical differences ($P < 0.05$), as shown in Figure 7.

3.4. Correlation Analysis between Clinical Symptoms and Degeneration Degree of Intervertebral Disc. Included discs were graded according to the Pfirrmann grading criteria, as shown in Figure 8. Patients were divided into lumbago group and nonlumbago group according to the clinical symptoms, and there was no statistical difference in the constituent ratio between the two groups ($P > 0.05$), indicating that there was little correlation between the intervertebral disc degeneration degree and clinical symptoms.

3.5. The Correlation between Structural Integrity of Cartilage Endplate and Pfirrmann Grading of Intervertebral Disc Degeneration. According to the different Pfirrmann grades of the lumbago group and the nonlumbago group, the $R \times C$ Chi-square test was performed on the integrity composition ratio of different cartilage endplates. The results showed that the χ^2 of the lumbago group and the nonlumbago group were 169.32 and 35.02, respectively, with a statistical difference ($P < 0.05$), indicating that intervertebral disc degeneration was correlated with the integrity of cartilage endplate. Kendall's was 0.512 and 0.547, respectively, showing a moderate correlation (Tables 3–4).

3.6. Satisfaction of Rehabilitation Nursing. The experimental results show that the nursing satisfaction of patients in the intervention group (97%) is significantly higher than that of patients in the control group (69%), and there is a statistical difference between the two groups ($P < 0.05$) (Figure 9).

4. Discussion

With a series of physiological and pathological changes, the internal permeability of the intervertebral disc nucleus pulposus reduces, and water loss gradually occurs, leading to fibrosis, and then nucleus pulposus tension is falling and intervertebral disc height changes, resulting in a material exchange between the cartilage endplate in dispersion effect.
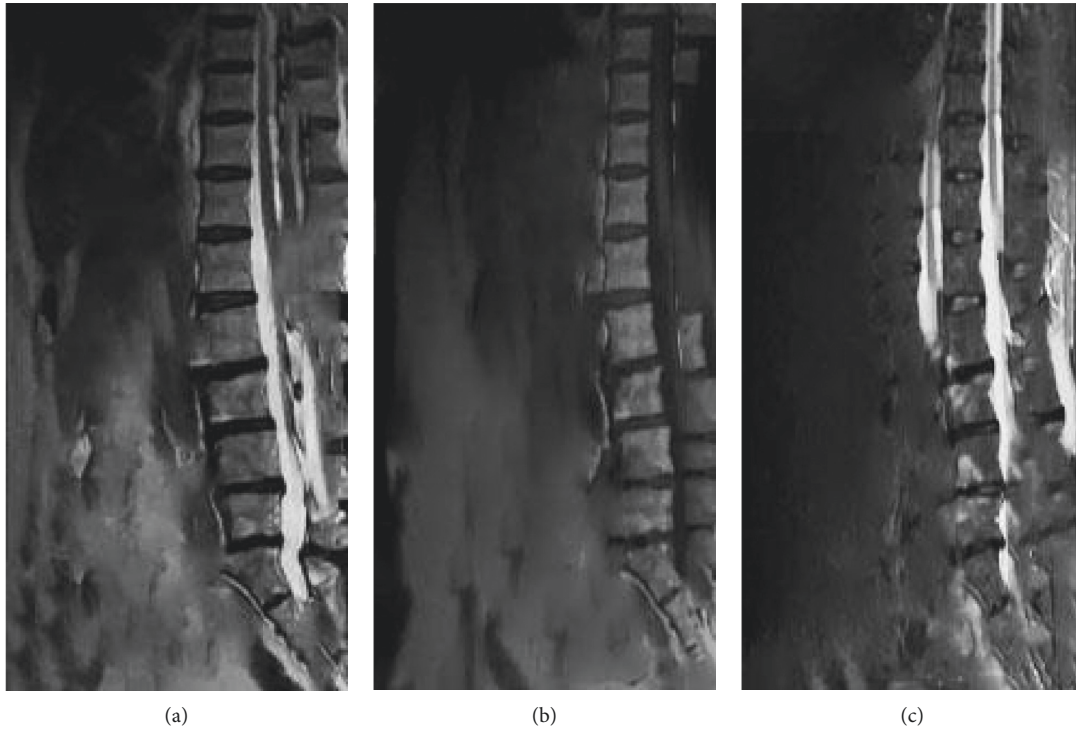
(a)   (b)   (c)

FIGURE 4: T2WI, T1WI, and UTE images of a female aged 53 who did not have low back pain. (a) T2WI; (b) T1WI; (c) UTE.

(a)   (b)   (c)
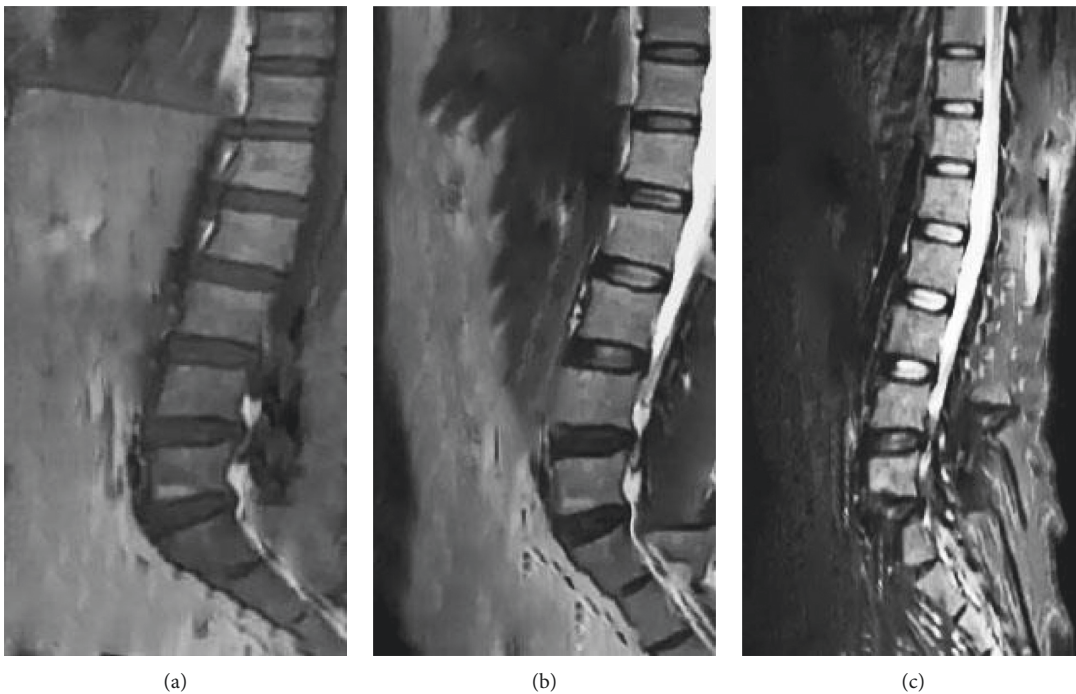
FIGURE 5: T2WI, T1WI, and UTE images of a male aged 65 who had suffered low back pain accompanied by radiating pain in the left limb for 5 years. (a) T2WI; (b) T1WI; (c) UTE.

Therefore, cartilage endplate degeneration is a major cause of intervertebral disc degeneration. MR imaging manifestations of intervertebral disc degeneration mainly include decreased T2 signal of the intervertebral disc, intervertebral disc vacuum changes, bone marrow changes, mutations, annulus fibrosus tears, calcification, ligament changes, and spinal stenosis [20–22]. Decreased disc T2 signal is due to changes in glycosaminoglycan concentration and water molecular content. As the disc develops, a vacuum will occur, which on MR imaging shows no signal on T1WI and
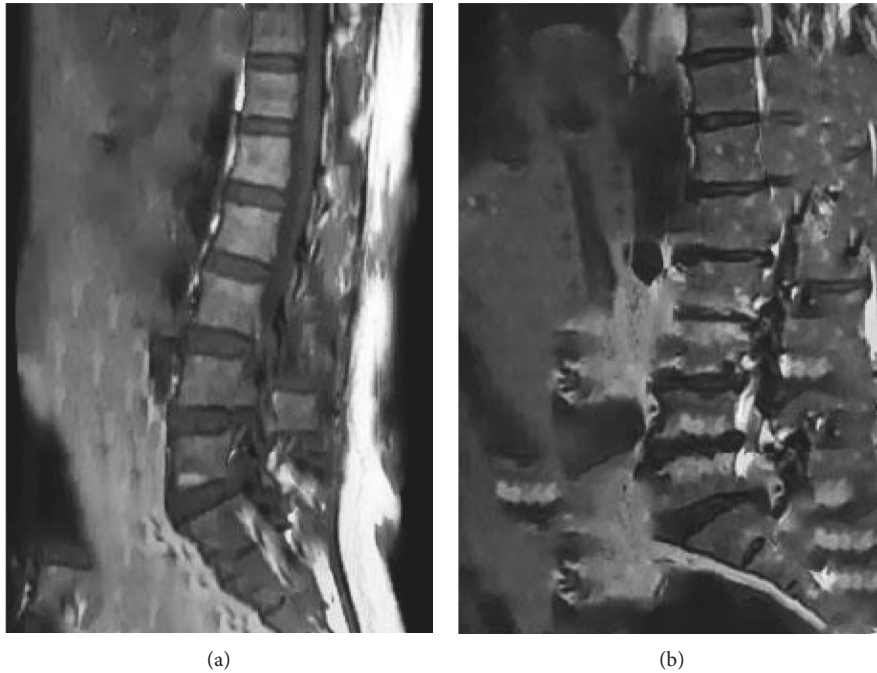
(a) (b)

Figure 6: T2WI and UTE images of a female aged 62 who had suffered repeated low back pain for 8 years. (a) T2WI; (b) UTE.
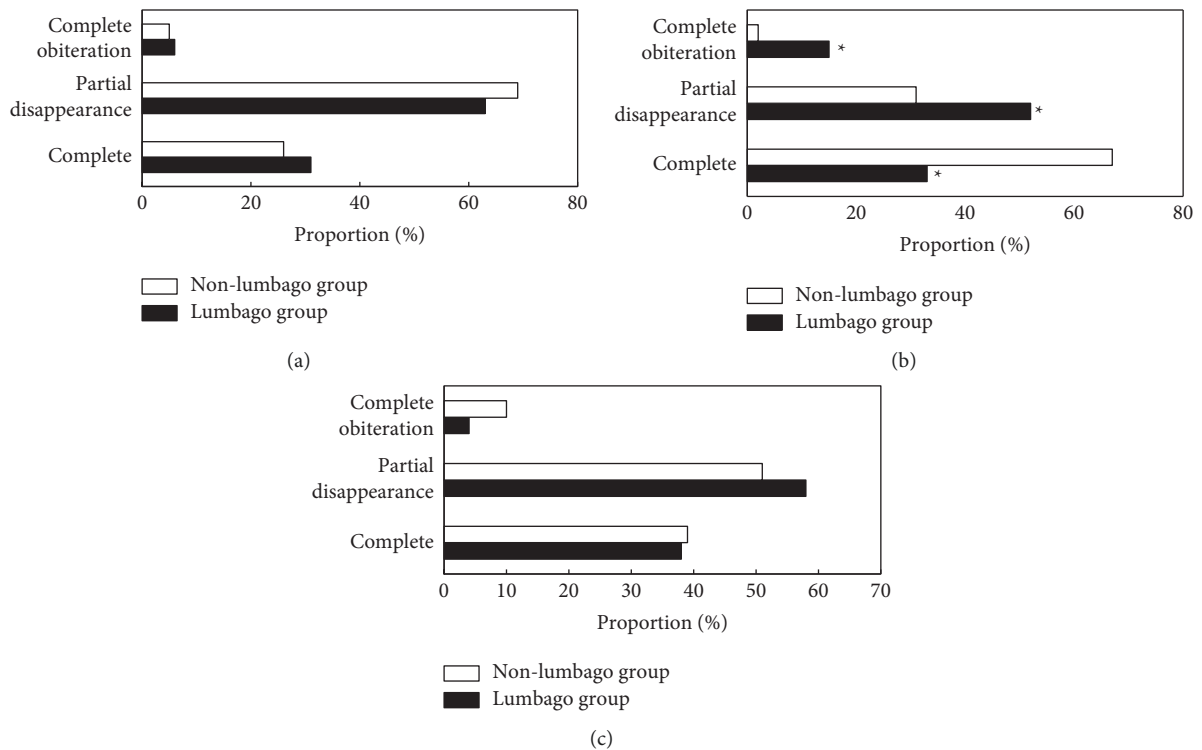

(a)

(b)

(c)

Figure 7: Bone integrity analysis of cartilage endplate, annulus fibrosus, and vertebral endplate. (a) Integrity of cartilage endplate; (b) annulus fibrous integrity; (c) integrity of vertebral endplates. *Compared with the nonlumbago group, $P < 0.05$.

T2WI images. When the intervertebral disc is calcified, there will be a low signal or no signal in the MR image. Pfirrmann grading scale is a T2WI sagittal grading method based on intervertebral disc nucleus pulposus structure, signal strength, intervertebral disc height, and annulus fibrosus boundary.

MR-UTE technology is a new technology for short T2 tissue imaging in the human body, which can reduce the
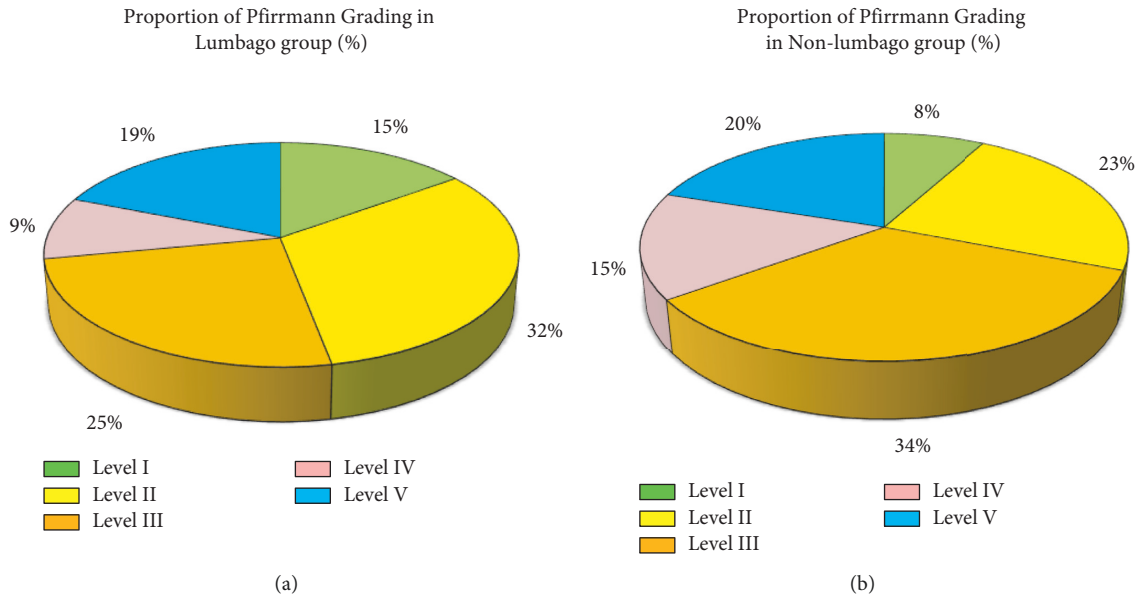
FIGURE 8: Degeneration degree of the intervertebral disc in different clinical symptoms. (a) Lumbago group; (b) nonlumbago group.

TABLE 3: The integrity of cartilage endplate and Pfirrmann grading distribution of intervertebral disc degeneration in the lumbago group.

| | Pfirrmann grading | | | | | χ^2 | P |
	Level I	Level II	Level III	Level IV	Level V		
Complete	75	65	18	15	2	169.32	0.000
Partial disappearance	21	32	78	81	62		
Complete obliteration	4	3	4	4	36		

TABLE 4: The integrity of cartilage endplate and Pfirrmann grading distribution of intervertebral disc degeneration in the nonlumbago group.

| | Pfirrmann grading | | | | | χ^2 | P |
	Level I	Level II	Level III	Level IV	Level V		
Complete	82	45	15	1	2	35.02	0.000
Partial disappearance	15	51	76	98	76		
Complete obliteration	3	4	8	1	22		

echo time and obtain images before the MR signal of short T2 tissue attenuates to 0 [23]. The cartilage endplate of intervertebral disc tissue is a kind of hyaline cartilage, rich in polysaccharides, collagen, and water. It shows no signal by conventional sequence, while UTE sequence can well display the cartilage endplate and short T2 tissue of the anterior and posterior longitudinal ligaments. In MR-UTE images, intact intervertebral discs and calcified cartilaginous endplates showed mainly medium-high signals near the cartilaginous endplate. In this study, Pfirrmann grades of T2WI sequences of patients with different degrees of disc degeneration were analyzed, and the results showed that there was little correlation between the disc degeneration degree and clinical symptoms, in line with the results of Sampara et al. [24].

Then, the morphological integrity of cartilage endplate in patients with and without lumbago was evaluated, which was divided into integrity, partial disappearance, and complete disappearance. The results showed that there was a statistical difference in the proportion of partial disappearance and complete disappearance of annulus fibrosus between the two groups ($P < 0.05$), indicating that low back pain was correlated with annulus fibrosus integrity. Next, the correlation between Pfirrmann grading and cartilage endplate integrity in two groups of patients with disc degeneration was analyzed, and the results showed that different degrees of disc degeneration were moderately correlated with cartilage endplate integrity, consistent with the results of Saberi et al. [25].

Finally, two groups of patients were compared for satisfaction with the nursing methods. The results showed that the patients in the lumbago group had good recovery effects, with high nursing satisfaction.
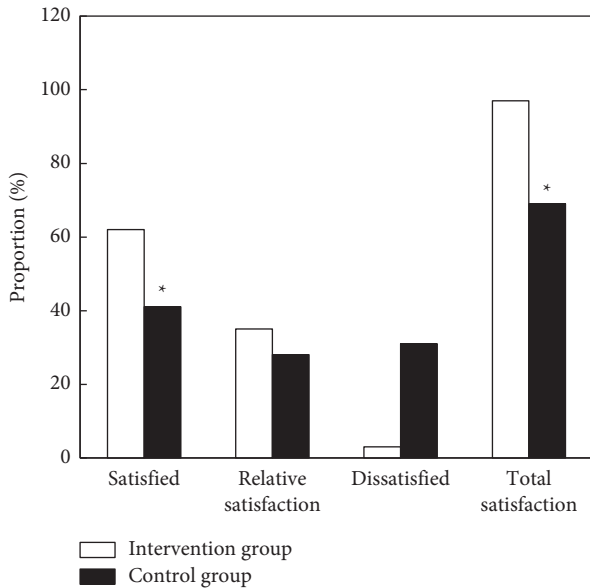
Figure 9: Comparison of rehabilitation nursing satisfaction. *Compared with the intervention group, $P < 0.05$.

5. Conclusion

In this study, MR-UTE imaging technology based on the CRN algorithm was used to analyze the images of 90 patients with intervertebral disc degeneration and to evaluate the therapeutic effect of rehabilitation nursing intervention. It was found that the CRN algorithm successfully removes artifacts and noise in the under-sampled image, that different degrees of intervertebral disc degeneration were moderately correlated with the integrity of cartilage endplate, and that cartilage endplate, annulus fibrosus, and bony endplate partially disappeared by the MR-UTE imaging technique. Rehabilitation intervention proved to have a positive effect on the treatment of patients with intervertebral disc degeneration and can improve patients' satisfaction. The limitation of this study is that the sample size is small, and the quality of MR-UTE data is different, which increases the evaluation error. Later, it is necessary to expand the sample size and include high-quality data for further in-depth discussion. In conclusion, MR-UTE imaging can clearly display the degeneration of disc cartilage, providing a new technique for the noninvasive evaluation of disc structure.

Data Availability

The data used to support the findings of this study are available from the corresponding author upon request.

Conflicts of Interest

The authors declare no conflicts of interest.

References

[1] J. Zhang, J. Zhang, Y. Zhang et al., "Mesenchymal stem cells-derived exosomes ameliorate intervertebral disc degeneration through inhibiting pyroptosis," *Journal of Cellular and Molecular Medicine*, vol. 24, no. 20, pp. 11742–11754, 2020.

[2] P. H. Wu, H. S. Kim, and I. T. Jang, "Intervertebral disc diseases part 2: a review of the current diagnostic and treatment strategies for intervertebral disc disease," *International Journal of Molecular Sciences*, vol. 21, no. 6, p. 2135, 2020.

[3] L. Kang, S. Liu, J. Li, Y. Tian, Y. Xue, and X. Liu, "The mitochondria-targeted anti-oxidant MitoQ protects against intervertebral disc degeneration by ameliorating mitochondrial dysfunction and redox imbalance," *Cell Proliferation*, vol. 53, no. 3, Article ID e12779, 2020.

[4] B. G. Ashinsky, E. D. Bonnevie, S. A. Mandalapu et al., "Intervertebral disc degeneration is associated with aberrant endplate remodeling and reduced small molecule transport," *Journal of Bone and Mineral Research*, vol. 35, no. 8, pp. 1572–1581, 2020.

[5] J. Lin, J. Zhuge, X. Zheng et al., "Urolithin A-induced mitophagy suppresses apoptosis and attenuates intervertebral disc degeneration via the AMPK signaling pathway," *Free Radical Biology and Medicine*, vol. 150, pp. 109–119, 2020.

[6] S. Veraa, W. Bergmann, I. D. Wijnberg et al., "Equine cervical intervertebral disc degeneration is associated with location and MRI features," *Veterinary Radiology & Ultrasound*, vol. 60, no. 6, pp. 696–706, 2019.

[7] U. Zehra, N. Noel-Barker, J. Marshall, M. A. Adams, and P. Dolan, "Associations between intervertebral disc degeneration grading schemes and measures of disc function," *Journal of Orthopaedic Research*, vol. 37, no. 9, pp. 1946–1955, 2019.

[8] W. Bergmann, N. Bergknut, S. Veraa et al., "Intervertebral disc degeneration in warmblood horses: morphology, grading, and distribution of lesions," *Veterinary Pathology Online*, vol. 55, no. 3, pp. 442–452, 2018.

[9] D. Nakashima, N. Fujita, J. Hata et al., "Quantitative analysis of intervertebral disc degeneration using Q-space imaging in a rat model," *Journal of Orthopaedic Research*, vol. 38, no. 10, pp. 2220–2229, 2020.

[10] Q. X. Zhang, D. Guo, F. C. Wang, and W. Y. Ding, "Necrosulfonamide (NSA) protects intervertebral disc degeneration via necroptosis and apoptosis inhibition," *European Review for Medical and Pharmacological Sciences*, vol. 24, no. 5, pp. 2683–2691, 2020.

[11] K. Ma, S. Chen, Z. Li et al., "Mechanisms of endogenous repair failure during intervertebral disc degeneration," *Osteoarthritis and Cartilage*, vol. 27, no. 1, pp. 41–48, 2019.

[12] L. Zhu, C. Yu, X. Zhang et al., "The treatment of intervertebral disc degeneration using traditional Chinese medicine," *Journal of Ethnopharmacology*, vol. 263, Article ID 113117, 2020.

[13] S. Senck, K. Trieb, J. Kastner, S. G. Hofstaetter, H. Lugmayr, and G. Windisch, "Visualization of intervertebral disc degeneration in a cadaveric human lumbar spine using microcomputed tomography," *Journal of Anatomy*, vol. 236, no. 2, pp. 243–251, 2020.

[14] K. Yang, H. Li, and C. Li, "Expression and role of Sphingosine 1-phosphate receptors in intervertebral disc degeneration," *Journal of Back and Musculoskeletal Rehabilitation*, vol. 33, no. 2, pp. 255–262, 2020.

[15] Z. Lv, L. Qiao, Q. Wang, and F. Piccialli, "Advanced machine-learning methods for brain-computer interfacing," *IEEE/ACM Transactions on Computational Biology and Bioinformatics*, vol. 18, no. 5, pp. 1688–1698, 2021.

[16] Z. Wan, Y. Dong, Z. Yu, H. Lv, and Z. Lv, "Semi-supervised support vector machine for digital twins based brain image fusion," *Frontiers in Neuroscience*, vol. 15, Article ID 705323, 2021.

[17] M. Hu, Y. Zhong, S. Xie, H. Lv, and Z. Lv, "Fuzzy system based medical image processing for brain disease prediction," *Frontiers in Neuroscience*, vol. 15, Article ID 714318, 2021.

[18] X. Zhou, Y. Li, and W. Liang, "CNN-RNN based intelligent recommendation for online medical pre-diagnosis support," *IEEE/ACM Transactions on Computational Biology and Bioinformatics*, vol. 18, no. 3, pp. 912–921, 2021.

[19] T. Oichi, Y. Taniguchi, K. Soma et al., "A mouse intervertebral disc degeneration model by surgically induced instability," *Spine 1976*, vol. 43, no. 10, pp. E557–E564, 2018.

[20] X. Zhou, T. Jin, L. Wang, E. Zhao, and X. Xiao, "Clinical practice of epidermal growth factor receptor-tyrosine kinase inhibitor targeted drugs combined with gadolinium oxide nanoparticles in the treatment of non-small cell lung cancer," *Bioengineered*, vol. 13, no. 1, pp. 128–139, 2022.

[21] C. Zhang, S. E. Gullbrand, T. P. Schaer et al., "Inflammatory cytokine and catabolic enzyme expression in a goat model of intervertebral disc degeneration," *Journal of Orthopaedic Research*, vol. 38, no. 11, pp. 2521–2531, 2020.

[22] K. Z. Lim, C. D. Daly, P. Ghosh et al., "Ovine lumbar intervertebral disc degeneration model utilizing a lateral retroperitoneal drill bit injury," *Journal of Visualized Experiments*, vol. 25, no. 123, Article ID 55753, 2017.

[23] Z. Li, X. Li, R. Tang, and L. Zhang, "Apriori algorithm for the data mining of global cyberspace security issues for human participatory based on association rules," *Frontiers in Psychology*, vol. 11, Article ID 582480, 2021.

[24] P. Sampara, R. R. Banala, S. K. Vemuri, G. R. Av, and S. Gpv, "Understanding the molecular biology of intervertebral disc degeneration and potential gene therapy strategies for regeneration: a review," *Gene Therapy*, vol. 25, no. 2, pp. 67–82, 2018.

[25] A. Saberi, Z. Salehi, B. Naderinabi, S. H. Ansari, and S. Mashayekhi, "Genetic dimension of intervertebral disc degeneration: polymorphism of matrix metalloproteinase 1 and 3 in the north Iranian population," *Turkish Neurosurgery*, vol. 28, no. 3, pp. 447–453, 2018.

Research Article

MRI Semi-Quantitative Evaluation of Clinical Features of Cartilage Injury in Patients with Osteoarthritis

Xianchao Zhou and Xiang Shen [ID]

First Department of Orthopedics, The Fourth Hospital of Changsha, Changsha 410006, Hunan, China

Correspondence should be addressed to Xiang Shen; 19409107@smail.cczu.edu.cn

This study aimed to investigate the correlation between magnetic resonance imaging (MRI) findings of articular cartilage and clinical symptoms in patients with osteoarthritis (OA). Eighty patients with OA were selected as the study subjects (OA group) and 80 healthy subjects during the same period were also selected as the control group. All subjects underwent knee sagittal PDW-SPAIR, sagittal T1WI-aTSE, sagittal T2WI-TSE, coronal PDW-SPAIR, sagittal 3D-WATSc, and sagittal T2 mapping scans. Thereafter, all subjects underwent clinical assessment. The whole-organ MRI score (WORMS) was adopted for MRI examination and semiquantitative analysis, and the T2 value was calculated. The correlation among T2 value, WORMS, and Western Ontario and Mc Master University OA Index (WOMAC) was then compared and analyzed. The correlation coefficients between T2 values and WORMS in each sub-region of patients with OA were 0.8, 0.55, −0.038, 0.811, and 0.743; the correlation coefficients between WORMS and WOAMC were 0.66, 0.71, 0.46, and 0.88; and the correlation coefficients between T2 values and WOAMC were 0.483, 0.33, 0.282, and 0.636, respectively. There was a significant positive correlation between the results of MRI semiquantitative analysis and clinical symptoms as well as disease severity in patients with OA.

1. Introduction

Osteoarthritis (OA), also known as degenerative joint disease, is the most common form of arthritis [1]. The disease is characterized by slow onset and gradual aggravation, so its clinical manifestations are often relatively insidious and often easily overlooked [2]. Clinically, it is generally divided into two types: primary and secondary, and OA usually refers to primary, and the disease is most often diagnosed in middle-aged and elderly women [3]. In recent years, with the rapid development of medical technology, the pathology, physiology, and diagnosis of OA have been greatly developed, but there is no unified and accurate conclusion on its pathogenesis [4]. In recent years, the disease has gradually shown a tendency to be younger, and its incidence is also increasing with age, with an incidence of approximately 30% in people over 65 years of age [5]. With the increasing population of obesity and the elderly, its incidence is still rising, and the World Health Organization predicts that OA will become the fourth leading cause of disability in the next few years [6].

In recent years, articular cartilage lesions have become the focus of research on the pathogenesis and progression of OA. Numerous clinical studies have shown that the pathogenesis of OA generally starts from the lesions of articular cartilage, and wear degeneration, or even stripping defects of cartilage can occur in the early stages of the disease [7, 8]. However, the absence of nerve distribution in cartilage does not directly produce pain, which is also the main reason that the insidious clinical symptoms of OA are not easily detected [9]. Therefore, monitoring the lesions of articular cartilage is very important for the diagnosis and treatment of OA. An arthroscopic biopsy is considered the gold standard for the diagnosis of cartilage damage in clinical practice, but as a seminal examination, it has the following disadvantages: this examination is invasive; it can only show the articular cartilage surface but not the full thickness of cartilage, so there are limitations in the visual field, so it cannot be

routinely used in clinical practice [10, 11]. In contrast, magnetic resonance imaging (MRI) shows a higher resolution for soft tissues and has gradually received clinical attention as a noninvasive and radiation-free inspection method [12]. Especially in recent years, with the emergence of high-intensity MRI and the continuous improvement of relevant software and hardware, MRI can completely and clearly show the articular cartilage [13, 14]. The current MRI diagnosis of knee OA cartilage lesions shows that the pathological changes of an early OA are closely related to cartilage damage caused by inflammation at the cartilage molecular level [15–17]. However, there are still controversies about the study results of MRI manifestations and the clinical correlation of knee OA cartilage defects all over the world. For example, some scholars have explored the diagnostic value of the total knee MRI scores for knee OA and found that the whole-organ MRI score (WORMS) was positively correlated with Western Ontario and Mc Master University Osteoarthritis Index (WOMAC) score, indicating that the pain, stiffness, and function of patients with the knee OA can be explained by imaging, and multiple linear regression analysis has been confirmed [18, 19]. However, some scholars have accurately measured the T2 of cartilage in each area of the knee joint using T2 maps generated by MR sagittal T2 mapping imaging sequences and found that cartilage T2 values were increased and weight-bearing areas were significant in patients with OA, but there was no significant correlation between clinical scores and cartilage T2 changes in all subjects [20]. In summary, further studies and confirmation are needed regarding the correlation between MRI findings and clinical symptoms.

The patients with OA were selected as the study subjects, and the clinical and MRI evaluations of the patients and the correlation between them were analyzed to provide a reference and basis for the treatment and diagnosis of related diseases in clinical practice.

2. Research Methods

2.1. Study Subjects.
Eighty patients with OA in the hospital from February 2019 to March 2020 were selected as the study subjects and included in the OA group. Two chief physicians selected the study subjects according to the diagnostic criteria for the knee OA in the 2007 *Guidelines for the Diagnosis and Treatment of Osteoarthritis*. Another 80 healthy subjects during the same period were also selected as the control group. Inclusion criteria: patients who meet the diagnostic criteria of knee OA; patients who have no history of trauma surgery, tumor, or rheumatoid arthritis; patients without claustrophobia and other diseases not suitable for MRI examination. The informed consent was obtained from patients and this study was approved by the ethics committee of the hospital.

Inclusion criteria were as follows: no clinical manifestations related to knee OA; no immediate family members with rheumatic immune disease or another medical history; no history of knee surgery, or trauma; and people with normal medical examination results. Exclusion criteria were as follows: patients with the WOMAC index higher than that

of grade II; patients with significant trauma; and patients with a history of surgery.

2.2. MRI Examination Method.
Examination equipment: 3.0 T superconducting magnetic resonance; coil: 8-channel knee coil postprocessing workstation: MR Workspace 2.6.3.5 workstation.

Preparation before examination: the contraindications of MRI examination were investigated and the patients were instructed to keep the knee joint still as much as possible during the examination. All subjects rested for 30 minutes before the MRI examination.

Scanning method: the ear plug was used and the patient was in the supine position with the feet advanced and the lower limbs straight. The knee of the examined side was placed in the 8-channel knee coil so that the coil center was directly opposite to the knee, and sponge pads were added to the knee of examined side and feet to make the patient's position comfortable. Sagittal PDW-SPAIR, sagittal T1WI-aTSE, sagittal T2WI-TSE, coronal PDW-SPAIR, sagittal 3D-WATSc, and sagittal T2 mapping were performed, respectively.

Scanning parameters: [sagittal PAW-SPAIR] TR = 3,484 ms, TE = 30 ms, FOV160 × 160 mm, matrix 176 × 135, NEX = 2, layer thickness: 4 mm, interslice distance: 0.4 mm, number of layers: 18, scanning time: 2 min and 12 s; [sagittal T1WI-aTSE] TR = 633 ms, TE = 20 ms, FOV 160 × 160 mm, matrix 224 × 181, NEX = 2, layer thickness: 4 mm, interlayer distance: 0.4 mm, number of layers: 18, scanning time: 139 s; [sagittal T2WI-TSE] TR = 3,890 ms, TE = 100 ms, FOV 160 × 160 mm, matrix 212 × 161, NEX = 2, layer thickness: 4 mm, interlayer distance: 0.4 mm, number of layers: 18, scanning time: 2 min and 20 s; [coronal PAW-SPAIR] TR = 3,329 ms, TE = 25 ms, FOV 160 × 160 mm, matrix 356 × 285, NEX = 2, layer thickness: 3 mm, interlayer distance: 0.3 mm, number of layers: 18, scanning time: 166 s; [sagittal 3D-WATSc] TR = 20 ms, TE = 5.1 ms, FOV 160 × 160 mm, matrix 320 × 319, NEX = 2, layer thickness: 1.5 mm, interlayer distance: 0 mm, number of layers: 18, scanning time: 4 min and 26 s; [Sagittal T2 mapping] TR = 2,000 ms, TE = 13, 26, 39, 52, 65, 78 ms, FOV 160 × 160 mm, matrix 268 × 266, NEX = 1, layer thickness: 2.5 mm, interlayer distance: 0.25 mm, number of layers: 12*6, scanning time: 672 s.

2.3. Clinical Evaluation.
All subjects filled in the WOMAC score form carefully under the guidance of orthopedic surgeons, which was required to be completed within 5 to 10 minutes. The WOMAC is currently the most widely used assessment tool for knee or hip arthritis in clinical practice. The severity and therapeutic effect of the patient are evaluated based on the patient's relevant symptoms and signs. The evaluation contents include three aspects: pain, stiffness, and joint function, and include a total number of 24 items, 5 pain items, 2 stiffness items, and 17 joint function items. Each item includes 5 scoring points (0: normal, 1: mild, 2: moderate, 3: severe, 4: very severe).
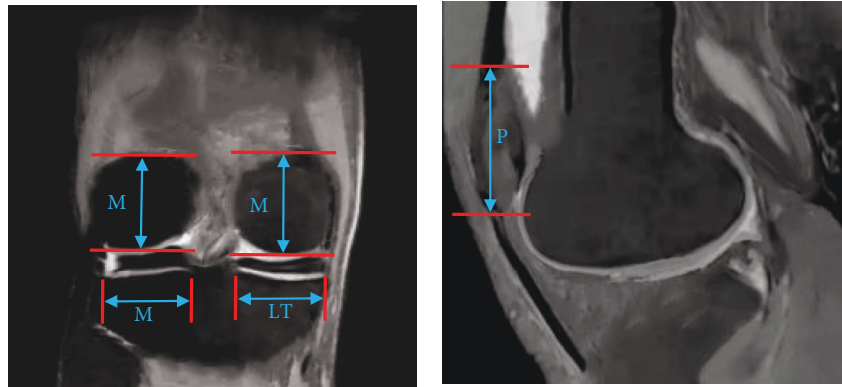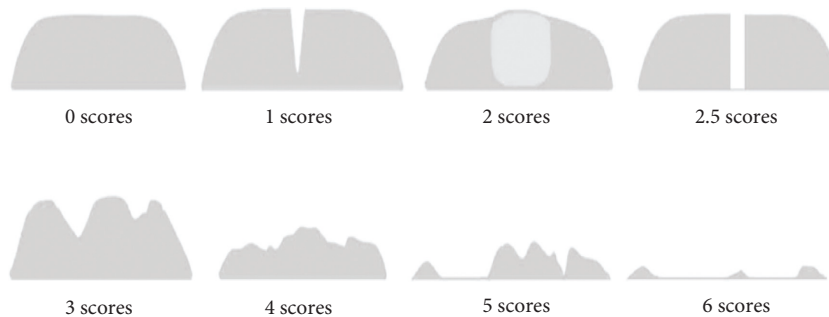
FIGURE 1: Knee cartilage partition method.

FIGURE 2: WORMS 8-point scoring for cartilage morphology.

TABLE 1: Comparison of general data between the two groups.

	Mean age	Gender (males/females)	Knee distribution	BMI	Course (month)
OA group ($n = 80$)	52.3 ± 11.2	48/32	41/39	22.3 ± 9.3	11.3 ± 4.6
Control group ($n = 80$)	51.1 ± 9.9	50/30	38/42	23.1 ± 11.02	10.08 ± 5.11
P	0.43	0.88	0.93	0.547	0.635

2.4. MRI Assessment. Before the MRI evaluation, it is necessary to reconstruct the coronal, sagittal, and axial images of the knee joint with the sagittal 3D-WATSc sequence image using the MPR multiplanar reconstruction group. WORMS was used to divide the knee cartilage into five subregions: medial region of femoral (MF), lateral region of femoral (LF), medial region of the tibia (MT), lateral region of the tibia (LT), and patella (P) (Figure 1).

MRI evaluation of cartilage morphology: according to 0–6 scores of WORMS 8 scoring points, the cartilage morphology in each sub-region of the knee joint was scored: 0: normal; 1: normal cartilage thickness but enhanced T2WI signal; 2: partial cartilage defects; 2.5: full-thickness cartilage defect; 3: multiple regional partial cartilage defects; 4: diffuse partial cartilage defect; 5: multi-regional full-thickness cartilage defect; 6: diffuse full-thickness cartilage defect. The specific scoring is shown in Figure 2.

According to the WORMS scores of each sub-regional cartilage of the patients, the sub-regional cartilage was divided into 0 and 1 scores as mild (OA1) group, and 2–3 scores as moderate (OA2) group. 4–6 scores as severe (OA3) group, and healthy control group as H group.

MRI measurement of the T2 value of each sub-region: sagittal T2 mapping sequence automatically generated the final T2 grayscale map by post-processing workstation, and manually delimited along the articular cartilage boundary on the T2 grayscale map. The T2 values of the five sub-regions of the knee joint were measured in turn. The T2 values of each region were measured three times and the average value was taken as the T2 value of each sub-region.

2.5. Statistical Analysis. The analysis of all data was completed by the SPSS 19.0 statistical software. Measurement data were expressed as (mean ± standard deviation), and the test method was an independent sample t-test. Enumeration data were expressed as frequency (percentage), and the test method was the chi-square test. $P < 0.05$ was considered statistically significant.
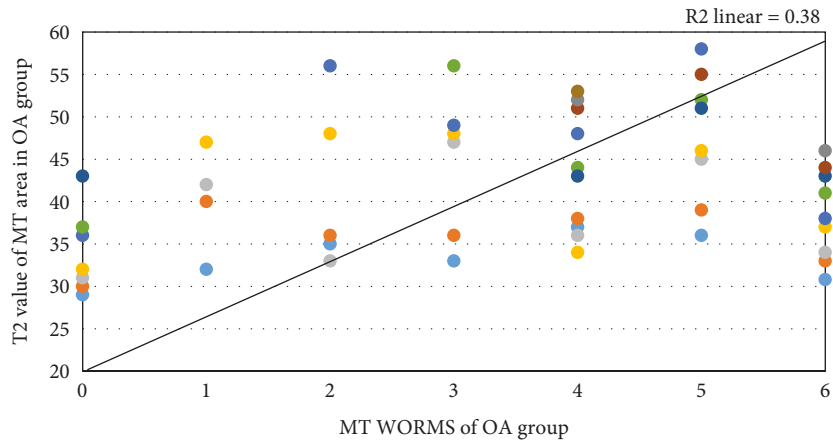
3. Results

3.1. General Data. The general data of patients in the two groups are shown in Table 1. It showed that the mean age of
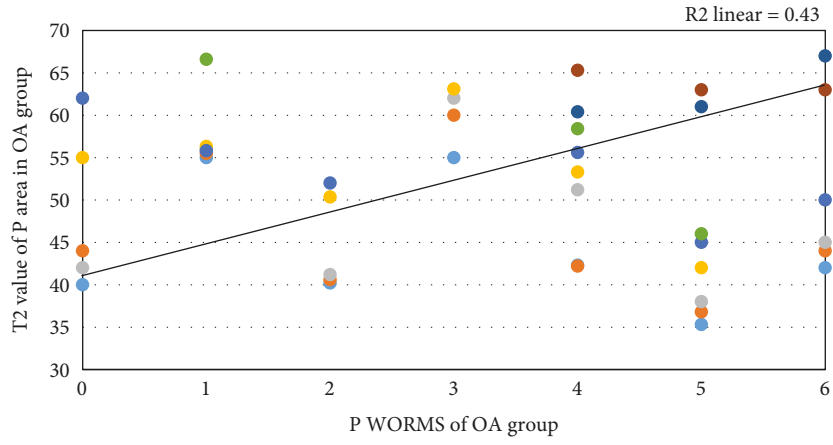
(a)
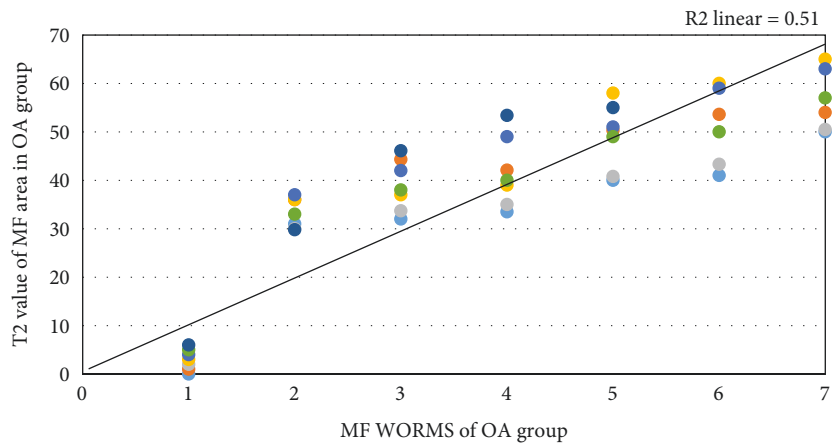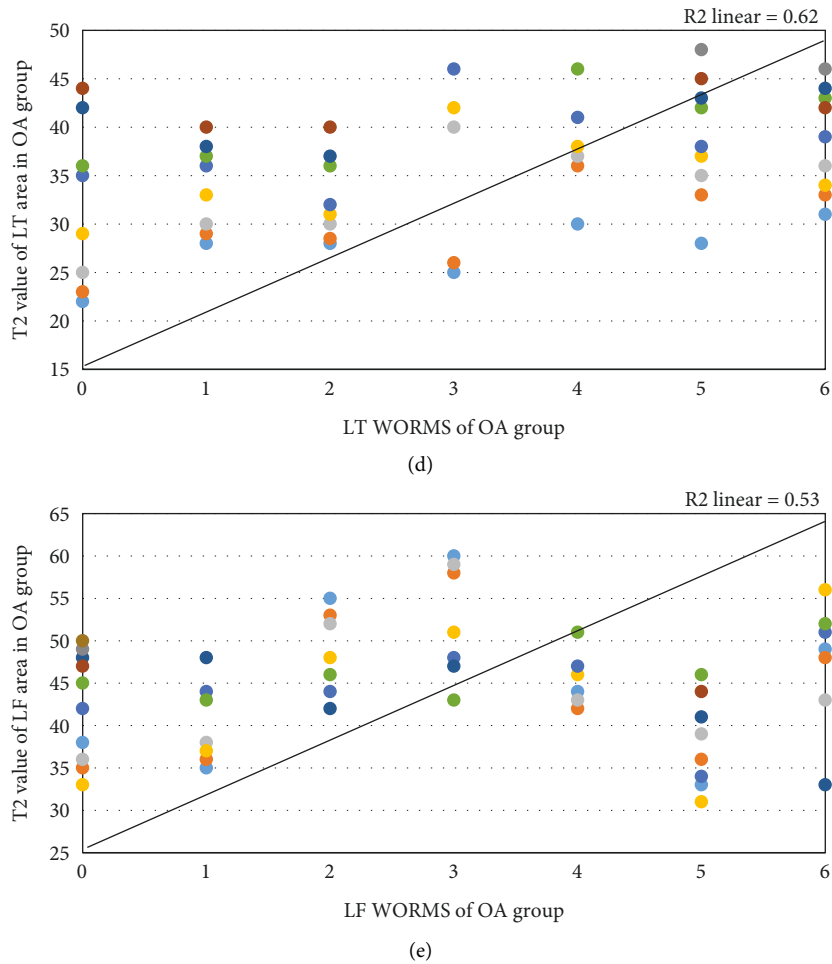

(b)

(c)

Figure 3: Continued.

(d)

(e)

FIGURE 3: Scatterplot of correlation analysis between T2 values and WORMS in each sub-region of patients with OA. A : P; B : MF; C : MT; D : LT; E : LF. Each dot represented a case.

patients in the OA group was 52.3 ± 11.2 years old, 48/32 males/females, 41 right knees, and 39 left knees; the mean age of the population in the control group was 51.1 ± 9.9 years old, 50/30 males/females, 38 right knees, and 42 left knees. There was no significant difference in age, gender, and knee distribution between the two groups, $P < 0.05$.

3.2. Correlation Analysis between T2 Values and WORMS in Each Sub-Region of Patients with OA.
The correlation analysis results between T2 values and WORMS in each sub-region of patients with OA are shown in Figure 3. Analysis of Figure 3 showed that in the OA group, the correlation coefficients between cartilage T2 values and WORMS were 0.8, 0.55, −0.038, 0.811, and 0.743 in the P, MF, MT, LT, and LF, respectively. The analysis showed that the T2 values of P, MF, MT, and LT were positively correlated with WORMS, and the T2 value of LF was not correlated with WORMS.

3.3. Correlation Analysis between Cartilage WORMS and WOAMC Scores in OA Group.
The results of the correlation analysis between cartilage WORMS and WOAMC scores in

the OA group are shown in Figure 4. The correlation coefficients between the cartilage WORMS score and the clinical WOAMC total score and each subdomain (pain, stiffness, joint function) score in the OA group were 0.66, 0.71, 0.46, and 0.88, respectively, indicating that cartilage WORMS was positively correlated with clinical WOAMC total score, pain score, stiffness score, and joint function score in the OA group. The correlation degree was divided into high correlation, moderate correlation, low correlation, and high correlation.

3.4. Correlation between Cartilage T2 Value and WOAMC Scores in the OA Group.
The results of the correlation analysis between the cartilage T2 value and the WOAMC scores in the OA group are shown in Figure 5. The correlation coefficients between the cartilage T2 value and the clinical WOAMC total score and each subdomain (pain, stiffness, joint function) scores in the OA group were 0.483, 0.33, 0.282, and 0.636, respectively, which indicated that the cartilage T2 value was positively correlated with the clinical WOAMC total score, pain score, stiffness score, and joint
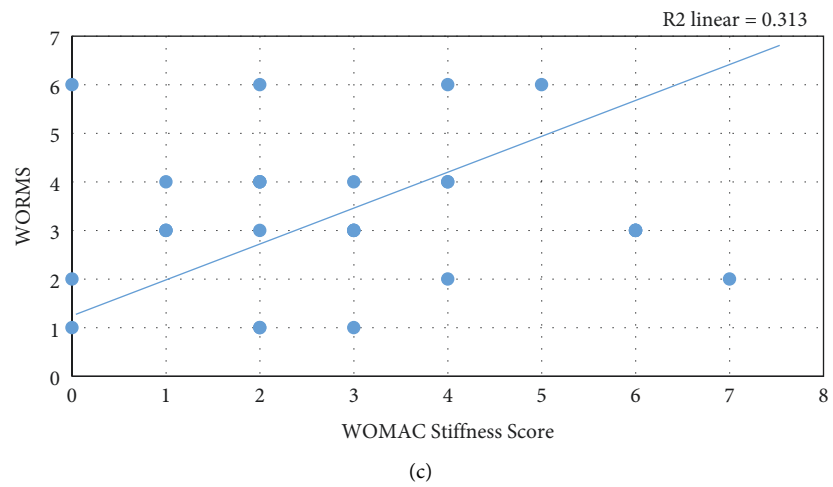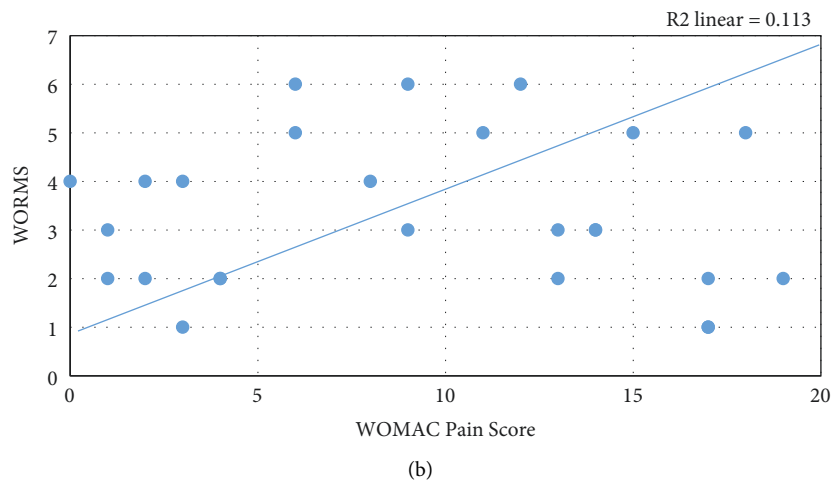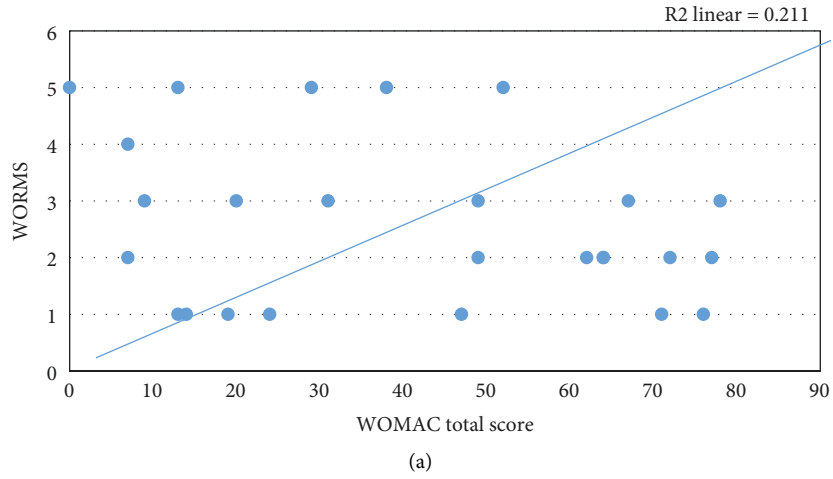
(a)
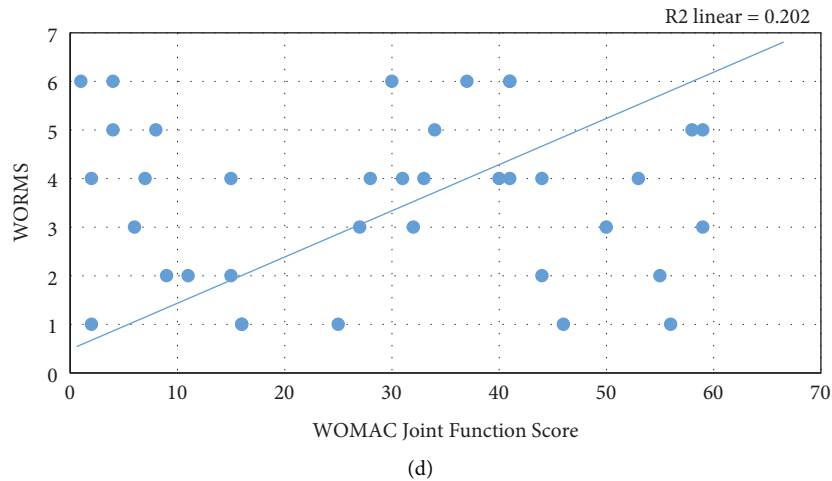

(b)

(c)

Figure 4: Continued.

FIGURE 4: Scatterplot of correlation analysis between cartilage WORMS and WOAMC scores in the OA group. (a) WOMAC total score; (b) WOMAC pain score; (c) WOMAC stiffness score; (d) WOMAC joint function score.

function score in the OA group, and the degree of correlation was divided into moderate correlation, low correlation, low correlation, and moderate correlation.

4. Discussion

The knee joint is composed of the lower end of the tibia, the upper segment of the tibia and fibula, and the patella, which carries 3/4 of the weight of the human body and is the most used sport's joint of the human body, so the probability of its lesions is also much higher than those of other joints [21]. Clinically, arthritis is generally divided into two types: primary and secondary. Primary degenerative arthritis mostly occurs in the elderly. The analysis of its etiology may be that the bones and joints of the elderly appear a certain degree of aging [22]. Secondary degenerative arthritis may occur at any age and is generally mainly caused by trauma, joint structure instability, and endocrine disorders [23]. Regardless of the type of degenerative arthritis, it can limit the patient's movement and seriously affect the patient's quality of life. The knee joint has hyaline cartilage between the tibia and femur in addition to internal components such as connective tissue and joint capsule. As a special connective tissue, when the human body moves, it will bear great gravity, absorb various mechanical oscillations and impacts at the same time, and it also has a more important linking effect, which will be transmitted to the underlying bone tissue, so it is highly susceptible to damage [24]. When OA occurs, the cartilage tissue becomes less transparent and the texture becomes hard, thus, further damaging the synovial tissue of the joint. This damage to articular cartilage is usually difficult to recover [25].

At present, there is no effective drug for the treatment of OA, and the main obstacle to the improvement of OA treatment is that there is no accurate and effective method for the examination of articular cartilage lesions. Photographs are a traditional method of examining OA, but their clinical application is limited because they cannot directly observe and evaluate cartilage changes [26]. In recent years, nuclear magnetic resonance technology has been continuously developed and advanced, and it has gradually become an effective method for the examination of OA [27]. MRI is mostly used to evaluate cartilage defects in the knee OA using WORMS. The results of relevant clinical studies have shown that WORMS has a high reliability for the detection of the occurrence of cartilage loss [28]. MR T2 mapping imaging is used to quantitatively analyze the changes in the tissue composition of articular cartilage by measuring T2 transverse relaxation time, to make a diagnosis for early cartilage lesions.

At present, the study results on the correlation between MRI findings of cartilage defects in the knee OA and clinical symptoms are inconsistent, and there is still great controversy. Some scholars have shown that the WOMAC score has no correlation with cartilage thickness and the degree of cartilage defect, and there is a significant correlation between cartilage thickness shown by MRI and the joint space width of the flat film [29]. Some scholars have studied the correlation between the degree of cartilage injury and knee joint pain, stiffness, and function WOMAC scores and found that the WOMAC scores of pain and function between different cartilage injury grades were statistically significant, while the WOMAC score of stiffness was not statistically significant [30]. There was no significant difference in WOMAC scores between the mild cartilage injury or normal group and the severe cartilage injury group [31].

WOMAC was used for clinical analysis of patients with OA, T2 mapping imaging sequence and WORMS were used for MRI analysis of patients, and the correlation among the three was analyzed. The results showed that T2 values in P, MF, MT, and LT were positively correlated with WORMS, while T2 value in LF was not correlated with WORMS; cartilage WORMS in the OA group was positively correlated with clinical WOAMC total score, pain score, stiffness score, and joint function score; cartilage T2 values in the OA group were positively correlated with the clinical WOAMC total
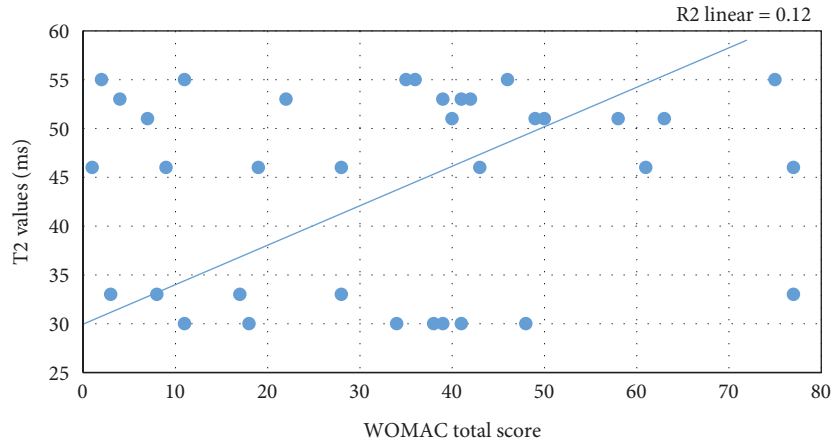
(a)
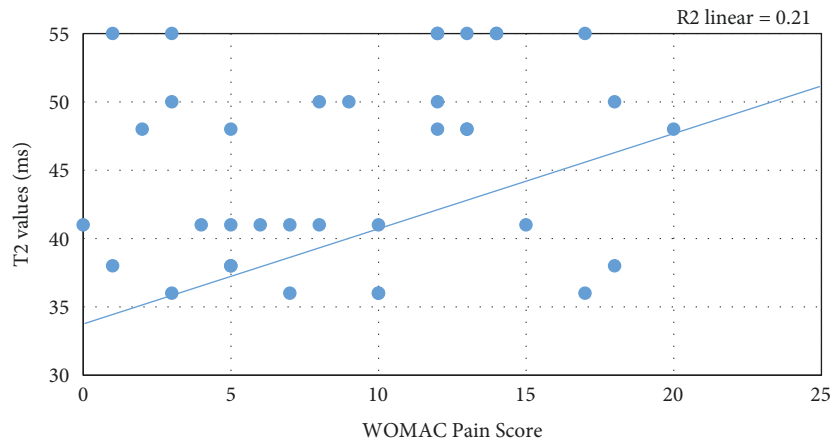
(b)

(c)

Figure 5: Continued.

FIGURE 5: Scatterplot of correlation analysis between cartilage T2 value and WOAMC score in the OA group. (a) WOMAC total score; (b) WOMAC pain score; (c) WOMAC stiffness score; (d) WOMAC joint function score.

score, pain score, stiffness score, and joint function score. There was a clear correlation between MRI findings and clinical symptoms in patients with OA, which is consistent with the results of some previous related studies.

5. Conclusion

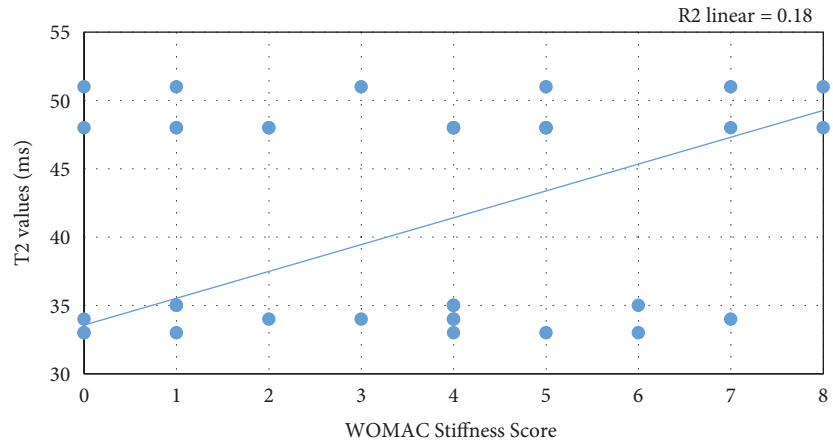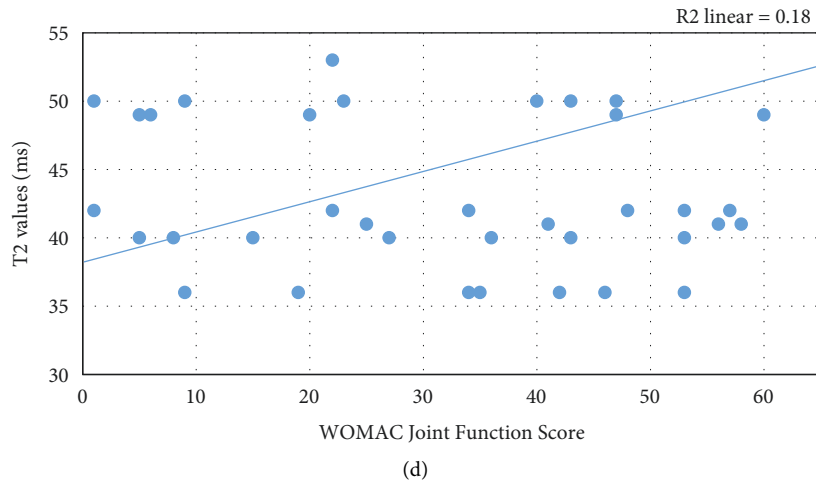Patients with OA were taken as the study subjects in this research, and WOMAC was utilized for clinical analysis of patients. T2 mapping imaging sequences and WORMS were used for MRI analysis of patients, and the correlation between the three was analyzed. A significant positive correlation was shown between the results of the MRI semi-quantitative analysis and the total WOAMC score. This indicated that MRI semi-quantitative analysis had a high clinical application value in the evaluation of clinical features of cartilage injury in patients with knee OA. But this work still had deficiencies. The cartilage WORMS score was somewhat subjective, and there was also a certain random error in the manual delimitation method for T2 value measurement. All of the above factors might lead to certain deviations in the research results. In the future study, the above-mentioned influencing factors would be avoided, and this issue would be further studied comprehensively and in-depth.

Data Availability

The data used to support the findings of this study are available from the corresponding author upon request.

Conflicts of Interest

The authors declare no conflicts of interest.

References

[1] A. Jena, S. Taneja, P. Rana et al., "Emerging role of integrated PET-MRI in osteoarthritis," *Skeletal Radiology*, vol. 50, no. 12, pp. 2349–2363, 2021.

[2] T. W. O'Neill and D. T. Felson, "Mechanisms of osteoarthritis (OA) pain," *Current Osteoporosis Reports*, vol. 16, no. 5, pp. 611–616, 2018.

[3] J. N. Katz, K. R. Arant, and R. F. Loeser, "Diagnosis and treatment of hip and knee osteoarthritis: a review," *JAMA*, vol. 325, no. 6, pp. 568–578, 2021.

[4] V. Juras, G. Chang, and R. R. Regatte, "Current status of functional MRI of osteoarthritis for diagnosis and prognosis," *Current Opinion in Rheumatology*, vol. 32, no. 1, pp. 102–109, 2020.

[5] R. Kijowski, S. Demehri, F. Roemer, and A. Guermazi, "Osteoarthritis year in review 2019: imaging," *Osteoarthritis and Cartilage*, vol. 28, no. 3, pp. 285–295, 2020.

[6] M. Derwich, M. Mitus-Kenig, and E. Pawlowska, "Interdisciplinary approach to the temporomandibular joint osteoarthritis-review of the literature," *Medicina*, vol. 56, no. 5, p. 225, 2020.

[7] A. S. Chaudhari, F. Kogan, V. Pedoia, S. Majumdar, G. E. Gold, and B. A. Hargreaves, "Rapid knee MRI acquisition and analysis techniques for imaging osteoarthritis," *Journal of Magnetic Resonance Imaging*, vol. 52, no. 5, pp. 1321–1339, 2020.

[8] M. Marshall, F. E. Watt, T. L. Vincent, and K. Dziedzic, "Hand osteoarthritis: clinical phenotypes, molecular mechanisms and disease management," *Nature Reviews Rheumatology*, vol. 14, no. 11, pp. 641–656, 2018.

[9] D. Shakoor, S. Demehri, F. W. Roemer, D. Loeuille, D. T. Felson, and A. Guermazi, "Are contrast-enhanced and non-contrast MRI findings reflecting synovial inflammation in knee osteoarthritis: a meta-analysis of observational studies," *Osteoarthritis and Cartilage*, vol. 28, no. 2, pp. 126–136, 2020.

[10] T. L. Vincent, "Peripheral pain mechanisms in osteoarthritis," *Pain*, vol. 161, no. 1, pp. S138–S146, 2020.

[11] A. G. Culvenor, B. E. Øiestad, H. F. Hart, J. J. Stefanik, A. Guermazi, and K. M. Crossley, "Prevalence of knee osteoarthritis features on magnetic resonance imaging in asymptomatic uninjured adults: a systematic review and meta-analysis," *British Journal of Sports Medicine*, vol. 53, no. 20, pp. 1268–1278, 2019.

[12] D. Hayashi, F. W. Roemer, and A. Guermazi, "Recent advances in research imaging of osteoarthritis with focus on

MRI, ultrasound and hybrid imaging," *Clinical & Experimental Rheumatology*, vol. 36, no. 5, pp. 43–52, 2018.

[13] A. Mahmoudian, L. S. Lohmander, A. Mobasheri, M. Englund, and F. P. Luyten, "Early-stage symptomatic osteoarthritis of the knee-time for action," *Nature Reviews Rheumatology*, vol. 17, no. 10, pp. 621–632, 2021.

[14] G. Cai, F. Cicuttini, D. Aitken et al., "Comparison of radiographic and MRI osteoarthritis definitions and their combination for prediction of tibial cartilage loss, knee symptoms and total knee replacement: a longitudinal study," *Osteoarthritis and Cartilage*, vol. 28, no. 8, pp. 1062–1070, 2020.

[15] T. Gorbachova, Y. Melenevsky, M. Cohen, and B. W. Cerniglia, "Osteochondral lesions of the knee: differentiating the most common entities at MRI," *Radio Graphics*, vol. 38, no. 5, pp. 1478–1495, 2018.

[16] B. Felfeliyan, A. Hareendranathan, G. Kuntze, J. Jaremko, and J. Ronsky, "MRI knee domain translation for unsupervised segmentation by CycleGAN (data from osteoarthritis initiative (OAI))," in *Proceedings of the Annual International Conference IEEE Engineering in Medicine Biology Society*, Mexico, 2021.

[17] J. Hirvasniemi, S. Klein, S. Bierma-Zeinstra, M. W. Vernooij, D. Schiphof, and E. H. G. Oei, "A machine learning approach to distinguish between knees without and with osteoarthritis using MRI-based radiomic features from tibial bone," *European Radiology*, vol. 31, no. 11, pp. 8513–8521, 2021.

[18] M. J. Haberfield, B. E. Patterson, K. M. Crossley et al., "Should return to pivoting sport be avoided for the secondary prevention of osteoarthritis after anterior cruciate ligament reconstruction? A prospective cohort study with MRI, radiographic and symptomatic outcomes," *Osteoarthritis and Cartilage*, vol. 29, no. 12, pp. 1673–1681, 2021.

[19] F. Pishgar, A. Guermazi, F. W. Roemer, T. M. Link, and S. Demehri, "Conventional MRI-based subchondral trabecular biomarkers as predictors of knee osteoarthritis progression: data from the Osteoarthritis Initiative," *European Radiology*, vol. 31, no. 6, pp. 3564–3573, 2021.

[20] J. W. MacKay, F. S. Nezhad, T. Rifai et al., "Dynamic contrast-enhanced MRI of synovitis in knee osteoarthritis: repeatability, discrimination and sensitivity to change in a prospective experimental study," *European Radiology*, vol. 31, no. 8, pp. 5746–5758, 2021.

[21] Ø Maugesten, S. J. Pedersen, M. S. Stoenoiu et al., "Reliability and agreement of proton density-weighted vs. gadolinium-enhanced T1-weighted MRI in hand osteoarthritis. An OMERACT MRI special interest group reliability exercise," *Seminars in Arthritis and Rheumatism*, vol. 51, no. 4, pp. 929–932, 2021.

[22] N. Zapata-Linares, F. Eymard, F. Berenbaum, and X. Houard, "Role of adipose tissues in osteoarthritis," *Current Opinion in Rheumatology*, vol. 33, no. 1, pp. 84–93, 2021.

[23] M. W. Little, M. Gibson, J. Briggs et al., "Genicular artEry embolizatioN in patiEnts with oSteoarthrItiS of the knee (GENESIS) using permanent microspheres: interim analysis," *CardioVascular and Interventional Radiology*, vol. 44, no. 6, pp. 931–940, 2021.

[24] S. G. Seo, J. S. Kim, D. K. Seo, Y. K. Kim, S. H. Lee, and H. S. Lee, "Osteochondral lesions of the talus," *Acta Orthopaedica*, vol. 89, no. 4, pp. 462–467, 2018.

[25] A. Frigg, D. Song, J. Willi, A. U. Freiburghaus, and H. Grehn, "Seven-year course of asymptomatic acromioclavicular osteoarthritis diagnosed by MRI," *Journal of Shoulder and Elbow Surgery*, vol. 28, no. 10, pp. e344–e351, 2019.

[26] F. E. Watt, "Posttraumatic osteoarthritis: what have we learned to advance osteoarthritis?" *Current Opinion in Rheumatology*, vol. 33, no. 1, pp. 74–83, 2021.

[27] J. B. Schiratti, R. Dubois, P. Herent et al., "A deep learning method for predicting knee osteoarthritis radiographic progression from MRI," *Arthritis Research and Therapy*, vol. 23, no. 1, p. 262, 2021.

[28] C. L. Daugaard, M. Henriksen, R. G. C. Riis et al., "The impact of a significant weight loss on inflammation assessed on DCE-MRI and static MRI in knee osteoarthritis: a prospective cohort study," *Osteoarthritis and Cartilage*, vol. 28, no. 6, pp. 766–773, 2020.

[29] M. D. Li and C. Y. Chang, "Beyond the AJR: machine-learning, MRI bone shape and important clinical outcomes in osteoarthritis: data from the osteoarthritis initiative," *American Journal of Roentgenology*, vol. 217, no. 2, p. 522, 2021.

[30] J. Huang, X. Chen, M. Xia, S. Lv, and P. Tong, "West lake staging: a new staging system orchestrated by x-ray and mri on knee osteoarthritis," *Journal of Orthopaedic Surgery*, vol. 29, no. 3, 2021.

[31] H. Alizai, W. Walter, I. Khodarahmi, and C. J. Burke, "Cartilage imaging in osteoarthritis," *Seminars in Musculoskeletal Radiology*, vol. 23, no. 05, pp. 569–578, 2019.

WILEY | Hindawi

Research Article

Awakening Effect of Transcranial Magnetic Stimulation with Multimodal Magnetic Resonance Imaging under Three-Dimensional Reconstruction Algorithm Combined with Wake-Up Nursing on Patients with Massive Cerebral Infarction

Bocan Chen,[1] Li Li,[2] and Xiaoxia Ji [1]

[1]*Department of Neurology, The Second Affiliated Hospital of Hainan Medical University, Haikou 570311, Hainan, China*
[2]*Department of Geriatrics, The Second Affiliated Hospital of Hainan Medical University, Haikou 570311, Hainan, China*

Correspondence should be addressed to Xiaoxia Ji; jixiaoxia@hainmc.edu.cn

This study was aimed to provide arousal treatment for disturbance of consciousness in patients with massive cerebral infarction, using multimodal magnetic resonance imaging (MRI)-assisted transcranial magnetic stimulation (TMS) under three-dimensional reconstruction algorithm combined with wake-up nursing. The application effect was also evaluated. 80 patients with massive cerebral infarction were selected as the research objects. These patients were divided into the control group (routine nursing and TMS) and the experimental group (routine nursing, multisensory stimulation wake-up nursing, and TMS) according to the even- and odd-numbered admission orders. There were 40 cases in each group, and the treatment effects of the two groups were compared and analyzed. The peak signal-to-noise ratio (PSNR) (800 dB) of the bilateral filtering algorithm was higher than that of the wavelet threshold denoising (321 dB) and the nonlocal mean filtering algorithm (455 dB). The segmentation accuracy of the improved region growing method/fuzzy spatial clustering algorithm (96.21% and 97.22%) was higher than that of the unimproved ones (82.11% and 79.99%). The Glasgow Coma Scale (GCS), Coma Recovery Scale-Revised (CRS-R), and Dysfunction Scale (DFS) scores of the experimental group were significantly higher than those of the control group 1 week and 2 weeks after treatment ($P < 0.05$). The awakening rate of patients in the experimental group (95%) was also significantly higher than that in the control group (72.5%), and the time needed for waking up was (2.28 ± 2.92) hours, lower than that in the control group (4.34 ± 3.49) hours ($P < 0.05$). The three-dimensional reconstruction algorithm could effectively improve the display effect of MRI images and assist in the examination of diseases. Multisensory stimulation wake-up nursing combined with TMS could promote patients to wake up more quickly and help the recovery of brain function of patients in the treatment of massive cerebral infarction and disturbance of consciousness.

1. Introduction

Disturbance of consciousness is one of the common main symptoms of patients with massive cerebral infarction, and it is closely related to the cerebral edema and neurotransmitter reduction and easily induces a series of complications [1–3]. Studies have revealed that the longer the disturbance of consciousness, the poorer the patients' recovery, and the higher the disability and mortality [4]. Therefore, promoting the recovery of patients' consciousness has received the

attention of global clinical research studies. Clinical studies have found that stimulation of peripheral signals plays an important role in the reorganization and compensation of damaged brain functions [5]. Multisensory stimulation wake-up nursing is to stimulate the senses such as hearing, vision, motion, touch, and smell, so as to promote the excitability of nerve cells and accelerate the recovery of consciousness [6–8]. Research studies have proved that wake-up nursing is worthy of recognition in promoting the self-repair of neurological function and the recovery of consciousness

state in patients with disturbance of consciousness [9, 10]. Multisensory stimulation wake-up nursing indirectly suggests the feasibility of transcranial magnetic stimulation (TMS) in the application of consciousness awakening in severe disturbances of consciousness [11]. TMS is a painless and noninvasive cranial therapy technique because it stimulates the neural excitatory or inhibitory functions of the cerebral cortex through magnetic signals [12]. TMS has been widely used for nonpharmacological treatment of neurological disorders [13] and psychiatric disorders [14]. However, there are few studies about TMS combined with wake-up nursing in the treatment of massive cerebral infarction, and further research is needed.

Due to the lack of specific manifestations in the early stage, the diagnosis of massive cerebral infarction is difficult, and the clinical efficacy is not significant. Therefore, the examination method has attracted attention [15]. Magnetic resonance imaging (MRI) examination has a good effect on massive cerebral infarction, but different MRI sequences have different effects on brain image display. For example, the cerebral cortex is shown by T1-weighted imaging (T1WI) and T2-weighted imaging (T2WI) mainly with high signals, while the equal signal is mainly displayed by diffusion-weighted imaging (DWI) and susceptibility-weighted imaging (SWI); the characteristics of each sequence are different [16]. Therefore, a multisequence MRI examination, multimodal MRI technology, has been proposed; this technology has been widely used in the diagnosis of various clinical diseases. However, the complexity of brain structure and individual differences lead to complex and difficult segmentation of MRI brain images of interest. Currently, the segmentation and three-dimensional reconstruction of MRI brain images are the hot topics in medicine and image processing. Three-dimensional reconstruction technology has been widely applied in diseases of the brain, pelvis, etc. Studies have also shown that three-dimensional reconstruction technology can assist the treatment of patients and improve the treatment effect and functional recovery of patients [17, 18]. The removal of noises and skull and tissue segmentation can affect the three-dimensional reconstruction of the image. The bilateral filtering algorithm has a good application effect in the denoising of medical images. Lee et al. [19] utilized the bilateral filtering algorithm for denoising in the skin surface three-dimensional reconstruction algorithm. The results showed that this method could reconstruct skin surfaces accurately. Marching cubes is also of great significance in three-dimensional image reconstruction, but the traditional marching cubes technology has poor smoothness of three-dimensional images. To improve the reconstruction effect, the improved regularized marching cube (RMC) method was adopted for three-dimensional reconstruction of images.

To sum up, it was to promote the development of neurocritical nursing and provide more effective treatment methods. The disturbance of consciousness in patients with massive cerebral infarction was treated with multimodal MRI-assisted TMS combined with wake-up nursing under the three-dimensional reconstruction algorithm. Its treatment effect was then evaluated, to provide a more effective

research basis for the formulation of treatment plans for patients with clinical disturbance of consciousness.

2. Research Methods

2.1. Research Objects. Eighty patients with massive cerebral infarction, who were admitted to the hospital from October 2020 to March 2022, were selected as research objects. There were 48 male patients and 32 female patients, aged 25–60 years, with an average age of 51.36 ± 9.06 years. Their body mass index (BMI) was $22–26 \, \text{kg/m}^2$, with an average BMI of $(23.73 \pm 0.99) \, \text{kg/m}^2$. The course of disease was 1–7 hours, and the average course of disease was 4.23 ± 2.11 hours. 52 cases were infarcted in anterior circulation and 28 cases in posterior circulation. According to the even and odd numbers of the admission orders, the patients were divided into control group and experimental group. The patients in the control group were given routine nursing and TMS, while those in experimental group was treated with a combined treatment of routine nursing, multisensory stimulation wake-up nursing, as well as TMS. 40 cases were in each group, and the patients in both groups were diagnosed with multimodal MRI under RMC three-dimensional reconstruction algorithm. After that, the treatment effects of the two groups were compared and analyzed. This study was approved by the ethics committee of the hospital.

Inclusion criteria were as follows: their age ≥18 years old, and the gender was not limited; Glasgow Coma Scale (GCS) score ≤14 points; the patients were diagnosed with massive cerebral infarction through computerized tomography or MRI of the head; the informed consent of patients' families was obtained.

Exclusion criteria were as follows: there were implanted metal objects in the body; the patients were complicated with refractory epilepsy or uncontrolled epilepsy; those patients had unstable vital signs, such as deep coma, mydriasis, and shock; those patients withdrew from the research due to various reasons.

2.2. Three-Dimensional Reconstruction Algorithm. The first was image denoising. To improve the quality of MRI brain images, bilateral filtering [20] was adopted for denoising. Bilateral filtering was on the basis of Gaussian filtering and optimized the spatial proximity weight of center point. The specific expression was as follows:

$$g(i, j) = \frac{\int_{(k,l) \in S(i,j)} f(k,l) w(i, j, k, l)}{\int_{(k,l) \in S(i,j)} w(i, j, k, l)}, \tag{1}$$

where $g(i, j)$ represented the output point, $S(i, j)$ represented the range centered on (i, j), $f(k, l)$ was the input point, and $w(i, j, k, l)$ was the value obtained by two Gaussian function calculations.

$$w = wG \cdot wR, \tag{2}$$

$$wG = \varepsilon \cdot - \left| (i - k)^2 + (j - l)^2 \right| \cdot \frac{1}{2\omega_G^2}, \tag{3}$$

$$wR = \varepsilon \cdot -|f(i,j) - f(k,l)|^2 \cdot \frac{1}{2\omega_R^2}. \tag{4}$$

In equations (2), (3), and (4), wG was the spatial proximity Gaussian function, while wR was the pixel similarity Gaussian function. ε represented the constant and ω was the Gaussian coefficient. To make the calculation easier, $w(i,j,k,l)$ was set to be q, and then the following equation was obtained:

$$g(i,j) = \frac{(f_1 \cdot q_1 + f_2 \cdot q_2 + \cdots + f_e \cdot q_e)}{(q_1 + q_2 + \cdots + q_e)} \tag{5}$$

$(q_1 + q_2 + \cdots + q_e) = Q$, from which the following equation was worked out:

$$g(i,j) = f_1 q_1 \cdot \frac{1}{Q} + f_2 q_2 \cdot \frac{1}{Q} + \cdots + f_e q_e \cdot \frac{1}{Q}. \tag{6}$$

The obvious expressions of the convolution operation between the image matrix and the kernel were observed from the above. $q_e \cdot (1/Q)$ stood for the weight of the e-th. The weighted sum was made by the convolution operator, and the output value was finally obtained.

The second was to remove skull in the image.

When the MRI skull was segmented, the more commonly used algorithm was the region growing algorithm, but this method was limited by the unclear border between the skull and brain tissues [21]. Therefore, a method combining automatic thresholding and boundary tracking was put forward. The specific steps were as follows:

The first step: the automatic threshold was adopted to obtain the MRI binary image, and then the pixel point $S(i,j)$ was obtained. The pixel point that satisfied equations (7), (8), and (9) was set as the starting point D.

$$S(i,j) = 0, \tag{7}$$

$$\begin{aligned} S(i-1,j) + S(i,j-1) \\ + S(i+1,j) + S(i,j+1) < 4, \end{aligned} \tag{8}$$

$$\begin{aligned} S(i-1,j) + S(i,j-1) \\ + S(i+1,j) + S(i,j+1) > 0. \end{aligned} \tag{9}$$

The second step: 8 neighborhood points of the coordinates of point D were found in a clockwise direction to satisfy equations (7), (8), and (9), and the satisfied point was set as the new point D. The second step was repeated. Otherwise, it was observed whether there was a D point in each neighborhood point; if it existed, it meant that the boundary search was successful; if not, the third step was carried out.

The third step: the stack was observed. If it was not empty, the top element of the stack was set as D and the first step was repeated. Otherwise, the boundary search failed, which indicated that there was no boundary point.

The fourth step: the algorithm terminated when two boundary points were found.

The third was tissue segmentation.

An improved fuzzy spatial clustering algorithm [22] was used to extract brain tissue in the image. It was supposed that the set of pixel grayscales in the image was expressed as

$$P = (p_1, p_2, \ldots, p_m). \tag{10}$$

Then, the expression of the fuzzy spatial clustering objective function could be expressed as

$$Az(U,V) = \int_{i=1}^{c} \int_{j=1}^{m} \delta_{ij}^{z} (x_i - v_i)^2. \tag{11}$$

where z represented the weighted index, and $1 < z < \infty$. v_i represented the pixel grayscale value of the i-th clustering center, and c represented the number of clustering centers. stood for the similarity measurement method between the data point and the clustering center, and (U,V) was the pixel point. The peak F was obtained by the automatic peak detection method and designated as clustering center. In the same way, the number of peaks was c. Thus,

$$2 \leq c \leq m, \tag{12}$$

$$\delta_{ij} = \frac{1}{\int_{k=1}^{c} \left\{ (x_j - v_i)/(x_j - v_k) \right\}^{2/(z-1)}}. \tag{13}$$

The membership function could be obtained with equation (13). Then, the spatial cost function K_{ij} was imported to suppress noise, and the expression of K_{ij} was as follows:

$$K_{ij} = \int_{k=\text{NB}(x_j)} \delta_{ik}. \tag{14}$$

$\text{NB}(x_j)$ represented the window centered on x_j. When the pixel grayscale values were the same, the value of K_{ij} was greater, so there was a new membership function of

$$\delta_{ij} = \frac{\delta_{ij}^{o} K_{ij}^{b}}{\int_{k=1}^{c} \delta_{ij}^{o} K_{ij}^{b}}. \tag{15}$$

o and b mainly controlled the importance of two functions. The membership function needed to satisfy equation (16), and the clustering center was updated through equation (17).

$$\int_{k=1}^{c} \delta_{ij} = 1, \begin{cases} 1 \leq j \leq m, \\ \\ \delta_{ij} \in [0,1], \end{cases} \tag{16}$$

$$v_{ij} = \int_{k=1}^{m} \frac{(\delta_{ij})^z \cdot x_k}{(\delta_{kj})^z}. \tag{17}$$

After that, the membership function matrix obtained by equation (13) was substituted into equation (11) to obtain a new objective function. When it satisfied $|A_z - A_{z-1}| \leq 3$, the iteration was terminated; otherwise, it was started over from the third step.

The denoised images, skull-removed images, and brain tissue segmentation images obtained by the above algorithms were reconstructed three-dimensionally using the RMC algorithm. The three-dimensional reconstruction method of RMC algorithm could be divided into three parts of surface judgment, merging of seed iso-surface, and iso-surface triangulation. The algorithm application steps were as follows. On the marching cube (MC) algorithm, the direction of the iso-surface was judged to get a surface lookup table, which would pave the way for the next step of iso-surface merging. The seed iso-surfaces were set, the normal was calculated, and the iso-surfaces were merged according to the conditions. The approximation plane was set, and all the vertices of the iso-surface boundary were projected to form a triangular mesh. So far, the three-dimensional reconstruction was completed.

For the evaluation indexes, the peak signal-to-noise ratio (PSNR) was used to evaluate the denoising effect, the segmentation accuracy was to evaluate the segmentation effect, and the three-dimensional reconstruction effect was evaluated by the subjective observation. The specific calculation is shown as follows:

$$PSNR = 10\log_{10}\left[\frac{225^2}{\sum_{i=1}^{Q}\sum_{j=1}^{E}\left(Y_{ij} - X_{ij}\right)^2/QE}\right]. \quad (18)$$

In the equation above, Y_{ij} and X_{ij} stood for the grayscale values of the reconstructed image and the original image, respectively. Q and E represented the row and column of the image, respectively. The higher the PSNR, the better the denoising effect.

$$Acc = \frac{1}{P} \cdot \sum_{j \in C}\left(\frac{R_i}{T_i}\right). \quad (19)$$

P was the number of samples in the test set, C was the set of pixels in the test set, R was the number of correct pixels in the predicted image, and T was the number of pixels of positive samples in the labeled image.

2.3. Examination Method. The examination was performed with 3.0 T MRI scanner and the head coils. The scanning range was from the cranial top to the lower border of the foramen magnum. The patients were instructed to take the supine position, and routine MRI plain scanning (T1WI and T2WI), DWI, and SWI were performed. The specific scanning parameters are shown in Table 1. All the examination images were uploaded to the postimage management system and were processed through three-dimensional reconstruction technology.

2.4. Treatment Methods. The control group received routine nursing and TMS. The routine nursing care included drug treatment as ordered by the doctor immediately after admission, nasogastric feeding to maintain water and electrolyte balance, indwelling catheterization, urethral orifice care, maintaining airway patency, and oral care. The nurse should also help the patients turn over, pat the back, suck phlegm, prevent from pressuring wounds, and place limbs in the good position. Traditional rehabilitation treatments such as acupuncture and physiotherapy were also included. Magnetic stimulation therapy adopted repetitive TMS. The research objects lay flat naturally and were connected to the magnetic stimulation device. For the parameter setting, the stimulation intensity was set to 80% of the motion threshold at rest, and the frequency was 20 Hz; after the stimulation for 1 s, the interval lasted for 6 s. 1200-pulse treatment was given for 7 minutes, once a day and 6 times a week. The stimulation sites were selected from the dorsolateral prefrontal cortex.

In addition to the routine nursing and TMS therapy in the control group, the patients in the experimental group were given multisensory stimulation wake-up nursing as well. The auditory stimulation consisted of the verbal wake-up method and music wake-up method. For the verbal wake-up method, a visit of the patient's relatives and friends (spouse, parents, children, etc.) was scheduled once a day. These relatives and friends were instructed to call the patients' name in the ear and talk to the patients with their favorite, most concerned, or other important things before the onset of the disease, which lasted for 30 minutes. For the music wake-up method, the music that the patients usually liked or were familiar with were repeatedly played at a moderate volume, as the music were understood and carefully selected by the patients' families. This method was carried out for 30 minutes each time, 4 times a day. The visual stimulation adopted the colorful lighting method. With adjustable colorful flashlight, the pupils of the patients were stimulated. It lasted for 30 s for each pupil alternately, 5 times a day. The tactile stimulation included massage stimulation and thermal stimulation. For the limb massage method, the cheeks, ears, arms, and legs of patients were gently touched, and the joints of the upper and lower limbs were massaged. The massage should be gentle, and the duration of each time was about 15–20 minutes, once in the morning and once in the evening. For the thermal stimulation method, two rubber gloves were taken, as one was filled with cold water and the other was filled with hot water. They were placed on the palm or sole of the patients. Each of the hot and cold stimulation lasted for 2 minutes, and the cold and hot stimulations were alternated for 5 times for each operation, once performed in the morning and once in the evening. The olfactory stimulation was the aromatherapy. 0.64 g vanilla essential oil was mixed with 100 mL distilled water, and 10 drops were dropped on a gauze. The gauze was placed about 10 cm away from the head of patients, and the stimulation lasted for 10 s each time, once a day. Taste stimulation was the stimulation of taste buds on the tongue. In the condition that the patients' oral secretions would not cause aspiration to the patients, a cotton swab dipped in saline or lime juice was used to stimulate the front part of the tongue, 5 stimulations each time, 2 times a day. Kinesthetic stimulation was about the limb movement sense. The charge nurse or rehabilitation physician conducted passive movements regularly such as extension, flexion, and external rotation of each joint of the limbs for the patients. The movements were gentle, and the vital signs of patients

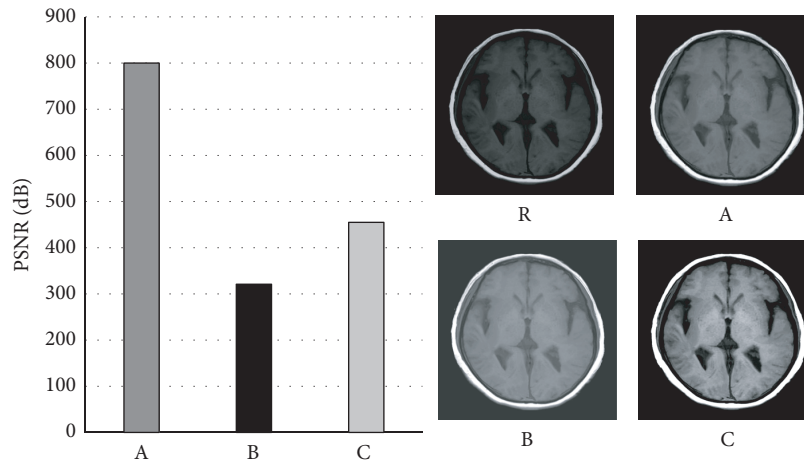|	T1WI	T2WI	DWI	SWI
Time of repetition (ms)	250	4000	5700	25
Time of echo (ms)	2.3	89	90	18
Layer thickness (mm)	4.5	4.5	4.5	2.0
Field of view (mm^2)	220×220	220×220	220×220	220×220
b value			10,1000	

FIGURE 1: Comparison of PSNR and images. R, A, B, and C indicated the original image, bilateral filtering algorithm, wavelet threshold denoising, and nonlocal mean filtering algorithm, respectively.

were also monitored during the movements. The amount of exercise could be gradually increased if the condition permitted, 15–30 minutes each time, twice a day in the morning and evening, respectively.

2.5. Observation Indexes. The GCS [23], Coma Recovery Scale-Revised (CRS-R) [24], and Dysfunction Scale (DFS) [25] were used as the evaluation indexes, which were collected at the same time period (at admission, 1 week after treatment, and 2 weeks after treatment) of patients in each group. The awakening rate and time needed for waking up of the two groups of objects were also observed.

2.6. Statistical Methods. SPSS 20.0 was used for analysis. The enumeration data were expressed as case (%), and the chi-square test or rank sum test was adopted for the comparison between groups. The measurement data were expressed as $(x(\_) \pm s)$, and the t-test was for the comparison between groups and within the group before and after treatment. $P < 0.05$ was considered to be statistically significant.

3. Results

3.1. Comparison of Image Processing Effects. As shown in Figure 1, the PSNR of bilateral filtering algorithm, the wavelet threshold denoising [26], and the nonlocal mean filtering algorithm [27] were compared. The results showed that the PSNR (800 dB) of the bilateral filtering algorithm

was higher than that of the wavelet threshold denoising (321 dB) and the nonlocal mean filtering algorithm (455 dB).

The segmentation accuracy was utilized to evaluate the skull segmentation results of the region growing algorithm before and after the improvement. It was concluded that the accuracy of the improved region growing method (96.21%) was higher than that of the unimproved region growing algorithm (82.11%), which could be observed from Figure 2. Besides, the segmentation effect on the brain tissue of the fuzzy spatial clustering algorithm was also evaluated before and after its improvement. The results in Figure 3 suggested that the segmentation accuracy of the improved fuzzy spatial clustering algorithm (97.22%) was higher than that of the unimproved algorithm (79.99%).

The three-dimensional reconstruction of the brain MRI image was performed on the grounds of the above three kinds of data, and Figure 4 displays the three-dimensional reconstruction images in different directions. The tissue structure of the brain could be clearly observed from the three-dimensional MRI images from the following two directions, suggesting that the three-dimensional reconstructed images had a certain usability.

3.2. Comparison of General Data. Figure 5 presents the distribution of gender, age, BMI, course of disease, and infarction location of patients of the two groups. It could be found that the gender distribution, average age, average BMI, average course of disease, and infarction location of patients in the experimental group were not significantly
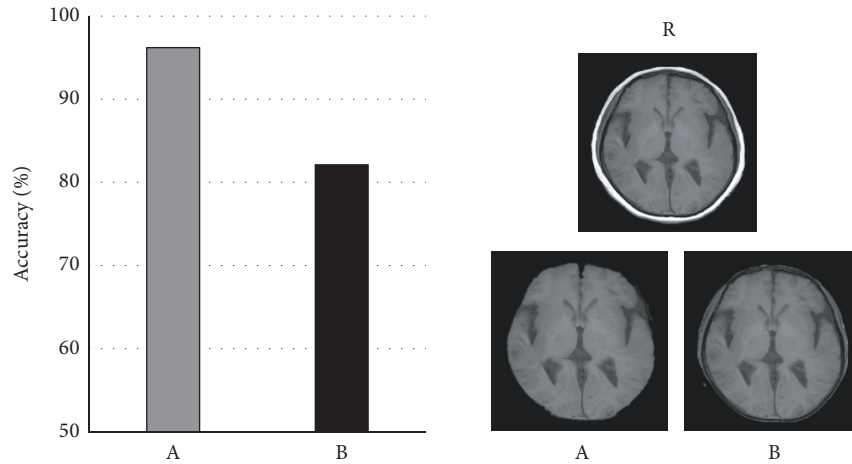
FIGURE 2: Comparison of skull segmentation effects. R: original image; A: improved region growing algorithm; B: region growing algorithm.
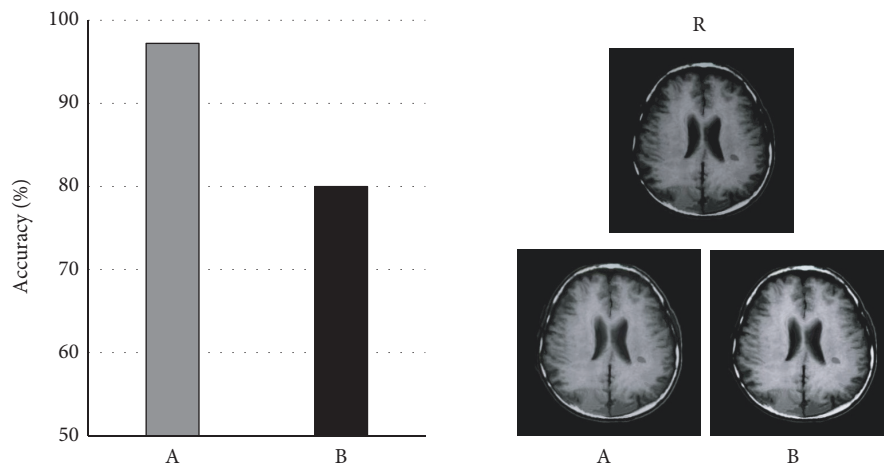

FIGURE 3: Comparison of brain tissue segmentation effects. R: original image; A: improved fuzzy spatial clustering algorithm; B: fuzzy spatial clustering algorithm.
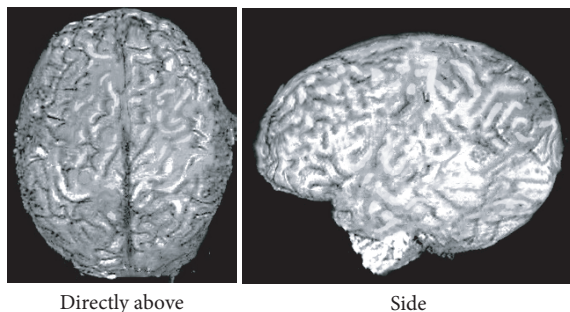

FIGURE 4: Display of the three-dimensional reconstruction effect.

different from those in the control group ($P > 0.05$). This suggested that there was certain feasibility of the research.

3.3. Comparison of Scores before and after Treatment. Figure 6 shows the GCS, CRS-R, and DFS scores of the two groups of patients at admission, 1 week after treatment, and 2 weeks after treatment. The GCS score of the experimental group was (5.97 ± 3.23), (9.32 ± 4.11), and (12.07 ± 3.18) at admission, 1 week after treatment, and 2 weeks after treatment, respectively. The GCS score of the control group was (5.69 ± 3.31), (7.22 ± 3.47), and (9.87 ± 3.98), respectively. At admission, 1 week after treatment, and 2 weeks after treatment, CRS-R score of the experimental group was (5.12 ± 2.03), (7.45 ± 2.76), and (9.76 ± 1.12), respectively, while that of the control group was (5.01 ± 2.12), (5.79 ± 2.62), and (7.91 ± 1.18), respectively. As for DFS score, that was (4.98 ± 3.41), (6.11 ± 4.21), and (7.06 ± 4.39) at admission, 1 week after treatment, and 2 weeks after treatment, respectively, in the experimental group. Then it was (5.00 ± 3.22), (5.47 ± 3.02), and (5.99 ± 4.41), respectively, in the control group. The GCS, CRS-R, and DFS scores of both groups after 1 week and 2 weeks of treatment were higher than those at admission. However, the scores of the experimental group after 1 week and 2 weeks of treatment were significantly higher than those of the control group ($P < 0.05$).
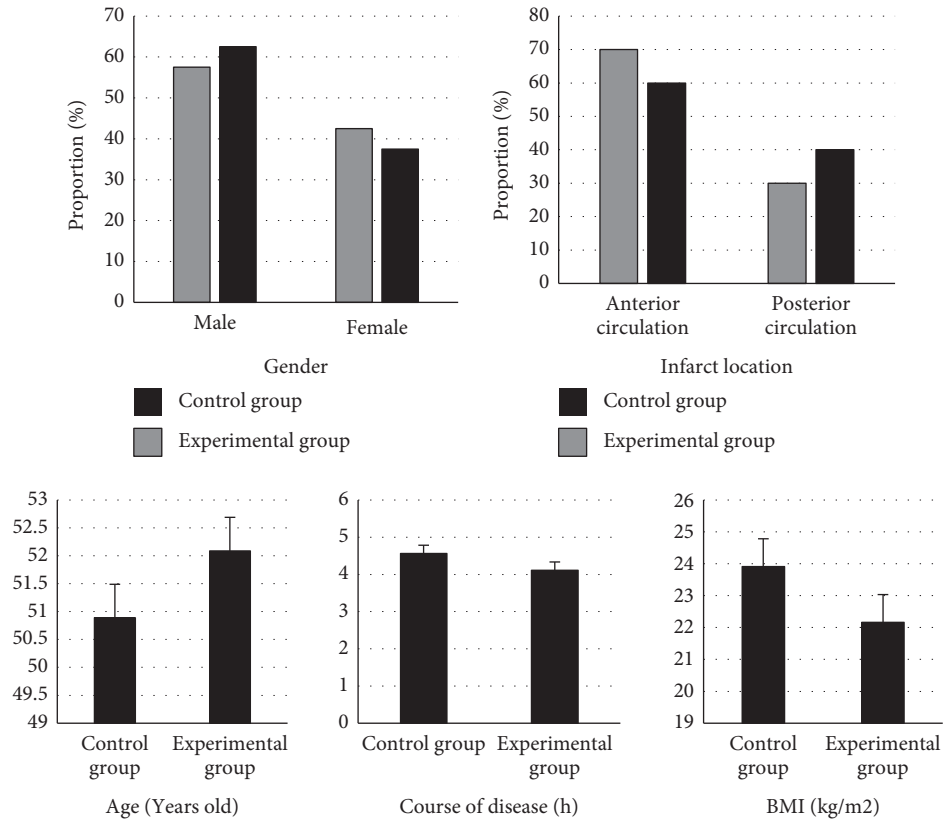
FIGURE 5: Comparison of general data of patients in two groups.
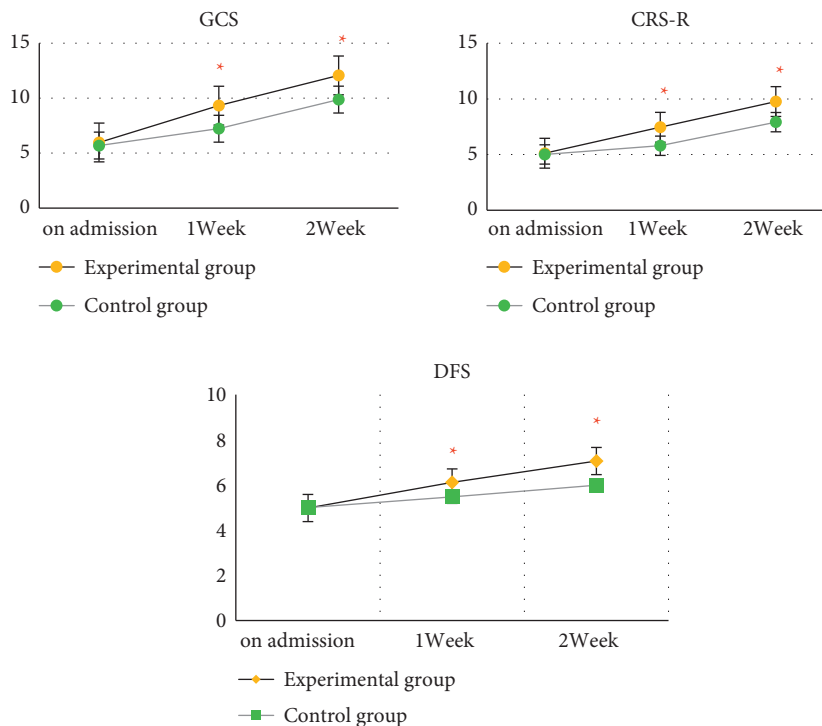

FIGURE 6: Comparison of GCS, CRS-R, and DFS scores. *Compared with control group, $P < 0.05$.
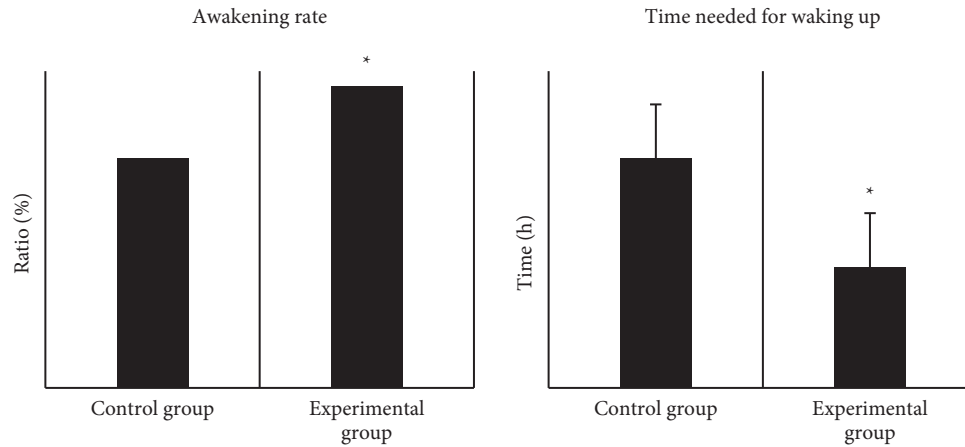
FIGURE 7: Comparison of the awakening status of the two groups of patients. *Compared with control group, $P < 0.05$.

3.4. Comparison of Awakening Situations. Among the 40 cases in the control group, 29 patients (72.5%) waked up after treatment, and the average time needed for waking up was (4.34 ± 3.49) hours. Among the 40 cases in the experimental group, 38 cases (95%) waked up with an average time needed of (2.28 ± 2.92) hours. The awakening rate of patients in the experimental group was significantly higher than that in the control group, and the time needed for waking up was shorter than that of the control group $(P < 0.05)$. The details are presented in Figure 7.

4. Discussion

The multisensory stimulation wake-up nursing was combined with TMS to treat patients with massive cerebral infarction concomitant with disturbance of consciousness, providing a new and effective treatment method for the treatment and prognosis. The results showed that the GCS, CRS-R, and DFS scores of the two groups 1 week and 2 weeks after treatment were higher than those at admission. But the GCS, CRS-R, and DFS scores of the experimental group 1 week and 2 weeks after treatment were significantly higher than those of the control group $(P < 0.05)$. Such results suggested that multisensory stimulation wake-up nursing combined with TMS was more beneficial to the recovery of brain function in patients with massive cerebral infarction and disturbance of consciousness. It has also been suggested that repeated TMS can stimulate neuronal activity in the cerebral cortex, thereby promoting the recovery of brain function and awakening the consciousness of patients [28, 29]. The multisensory stimulation wake-up nursing also helps the recovery of the human central nervous system and enhances the activity of neurons in the upper cerebral cortex, thereby enhancing the connection between the cortex and the subcortical tissue and promoting the awakening of patients [30, 31]. Hong et al. [32] proposed that repeated TMS therapy could improve the neurological function of patients with massive cerebral infarction concomitant with impaired consciousness. The results here also showed that the awakening rate of the patients in the experimental group was significantly higher than that in the control group, while the time needed to wake up was shorter than that in the

control group $(P < 0.05)$. It meant that multisensory stimulation wake-up nursing combined with TMS was more helpful than single TMS treatment for the awakening of consciousness of patients. This supported the above results, which were also consistent with those of Zhong et al. [33].

To make the findings more accurate, the three-dimensional reconstruction-based multimodal MRI images for guided treatment of patients. Ichikawa et al. [34] proposed in their study that the three-dimensional reconstruction algorithm under bilateral filtering algorithm provided the better edge-preserving noise reduction for low-dose computed tomography images. Therefore, in this work, the three-dimensional reconstruction algorithm improved by bilateral filtering algorithm was applied in reconstructing the MRI images of the brain, to assist the treatment of patients. It was shown from the results that the PSNR of the bilateral filtering algorithm (800 dB) was greatly higher than that of the wavelet threshold denoising (321 dB) and the nonlocal mean filtering algorithm (455 dB). This was consistent with the findings of Li [35]. The segmentation accuracy of the improved region growing method/the improved fuzzy spatial clustering algorithm (96.21% and 97.22%) was higher than that of the unimproved ones (82.11% and 79.99%). It was suggested that the combination of automatic threshold and boundary tracking could optimize the region growing algorithm, and the automatic peak detection method could improve the segmentation effect of the fuzzy spatial clustering algorithm. Khodaverdi et al. [35] came up with an automatic threshold and boundary tracking algorithm that could distinguish the target from the background, which was more conducive to image segmentation. Chen and Maharatna [36] proposed that the peak automatic detection method could improve the retrieval efficiency of the clustering centers in the fuzzy spatial clustering algorithm. Therefore, after the optimization of the above algorithms, the reconstruction effect of three-dimensional MRI images became better.

5. Conclusion

In summary, the three-dimensional reconstruction algorithm could effectively improve the display effect of MRI images and played an auxiliary role in the examination of

diseases. Multisensory stimulation wake-up nursing combined with TMS could promote faster awakening in patients with massive cerebral infarction and contributed to the recovery of brain function. However, the sample size selected was relatively small, the scope was relatively limited, and the representativeness was not strong enough. The research scope needed to be further expanded. Multisensory stimulation wake-up nursing had a good auxiliary effect on the treatment of TMS and had a great application prospect worth exploring in clinical practice.

Data Availability

The data used to support the findings of this study are available from the corresponding author upon request.

Conflicts of Interest

The authors declare no conflicts of interest.

Authors' Contributions

Bocan Chen and Li Li contributed equally to this work.

Acknowledgments

References

[1] X. Du, Q. Liu, Q. Li et al., "Prognostic value of cerebral infarction coefficient in patients with massive cerebral infarction," *Clinical Neurology and Neurosurgery*, vol. 196, Article ID 106009, 2020.

[2] X. Wang, Y. Sun, S. Dong, X. Liu, and J. Ji, "Butyphthalide in the treatment of massive cerebral infarction," *Pakistan Journal of Medical Sciences*, vol. 35, no. 1, pp. 220–225, 2019.

[3] T. Kako, F. Azuma, K. Nokura, and H. Izawa, "Clinical study on the cerebral infarction accompanied with septic disseminated intravascular coagulation," *Fujita Medical Journal*, vol. 7, no. 3, pp. 99–104, 2021.

[4] Y. Shimoda, S. Ohtomo, H. Arai, T. Ohtoh, and T. Tominaga, "Subarachnoid small vein occlusion due to inflammatory fibrosis-a possible mechanism for cerebellar infarction in cryptococcal meningoencephalitis: a case report," *BMC Neurology*, vol. 17, no. 1, p. 157, 2017.

[5] Y. Huang, F. Li, Z. Chen et al., "Predictive value of degranulating factors of neutrophils in massive cerebral infarction," *Cell Transplantation*, vol. 30, Article ID 9636897211004089, 2021.

[6] H. K. Lee, I. D. Kim, H. Lee, L. Luo, S. W. Kim, and J. K. Lee, "Neuroprotective and anti-inflammatory effects of a dodecamer peptide harboring ninjurin 1 cell adhesion motif in the postischemic brain," *Molecular Neurobiology*, vol. 55, no. 7, pp. 6094–6111, 2018.

[7] X. Zhang, X. Zhao, C. Zhang, and Z. Lyu, "Improvement of neurological function and stress in patients with acute massive cerebral infarction by mild hypothermia: a prospective randomized controlled study," *Zhonghua Wei Zhong Bing Ji Jiu Yi Xue*, vol. 31, no. 8, pp. 958–961, 2019, in Chinese.

[8] A. J. Martorell, A. L. Paulson, H. J. Suk et al., "Multi-sensory gamma stimulation ameliorates alzheimer's-associated pathology and improves cognition," *Cell*, vol. 177, no. 2, pp. 256–271, 2019.

[9] J. Kim and J. Y. Kim, "Fixation differences in spatial visual perception during multi-sensory stimulation," *Frontiers in Psychology*, vol. 11, p. 132, 2020.

[10] J. Zuo, Y. Tao, M. Liu, L. Feng, Y. Yang, and L. Liao, "The effect of family-centered sensory and affective stimulation on comatose patients with traumatic brain injury: a systematic review and meta-analysis," *International Journal of Nursing Studies*, vol. 115, Article ID 103846, 2021.

[11] D. J. Stultz, S. Osburn, T. Burns, S. Pawlowska-Wajswol, and R. Walton, "Transcranial magnetic stimulation (TMS) safety with respect to seizures: a literature review," *Neuropsychiatric Disease and Treatment*, vol. 16, pp. 2989–3000, 2020.

[12] R. E. Sondergaard, D. Martino, Z. H. T. Kiss, and E. G. Condliffe, "TMS motor mapping methodology and reliability: a structured review," *Frontiers in Neuroscience*, vol. 15, Article ID 709368, 2021.

[13] A. I. Sonmez, D. D. Camsari, A. L. Nandakumar et al., "Accelerated TMS for depression: a systematic review and meta-analysis," *Psychiatry Research*, vol. 273, pp. 770–781, 2019.

[14] I. G. Iriarte and M. S. George, "Transcranial magnetic stimulation (TMS) in the elderly," *Current Psychiatry Reports*, vol. 20, no. 1, p. 6, 2018.

[15] T. Sakai, M. Kondo, Y. Kawana, T. Nakagawa, and H. Tomimoto, "Clinical features of very elderly patients aged 90 years or above with acute ischemic stroke: a study by using diffusion weighted brain magnetic resonance imaging," *Brain and Nerve*, vol. 69, no. 11, pp. 1337–1345, 2017.

[16] S. Escalard, V. Chalumeau, C. Escalard et al., "Early brain imaging shows increased severity of acute ischemic strokes with large vessel occlusion in COVID-19 patients," *Stroke*, vol. 51, no. 11, pp. 3366–3370, 2020.

[17] B. Zhang, L. Qiu, W. Xiao et al., "Reconstruction of the hypothalamo-neurohypophysial system and functional dissection of magnocellular oxytocin neurons in the brain," *Neuron*, vol. 109, no. 2, pp. 331–346, 2021.

[18] J. Wu, K. Xie, D. Luo et al., "Three-dimensional printing-based personalized limb salvage and reconstruction treatment of pelvic tumors," *Journal of Surgical Oncology*, vol. 124, no. 3, pp. 420–430, 2021.

[19] K. Lee, M. Kim, and K. Kim, "3D skin surface reconstruction from a single image by merging global curvature and local texture using the guided filtering for 3D haptic palpation," *Skin Research and Technology*, vol. 24, no. 4, pp. 672–685, 2018.

[20] J. Dang, T. You, W. Sun et al., "Fully automatic sliding motion compensated and simultaneous 4D-CBCT via bilateral filtering," *Frontiers in Oncology*, vol. 10, Article ID 568627, 2020.

[21] Z. N. Isfahani, I. Jannat-Dastjerdi, F. Eskandari, S. J. Ghoushchi, and Y. Pourasad, "Presentation of novel hybrid algorithm for detection and classification of breast cancer using growth region method and probabilistic neural network," *Computational Intelligence and Neuroscience*, vol. 2021, Article ID 5863496, 19 pages, 2021.

[22] M. Hu, Y. Zhong, S. Xie, H. Lv, and Z. Lv, "Fuzzy system based medical image processing for brain disease prediction," *Frontiers in Neuroscience*, vol. 15, Article ID 714318, 2021.

[23] F. B. Mesfin, N. Gupta, A. Hays Shapshak, and R. S. Taylor, *Diffuse Axonal Injury* StatPearls, Treasure Island, FL, USA, 2021.

[24] J. Annen, M. M. Filippini, E. Bonin et al., "Diagnostic accuracy of the CRS-R index in patients with disorders of consciousness," *Brain Injury*, vol. 33, no. 11, pp. 1409–1412, 2019.

[25] A. Shakarami, M. Iravani, M. Mirghafourvand, and M. A. Jafarabadi, "Psychometric properties of the persian version of delivery fear scale (DFS) in Iran," *BMC Pregnancy and Childbirth*, vol. 21, no. 1, p. 147, 2021.

[26] X. Tan, J. Ye, X. Zhang, C. Li, J. Zhou, and K. Dou, "Application of improved wavelet threshold in denoising of ECG signals," *Zhongguo Yi Liao Qi Xie Za Zhi*, vol. 45, no. 1, pp. 1–5, 2021, in Chinese.

[27] D. Ding, S. Ram, and J. J. Rodriguez, "Image inpainting using nonlocal texture matching and nonlinear filtering," *IEEE Transactions on Image Processing*, vol. 28, no. 4, pp. 1705–1719, 2019.

[28] D. Cappon, T. den Boer, C. Jordan, W. Yu, E. Metzger, and A. Pascual-Leone, "Transcranial magnetic stimulation (TMS) for geriatric depression," *Ageing Research Reviews*, vol. 74, Article ID 101531, 2022.

[29] M. M. Zugliani, M. Fidry, R. E. Steffen et al., "Clinical effectiveness of non-TMS neurostimulation in depression: clinical trials from 2010 to 2020," *Progress in Neuro-Psychopharmacology and Biological Psychiatry*, vol. 110, Article ID 110287, 2021.

[30] X. Y. Yang, B. B. Zhang, L. Zhao, and X. Chen, "Effect of multi-sensory stimulation on children with global developmental delay," *Asian Journal of Surgery*, vol. 44, no. 10, pp. 1308-1309, 2021.

[31] D. Adair, D. Truong, Z. Esmaeilpour et al., "Electrical stimulation of cranial nerves in cognition and disease," *Brain Stimulation*, vol. 13, no. 3, pp. 717–750, 2020.

[32] Y. Hong, Q. Liu, M. Peng et al., "High-frequency repetitive transcranial magnetic stimulation improves functional recovery by inhibiting neurotoxic polarization of astrocytes in ischemic rats," *Journal of Neuroinflammation*, vol. 17, no. 1, p. 150, 2020.

[33] M. Zhong, C. Cywiak, A. C. Metto, X. Liu, C. Qian, and G. Pelled, "Multi-session delivery of synchronous rTMS and sensory stimulation induces long-term plasticity," *Brain Stimulation*, vol. 14, no. 4, pp. 884–894, 2021.

[34] K. Ichikawa, H. Kawashima, M. Shimada, T. Adachi, and T. Takata, "A three-dimensional cross-directional bilateral filter for edge-preserving noise reduction of low-dose computed tomography images," *Computers in Biology and Medicine*, vol. 111, Article ID 103353, 2019.

[35] W. Li, "Evaluation of left ventricular diastolic function of patients with coronary heart disease by ultrasound images on bilateral filtering image noise reduction algorithm combined with electrocardiogram," *Pakistan Journal of Medical Sciences*, vol. 37, no. 6, pp. 1699–1704, 2021.

[36] A. Khodaverdi, T. Erlöv, J. Hult et al., "Automatic threshold selection algorithm to distinguish a tissue chromophore from the background in photoacoustic imaging," *Biomedical Optics Express*, vol. 12, no. 7, p. 3836, 2021.

[37] H. Chen and K. Mahxaratna, "An automatic R and T peak detection method based on the combination of hierarchical clustering and discrete wavelet transform," *IEEE Journal of Biomedical and Health Informatics*, vol. 24, no. 10, pp. 2825–2832, 2020.